

**Engineered morphologic material structures: physical/chemical
properties and applications**

Xiangbiao Liao

Submitted in partial fulfillment of
the requirements for the degree of
Doctor of Philosophy
in the Graduate School of Arts and Sciences

COLUMBIA UNIVERSITY

2019

Copyright 2019

Xiangbiao Liao

All Rights Reserved

ABSTRACT

Engineered morphologic material structures: physical/chemical properties and applications

Xiangbiao Liao

Morphologies include the study of shape, size and structure for materials from atomic scale to macroscales. Properties/functions of material structures in general are dependent on morphologies, and thus tunable properties in chemistry and physics can be realized through changing morphologies on surfaces and in bulk systems of materials. For low-dimensional materials, atomic modification or crystal lattice can introduce varieties of fascinating phenomena and unconventional intrinsic properties in electric, mechanics chemistry and *etc.* The reason behind such controllability is that morphological undulation usually is consistent with the mapping of strain, which is related to atomic structures of materials. For micro/macro scale materials, interactions of surface tension, mechanical stress, *etc.* dominate morphological evolutions. Structural design and morphological control can achieve desirable functionalities, for example mechanical flexibility and liquid wettability for practical applications.

Herein, strain-engineering strategies including mechanical loading and atomic engineering are applied to modify and control morphologies in materials with different length scales. We firstly investigate the fundamental mechanism of morphological evolution through various load strategies, and the relationship between morphologies and the properties of material structures across from nanoscale, microscale to macroscale, including graphene, phosphorene, core-shell microparticles and soft materials/bilayers, *etc.* Furthermore, we demonstrate two applications of utilizing designed morphologies, which

targeted to figure out challenges in the field of energy conversion and storage to close energy loop. Therefore, we mainly focus on the relation of engineering strategy-morphology-mechanism/property-functional devices in this thesis.

Firstly, engineered morphologies in nanomaterials of graphene and phosphorene were investigated through loading strategies of strain-localization, gradient strain, bending/pressing. The effects of surface morphologies on fundamental properties including thermal conductivities, mechanics, electrics, surface energy and chemical reactivities were studied through molecular dynamics (MD) simulations and first-principle calculations combined with experimental verifications:

- Increased applications of nanoporous graphene in nanoelectronics and membrane separations require ordered and precise perforation of graphene, whose scalability and time/cost effectiveness represent a significant challenge in existing nanoporation methods, such as catalytic etching and lithography. We reported a strain-guided perforation of graphene through oxidative etching, where nanopores nucleate selectively at the bulges induced by the pre-patterned nano-protrusions underneath. Using reactive molecular dynamics and theoretical models, we uncover the perforation mechanisms through the relationship between bulge-induced strain and enhanced etching reactivity. Parallel experiments of CVD graphene on SiO₂ NPs/ SiO₂ substrate verify the feasibility of such strain-guided perforation and evolution of pore size by exposure durations to oxygen plasma.
- When a nanodroplet is placed on a lattice surface, an inhomogeneous surface strain field perturbs the balance of van der Waals force between the nanodroplet and surface, thus providing a net driving force for nanodroplet motion. Using molecular dynamics

and theoretical analysis, we studied the effect of strain gradient on modulating the movement of a nanodroplet. Both modeling and simulation showed that the driving force is opposite to the direction of strain gradient, with a magnitude that is proportional to the strain gradient as well as nanodroplet size. Two representative surfaces, graphene and copper (111) plane, were exemplified to demonstrate the controllable motion of nanodroplet. When the substrate underwent various types of reversible deformations, multiple motion modes of nanodroplets could be feasibly achieved, including acceleration, deceleration and turning, becoming a facile strategy to manipulate nanodroplets along a designed 2D pathway.

- Using molecular dynamics (MD) simulations, we explored the structural stability and mechanical integrity of phosphorene nanotubes (PNTs), where the intrinsic strain in the tubular PNT structure plays an important role. It was proposed that the atomic structure of larger-diameter armchair PNTs (armPNTs) could remain stable at higher temperature, but the high intrinsic strain in the hoop direction renders zigzag PNTs (zigPNTs) less favorable. The mechanical properties of PNTs, including the Young's modulus and fracture strength, are sensitive to the diameter, showing a size dependence. A simple model is proposed to express the Young's modulus as a function of the intrinsic axial strain which in turns depends on the diameter of PNTs.
- A new phosphorous allotrope, closed-edged bilayer phosphorene nanoribbon, was proposed via radially deforming armchair phosphorene nanotubes. Using molecular dynamics simulations, the transformation pathway from round phosphorene nanotubes falls into two types of collapsed structures: arc-like and sigmoidal bilayer nanoribbons, dependent on the number of phosphorene unit cells. The fabricated nanoribbons are

energetically more stable than their parent nanotubes. It was also found via *ab initio* calculations that the band structure along tube axis substantially changes with the structural transformation. The direct-to-indirect transition of band gap was highlighted when collapsing into the arc-like nanoribbons but not the sigmoidal ones. Furthermore, the band gaps of these two types of nanoribbons showed significant size-dependence of the nanoribbon width, indicative of wider tunability of their electrical properties.

Secondly, we studied fundamental mechanisms of generating fascinating surface morphologies on the micro materials/structures of core/shell microsphere driven by surface instability, which is not different those in nanoscale. The island-like dot pattern on spherical substrate were investigated:

- Through strain-induced morphological instability, protruding patterns of roughly commensurate nanostructures are self-assembled on the surface of spherical core/shell systems. A three-dimensional (3D) phase field model was established for closed substrate. We investigated both numerically and analytically the kinetics of the morphological evolution, from grooves to separated islands which are sensitive to substrate curvature, misfit strain and modulus ratio between core and shell. The faster growth rate of surface undulation was associated with the core/shell system of harder substrate, larger radius or misfit strain. Based on a Ag core/SiO₂ shell system, the self-assemblies of SiO₂ nano-islands were explored experimentally. The numerical and experimental studies herein could guide the fabrication of ordered quantum structures *via* surface instability on closed and curved substrates.

Up to macroscale material structures, the variety and controllability surface morphologies on soft materials and bilayer films were realized through pre-pattern defects

of cavities and in-plane compression. The checkboard and wrinkling surface patterns were observed in different systems through both finite element simulations and 3D printing technique:

- A rich diversity of surface topologies is controllably engineered by patterning cavities embedded beneath the surface of soft materials. Upon external compression, the surface undergoes the reversible transformation from the flat surface to various surface topographies, including the periodic checkerboard pattern with alternatively convex and concave features. To design the surface features, both 2D and 3D finite element based-simulations were performed. It was demonstrated that the periodic surface features with controllable morphology, such as 1D waves, checkerboard pattern and mutually perpendicular apexes, etc. can be realized through varying cavity geometries (e.g., relative inter-cavity distance, shapes and biaxial/uniaxial load). Based on 3D printed prototypes, we further conducted experiments to validate the simulation results of 2D morphologies. The patterned cavities in soft materials made designing a variety of reversible surface features possible, offering an effective fabrication approach for wide application across multiple scales.
- Wrinkle formation followed by sharp strain localization is commonly observed in compressed stiff film/soft substrate systems. However, cavities or defects beneath the film may directly trigger the formation of local ridges and then folding configurations at a relatively small compressive strain, and a mixture of wrinkles and folds upon further compression. The morphological transition is different than those of defect-free substrates. Numerical simulations of continuously compressed bilayer with pre-patterned cavities were carried out to elucidate the transition mechanism of surface

patterns. Parallel experiments of cavities-patterned bilayer prototypes by 3D-printing were also performed to validate the findings in simulations. A rich diversity of periodic surface topologies, including overall spreading waves, localizations, saw-like and co-existing features of folds and wrinkles can be obtained by varying the diameter, depth and spacing of cavities, which provides a potential approach to engineer various surface patterns for applications.

Since these discussed material structures are promising candidates for energy/environmental applications, two device-level functional systems/products here utilize intriguing morphologies in both nanoscale and macroscale. To close energy loop, the energy conversion reactor (chemical loop reduction of CO₂) and the energy storage device (flexible lithium ion battery) were demonstrated:

- We reported an effective reduction method for splitting air-containing CO₂ into CO for high-value chemicals, through a chemical looping redox scheme with Cu-doped LaFeO₃ perovskites as efficient oxygen carriers for splitting CO₂ with a high-concentration of O₂ (e.g. 1:5 O₂/CO₂ molar ratio, mimicking 1:1 CO₂/air mixture). Up to 2.28 mol/kg CO yield was achieved with good stability in the CO₂ splitter, five times higher than that with the conventional pristine LaFeO₃ perovskite. Through *ab initio* calculations, we uncovered that the exsolution of metallic Cu on the surface of reduced perovskite is capable of mitigating the competition between CO₂ and O₂ for the re-oxidation step. This air-stable and scalable scheme can economically integrate with upstream DAC and downstream gas-to-liquids plants, exhibiting up to 94.5% and 42.8% reduction in net CO₂ emission for valuable chemicals production (methanol

and acetic acid) when compared with the coal gasifier-based route and this redox scheme using pure CO₂, respectively.

- Flexible batteries, seamlessly compatible with flexible and wearable electronics, attract a great deal of research attention. Current designs of flexible batteries are unable to meet one of the most extreme yet common deformation scenarios in practice, folding, while retaining high energy density. Inspired by origami folding, we proposed a novel strategy to fabricate zigzag-like lithium ion batteries with superior foldability. The battery structure could approach zero-gap between two adjacent energy storage segments, achieving an energy density that is 96.4% of that in a conventional stacking cell. A foldable battery thus fabricated demonstrated an energy density of 275 Wh L⁻¹ and was resilient to fatigue over 45,000 dynamic cycles with a folding angle of 130°, while retaining stable electrochemical performance. Additionally, the power stability and resilience to nail shorting of the foldable battery were also examined.

Table of Contents

List of Figures	iv
Acknowledgements	xi
Chapter 1 Introduction	1
1.1 Motivation and Progress Overview.....	1
1.2 Backgrounds of Multiscale Morphologies	4
1.2.1 Engineered morphologies on nanomaterial structures.....	4
1.2.2 Engineered morphologies on bulk 3D material structures	6
1.3 Modeling Methods	9
1.3.1 Density Functional Theory	9
1.3.2 Molecular Dynamics.....	10
1.3.3 Phase Field Method	12
1.3.4 Finite element method	13
1.4 Thesis organization	14
Chapter 2 Engineered morphologies on nanoscale material structures	16
2.1 Strain-guided oxidative nanoporation on graphene	16
2.1.1 Introduction	16
2.1.2 Modeling and Experimental Methods	18
2.1.3 Results in Molecular Simulation	20
2.1.4 Results in Theoretical Modeling.....	23
2.1.5 Experimental Verification	24
2.1.6 Conclusion	28
2.1.7 Appendix	29
2.2 Rapid programmable nanodroplet motion on a strain-gradient surface	39
2.2.1 Introduction	39
2.2.2 Modeling and method.....	40
2.2.3 Wetting behavior of strained substrate	41
2.2.4 Nanodroplet movement driven by strain gradient substrate	42
2.2.5 Molecular mechanism.....	44
2.2.6 Actuation by 2D strain gradient: nonlinear pathway.....	46
2.2.7 Generalized substrate.....	48
2.2.8 Conclusion	49

2.2.9 Appendix	50
2.3 Phosphorene nanotube.....	56
2.3.1 Introduction	56
2.3.2 Model and Method.....	58
2.3.3 Thermal stability of PNTs	60
2.3.4 Size-dependent tensile properties	63
2.3.5 Size-dependent thermal conductivity	69
2.3.6 Conclusions	72
2.4 Closed-edged Bilayer Phosphorene Nanoribbons.....	73
2.4.1 Introduction	73
2.4.2 Model and Method.....	75
2.4.3 Deformation and collapsing of PNTs	76
2.2.4 Electronic Properties of Closed-edged Bilayer Nanoribbons.....	80
2.4.5 Conclusion	84
Chapter 3 Engineered morphologies on microscale material structures	85
3.1 Self-Assembly of Islands on Spherical Substrates by Surface Instability	85
3.1.1 Introduction	85
3.1.2 Phase Field Modeling and Experimental Methods.....	89
3.1.3 Linear Stability Analysis	90
3.1.4 Nonlinear Dynamics Simulation	92
3.1.5 Experimental Verification	98
3.1.6 Conclusion	101
3.1.7 Appendix	102
Chapter 4 Engineered morphologies on macroscale material structures.....	106
4.1 Tunable Surface Morphology via Patterned Cavities in Soft Materials.....	106
4.1.1 Introduction	106
4.1.2 Model and Method.....	107
4.1.3 Results in 2D Modeling.....	108
4.1.4 Results in 3D Modeling.....	111
4.1.5 Conclusion	116
4.2 Unconventional Localization Prior to Wrinkles and Controllable Surface Patterns of Film/Substrate Bilayers through Patterned Cavities	117
4.2.1 Introduction	117

4.2.2 Modeling and Experimental Method.....	119
4.2.3 Results and Discussion.....	120
4.2.4 Conclusion.....	127
Chapter 5 Functional devices enabled by morphology manipulation.....	128
5.1 Reduction of Air-containing CO ₂ : Chemical Looping Based on Perovskite Nanocomposites by Cu doping.....	128
5.1.1 Introduction.....	128
5.1.2 Model and Method.....	132
5.1.3 Performance of Cu-doped LaFeO ₃	135
5.1.4 Structural evolution during redox cycles.....	138
5.1.5 Mechanistic investigation.....	141
5.1.6 Redox stability.....	145
5.1.7 Conclusion.....	146
5.1.8 Appendix.....	149
5.2 High-Energy-Density Foldable Battery Enabled by Zigzag-like Design.....	163
5.2.1 Introduction.....	163
5.2.2 Model and Method.....	166
5.2.3 Structure-Mechanical Property Relation.....	167
5.2.4 Electrochemical Performance of Foldable Batteries.....	169
5.2.5 Application Demonstration.....	174
5.2.6 Conclusion.....	176
5.2.7 Appendix.....	176
Chapter 6 Summary.....	181
Chapter 7 Perspectives.....	187
7.1 Energy cycle.....	187
7.1.1 Structural Batteries.....	187
7.1.2 Morphable Structures.....	190
7.2 Carbon Cycle.....	191
7.2.1 Electrocatalytic reduction.....	191
7.2.2 Photocatalytic reduction.....	192
7.3 Water Collection.....	192
Bibliography.....	194

List of Figures

Figure 1.1.1 Schematics of research logistics.....	3
Figure 1.1.2 Schematic of motivation and overview for research progresses.....	3
Figure 1.4.1 Progresses of research work in the thesis.....	14
Figure 2.1.1 Schematic of strain-guided perforation on 2D materials through pre-patterned NPs underneath.....	18
Figure 2.1.2 r-MD simulations demonstration. (a) Strain distribution of graphene adhered to the substrate decorated with NPs array having diameter of 1 nm and periodicity of 5 nm; (b) The morphological evolution of etched graphene with respective to simulation time; (c) The area of created pores as a function of simulation time for graphene and h-BN.....	22
Figure 2.1.3 Mechanism clarification. (a) Spatially continuous distribution of perforation probability by SBA model; (b) Spatially discrete distribution of perforation probability by SFN model, where a single NPs is covered by graphene with periodic boundary condition.....	24
Figure 2.1.4 Morphological characterization of graphene before/after exposure to oxygen plasma. (a) The SEM image of CVD graphene; (b) The magnified SEM image of a graphene bulge; (c) The 2D AFM image of a graphene bulge; (d) Raw Raman spectra of graphene before and after adhering to SiO ₂ NPs/SiO ₂ substrate; (e) The SEM image of graphene with exposed NPs (red arrows) after exposure to plasma oxygen for 6 s; (f) The magnified SEM image of nucleated pore after removing NPs; (g) The 3D AFM image and (h) height profile of created pore with a well-like structure.....	26

Figure 2.1.5 The effect of exposure time on pore growth. Time evolution of (a)-(d) SEM images of created pores. (e) Raman spectra of graphene with increasing exposure durations to oxygen plasma; (f) The ratio of I_D/I_G and I_{2D}/I_G for etching graphene undergoing different exposure times; (g) Statistical summary on the number ratio of unexposed NPs to total sampling NPs as a function of different exposure time.....28

Figure 2.2.1 (a) Top and side view of a 500-water-molecule droplet on a monolayer graphene with a constant strain ϵ . (b) Variation of the contact angle with the strain ϵ42

Figure 2.2.2 (a) Top view and side view of a 500-water-molecule droplet on a monolayer graphene. (b) The time history of the displacement of the mass center of droplet along the x direction. (c) The time history of the velocity of the mass center of droplet along the x direction and y direction. (d) The [variation](#) of interactive vdW potential energy and the system total potential energy with respect to the transport distance x.....44

Figure 2.2.3 (a) The time history of the displacement of the mass center of the 500-water-molecule droplet for various strain gradient G_x . (b) The acceleration of the mass center of the droplet with respect to strain gradient G_x for various sizes of the droplet.....46

Figure 2.2.4 Trajectory of water droplet on a monolayer graphene with tunable strain gradient direction.....48

Figure 2.2.5 (a) Top view and side view of 500-water-molecule droplet on copper (111) surface. (b) Comparison of displacement-time curves of 500-water-molecule droplet on graphene and copper (111) surface.....49

Figure 2.3.1 (a) Top view: crystal structure of 2D phosphorene ($a_1 = 3.3 \text{ \AA}$ and $a_2 = 4.5 \text{ \AA}$); (b) The zigPNT is bended from phosphorene sheet along the wrapping vector $(m, 0) (r$

= $ma_1/2\pi$); (c) the armPNT is bended from MBP along the wrapping vector ($r = a_2/2\pi$); (d) An arm-PNT is divided into $2N$ layers, with the cold layer 1 and hot layer $N+1$60

Figure 2.3.2 The phase diagrams for thermal-stability of (a) armPNTs and (b) zigzagPNTs with varying temperature and wrapping vector of nanotube; (c) The strain energy stored in wrapped PNTs as function of the diameter of armPNTs (black triangular) and zigPNTs (red circles) at $T = 0$ K; (d) The strain energies of (50, 0) zigPNT (red) and (0, 20) armPNT (black) change with temperature.....62

Figure 2.3.3 The axial tensile stress-strain curves for (a) armPNTs and (b) zigPNTs with various wrapping indexes at $T = 0$ K.....64

Figure 2.3.4 Size-dependent mechanical properties at $T = 0$ K. Young's modulus of (a) armPNTs and (b) zigPNTs, fracture strength of (c) armPNTs and (d) zigPNTs. (e) The atomic stress (unit: eV/atomic volume) of PNT structures. (f) The intrinsic axial strain in each sublayer of equilibrium armPNTs (black line) and zigPNTs (red line) at $T = 0$ K.....66

Figure 2.3.5 The nonlinear stress-strain curves of a 2D phosphorene sheet simulated by MD at $T = 0$ K along the (a) zigzag direction and (b) armchair direction; The Young's moduli of the phosphorene sheet along zigzag direction (red line) and armchair direction (blue line) are fitted and plotted as a function of the applied strain, in (c).....69

Figure 2.3.6 (a) An arm-PNT is divided into $2N$ layers, with the cold layer 1 and hot layer $N + 1$; (b) The diameter-dependent thermal conductivity of arm-PNT; (c) The thermal conductivity κ of arm-PNT with varying axial length under temperature $T = 300$ K; (d) Linear fitting of the relationship between the inverse of κ and the inverse of L71

Figure 2.4.1 (a) The schematic of deforming armchair PNT; (b) The deformation pathways of (0,15) and (0,30) armchair PNTs (left) projected to the $d - W$ plane; (c) The strain energy ΔE along deformation pathway as a function of W 76

Figure 2.4.2 (a) The CBPNR configurations derived from the PNTs with odd or even value of n .; (b) The formation energy of PNTs and CBPNRs relative to that of monolayer phosphorene is dependent on the size n78

Figure 2.4.3 The band structures of the (0,14) (a) pristine nanotube and (b) corresponding sigmoidal nanoribbon; The band structures of the (0,15) (c) pristine nanotube and (d) corresponding arc-like nanoribbon.....80

Figure 2.4.4 The spatial charge density associated with the VBM and CBM for the (a, c) PNTs and (c, d) CBPNRs for the size (0,14) and (0,15). The isosurface is set to $0.008 e/b_0^3$, and b_0 is the lattice parameter along nanotube axis. (e)The band gaps of armchair PNTs and CBPNRs are plotted as a function of tube size n82

Figure 3.1.1. The schematic of a spherical core/shell structure: the radius of core is denoted by R and the shell have thickness h88

Figure 3.1.2 The dimensionless growth rate plots as a function of various fluctuation mode degree l characterizing the evolved morphology at various values of (a) normalized size R/h , (b) intrinsic strain ϵ^* and (c) modulus ratio β92

Figure 3.1.3 (a) The evolution of strain energy of the spherical core/shell particle ($R = 50l, h = 4l, \beta = 1/3$) as a function of dimensionless time. (b) The coverage parameter ξ as a function of simulation time for three cases: $R/h = 12.5; R/h = 6.67; R/h = 5.0$95

Figure 3.1.4. Diagrams for surface morphology at given time (a) $t = 80 \tau$ and (b) $t = 100 \tau$. The morphologies of the structure ($R/h = 12.5$) at $t = 200 \tau$ are shown on right sides of (a) and (b)......97

Figure 3.1.5 Three representative surface patterns of the Ag core/SiO₂ shell microstructures with approximate radius of 2.5 μm : (a) smooth surface; (b) uniform islands; (c) relatively sparse and bigger islands.....100

Figure 3.1.6 SEM micrographs of the Ag core/SiO₂ shell microstructures annealed for 10 min, with approximate radii (a) 2.5 μm , (b) 4.0 μm and (c) 7.5 μm . A broken sample with smooth Ag core partially covered by SiO₂ shell is shown in (d) under a cooling rate of 500 K/min.....101

Figure 4.1.1 (a) The top figure: a representative segment of a CESM under a global compressive strain and with labeled geometrical dimensions; the bottom figure: the experimental setup of uniaxial compressing the 3D printed material. (b) The phase diagram of simulated surface textures with respective to the uniaxial compressive strain.....109

Figure 4.1.2 (a) Experimental surface evolutions of 3D-printed CESM prototypes with different values of α . (b) The comparison of amplitude-wavelength ratio between the simulation and experiment for $\alpha = 0.45$111

Figure 4.1.3 Schematics of representative CESMs with patterned cuboidal cavities.....112

Figure 4.1.4 (a) The phase diagram of simulated surface textures and (b) the surface morphologies of cuboidal cavity embedded CESMs for $\gamma = 1$ and $\gamma = 2$ at the uniaxial global compression of 14%. (c) Theoretically critical membrane forces of plates for different buckling modes m as a function of the aspect ratio γ113

Figure 4.1.5 The surface morphologies of cuboidal cavity embedded CESMs with α undergoing the same biaxial global compression of 12%.....	114
Figure 4.1.6 The surface morphologies of CESMs with square patterns of (a) spherical and (b) hemispherical cavities undergoing different biaxial global compression. The surface morphologies of CESMs with one column of (c) spherical and (d) hemispherical cavities undergoing different uniaxial global compression.....	116
Figure 4.2.1 A representative segment of thin film (red) adhered to defected substrate (blue) with pre-patterned holes.....	120
Figure 4.2.2 Simulation (a) and experiment (b) images of the defected bilayer structure at various compressive strains, where $D/\lambda_{wc} = 1$, $h/\lambda_{wc} = 0.1$ and $L/\lambda_{wc} = 5$	123
Figure 4.2.3. The strain for first bifurcation as a function of spacing L in the bilayer with cavities having different diameters and depths.....	124
Figure 4.2.4. The diagram of buckling morphologies for the defected structures ($D/\lambda_{wc} = 1$ and $h/\lambda_{wc} = 0.1$) against applied strain and normalized spacing.....	125
Figure 4.2.5. The diagram of surface morphologies for the defected structures ($h/\lambda_{wc} = 0.1$), where the applied strain is fixed at $\varepsilon_a = 0.02$, against normalized diameter D/h and normalized spacing L/λ_{wc}	126
Figure 5.1.1. Schematic of cyclic redox scheme and its contribution to close the carbon looping.....	131
Figure 5.1.2 Redox performances of Cu-doped LaFeO ₃	136
Figure 5.1.3 Structural and compositional characterizations for fresh and spent La _{0.95} Cu _{0.05} FeO _{3-δ}	140
Figure 5.1.4 DFT simulation results.....	144

Figure 5.1.5 Redox stability of $\text{La}_{0.95}\text{Cu}_{0.05}\text{FeO}_3$ over 50 cycle.....	146
Figure 5.1.6. ASPEN simulation results.....	148
Figure 5.2.1 Fabrication process of the zigzag-like foldable battery.....	166
Figure 5.2.2 Structural design for the zigzag foldable battery.....	169
Figure 5.2.3. The electrochemical performance of the foldable battery undergoing different types of deformations.....	173
Figure 5.2.4 Dynamic loading test of the foldable battery at 1 C.....	174
Figure 5.2.5 a) Voltage profile for the foldable battery under continuously and manually 90° and 180° folding during discharge. b-d) Practical applications of foldable battery to power a series of LEDs in flat, bent and folded configurations.....	175
Figure 7.1.1 The morphologies of elastic rings confined in annular solid constraints.....	188
Figure 7.1.2 Schematic of PVDF/palygorskite nanowires composite as solid electrolyte.....	190
Figure 7.3.1 Schematic of geometrics in micro-pillars.....	193
Figure 7.3.2 Schematic of controlling the local geometrics of micro-pillars through pneumatic elastomer with microchannels.....	193

Acknowledgements

This thesis would not have been possible without guidance, teamwork from many individuals and supports from organizations, although only one single author is stated in this academic dissertation. I acknowledge here those whom I recall at this moment of writing, and express equally gratefulness for those I have forgotten.

First and foremost, I would like to express my special appreciation to my supervisor, Prof. Xi Chen, for his patient instructions, his leadership and his generosity. His well-known creativity, enthusiasm and rigorousness in science/teaching have opened new doors for my horizons and motivated me to energetically face challenges. Most importantly, I am grateful for his friendship and selfless support, which have gave me happy times during the Ph.D. pursuit.

The Prof. Chen's group has become my academic family in the last three and a half years, and I am greatly indebted to their collegiality and support. I am especially thankful to the seniors, Dr. Junfeng Xiao, Dr. Feng Hao, Dr. Xiaoyang Shi for their help questions at group meetings, to Dr. Hang Xiao, Dr. Youlong Chen, Dr. Liangliang Zhu, Mr. Pengfei Yang for their simulation and theory supports, to Dr. Jun'an Pan, Mr. Xiaolong Wu and Mr. Zechen Xiong for his sense of humor and many others for making Prof. Chen's group into a warm harbor.

For this dissertation, I would like to thank the esteemed members of my oral defense committee, Prof. Ponisseril Somasundaran, Prof. Xi Chen, Prof. Robert Farrauto, Prof. Yuan Yang and Prof. Ling Liu for their time and insightful questions. Their advice on both research as well as on my career have been invaluable.

I am particularly indebted to Prof. Yuan Yang from Department of Applied Physics and Applied Mathematics at Columbia University, who welcomed me in his group. It was a big inspiration to be a part of his team and have his great insights. His knowledge along with his inspiration have opened new doors to me, especially at the intersection between mechanics and high-performance battery. I am especially thankful for exchanging ideas and collaborative works with Dr. Haowei Zhai, Dr. Qian Cheng, Mr. Aijun Li, Dr. Bing Zhu, Mr. Changmin Shi, Mr. Tianyang Wang, Mr. Boyu Qie, Dr. Guoyu Qian etc. in his group.

I would like to thank my coauthors, Dr. Kongzhai Li and Dr. Yan'e Zheng, for insightful and creative discussions in Chapter 5.1, which highly motivated me to design new opportunities in future research. I am grateful to Dr. Yonezu Akio and his group for collaborative works in excellent experiments and helpful discussions in Chapter 4. I am especially thankful for my coauthors, Dr. Yong Ni and Mr. Baidu Zhang, for their collaborative efforts in simulations in Chapter 2.1 & 2.2.

I greatly thank to my roommates, Xun Wang and Kaibo Gui, for making home feel like home, and to my basketball partners and accomplices, Ji Wu, Yeping Zhao, Muiyang Li, Huate Li, Haiyun Li, Junan Pan, Zhixing Mao, Yu Tong, Yehua Xie, Zhaozhao Chang, Jing Zhong, Yicong Li, *etc.* who shared endless happiness with me during the Ph.D pursuit.

Lastly, I gratefully thank my parents, Mr. Qiaoyuan Liao and Mrs. Qiumei He and my sisters, Mrs. Yan Liao and Mrs. Duo Liao for all their great love, patience and encouragement in all my pursuits. I would like to express the deepest appreciation to my partner for life, Ms. Taoyuan Xie, and her selfless support and love have always being a source of brightness and happiness in the past months.

Chapter 1 Introduction

1.1 Motivation and Progress Overview

Driven by the expanding demands in sustainable growth, energy security, lower carbon footprint, and effective resource management, the development of advanced materials has become one of the vital components of the next generation of industrial production. Morphology is critical for properties/functions in general, including the study of shape, size and structures of materials^{1,2}. It not only links fabrication, properties and applications, in terms of fabrication-properties-applications relations, and it ranges from atomic scale to macroscale through discrete levels of structural levels. Importantly, most physical/chemical phenomena take place on surface³, including exchange of energy and catalytical reactions, which are unusual with the reduction of dimensions down to nanoscale since the comparable size of nanomaterial to molecule size⁴⁻⁸. To achieve advanced properties (mechanical, optics, electronic, thermal, *etc.*), material scientists have been traditionally used to looking for new compositions, but engineering morphologies of material structures currently provides another strategy for optimizing properties^{3, 9, 10}. Strain, as one of the most powerful tools for manipulating morphology, can either displaces atoms slightly from those equilibrium positions in nanostructured materials for speeding up chemical reactivity (*e.g.* oxidative, catalytical, electrochemical, *etc.*), or change surface topologies of micro/macro materials to achieve functional physical properties (*e.g.* thermal, bandgap, optical, hydrophobicity, *etc.*) for specific technologies¹¹⁻¹⁴. It's great potential for both fundamental mechanism of strain-engineering morphologies and property-morphology relationship, and further for applied technologies in multiscale material structures¹⁵.

The theme of this dissertation is to investigate various morphologies in multiscale material structures through strain-engineering, to investigate fundamental mechanism of morphological formation and the relation properties/morphologies, and finally to search for device-level applications and fabricate products by utilizing morphologies, as shown in **Figure 1.1.1**. Thanks to remarkable advances in multiscale simulations in material science, it's feasible and cost-efficient to understand, design and predict varieties of morphologies from nanomaterials to macro-material structures. Multiscale interactions can be easily incorporated to fundamentally understand mechanisms behind morphological formation and modified properties, including electron-electron interaction, bond and van der Waal interaction, surface tension, stress interaction, *etc.* As an overview in the thesis shown in **Fig 1.1.2**, The materials/structures are exemplified from nanoscale (graphene, phosphorene), microscale (core/shell microsphere) to macroscale (soft materials of PVDF, PDMS, and bilayer structures). The loading strategies of pre-patterned substrate, compression, folding, stretching and bending are adopted to stimulate self-assembly of multi-dimensional morphologies (0D, 1D, 2D and 3D) including nanotube, bilayer ribbon, gradient-crystal, island-like dots on spherical substrates, wrinkling and checkboard surfaces, and so on. Through utilizing the optimized chemical/physical properties in designed morphologies, the applications of carbon reduction, lithium-ion batteries and collection of water droplet are exemplified.

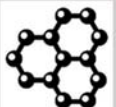
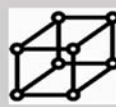
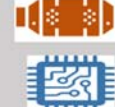
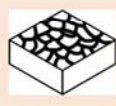
Length Scale	Material Structures	Loading Strategy	Engineered Morphology	Mechanism Properties	Applications /Products
Nanoscale					
Microscale					
Macroscale					

Figure 0.1.1.1 Schematics of research logistics

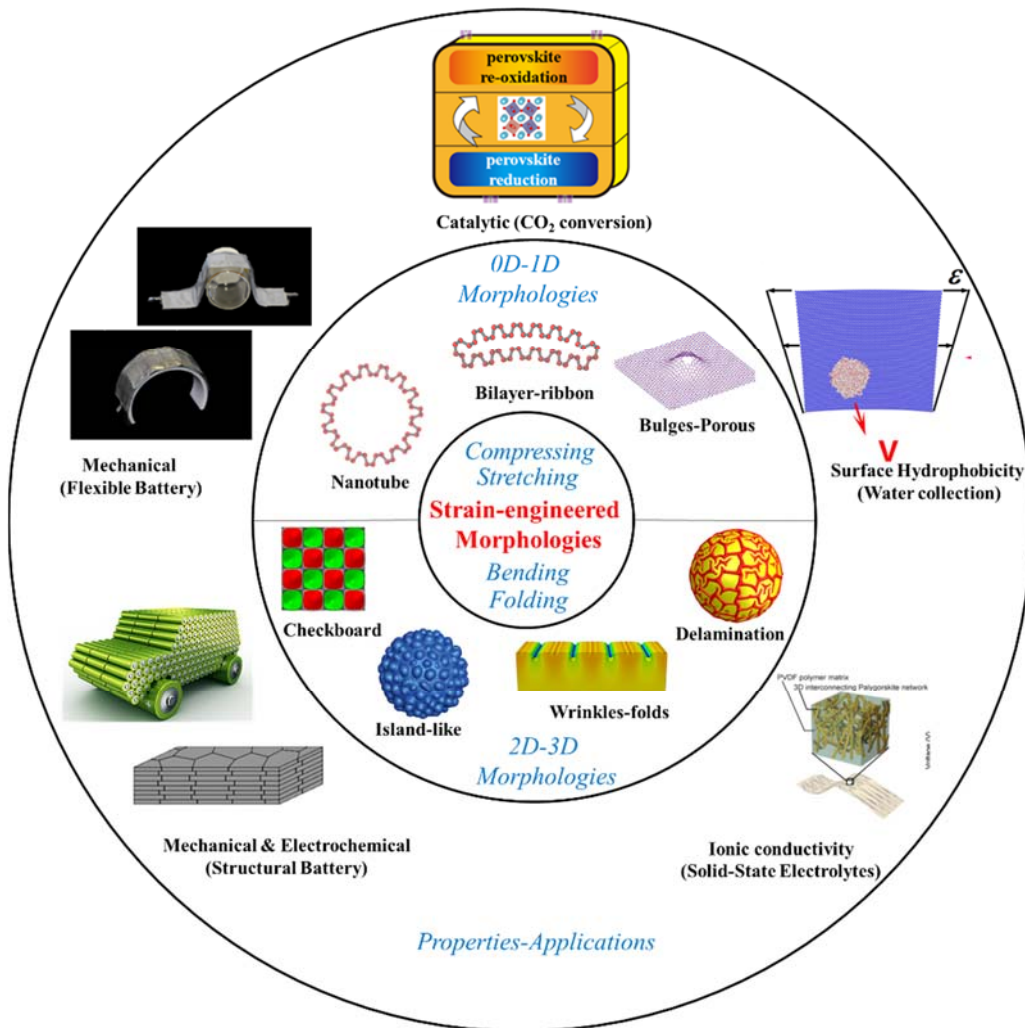


Figure 1.1.1 Schematic of motivation and overview for research progresses

1.2 Backgrounds of Multiscale Morphologies

1.2.1 Engineered morphologies on nanomaterial structures

Nanomaterials, with at least one of dimensions constrained to nanoscale, exhibit unusual chemical/physical properties due to quantum confinement effect, thus attractive for a huge amount of applications in the fields of energy, environment and electronics. Two-dimensional nanosheets, as one of the typical formations of low-dimensional nanomaterials, mainly have the hexagonal topology: 1) the planar hexagonal structure (e.g. graphene, h-BN); 2) the buckled hexagonal structure (e.g. phosphorene, silicene, germanene, stanene); 3) the three atomic layers hexagonal structure (MoS₂, MoSe₂, WS₂, WSe₂). Unlike the bulk materials with the presence of lattice defects and low failure strain, the 2D nanomaterials are promising for strain engineering due to the capability of withstanding larger strain before rupture. 2D nanomaterials exhibit a rich variety of surface morphologies, includes wrinkles, ripples and crumples under either intrinsically thermal vibrations, defects or externally applied strain. The variation of surface morphologies can shift atomic structures of bond configurations and interaction between electronic orbitals. enabling modifications in both chemical activity and physical properties (phonon vibrations, thermal conductivity, polarization, electronic and optical device performances).

To introduce new morphologies in 2D nanomaterials, amounts of strain-engineered strategies are summarized here¹²:

- **Chemical doping/surface anchorage:** Incorporation of smaller/larger atoms into 2D materials can change the atomic morphology locally and thus introduce compressive/tensile strain.

- **Intrinsic thermal ripples:** The thermal fluctuation allows the out-of-plane bending of 2D materials at room temperature, and spontaneous ripples with paradox configuration typically have the characteristic ratio between lateral length and amplitude of ~ 10 . For example, the size distribution of graphene ripples peaks around 8 nm.
- **Delamination from rigid substrate:** 2D nanomaterials can partially delaminate due to the relative weak van der Waals interaction between 2D nanosheets and the substrate, however, the interplay between bending energy of 2D nanosheets and interfacial surface energy can result in the formation of wrinkling morphologies. For example, MoS₂ wrinkles forms on silicon oxides wafer by the mechanical exfoliation.
- **Deformation of flexible substrates:** After transferring 2D materials into flexible substrate (e.g. PDMS), the nanosheets experience strain to conform the deformed configuration of substrate. For example, the method of prestretched substrate can produce well-aligned 1D periodic wrinkles of MoS₂ with the wavelength of $\sim \mu\text{m}$ and the amplitude of 50-350 nm.
- **Modification of substrate topography:** the atomic thickness and interfacial adhesion in 2D nanomaterials allow the sheet to conform to most surface morphologies of substrate, like protruding features. Therefore, local morphologic curvatures are able to manipulate the strain in 2D materials.
- **Pressurized blisters:** Once the fabricated 2D materials are transferred on the pre-patterned cavities, pressure difference can induce blisters due to the impermeability of gas molecules for 2D materials.

Graphene, as one of most promising 2D nanomaterials, exhibits high flexibility for strain-engineered properties via varying surface morphologies thanks to its excellent

mechanical properties (tensile strength of 130 GPa, Young's modulus of 1 TPa, and atomic thickness).¹¹ The tunability of bandgap and pseudomagnetic field can be achieved in graphene-based electronics through orderly perforation graphene (e.g. porous graphene, graphene nanoribbons) and formation of graphene corrugations. Wrinkled graphene exhibits controllable wettability and transparency via stretching/contracting substrate. Due to high surface area and allowance for volume expansion, the charge capacity and power density of crumpled graphene used in energy storage devices can be enhanced significantly compared with flat graphene.⁹ Furthermore, it has been discovered that the topology of graphene governs the relation between electron-hole puddling and functionalization affinity due to strain localizations, thus influencing the chemical reactivity of graphene, which is highly promising for energy applications, for example, hydrogen storage. Thus, it's still possible to design new classes morphologies on low-dimensional nanomaterials and fundamentally understand the formation through strain-engineering.

1.2.2 Engineered morphologies on bulk 3D material structures

Surface geometrical features depend on manufacturing technologies, which thus are related to the surface functionality. In early 1900s, the manufacturing technology of honing were used to allow the control of surface roughness to improve the properties, such as resistance, frictional behaviors, etc. Photolithography is the most popular patterning technique for fabricating surface morphologies in micro/nanoscale due to high efficiency. After the substrate coated with a geometric pattern of light-sensitive polymer (photoresist), a series of chemical processes then etches the exposure pattern into the material, enabling modern electronics. However, there are several limitations of high-cost (polymer materials

and equipment), limited resolution and poor compatibility with soft materials and nonplanar substrate. Although the recent advances of soft lithography, 3D printing and imprint lithography, no single method figures out all the limitations. To address these issues, the self-organization and self-folding of morphologies driven by molecular-scale forces, capillary forces or mechanical forces, is an attractive option for fabricating complex patterns with minimal steps and overcome resolution limits of photolithography. These new methods for engineering the morphology of bulk structures, especially for soft materials, provides opportunities a rich variety of material functionalities in coupling disciplines of materials, optics, chemistry and microelectronics. By harnessing mechanical forces, the transformation of structural morphologies is triggered through instabilities that minimize energy between competing forces, including surface instability, mechanical buckling in thin film, collapse of cellular solids.

- **Surface instability.** Surface instability induces morphological evolution of materials as a result of relaxation or phase separation. Material migration is typically facilitated by field gradients (*e.g.* electric, temperature and mechanical stress) capable of overcoming the surface tension, and surface undulations/regular patterns form with the energy balance between inherent entropy and increased surface area. Strained epilayers resulting from lattice mismatch are widely used in semiconductor systems due to the formation of strained heterostructures (*e.g.* quantum dots), which provides possibilities for nanodevice engineering ¹⁶⁻¹⁸.
- A confined thin film can evolve into a state with lower strain energy by spontaneously morphologic transformation, that's the structural buckling. As a representative, wrinkles with sinusoidally undulating morphology occur on stressed

layered structures. The controllable wrinkling has been used in tuning surface properties, such as adhesion, wetting, optics and micro fluids/electronics. Beyond wrinkling, other new modes of surface morphologies have been discovered experimentally and numerically, including, strain localizations (creasing, folding, ridging) and delamination buckling, which open pathways to exploit diverse surface patterns for new applications. In addition, 2D planar surface patterns can transform into out-of-plane and 3D structures through origami and kirigami strategies under the mechanism of structural buckling. Such self-folding methods have been applied to soft robotics, microgrippers and energy harvesting devices^{19, 20}.

- Cellular materials are ubiquitous in both natural systems and synthetic material structures due to the promising properties in acoustics, energy-adsorption and auxetic materials. It has been found that mechanical buckling can trigger the transformation of void organization in porous materials above a critical value of the applied strain and in a reversible way. Although the void collapsing was traditionally regarded as failure modes, the dramatic change of void morphology provides new opportunities for designing structures with switchable properties and functions²⁰⁻²².

Therefore, it's vital to understand the fundamental mechanism for controlling morphologies by strain-engineering and explore the effect of morphology on physical/chemical through both simulation and experiment tools. We are facing the challenges of energy security, environmental degradation and climate change with the global economic growth in the past century, thus incentivizing scientist and engineers to

search for alternative solutions of renewable energy and clean resources. Advanced materials and structures are the key factors for managing problems from generating clean energy and existing energy sources. Due to the morphology-dependence of chemical/physical properties in materials, we can achieve desired functionalities for potential applications through engineered designs, especially strain-engineering strategies. In this thesis, we mainly focus on applications in the field of energy conversion/storage and water collection, including reduction of carbon dioxide, lithium ion battery, water droplets harvesting and cooling systems.

1.3 Modeling Methods

Due to the increasing efficiency in computer simulations, computational material science in chemistry/physics is a promising tool to predict new material structures, explore their mechanism and finally provide guidelines for experiments. Since morphologies ranging from atomistic scale to macroscopic scale are explored, multiscale computational methods are employed in this thesis including Density Functional Theory (DFT), Molecular Dynamics (MD), phase field method and finite element methods (FEM).

1.3.1 Density Functional Theory

DFT simulation, as a quantum method considering the electronic interactions and exchange energies, can predict the electronic properties of materials in atomic systems. Since the expense of computational time, this method is limited to the system with several hundreds of atoms in the time scale of \sim picoseconds. The electronic structure is evaluated in the framework of Hohenberg-Kohn theorems²³:

- The ground state energy E_0 of a many-electron system is a functional of electron density with respect to three spatial coordinates $\rho(\mathbf{r})$,

$$E_0(\rho) = \int V_{ext}(\mathbf{r})\rho(\mathbf{r})d\mathbf{r} + F(\rho)$$

in which $V_{ext}(\mathbf{r})$ is the external potential acting on electrons and $F(\rho)$ is the functional including the electron-electron correlation and their kinetic energy.

- The electron density at correct ground state minimize the the energy functional for an atomic system

Based on the Born-Oppenheimer approximation, a stationary electronic state can be determined by a wavefunction $\Phi(\mathbf{r}_1, \dots, \mathbf{r}_N)$, which can satisfy the time-independent Schrodinger equation,

$$\tilde{\mathbf{H}}\Phi = E\Phi$$

where $\tilde{\mathbf{H}}$ and E are the Hamiltonian and total energy for the N -electron system. The wavefunction Φ and electron density can be related by,

$$\rho(\mathbf{r}) = N \int d^3r_1 \dots \int d^3r_N \Phi^* \Phi$$

With high accuracy, the DFT method has been used in different disciplines including spin properties, electric and magnetic properties, intermolecular interactions, catalysis and chemical reactivity. In this thesis, DFT method is employed to calculate the electronic structures of nanomaterials undergoing strain-engineering²⁴.

1.3.2 Molecular Dynamics

Molecular dynamics (MD) is a popular simulation method mostly applied in the fields of material science and bio/chemical physics. It studies the movements of atoms and molecules and the dynamic evolution of atomic system during a fixed period of time. The trajectory of particles (atoms, molecules) is determined by solving Newton's second law,

and the forces between particles are calculated using interatomic potentials (non-reactive or reactive force fields). These potentials are classical and non-electron interaction is involved, for example, harmonic potentials as one of non-reactive force fields, which accounts for bonds, angles, torsion, electrostatic and van der Waals interactions. With an initial configuration and a set of constraints, MD simulations can compute the behaviors and evolution of a larger system ($10^3 \sim 10^9$ atoms) over a physically meaningful timescale (1ns~1 μ s) when compared with DFT methods. Thus, the MD method enable us to cost-effectively investigate underlying mechanisms behind material systems and predict/design new and desirable material properties, which are hardly observed in physical experiments. In the thesis, classical MD simulations are used to model mechanical and thermal behaviors of varieties of nanostructures, like graphene and phosphorene.²⁵

However, modeling of chemical reactions requires description for breaking and forming of bonds, as called reactive MD. A bond-order formalism is adopted to describe reactive events, where bond order is empirically interatomic distance dependent in reactive force fields (ReaxFF)²⁶, but without explicit consideration of quantum mechanics. Since reactive MD bridges the gap from DFT methods to classical MD with lower computational expense, simulation scales can be several orders of magnitude beyond those for DFT methods²⁷. Here we employ reactive MD to understand interactions between oxygen with nanomaterials, where is critical for nanopatterning topologies of 2D materials.

1.3.3 Phase Field Method

Microstructures of compositional and morphological inhomogeneities (e.g. crystal grains, soft/hard inclusions) play a dominating role in the physical properties of most engineered materials (e.g. steels), and microstructure evolution is common to be observed in fields of chemical reactions and phase transformation. DFT and MD simulations are difficult to model and predict structural features having a mesoscopic length scale from nanometers to microns (10 nm~10 μ m) and a diffusive time scale, and numerical methods are employed to track interface positions separating compositional or morphological domains. The phase field method, based on the diffuse-interface description, is one of most effective and flexible approaches for modeling microstructure evolution.²⁸

The microstructure is described by continuous field variables and the microstructure interface have a finite width where field variables transit between values (e.g. 0 and 1). The microstructure evolves to reduce free energy F , and is governed by a pair of equations: the Cahn-Hilliard nonlinear diffusion equation and the time dependent Ginzburg-Landau equation²⁹:

$$\frac{\partial C(\mathbf{r}, t)}{\partial t} = \nabla M \nabla \frac{\delta F}{\delta C(\mathbf{r}, t)}$$
$$\frac{\partial \eta(\mathbf{r}, t)}{\partial t} = -L \frac{\delta F}{\delta \eta(\mathbf{r}, t)}$$

where M and L are the interface mobility, C and η are conserved and non-conserved field variables, respectively. The free energy F typically includes bulk chemical free energy, interfacial energy elastic strain energy, electrostatic energy, and ones induced by external fields, for example, applied temperature, stress, magnetic fields. Besides applications of solidification and solid-state phase transformation, phase field methods recently have been

extensively applied to a number of material processes, including thin film growth, stress-induced formation of surface pattern, crack propagation and dislocations. Herein, the phase-field approach is employed to model the surface instability in core/shell spherical microparticles induced by strain mismatch.

1.3.4 Finite element method

The finite element method subdivides a large problem into smaller and simpler parts, as called finite elements, and simple equations for modeling these finite elements are then assembled into a system of algebraic equations. It serves as the most powerful numerical approach to approximately get the real results of partial differential equations. Despite of capability to solve problems in engineering and mathematical physics, the finite element method is here used for modeling the mechanical instability of bilayer structure at the scale of $> 10 \mu\text{m}$. Due to strong geometrical and material non-linearities, the nonlinear finite element method based on ABAQUS software is applied to capture the morphological transformation induced by instabilities. To reduce the computational cost associated with singularities, an artificial damping coefficient is introduced to track the bifurcations during compressing bilayer structures.³⁰

1.4 Thesis organization

The logistic of research works is illustrated in **Fig 1.4.1** and discussed as below:

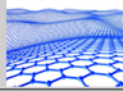
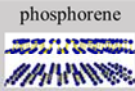
Length Scale	Material Structures	Loading Strategy	Engineered Morphology	Mechanism	Applications /Products
Nanoscale (Chapter 2)	graphene 	strain localization	nanopore (0D)	strain-enhanced reactivity	separation membrane
		strain gradient	gradient crystal surface (2D)	gradient surface energy	droplet manipulation
	phosphorene 	bending	nanotube (1D)	tunable mechanical	flexible electronics
		pressing	close-edge bilayer (2D)	tunable electrical properties	nanoelectronics
Microscale (Chapter 3)	core/shell sphere 	misfit strain	ordered quantum dots (3D)	surface instability	<ul style="list-style-type: none"> optical devices micro/nano fabrication
Macroscale (Chapter 4)	soft materials 	<ul style="list-style-type: none"> patterned cavities in-plane compression 	checkboard undulation (2D)	mechanical buckling	<ul style="list-style-type: none"> self-assembly fabrication reversible surfaces
	bilayer film		wrinkles/folds (1D)		
Device-level (Chapter 5)	chemical looping 	atomic displacement and doping	<ul style="list-style-type: none"> strained lattice Oxygen vacancy (3D) 	enhanced catalytic and redox activity	reduction of CO ₂ captured directly from air
	electrodes 	origami folding	zigzag-like stripe (1D)	flexible thin joints	<ul style="list-style-type: none"> flexible battery wearable electronics

Figure 1.4. 1 Progresses of research work in this thesis

Chapter 2 reports on various morphologies on nanomaterial structures through strain engineering of strain-localization, gradient strain and the regular load of bending and pressing. The fundamentals of morphological formation and nanostructure evolution, including porous graphene, gradient crystal surface, phosphorene nanotube and bilayer nanoribbon are discussed in this chapter. We explored the relationship between such engineered morphologies and electronic/thermal/mechanical properties, surface energy and chemical reactivity. These well-designed morphologies are potentially beneficial for applications in separation membrane, droplet manipulation and nanoelectronics.

As an example of microscale material structures, surface morphological evolution on the core/shell microsphere are discussed in Chapter 3. Utilizing misfit strains initiated from thermal or lattice difference, the flat surface transforms into island-like dots on spherical substrate driven by surface instability involving surface energy. The controllable microfabrication strategy is critical for optical technologies.

The surface morphology of soft material as popular substrates for nanomaterials is important for transferring and fabricating nano/micro structures. In Chapter 4, the strategies of pre-patterned cavities and in-plane compression are used to initiate morphological transformation in macro-material structures of soft materials and bilayers.

Not limited to material level, Chapter 5 then turns to device-level functional products using strain-engineered morphologies. The engineered strategy of atomic doping is adopted here to modify the lattice of perovskites for the system of chemical looping-reduction of CO₂, while lithium-ion batteries with flexibility are demonstrated through origami-folding design on electrodes.

Finally, Chapter 6 goes beyond these doctoral works in multiscale material structures for energy conversion/storage applications. The future studies firstly focus on the field of energy including structural/high-safety batteries and morphable structures for energy conversion. Secondly, other opportunities for reducing CO₂ from direct air capture in the field of carbon cycle will be discussed. Finally, fundamentals and devices for water droplet collection will be extended.

Chapter 2 Engineered morphologies on nanoscale material structures

2.1 Strain-guided oxidative nanoperforation on graphene

Graphene with atomic thickness is one of the most popular nanomaterials are promising candidates for applications in the fields of energy and environment due to extraordinary chemical/physical properties³¹⁻³³(Lee, Wei et al. 2008, Geim 2009, Li, Cai et al. 2009)[31-33][30-32][30-32][30-32][30-32][30-32][30-32][30-32][30-32][30-32][30-32][30-32][30-32] of graphene. In this Section 2.1, strain-localization by pre-patterned substrates was used to specify the regions with high chemical reactivity, and guide perforation on graphene by oxidative etching. The porous graphene with separate and uniform nanopores are critical for electrodialysis and membrane separation.

2.1.1 Introduction

Nanoporous graphene, a monolayer graphene perforated by nanoscale pores^{34, 35}, has been used in various separation fields including DNA sequencing³⁶, water desalination^{37, 38} and gas separation^{39, 40}. The pores of several nanometers, even comparable with Debye screening length, can be used as effective filters based on molecular sizes and charges^{37, 41-43}. The tunable pore size of a nanoporous graphene may yield promising performances over traditional polymer-based membrane technologies in water/gas permeability and separation selectivity^{37, 38, 44}. These membrane applications necessitate facile and scalable fabrication/synthesis of nanoporous graphene sheets.

Various fabrication methods have been proposed for generating tiny pores with controllable size in graphene sheets^{34, 45}. The top-down nanolithography (e.g. electron

beam and ion beam bombardment)⁴⁶⁻⁴⁸ and the bottom-up organic/on-surface syntheses⁴⁹ have been developed to create pores with desired size of 2 nm ~ 100 nm, however, both with complexity and time-expansiveness that hinder scalable applications. Chemically etching methods could treat large-area graphene but often introduce randomly distributed pores with poor edge quality^{38, 40, 50, 51}. Structurally uniform nanopores, especially with the pore size/neck width as narrow as several nanometers, are essential to achieve tunable bandgaps on a large sheet of graphene for electronic applications^{46, 49}. Previously reported precise fabrication methods, such as barrier-guided chemical vapor deposition and thermally/catalytically activated noble metal nanoparticles apart from block copolymer lithography^{35, 45, 52, 53}, also experience high-cost and low scalability that are detrimental to industrial applications. A facile and cost-efficient fabrication for selective nanoporation with desired size/pattern on graphene still represents a challenge.

We proposed a simple and scalable strain-guided perforation method, where structural nanopores can be selectively fabricated on a strain-modulated 2D material (e.g. graphene, boron nitride) sheet by pre-patterned nanoparticles (NPs) on substrate. As illustrated in **Fig 2.1.1**, NPs are firstly deposited on the substrate. Then, a monolayer of 2D material is transferred to cover and geometrically conform the NPs-decorated substrate, followed by oxidative etching. In essence, the high-strain magnitude near the bulges enhances the chemical potential for etching and initiation of nanopores. Note that unlike the constraint of catalytic performances^{52, 53}, the local bulge morphology may be induced and manipulated by a significant variety of NPs, such as carbon fullerence, inorganic NPs (e.g. SiO₂ and metal) and polymer blocks, and the engineered strain contour may affect oxygen adsorption and perforation probability, hence pore geometry. In the following, we

validate the mechanism using reactive molecular dynamic (r-MD) simulation, continuum shell-based analytical model (SBA model), and discrete space frame numerical model (SFN model). We also perform parallel experiments of plasma oxygen etching CVD graphene on a SiO₂ NPs/ SiO₂ substrate. The feasibility and controllability of such strain-guided perforation are verified through scanning electronic microscopy (SEM), Raman analysis and atomic force microscopy (AFM).

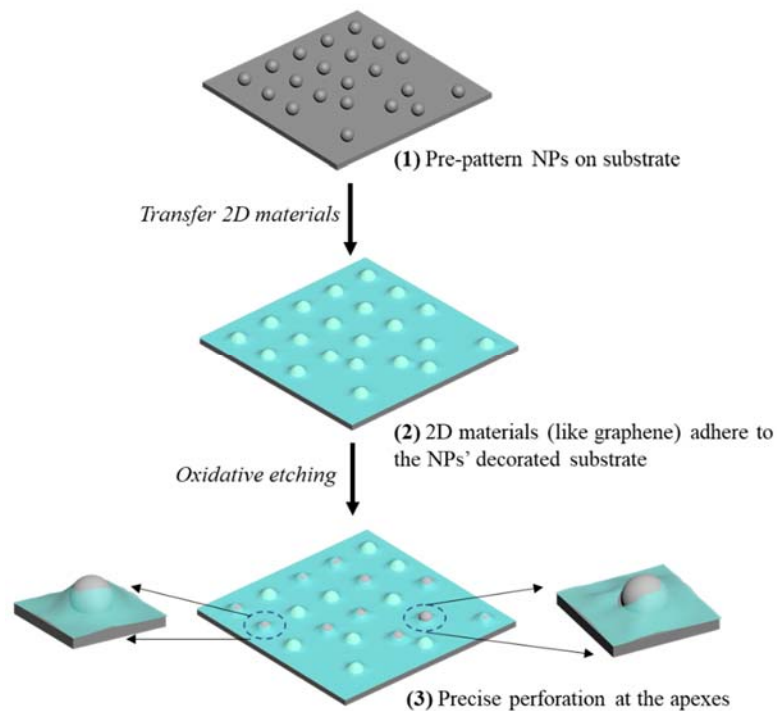


Figure 2.1.1 Schematic of strain-guided perforation on 2D materials through pre-patterned NPs underneath

2.1.2 Modeling and Experimental Methods

Reactive MD Simulation Method. All of the MD simulations were carried out on the LAMMPS package⁵⁴. For the pre-patterned etching shown in **Fig 2.1.2**, the simulation

box consists of a monolayer graphene and a rigid substrate with 2×2 rigid nanoparticles decorated. The oxygen atoms randomly distribute above the graphene. The ReaxFF-CHO force field⁵⁵ was used to model the graphene and the oxygen plasma, and the 12-6 Lennard-Jones pair potential was used to describe the interaction of graphene and substrate⁵⁶. For h-BN, the ReaxFF-AB was used instead⁵⁷. The periodic boundary condition was applied to the x and y directions. A reflect wall was set at the top of z direction. The simulation was first performed in NPT ensemble at 300K and 1 atm for 200 ps with a timestep of 1 fs until the equilibrium was reached and the graphene adheres to the substrate. During the equilibrium, there is no reaction between the oxygen atoms and graphene. Then the temperature was slowly increased to 1500K in 100 ps with a timestep of 0.2 fs and then maintained unchanged. The oxygen atoms would adsorb to the bulges of graphene and etch carbon atoms as the form of CO or CO₂. The number of carbon atoms etched with the respect to simulation time was recorded.

NPs arrangement on SiO₂ plate: We used commercial slide glass SiO₂ plate with 18 mm x 15 mm x 2 mm (S1214, Matsunami Glass Corp.). On this plate, NPs of SiO₂ with 50 nm diameter (Sicstar, Micromod Partikeltechnologie GmbH) were aligned using a dip coating technique. We first prepared NPs solution, which is diluted by 100 times using high distilled water. Subsequently, the SiO₂ plate was immersed into the NPs diluted solution with the speed of 4.5 m/s using a ball screw stage (SGSP33-100, Sigmakoki Corp.). And then, it was pulled out to atmosphere with the same speed. After that, the SiO₂ plate is dried at room temperature.

Oxygen plasma etching: Oxygen plasma etching equipment (Compact Etcher FA-1, Samco Inc.) was used to nucleate nanopores in graphene. We set the power of 20 W and

oxygen flux of 20 ml/min. This study conducted four different etching time (1.5 s, 3 s, 4.5 s and 6 s). Noted that since oxygen plasma etching is relatively strong for graphene, cover plate was used during etching process to avoid direct etching against the graphene.

Removal of NPs: To observe nucleate nanopore of graphene, the etched sample was immersed into deionized water with 1200 $\mu\text{m/s}$ using the above dip coating system. We immersed the sample in deionized water for about 30s.

FESEM and AFM: To observe NPs and nanopores on graphene, FESEM (JSM-7001F, JEOL Ltd.) and AFM (AFM-5300E, Hitachi High-Technologies Corp.) were used. For FESEM observation, accelerate voltage was set to 15.0 kV and magnifications were from 50k to 200k times. For AFM measurement, silicon tip of AFM cantilever (SI-DF3, Hitachi High-Technologies Corp.) was used and dynamic force mode was employed. Scanning speed was set to from 190 nm/s to 3800 nm/s.

2.1.3 Results in Molecular Simulation

We first employed r-MD simulations to demonstrate the feasibility and controllability of perforating graphene. **Fig 2.1.2(a)** shows the strain contour on the graphene sheet adhered to the substrate decorated with a square pattern of NPs. Strong adhesion between graphene and substrate induces the periodical bulges with a maximum strain of 6.0% at the dome, where the C-C bonds are stretched. Note that NPs with the diameter $D = 1 \text{ nm}$ are simulated without loss of generality due to the size independence of the maximum strain and the self-similarity in bulge geometric with increasing NP's size (**Figure 2.1.S1**), and the inter-distance $L = 5 \text{ nm}$ between NPs is far enough to eliminate

NPs' interaction. Next, upon an atmosphere with the oxygen number density $1.2 \times 10^{-3} / \text{\AA}^3$ and the temperature 1500 K, the oxygen atoms reacts with the strain modulated graphene and the temporal evolution of graphene topology is demonstrated in **Fig 2.1.2(b)**. At the initial stage (0 ~ 70 ps), oxygen atoms are preferably adsorbed at the high-strain concentration, and the pores are selectively initiated through the breaking of C-C bonds, followed by the formation of single vacancy defects and removal of carbon atoms in the form of carbon dioxides or carbon monoxides (70 ps ~ 100 ps) (**Figure 2.1.S2**). Subsequent carbon atoms are continuously removed and the pore size is grown, while other regions keep intact despite minor oxygen adsorptions. Finally, an ordered pattern of pores with diameter of 0.86 nm is achieved at 280 ps, and the pore edges are decorated with oxygen atoms. Note that the nanopore periodicity can be easily tuned through the inter-distance of assembled NPs. Comprehensive simulations further demonstrate that both higher temperature and oxygen concentration can lead to a larger perforation rate (**Figure 2.1.S3**), which suggests a controllable perforation method on graphene. **Fig 2.1.2(c)** quantitatively indicates that such initiated pores expand slowly at the starting stage (0 ps ~ 100 ps) and then grow almost linearly at the rate of $0.43 \text{\AA}/\text{ps}$, indicating that the perforation rate limited by the initial steps of oxygen adsorption and single vacancy formation. However, the activities of such rate-limited steps could be highly enhanced at high-strain bulges, since the oxygen adsorption energy increases significantly with increasingly elongated C-C bonds⁵⁸, confirmed by our r-MD results (**Figure 2.1.S4**).

To illustrate the transferability to other 2D materials, the single layer of boron nitride (BN) is exemplified to be perforated by the same method (**Figure 2.1.S5**), although its perforation rate is faster than that for graphene monolayer shown in **Fig 2.1.2(c)**, since

boron atoms exhibit higher reactivity with oxygen compared with carbon atoms⁵⁹. Furthermore, the success of perforation using chemically stable C₆₀ fullerene (**Figure 2.1.S6**) as strain-initiators verified that the local reactivity on 2D materials is only enhanced by the bending-induced strain, unlike the catalytical etching by using Pt NPs, which is much more expensive^{52, 53}. This viability implies a broad choice of strain-initiator, and the pre-patterned NPs can provide a feasible template for controllably and selectively perforating various 2D materials through strain-guided oxidative etching.

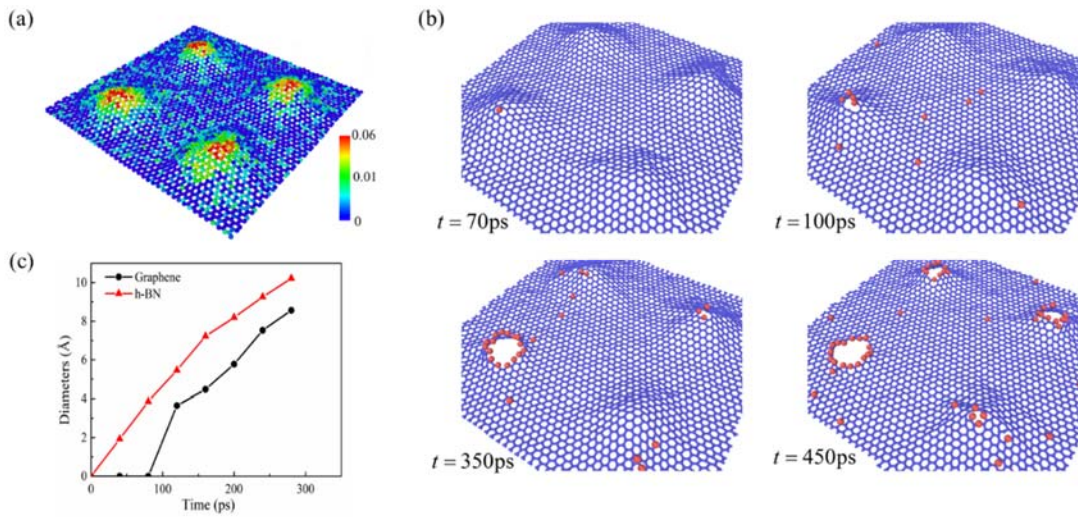


Figure 2.1.2 r-MD simulations demonstration. (a) Strain distribution of graphene adhered to the substrate decorated with NPs array having diameter of 1 nm and periodicity of 5 nm; (b) The morphological evolution of etched graphene with respective to simulation time; (c) The area of created pores as a function of simulation time for graphene and h-BN.

2.3.4 Results in Theoretical Modeling

To quantify the spatial selectivity of oxidative etching, the perforation probability ρ is deduced to elucidate the strain-guided mechanism. Based on r-MD simulations, we assume that the distribution of perforation probability is associated with the spatial variation in relative chemical activity \tilde{a} of 2D materials. The relative perforation probability scales as

$$\rho(x, y)/\rho_0 \sim \tilde{a}(x, y) = e^{\frac{\Delta\mu(x, y)}{RT}}$$

where $\Delta\mu(x, y)$ represents the change of chemical potential on the dome with respect to the unstrained flat region, ρ_0 is the reference perforation probability in unstrained graphene, and R and T are the gas constant and absolute temperature, respectively. For simplicity, the NPs-induced strain energy ε is considered as the only contribution to $\Delta\mu$. Here, two different models are developed to estimate the distribution of $\varepsilon(x, y)$: 1) The shell-based analytical model (SBA model) considers the graphene as a continuum elastic film with effective mechanical properties⁶⁰; 2) A space-frame numerical model (SFN model), where primary and secondary beams are used to bridge the nearest and next-nearest carbon atoms, associated with bond stretching and angle variation⁶¹, respectively. For an infinite graphene supported by a single nanoparticle, the maximum strain calculated by the SBA model is 6.8% at the dome (**Figure 2.1.S7**) and the SFN model predicts a locally concentrated strain energy distribution (**Figure 2.1.S8**). Note that the SBA model further verifies that the maximum strain at the film dome is independent to the size of NPs (**Figure 2.1.S9**). The continuous distribution of perforation probability is given in **Fig 2.1.3(a)**, and NPs-induced dome encompass 4 orders of probability higher than those in flat region, and the perforation

probability decays exponentially in the range of particles' radius. The discrete perforation probability of carbon atoms deduced from the SFN model is shown in **Fig 2.1.3(b)**. Both models confirm the priority for oxygen reacting with carbon atoms at strain concentrations. Therefore, through engineered strain distribution, the supporting NPs serve as a tunable template for controlling reactive activity of carbon atoms and thus guiding perforation sites.

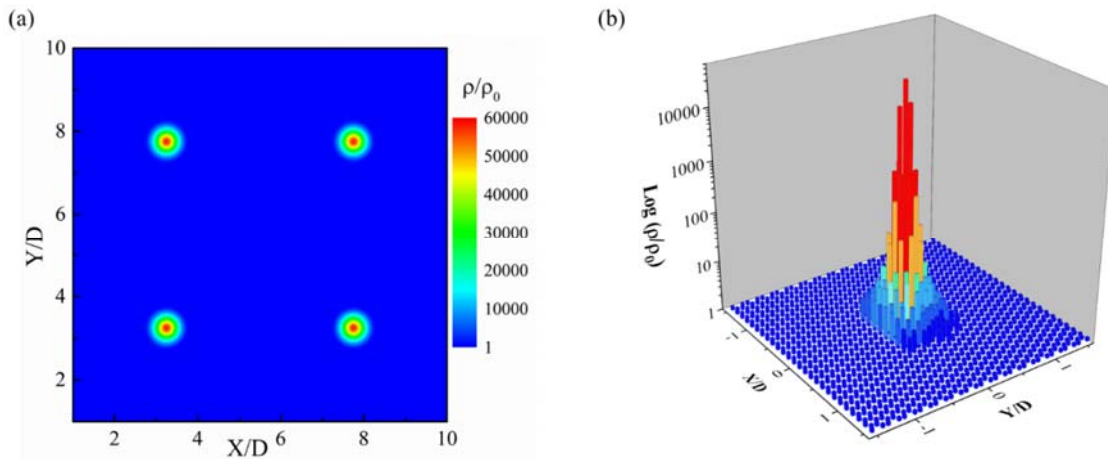


Figure 2.1.3 Mechanism clarification. (a) Spatially continuous distribution of perforation probability by SBA model; (b) Spatially discrete distribution of perforation probability by SFN model, where a single NPs is covered by graphene with periodic boundary condition.

2.3.5 Experimental Verification

Oxygen plasma with high chemical reactivity to carbon-based material is adopted to study oxidative etching graphene supported by NPs. Due to the size independence of the NPs-induced maximum strain, SiO_2 NPs with diameter of ~ 50 nm are demonstrated here. The isolated SiO_2 NPs with insulating and clean surfaces are prepared on SiO_2 substrate

through a dip coating method, and the micro-morphologies of bare NPs are demonstrated in **Figure 2.1.S10**. Next, a single layer graphene, synthesized using chemical vapor deposition (CVD), is transferred to the SiO₂ NPs/SiO₂ substrate through a polymer transfer method. As shown in **Fig 2.1.4(a)** and **2.1.4(b)**, SEM images reveal that while keeping flat in most regions, graphene locally delaminates from the SiO₂ substrate and forms dome-like morphology conforming to the NP. Illustrated by the AFM image (**Fig 2.1.4(c)**), the graphene apex of bulge is vertically displaced by 30 nm and the span of delaminated region is roughly 120 nm. We also observe ridge-like wrinkling features surrounding bulges in **Fig 2.1.4(a)** and **2.1.4(b)**, confirmed by our r-MD simulations (**Figure 2.1.S11**), which is attributed to the geometrical perturbation of graphene film on spherical NPs. To examine the strain on graphene after bulge formation, the Raman spectra in **Fig 2.1.4(d)** shows a strong G peak (1588.7 cm⁻¹) with negligible intensity of the defect D peak (1342.0 cm⁻¹), which suggests the high-quality of as-prepared graphene without NPs supported, and the nature of single-layer is confirmed by the significant intensity of the 2D peak (2683.0 cm⁻¹). After transferring graphene to the SiO₂ NPs/SiO₂ substrate, these blue shifts in the G (1585.1 cm⁻¹) and 2D peaks (2673 cm⁻¹) confirm the discernible strain modulated. Note that the strain induced by bending at bulges and wrinkles can contribute these blue shifts, and detailed correlation analysis in Raman spectra is subjected to future studies.

The thus-obtained bulged graphene sample is etched through exposure to oxygen plasma for 6 seconds. **Fig 2.1.4(e)** illustrates the exposed SiO₂ NPs due to successful perforation of graphene occurring at locations adhering to pre-deposited NPs. The etched sample is then immersed into deionized water in order to remove fully exposed NPs and the formed nanopore is shown in **Fig 2.1.4(f)**. The size of created nanopore is comparable

with the diameter of NPs (50 nm), owing to the fast reaction rate under the intensive plasma oxygen⁵¹. AFM characterization of the nanopore profile in **Fig 2.1.4(g)** and **2.1.4(h)** show that while flat elsewhere, a well-defined pore morphology is formed with pore diameter of ~50 nm and crater ridge height of about 25 nm. The adhesion between NP and graphene can cause the out-of-plane displacement of crater edges. It's noted that nanopores can also be initiated at wrinkling ridges of graphene (**Figure 2.1.S12**), and the wrinkle-induced perforation at such ridges is verified by MD simulations (**Figure 2.1.S13**). Therefore, the modulated strain by pre-deposited NPs provides a feasible way for selective perforation on graphene.

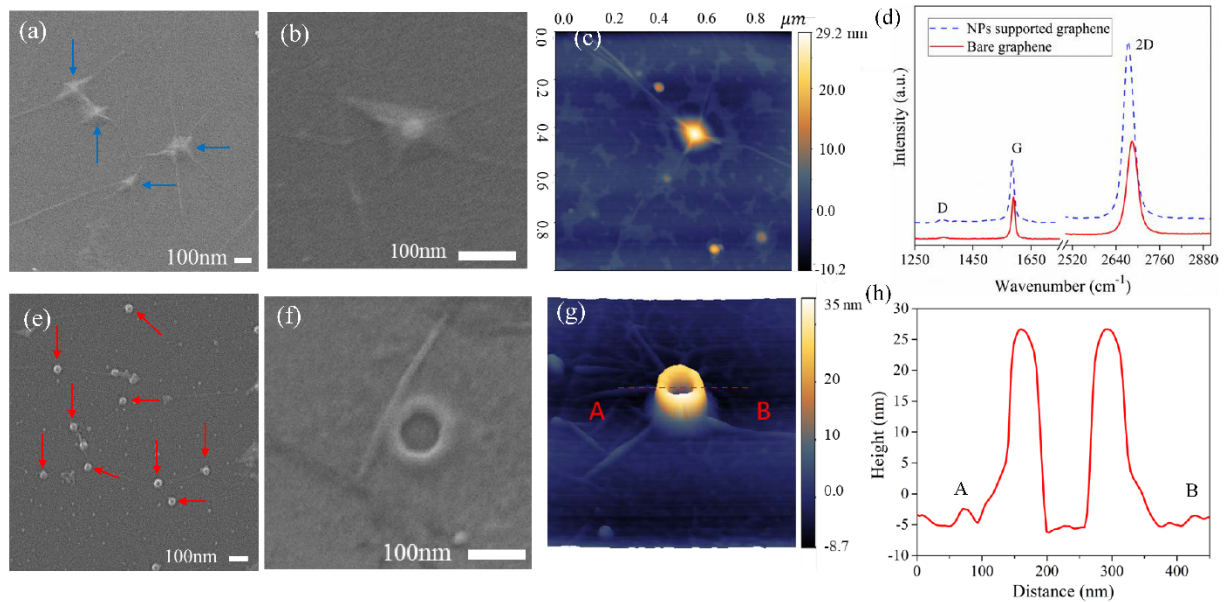


Figure 2.1.4 Morphological characterization of graphene before/after exposure to oxygen plasma. (a) The SEM image of CVD graphene; (b) The magnified SEM image of a graphene bulge; (c) The 2D AFM image of a graphene bulge; (d) Raw Raman spectra of graphene before and after adhering to SiO₂ NPs/SiO₂ substrate; (e) The SEM image of graphene with exposed NPs (red arrows) after exposure to plasma oxygen for 6 s; (f) The

magnified SEM image of nucleated pore after removing NPs; (g) The 3D AFM image and (h) height profile of created pore with a well-like structure.

To demonstrate the evolution of perforation, we expose the pristine graphene adhered to SiO₂ NPs/SiO₂ substrate to oxygen plasma for different durations. **Fig 2.1.5(a)-2.1.5(d)** show the time evolution of nanopore morphologies under increasing reactive durations and the formed pore grows up (the pore sizes: ~15 nm at 1.5 s, ~40 nm at 3.0 s and ~60 nm at 4.5 s) with the underlying NP gradually uncovered. It's not easy to capture the initial reaction stage due to the highly intensive reactivity of plasma oxygen⁵¹. Shown in the Raman spectra in **Fig 2.1.5(e)**, the intensity of the D peak increases with increasing exposure time and the G peak broadens. After a longer exposure of 4.5 s, the ratio of I_D/I_G , as a measure of graphene disintegrality, increases to 2.41, while the ratio of I_{2D}/I_G decreases to 0.83 (**Fig 2.1.5(f)**). These evidences indicate significant defect formation. Although Raman analysis cannot comprehensively distinguish the types of defects that may be present, the time-evolving morphologies confirm the contribution to defects from pore initiation and growth. Finally, based on ~500 NPs in SEM images with the observation area of 3000 μm^2 , we statistically summarize the number ratio of unexposed NPs to total observed NPs as a function of exposure time in **Fig 2.1.5(g)**. The exposed ratio increases with increasing exposure time, further verifying the growth of nanopore size and newly initiated pores. The dependence of pore size on exposure time illustrates the potential controllability of such strain-guided perforation. However, more precise controllability necessitates other mild etching agents, for example, O₂ at high temperature, where the controlling factors includes temperature, oxygen concentration, *etc*⁴⁰. In addition, other protruding nanostructures with various shapes and sizes can be introduced to modulate the

magnitude and distribution of strain⁶²⁻⁶⁴, and to enable overarching tunability of perforation on 2D materials.

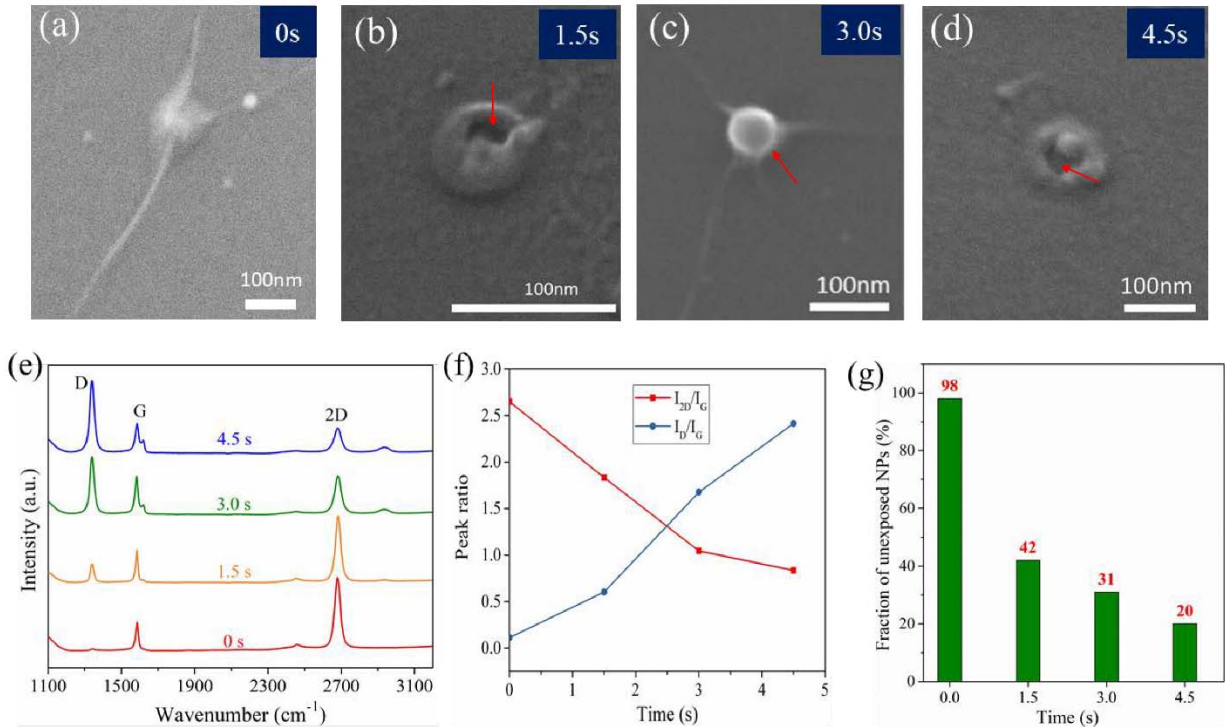


Figure 2.1.5 The effect of exposure time on pore growth. Time evolution of (a)-(d) SEM images of created pores. (e) Raman spectra of graphene with increasing exposure durations to oxygen plasma; (f) The ratio of I_D/I_G and I_{2D}/I_G for etching graphene undergoing different exposure times; (g) Statistical summary on the number ratio of unexposed NPs to total sampling NPs as a function of different exposure time.

2.1.6 Conclusion

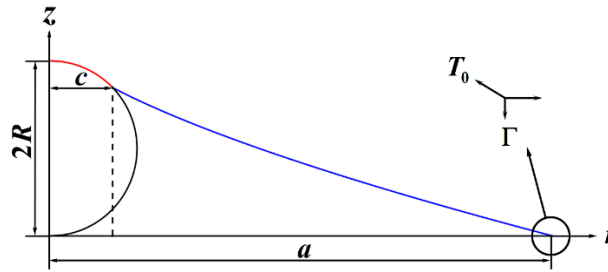
We proposed a novel perforation process on graphene through modulated strain on pre-deposited SiO₂ NPs beneath the monolayer, and the perforation process was tunable by varying the oxidative time, size and pattern of the NPs. r-MD simulations was employed

to verify the potential of periodical nanoporation and the broad applicability of such strain-guided method to a variety of 2D materials and arbitrary choice of nano-protrusions as strain initiators. Both simulation and modeling efforts revealed the mechanism where the C-C bonds are stretched and the reactivity of carbon atoms is highly enhanced in the strain concentrated dome, triggering larger perforation probability. This facile and scalable strain-guided method provides a practical route to efficiently nanopatterning 2D materials.

2.1.7 Appendix

1) Shell-based analytical model

The schematic of an elastic membrane resting on a spherical particle which is adhered to a substrate is given below.



The axial symmetry Föppl-Hencky membrane equations describe the normal displacement w and the radial membrane force T_r as^{65, 66}:

$$r^2 \frac{d^2 T_r}{dr^2} + 3r \frac{dT_r}{dr} + \frac{Eh}{2} \left(\frac{dw}{dr} \right)^2 = 0$$

$$\frac{1}{r} \frac{d}{dr} \left(r T_r \frac{dw}{dr} \right) + p = 0$$

Here, E is Young's modulus of the membrane, h is the thickness of the membrane and p is the force density along z direction. The relationships of membrane force and strain give:

$$T_\theta = \frac{d}{dr}(rT_r)$$

$$\varepsilon_r = \frac{1}{Eh}(T_r - \nu T_\theta)$$

$$\varepsilon_\theta = \frac{1}{Eh}(T_\theta - \nu T_r)$$

where ν is the Poisson's ratio.

The membrane can be separated into two regions, as shown in the red and blue contours in the sketch. For the red region the contact is assumed frictionless. Thus, the normal displacement is given as:

$$w = R + \sqrt{R^2 - r^2} \quad 0 \leq r < c$$

The boundary condition at $r = 0$ is:

$$T_r \neq \infty$$

The membrane force is then obtained as:

$$T_r = -\frac{Eh}{8r^2} \ln\left(1 - \frac{r^2}{R^2}\right)(R^2 - r^2) + C_1$$

where C_1 is an integral constant.

For the blue detached part, the force density is $p = 0$ and the boundary condition at $r = a$ is:

$$w = 0, T_r = T_0$$

A set of analytic solutions of w and T_r are:

$$T_r = T_0 \left(\frac{a}{r}\right)^{\frac{2}{3}}$$

$$w = 2 \sqrt{\frac{T_0}{Eh} \left(a - a^{\frac{1}{3}} r^{\frac{2}{3}}\right)}$$

and

$$\beta = -\frac{dw}{dr} = \frac{4}{3} \sqrt{\frac{T_0}{Eh}} \left(\frac{a}{r}\right)^{\frac{1}{3}}$$

By using the conditions of balanced forces at $r = a$ and the continuity of w, ε_r and ε_θ at $r = c$, we can deduce

$$T_0 \beta(a) = \Gamma$$

$$T_0 = \left(\frac{3}{4} \Gamma \sqrt{Eh}\right)^{\frac{2}{3}}$$

$$R + \sqrt{R^2 - c^2} = 2 \sqrt{\frac{T_0}{Eh}} \left(a - a^{\frac{1}{3}} r^{\frac{2}{3}}\right)$$

$$\frac{(1-\nu)c^2 - (1+\nu)R^2}{8c^2} \ln\left(1 - \frac{c^2}{R^2}\right) - \frac{\nu}{4} + \frac{(1-\nu)C_1}{Eh} = \frac{T_0}{Eh} \left(1 - \frac{\nu}{3}\right) \left(\frac{a}{c}\right)^{\frac{2}{3}}$$

$$\frac{(1-\nu)c^2 + (1+\nu)R^2}{8c^2} \ln\left(1 - \frac{c^2}{R^2}\right) + \frac{1}{4} + \frac{(1-\nu)C_1}{Eh} = \frac{T_0}{Eh} \left(\frac{1}{3} - \nu\right) \left(\frac{a}{c}\right)^{\frac{2}{3}}$$

After numerically solving the parameters a , c and C_1 , the fields of strain, displacement and energy density can be deduced.

2) SFN model

The finite element calculations were performed using the commercial code ABAQUS⁶⁷. The graphene sheet (6.038 nm×6.146 nm) is equivalent to a beam frame network, constructed by interconnected circular beams with section radius $r = 0.05$ nm and modulus $E = 31.7$ TPa, to model the strain energy on each atom; these beams link the carbon atoms and have identical length as C–C bonds. It was verified that bond radius is not small compared with length, thus having negligible bending effect⁶¹. Therefore, the shear-

flexible, quadratic Timoshenko beam element (B32) was adopted for numerical analysis, which provides robust finite-strain solutions for both thick as well as slender beams. The nanoparticle is simplified as a rigid sphere with diameter of 2 nm, and the substrate is also regarded as a rigid plate with the size much larger than graphene sheet. Besides, to drive the formation of graphene bulges, gravity is introduced as a simplification of interaction between them the graphene sheet and NPs as well as the substrate.

The etching probability of the carbon atoms can be determined from the strain energy of each carbon atom. Here, the atom strain energy is calculated by summation of halves of strain energies of three main bonds and other three secondary bonds connected to the atom, because each bond contributes to two carbon atoms.

3) Supplementary Figures and Tables

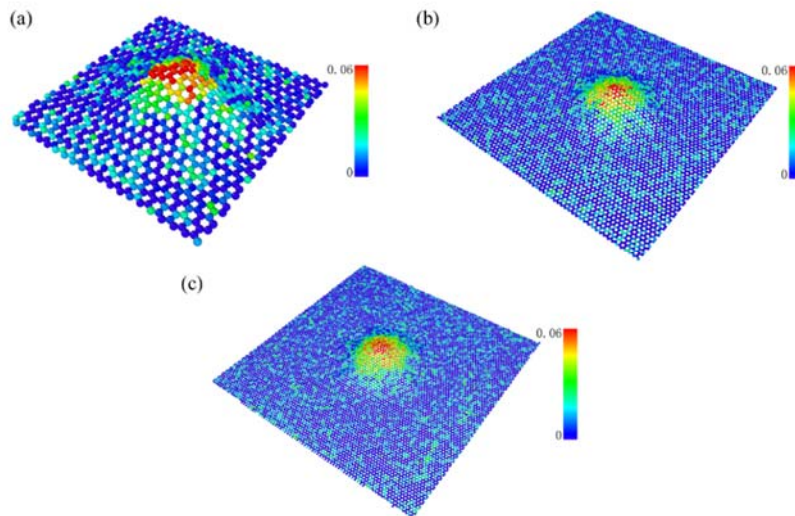


Figure 2.1.S1. Strain distributions of graphene adhered to the substrate decorated with a NP having diameter of (a) 0.8 nm, (b) 1.5 nm and (c) 2.5 nm. Both the strain contours show the same maximum strain 6% at the dome apex with that for the NP having diameter of 1.0

nm in Figure 2a, which means the size-independence of maximum strain. With increasing NP's size, the NP-induced dome morphologies have the self-similarity in geometric.

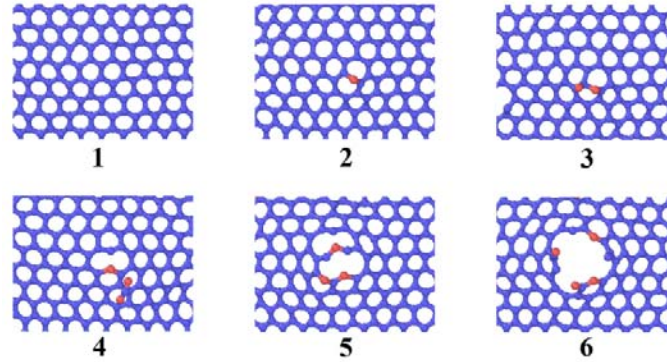


Figure 2.1.S2. The simulated perforation process on graphene by oxygen at the atmosphere with the oxygen number density $4 \times 10^{-3} / \text{\AA}^3$ and the temperature 1300 K: 1) bare graphene (0 ps); 2) oxygen adsorption (70 ps); 3) lattice distortion (105 ps); 4) bond breaking (125 ps); 5) single vacancies (150 ps); 6) pore growth (165 ps). In this simulation, the diameter of NP underneath is 1 nm.

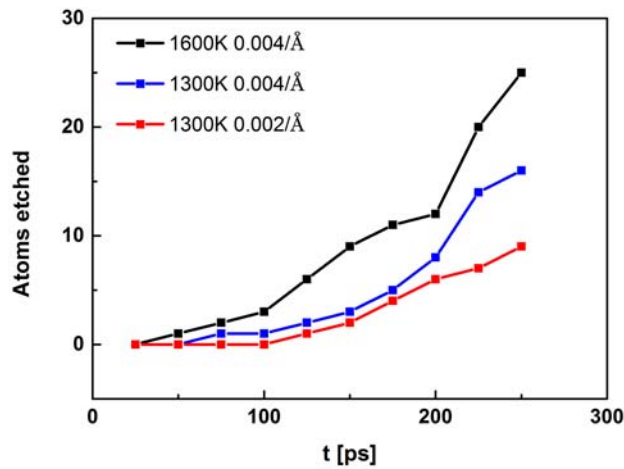


Figure 2.1.S3. The etched carbon atoms as a function of reactive simulation time by varying temperatures and oxygen concentrations. Higher temperature and oxygen

concentration can lead larger perforation rate. In this simulation, the diameter of NP underneath is 1 nm.

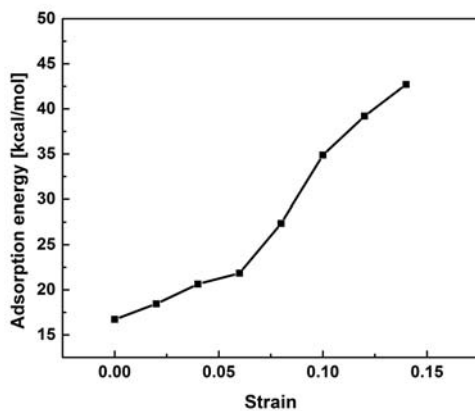


Figure 2.1.S4. Oxygen adsorption energy as a function of strain on graphene. The adsorption energy increases significantly with increasing bend-induced strain.

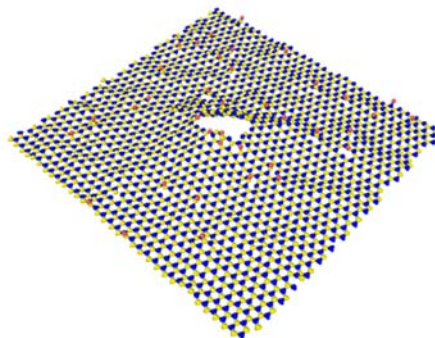


Figure 2.1.S5. The nucleation of pore on a single layer of boron nitride (BN) with a SiO₂ NP supported (1 nm) at 170 ps. This is exemplified to show the applicability of strain-guided perforation to a broad variety of 2D materials. Simulation parameters: temperature of 1600K, oxygen concentration of $4 \times 10^{-3} / \text{\AA}^3$.

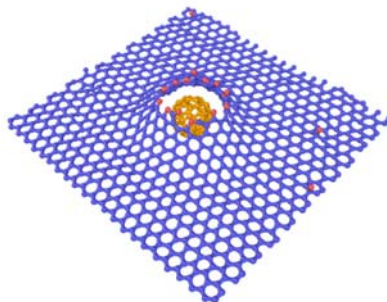


Figure 2.1.S6. Perforation of graphene with NPs of chemically stable C60 fullerence. Simulation parameters: NPs' size (7Å), snapshot time (220ps), temperature (1600K), oxygen concentration ($4 \times 10^{-3} / \text{Å}^3$).

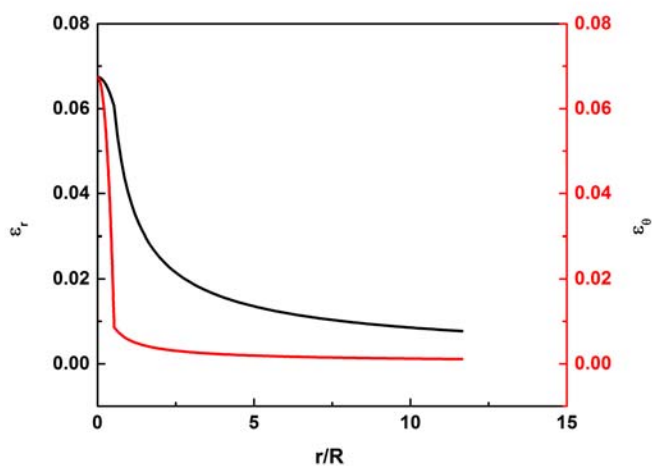


Figure 2.1.S7. Continuous distributions of radial strain ϵ_r and tangential strain ϵ_θ as a function of the horizontal distance away from the NP's center, which is calculated by SBA model.

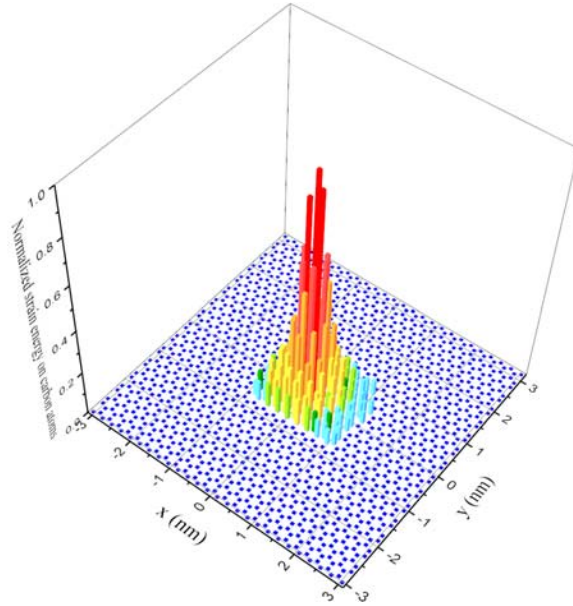


Figure 2.1.S8. Spatially discrete distributions of normalized strain energy ϵ on each carbon atoms calculated by SFN model.

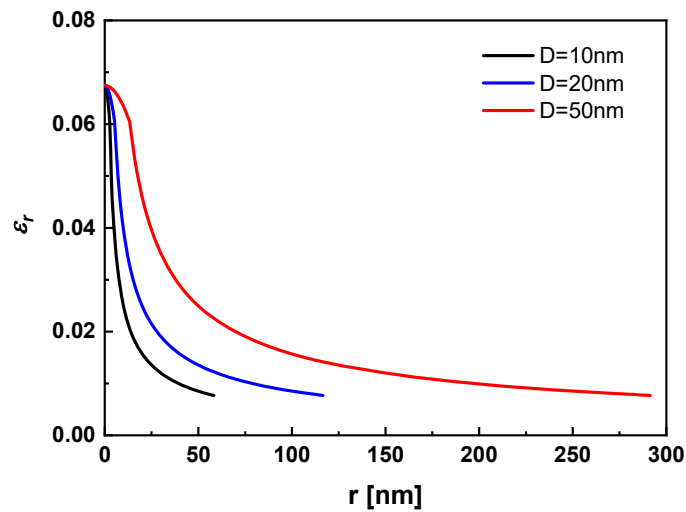


Figure 2.1.S9. Continuous distributions of radial strain ϵ_r for the NPs with different size, which calculated by SBA model. This result verifies the independence of maximum strain at the dome apex on the size of NP.

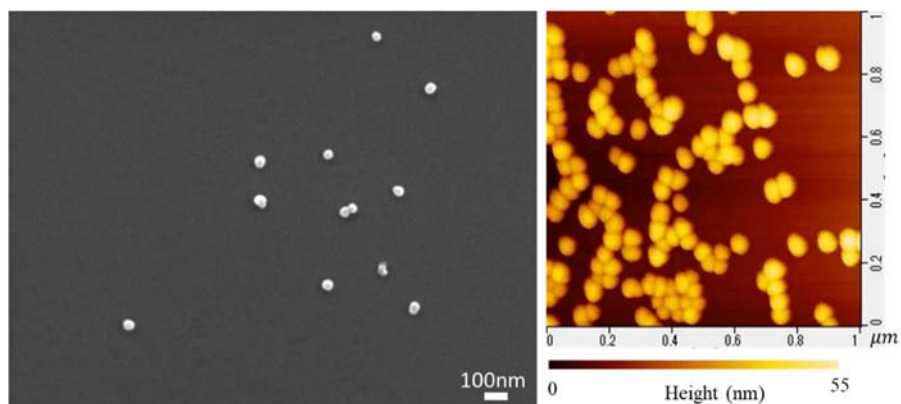


Figure 2.1.S10. SEM and AFM images of SiO₂ NPs on SiO₂ substrate, showing the diameter of NPs is roughly 50 nm

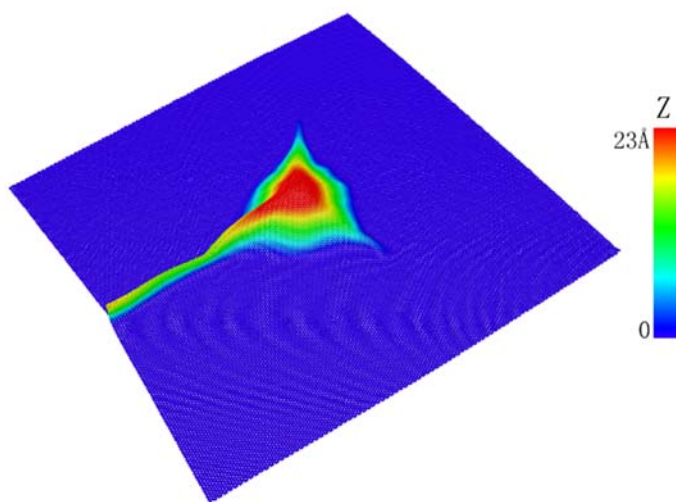


Figure 2.1.S11. Simulated wrinkling features surrounding bulges in r-MD simulations. The underneath NPs' diameter is 2 nm.

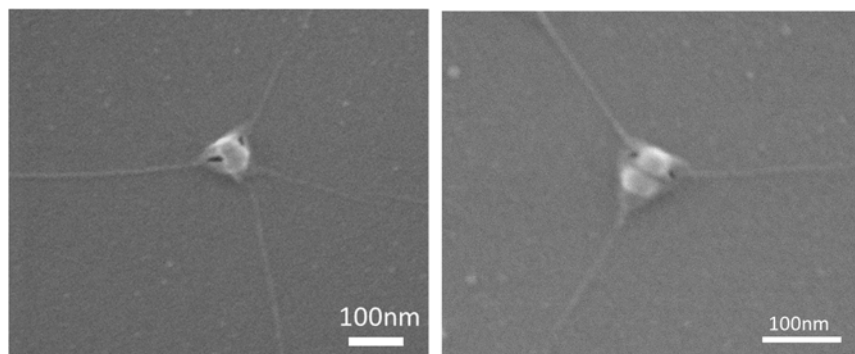


Figure 2.1.S12. SEM images of initiated perforation at wrinkling ridges of graphene after exposure to oxygen plasma for 1.5 s

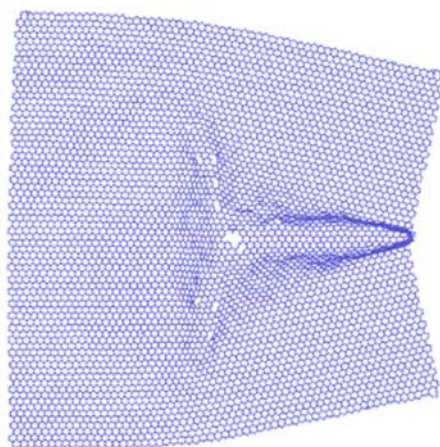


Figure 2.1.S13. r-MD simulation result of initiated perforation at wrinkling ridges. Simulation parameters: NPs' size (2 nm), snapshot time (65 ps), temperature (1600K), oxygen concentration ($3 \times 10^{-3} / \text{\AA}^3$).

2.2 Rapid programmable nanodroplet motion on a strain-gradient surface

When interacting with water and other liquids, the surface crystal structure determines the surface energy and thus the hydrophobicity. In-plane gradient strain applied to a flat crystal surface can create a surface morphology with hydrophobicity gradient, capable of driving the movement of water droplet. In this Section 2.2, the nanomaterial of graphene is used as a model crystal to investigate the effect of strain-gradient on nanodroplet motion, which is potential to advanced devices of water collection. ⁶⁸

2.2.1 Introduction

Surfaces capable of directionally transporting water droplets are observed in ubiquitous biological systems, including rice leaves, striders' legs liquid droplets and cicada wings, resulting from directional and gradient nanostructures on these organism surfaces⁶⁹⁻⁷⁴. Inspired by the nature, engineered strategies to manipulate liquid droplet motion have attracted extensive attentions due to potential applications in microfluidics^{75, 76}, energy conversion⁷⁷ and smog removal⁷⁸. A variety of strategies based on wettability gradient were reported, including permanent chemical (e.g. doping of functional groups^{79, 80}) and physical (e.g. surface roughness⁸¹⁻⁸³, structural topology, combination of multiple gradients, etc.) modifications to surfaces or droplet. These irrecoverable and passive treatments only for specific purposes are not suitable for reconfigurable platform of droplet manipulation, and slow droplet velocity of micrometers per second was induced. Additionally, droplet motions can be responsive to external stimuli by electromagnetic field, pH, temperature and light⁸⁴⁻⁸⁸. However, additions of chemicals into liquids were employed and thus involved either undesirable contaminations or slow response time. Recently, the gradient of substrate curvature presented a strategy for fast droplet transporting with the velocity up to 0.4 m/s⁸⁹, but the droplet may stagnate on the conical substrate instead of moving forward at a critical ratio of the local substrate radii to droplet radii. Up to now, facile fabrication of such curvature-gradient substrates

and active manipulation on 2D platform are challenging, which is the gap we aim to bridge in this study.

Recently, strain-engineering has been widely studied experimentally and theoretically for tuning material properties^{90,91}. Externally applied strain to substrate were experimentally adopted to actuate the migration of fibroblasts in the direction of principal strain, and the rolling motion of biological organisms, like zoosperms, was driven by the strain-gradient induced by muscle contraction^{92,93}. Not limited to biological systems, as one of effective strategies, the strain-gradient based method has been realized in nanosystems, including transport of 2D nanoflakes on graphene⁹⁴. To best of our knowledges, no explicit study has been reported on manipulating the motion of water nanodroplets in a more controllable way through deforming substrates.

In this study, we propose a mechanism for rapid transporting nanodroplets through strain engineering, and achieve controllable manipulation of both speed and direction of the nanodroplet along linear and nonlinear paths. Through molecular dynamics (MD) simulations and theoretical modeling, the strain-gradient externally applied to substrates is able to shift the balance of van der Waals force between the substrate (graphene or copper) and the nanodroplet, thus providing the driving force. The programmable strategy suggests broad applications of directional droplet transport.

2.2.2 Modeling and method

All of the MD simulations were carried out on the LAMMPS package. The AIREBO potential field was used to describe the graphene, and the long range TIP4P water model was used to model the droplet. The 12-6 Lennard-Jones pair potential, $V = 4\epsilon_{ij}(\sigma_{ij}^{12}/r_{ij}^{12} - \sigma_{ij}^6/r_{ij}^6)$, was used to describe the interactions between water molecules and graphene³⁶, with $\epsilon_{CO} = 4.063 \text{ meV}$, $\sigma_{CO} = 3.19\text{\AA}$, $\epsilon_{CH} = 0$ and $\sigma_{CH} = 0$. All simulations were performed using a time step of 1 fs.

2.2.3 Wetting behavior of strained substrate

We firstly study the wetting behavior of water droplet on a strained substrate, where graphene is employed as an illustrative example. A constant displacement is applied to the boundary atoms to achieve a uniaxial strain, then the graphene is fixed. **Fig 2.2.1(a)** shows the schematics of a 500-water-molecule droplet on a monolayer graphene with constant uniaxial strain ε . After equilibrium in NVT ensemble with 300 K for 500 ps, the configuration of water molecules is extracted and we calculate the contact angle by fitting the profile of the outermost molecules of water droplet. As shown in **Fig 2.2.1(b)**, when no strain is applied, the corresponding contact angle of water droplet is 86.95° , consistent with previous calculations using the same parameters. With the strain increasing from 0 to 0.2, the contact angle increases monotonously from 86.95° to 98.99° , indicating the wettability of water droplet on graphene changing from hydrophilicity to hydrophobicity. The reason is that the larger tensile strain applied to graphene induce smaller areal density of carbon atoms, which results in the decrease of liquid-solid surface energy and increase of contact angle. Note that no significant change in the contact angle is observed for larger droplets with more water molecules involved in simulations (see **Fig 2.2.S1**). Thus, the contact angle of water droplet can be controlled by external force applied to the substrate.

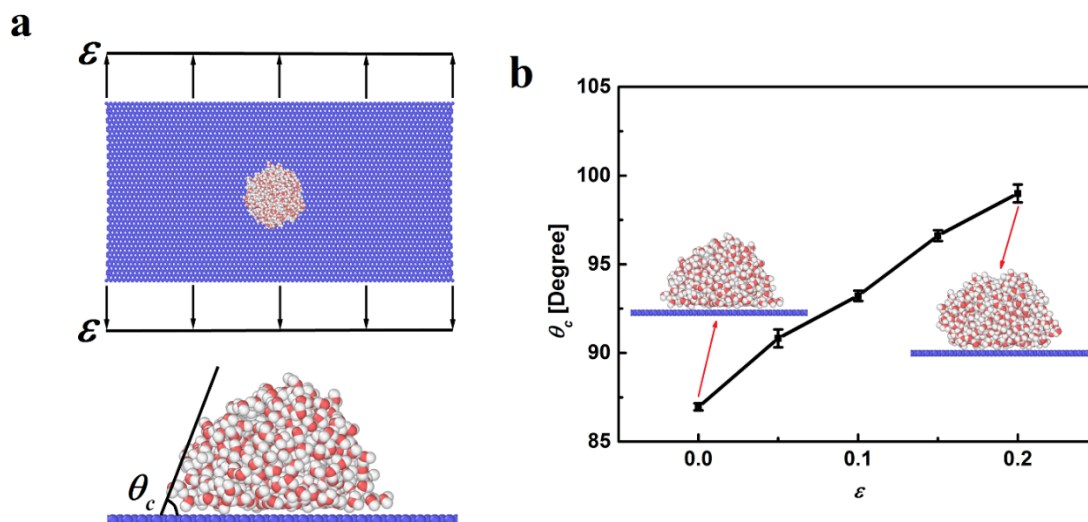


Figure 2.2.1. (a) Top view and side view of a 500-water-molecule droplet on a monolayer graphene with a constant uniaxial strain ϵ . (b) Variation of the contact angle with the strain ϵ .

2.2.4 Nanodroplet movement driven by strain gradient substrate

Based on the strain-dependent wettability, continuous variation of wettability may be achieved by applying strain with a directional gradient, becoming a tunable driving force for water droplet motion. The motion of a droplet on a monolayer graphene with a constant strain gradient is investigated herein. Shown in the top of **Fig 2.2.2(a)**, the simulation system includes a nanodroplet of 500 water molecules and a monolayer graphene with a dimension of $197 \text{ \AA} \times 84 \text{ \AA}$. The system is first relaxed in the NVT ensemble at 300 K for 500 ps with the mass center of the nanodroplet fixed in both x and y directions with all graphene atoms fixed. Then, linearly distributed displacements in the y direction are applied to the boundary atoms along the x direction of graphene, thus creating a constant strain gradient $G_x = d_{max}/wL$ along the x direction. The continuous variation of strain

leads to an asymmetrical configuration with different contact angle along the direction of strain gradient in the bottom of **Fig 2.2.2(a)**, providing the driving force for droplet motion. The droplet is subsequently released and its motion was simulated using NVE ensemble.

To save computational cost and clearly demonstrate the droplet motion on a timescale of hundreds of picoseconds, the strain gradient $G_x = 9.15 \times 10^{-4} / \text{\AA}$ is taken as a representative example. The time histories of the displacement and velocity of the mass center of droplet are shown in **Fig 2.2.2(b) and 2(c)**. The droplet speeds up along the x direction with the acceleration of $a_x = 3.31 \times 10^{-3} \text{\AA}/\text{ps}^2$ and the displacement along the y direction can be neglected, indicating that the net driving force is along the opposite direction of the strain gradient. In the present study, the velocity of the nanodroplet can reach 50 m/s. It is evident from **Fig 2.2.2(d)** that the interactive vdW potential between water droplet and graphene decreases with the movement of droplet, indicating that the potential energy has been converted to kinetic energy.

The driving force for nanodroplet motion can be qualitatively explained by the wettability gradient resulting from the strain gradient. For a spherical-cap drop on a solid surface induced by wettability gradient, the driving force can be written as

$$F_{driving} = \pi R^2 \gamma \frac{\partial \cos \theta_c}{\partial x} = \pi R^2 \gamma \frac{\partial \cos \theta_c}{\partial \varepsilon} G_x$$

where R is the radius of the drop, γ is the liquid-gas interfacial tension, G_x is the strain gradient and θ_c is the contact angle between drop and solid surface. Based on this relationship, the driving force is proportional to the strain gradient and the contact area of droplet, qualitatively agreeing with our simulation results (**Fig 2.2.3**). However, the term $\partial \cos \theta_c / \partial \varepsilon$ is hard to be accurately determined and more insights need to be explored from molecular mechanism.

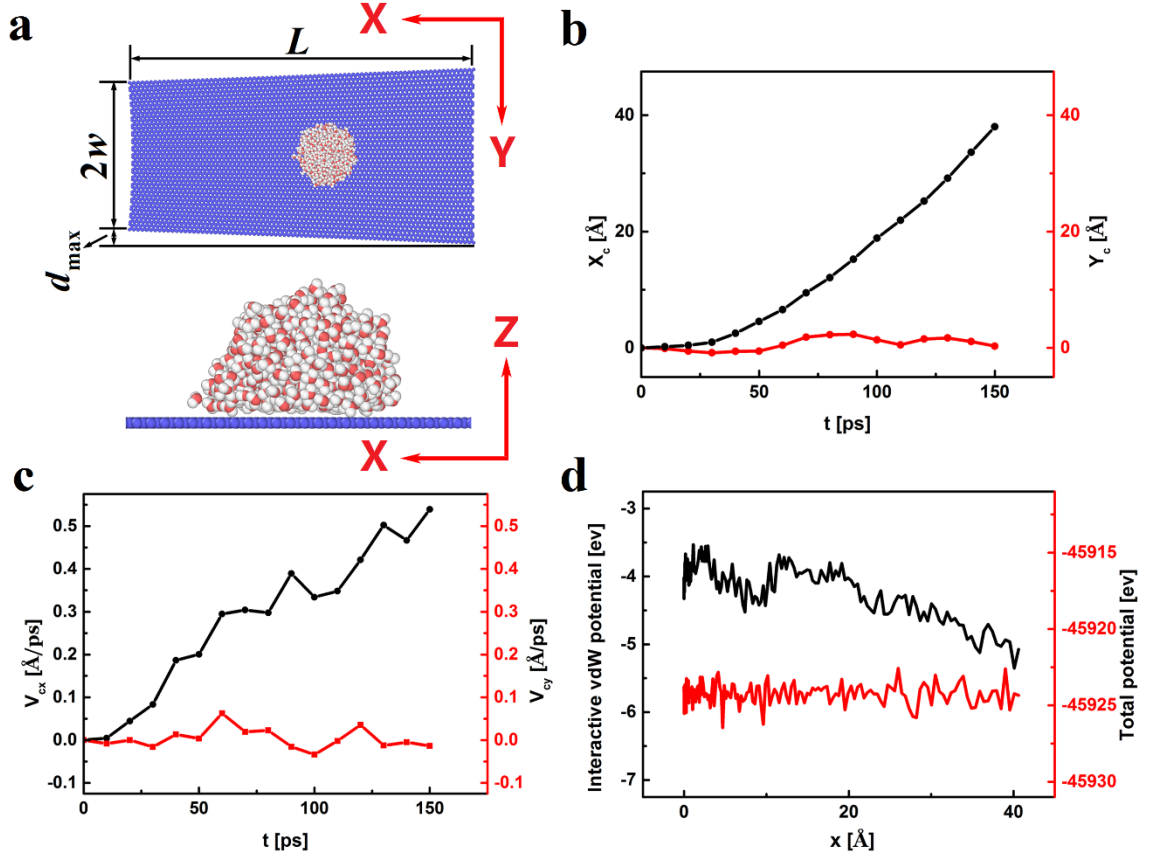


Figure 2.2.2 (a) Top view and side view of a 500-water-molecule droplet on a monolayer graphene. (b) The time history of the displacement of the mass center of droplet along the x direction. (c) The time history of the velocity of the mass center of droplet along the x direction and y direction. (d) The [variation](#) of interactive vdW potential energy and the system total potential energy with respect to the transport distance x .

2.2.5 Molecular mechanism

An analytical model based on vdW interaction is developed, from which one may derive the net driving force exerted on a spherical-cap droplet (with a molecular density of ρ and radius of R) sitting on a substrate with a strain gradient $\varepsilon_y = \varepsilon_0 + xG_x$:

$$F_{driving} = -4\pi^2\sigma_0\epsilon\rho(1 - \nu)G_x \left(\frac{-(R^2 - z_0^2)\sigma^{12}}{45z^9} + \frac{(R^2 - z_0^2)\sigma^6}{6z^3} + \frac{\sigma^{12}}{35z^7} - \frac{\sigma^6}{2z} - \frac{z_0\sigma^{12}}{20z^8} + \frac{z_0\sigma^6}{2z^2} \right) \Big|_{\Delta}^{R+z_0}$$

in which Δ is the distance between droplet's bottom surface and substrate, ν is the Poisson's ratio of substrate, σ_0 is the areal density of atoms on unstrained substrate, ϵ and σ are LJ parameters and z_0 is the height of the center of the droplet with respect to the substrate surface $Z=0$ (**Fig 2.2.S2**).

Through minimization of the interactive vdW potential energy between bulk water and graphene, one obtains $\Delta = \sqrt[6]{0.4}\sigma$. Therefore, the driving force and acceleration can be written as

$$F_{driving} \approx -0.703\pi^2\sigma_0\epsilon\rho(1 - \nu)G_x R^2 \sigma^3 \sim G_x R^2$$

$$a = F_{driving}/m \sim G_x/R$$

which shares the same scaling law with the previous phenomenological contact angle theory. m is the droplet mass. Note that the present driving force may be similar to that induced by the stiffness gradient of the substrate, in the sense that the driving force is resulted from the redistribution of the van der Waals potential energy, nevertheless, the strain gradient is readily tunable in practice but the surface stiffness gradient is not.

To verify the theory, several MD simulations are conducted by varying the strain gradients and nanodroplet sizes. The relevant parameters σ_0 ($0.382/\text{\AA}^2$), ν (0.186), R (18 \AA for 500-water-molecule droplet and 22.5 \AA for 1000-water-molecule droplet) and ρ ($0.0415/\text{\AA}^3$) can be deduced from simulation. **Fig 2.2.3(a)** shows the displacement of a 500-water-molecule droplet as a function of time for different strain gradients, and the

curves of acceleration vs strain gradient for the 500-water-molecule and 1000-water-molecule droplets are plotted in **Fig 2.2.3(b)**. The simulation trends are consistent with our theoretical model, and both the simulation and theory suggest that the acceleration is in directly and inversely proportion with the strain gradient and the droplet radius, respectively.

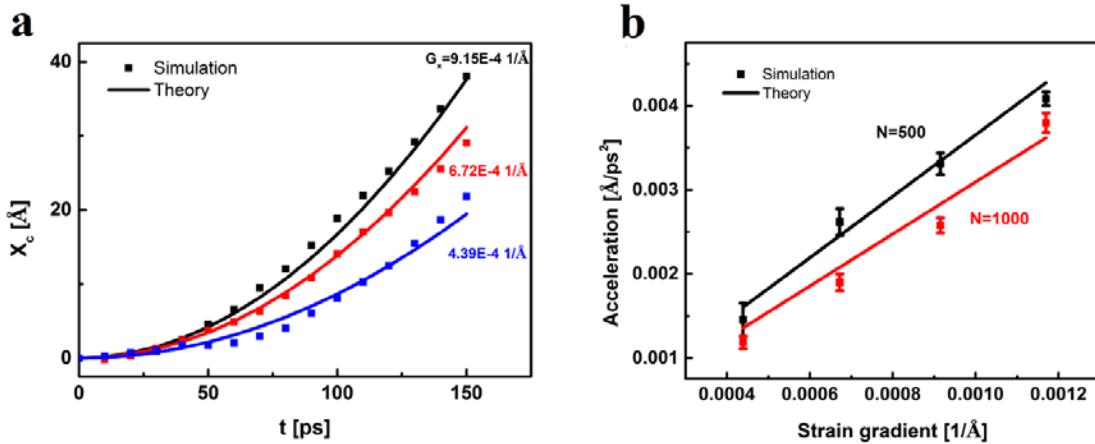


Figure 2.2.3 (a) The time history of the displacement of the mass center of the 500-water-molecule droplet for various strain gradient G_x . (b) The acceleration of the mass center of the droplet with respect to strain gradient G_x for various sizes of the droplet.

2.2.6 Actuation by 2D strain gradient: nonlinear pathway

The driving force is relevant to the strain gradient and the size of droplet, thus offering a way to precisely control the linear straight movement of droplet. Certain applications, however, such as drug delivery, fog collection and cell motility control, may require the movement of droplet in complex curved paths; this can be achieved adjusting strain gradients in two directions and loading sequences. The fundamental pathway of turning is illustrated here. Considering a $150\text{Å} \times 147\text{Å}$ single layer graphene and a droplet

containing 1000 water molecules, it first experiences equilibrium at 300K in NVT ensemble for 500 ps while the mass center is fixed, so that an initial stable configuration of droplet (State A) is obtained. Next, displacement loading along the y direction is slowly applied to the atoms on the two boundaries along the x direction of graphene in 50 ps to obtain a $1.16 \times 10^{-3}/\text{\AA}$ strain gradient along the x direction, after which the displacement boundary condition is fixed and droplet is released (see the schematics in **Fig 2.2.4**). The strain gradient drove droplet to move along the x direction from the high strain end to the low strain regime for 200 ps (State B). Afterwards, the strain gradient in the graphene is slowly released to pristine state within 50 ps, while the droplet keeps move in the x direction (see **Fig 2.2.S3**). Thereafter, the graphene is slowly stretched again (within 50 ps), achieving a new strain gradient in the y direction of $1.16 \times 10^{-3}/\text{\AA}$ and then the boundary is fixed, and this new strain gradient drove the droplet to accelerate along the y direction (see **Fig 2.2.S4**). **Fig 2.2.4** shows the trajectory of droplet in a parabolic path, which agrees quite well with parallel theoretical prediction. Note that the decay of velocity in x direction is attributed to the nonuniaxial strain gradient and thus distorted areal density of carbon atoms near boundaries, subjected to future studies. This example suggests that by adjusting the loading amplitude (gradient), direction and sequence, it is possible to manipulate a small droplet moving along complex pathways.

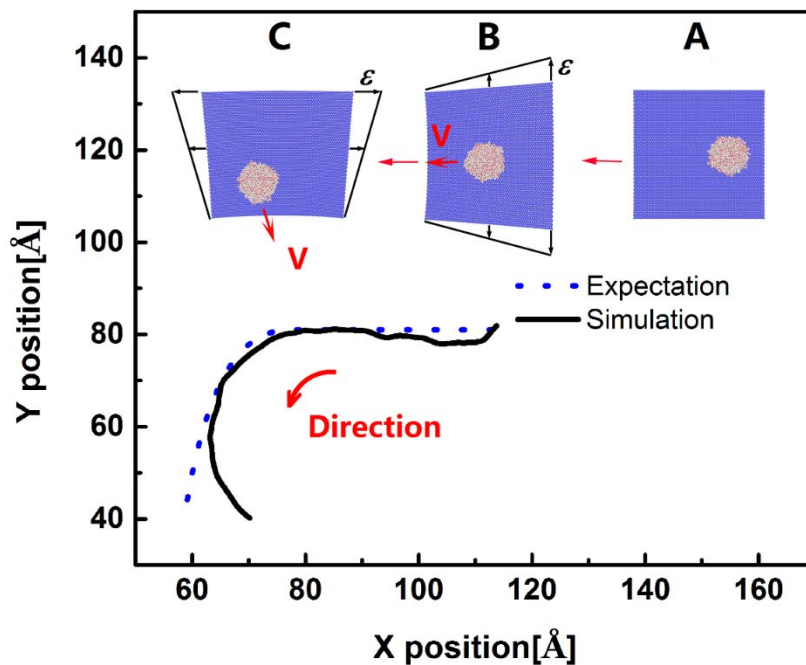


Figure 2.2.4 Trajectory of water droplet on a monolayer graphene with tunable strain gradient direction.

2.2.7 Generalized substrate

The above principles are not limited to the surface of graphene. To illustrate the broader applications, motion of water droplet on a (111) copper surface was simulated. The EAM potential³⁹ is used to describe the copper substrate and 500 water molecules are contained in the droplet. Due to small failure strain of copper (less than 8% in EAM potential), the length of substrate is reduced to achieve the same strain gradient (strain gradient: $9.15 \times 10^{-4} / \text{\AA}$) as that of graphene, as shown in **Fig 2.2.5(a)**. Compared with graphene, copper has smaller areal density of atoms σ_0 ($0.176 / \text{\AA}^2$), larger Poisson's ratio ν (0.3) and larger interactive vdW potential with water ϵ_{Cu-O} (7.394 meV). Also, the water

droplet on copper has smaller radius R (16 Å), leading to a smaller driving force of droplet on copper (111) than that on graphene. Shown in **Fig 2.2.5(b)**, the movement of droplet on (111) copper surface is about 40% slower than that on graphene. This example indicates that the motion of water droplet can be controlled on any general surface with properly applied strain gradient.

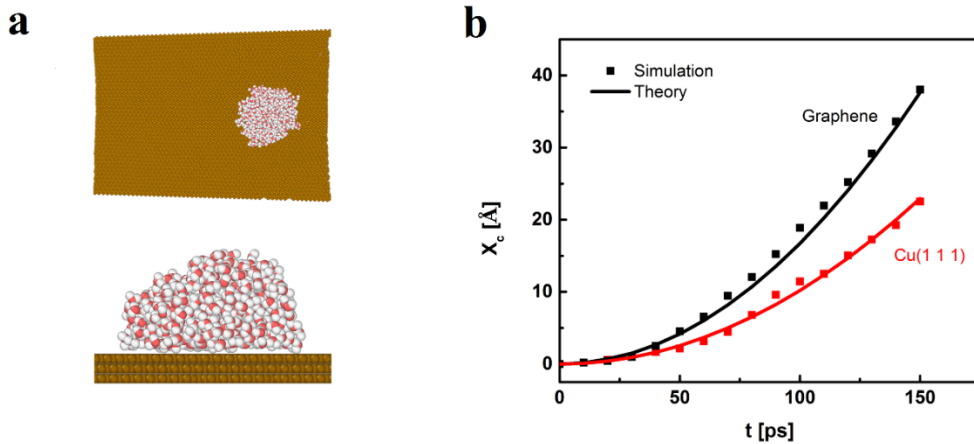


Figure 2.2.5 (a) Top view and side view of 500-water-molecule droplet on copper (111) surface. (b) Comparison of displacement-time curves of 500-water-molecule droplet on graphene and copper (111) surface.

2.2.8 Conclusion

A novel method to control the movement of a nanodroplet on a substrate using strain gradient was proposed, and verified using both MD simulations and theoretical analysis. The driving force, originating from the imbalance of Van der Waals force between the substrate surface and droplet, is in the opposite direction of the applied strain gradient, and its magnitude is proportional to the magnitude of the strain gradient and the square of droplet radius. By properly adjusting the strain gradient and its direction, as well as loading

sequence, one may precisely control the acceleration and deceleration the droplet, and even its trajectory.

2.2.9 Appendix

1) Contact angle of water droplet on graphene with strain

We calculated the contact angle of the droplet through fitting the profile of the outermost molecules of water droplet. We performed 5 MD simulations for each strain and obtain the average and standard deviation of contact angle. The contact angles of water droplet with different sizes were also calculated (see Figure S1). The droplet size does not significantly affect the contact angle.

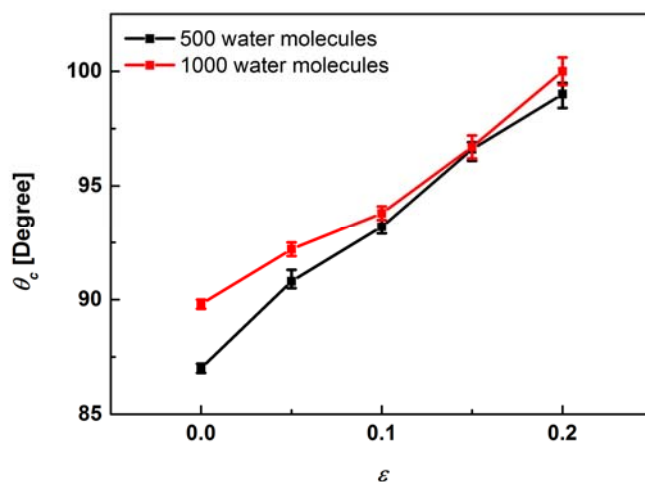


Figure 2.2.S1. Variation of the contact angle with the strain ε and size of the droplet.

2) Driving force of droplet

As shown in Figure S1, a spherical-cap droplet on a substrate with a gradient strain $\varepsilon_y = \varepsilon_0 + xG_x$, where ε_0 is the strain at $(0,0,0)$. The center of droplet, with a radius R and atomic number density ρ , locates at $(0,0,z_0)$, and the substrate top surface is on the plane

$Z=0$. The atomic interactions between substrate and water molecules are described by 12-6 Lennard–Jones pair potential, $V = 4\epsilon(\sigma^{12}/r^{12} - \sigma^6/r^6)$.

Firstly, we calculated the potential energy between single water molecule and top-layer atoms of substrate

$$\Phi = \iint_D \sigma_c V dA$$

Here, σ_c is the areal density of atoms on substrate, which can be expressed as a function of strain:

$$\sigma_c = \frac{\sigma_0}{1 + \epsilon_x + \epsilon_y} = \frac{\sigma_0}{1 + (1 - \nu)\epsilon_y}$$

in which σ_0 is the areal density of atoms on unstrained substrate; ν is the Poisson's ratio of substrate. Therefore, the potential energy can be rewritten as

$$\begin{aligned} \Phi &= \int_{-\infty}^{+\infty} \int_{-\infty}^{+\infty} \frac{4\sigma_0\epsilon}{1 + (1 - \nu)\epsilon_y} \left[\frac{\sigma^{12}}{(x^2 + y^2 + z^2)^6} - \frac{\sigma^6}{(x^2 + y^2 + z^2)^3} \right] dx dy \\ &= \int_{-\infty}^{+\infty} 4\sigma_0\epsilon [1 - (1 - \nu)\epsilon_y + O(\epsilon_y^2)] \left[\frac{63\pi\sigma^{12}}{256(x^2 + z^2)^{\frac{11}{2}}} - \frac{3\pi\sigma^6}{8(x^2 + z^2)^{\frac{5}{2}}} \right] dx \end{aligned}$$

Due to symmetry, the force applied to this single water molecule by substrate is

$$f = -\frac{\partial\Phi}{\partial x} = -\frac{\partial\Phi}{\partial\epsilon_y} \frac{\partial\epsilon_y}{\partial x}$$

$$\begin{aligned}
&\approx G_x \int_{-\infty}^{+\infty} -4\sigma_0\epsilon(1-\nu) \left[\frac{63\pi\sigma^{12}}{256(x^2+z^2)^{\frac{11}{2}}} - \frac{3\pi\sigma^6}{8(x^2+z^2)^{\frac{5}{2}}} \right] dx \\
&= -4\pi\sigma_0\epsilon(1-\nu)G_x \left(\frac{\sigma^{12}}{5z^{10}} - \frac{\sigma^6}{2z^4} \right)
\end{aligned}$$

Consider a spherical-cap droplet with a molecular density ρ , the center at $(0,0,z_0)$ and a radius R , as well as a substrate located on the plane $Z=0$ with a gradient strain $\epsilon_y = \epsilon_0 + xG_x$. Then, the total driving force exerted on the droplet is

$$\begin{aligned}
F_{driving} &= \int_V \rho f dV \\
&= -4\pi\sigma_0\epsilon\rho(1-\nu)G_x \int_{\Delta}^{R+z_0} \left(\frac{\sigma^{12}}{5z^{10}} - \frac{\sigma^6}{2z^4} \right) dz \int_0^{\sqrt{R^2-(z-z_0)^2}} r dr \int_0^{2\pi} d\theta \\
&= -4\pi\sigma_0\epsilon\rho(1-\nu)G_x \left(\frac{-(R^2-z_0^2)\sigma^{12}}{45z^9} + \frac{(R^2-z_0^2)\sigma^6}{6z^3} + \frac{\sigma^{12}}{35z^7} - \frac{\sigma^6}{2z} - \frac{z_0\sigma^{12}}{20z^8} + \frac{z_0\sigma^6}{2z^2} \right) \Big|_{\Delta}^{R+z_0}
\end{aligned}$$

in which Δ is the distance between droplet's bottom surface and substrate. Due to the geometry of droplet close to a hemisphere (the contact angle is around 90°), we can assume $R \gg z_0$.

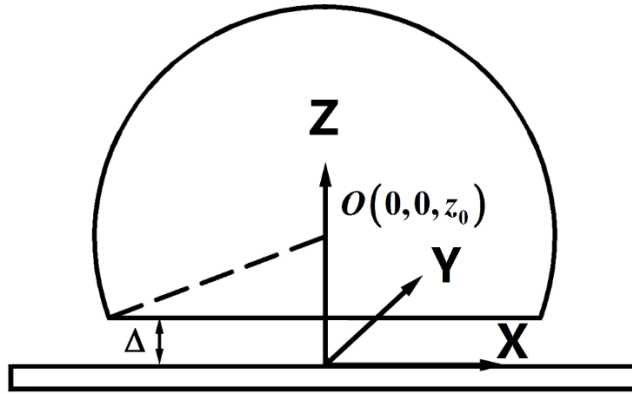


Figure 2.2.S2. Sketch of a spherical-cap drop in the coordinate system.

3) The theoretical pathway of droplet

From State A to state B, the droplet is accelerated along the x direction and the pathway is a straight line, shown as the blue dash line in Figure S3. From State B to State C, the velocity component along x direction is initially kept but reduced by the. Since the direction of driving force is switched to the y direction, the velocity component along y direction linearly increase. The friction force in x direction can be evaluated by:

$$F_{friction} = -\lambda\pi R^2 V_B$$

So the displacement in the x direction is:

$$x = \frac{mV_B}{\lambda\pi R^2} \left(1 - e^{\frac{-\lambda\pi R^2}{m}t} \right)$$

shown as the red dash line in Figure S3. Based on the previous study⁹⁶, the friction coefficient λ is $1.2 \times 10^4 \text{Ns/m}^3$ and V_B is 21 m/s according to the MD simulation result.

The driving force along the y direction is:

$$F_y = -0.703\pi^2\sigma_0\epsilon\rho(1-v)G_yR^2\sigma^3$$

And the displacement in the y direction is: $y = \frac{F_y t^2}{2m}$

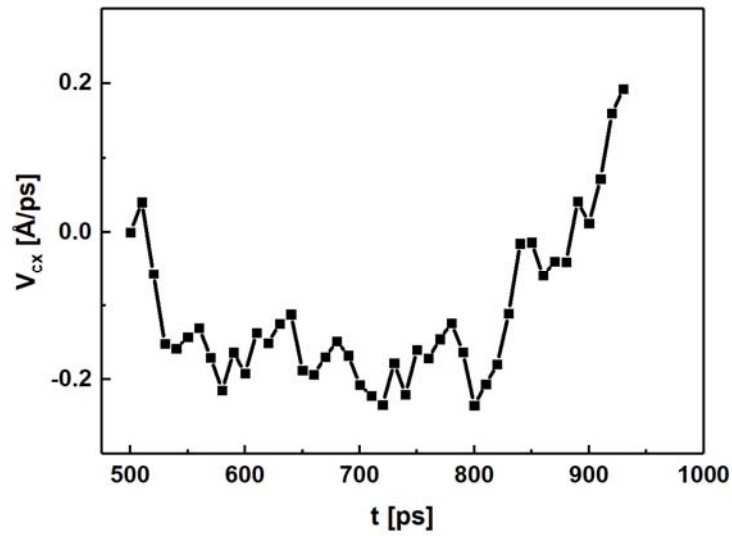


Figure 2.2.S3 The time history of velocity component in the x direction for water droplet on a monolayer graphene with tunable strain gradient direction.

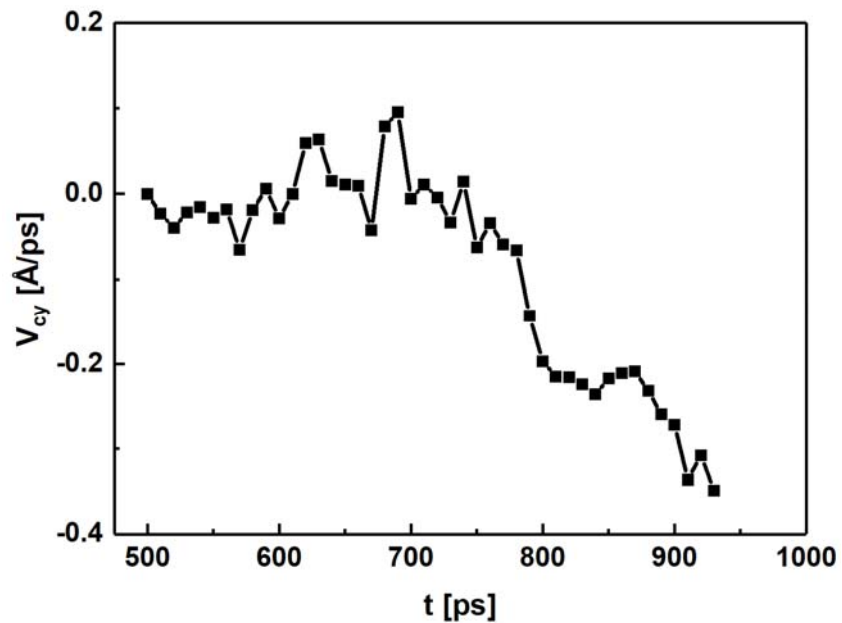


Figure 2.2.S4. The time history of velocity component in the y direction for water droplet on a monolayer graphene with tunable strain gradient direction.

2.3 Phosphorene nanotube

Besides graphene, the novel two-dimensional (2D) functional phosphorene has become the focus of significant research effort recently, thanks to the successful fabrications by micromechanical cleavage, Ar⁺ plasma thinning process and liquid exfoliation methods. Using bending load, 2D phosphorene monolayer can be rolled up to a tube-like structure, in terms of phosphorous nanotube discussed in the Section 2.3. The new morphology exhibits unusual and tunable mechanical and thermal properties for future nanoelectronics.^{6,97}

2.3.1 Introduction

Two-dimensional (2D) structures of graphene⁹⁸, silicene, boron nitride^{99, 100} and MoS₂¹⁰¹ monolayer have attracted intensive attentions of scientist due to their novel properties. Meanwhile, a wide range of applications in nanoelectronics have been also based on their tubular nanostructures such as carbon nanotubes¹⁰², boron nitride nanotubes¹⁰³ and silicon carbide nanotubes¹⁰⁴, thanks to their stable structures^{102, 105, 106}, robust mechanical behaviors^{104, 107-109}, and remarkable electrical properties^{110, 111}. Black phosphorus monolayer (BPM) is a new member of 2D materials. The layered structure possessing the strong intralayer strength and weaker interlayer interaction like graphite¹¹². The novel two-dimensional (2D) functional phosphorene has become the focus of significant research effort recently, thanks to the successful fabrications by micromechanical cleavage¹¹³, Ar⁺ plasma thinning process¹¹⁴ and liquid exfoliation methods¹¹⁵. Not only does phosphorene exhibit comparably high carrier mobility (~10000 cm²V⁻¹s⁻¹), it is also a semiconductor with band gap (0.3–2 eV)¹¹⁶ larger than semimetallic

graphene⁹⁸. Additionally, the puckered structure of phosphorene, shown in **Fig. 2.3.1(a)**, enables its significant anisotropy of band dispersion¹¹⁷, electrical and thermal conductivity¹¹⁷⁻¹¹⁹, mechanical properties¹²⁰⁻¹²². These properties suggest extensive potential applications in phosphorene-based nanodevices, including transistors, advanced batteries and optoelectronics^{123, 124}.

Despite these advances, limited attention has been paid thus far to the phosphorus allotrope, the phosphorene nanotubes. PNTs were theoretically designed and predicted by rolling up a phosphorene sheet along armchair or zigzag direction, forming two types of nanotubes, $(m, 0)$ zigPNTs and $(0, n)$ armPNTs shown in Figs. 1(b) and 1(c), respectively^{125, 126}. The configuration of a PNT was characterized by the integer indexes (m, n) . Further, a wrapping vector $\mathbf{R} = m\mathbf{a}_1 + n\mathbf{a}_2$ has been defined^{127, 128}. Indeed, PNTs' anisotropies in energetic viability and phase transition^{125, 129, 130} were assessed and predicted through first principle calculations, leading to the possibility of synthesis of α -PNTs and β -armPNTs wrapping from blue and black phosphorene¹³⁰, respectively. However, the β -zigPNT structure was regarded as unfavorable due to large strain energy¹³⁰. Furthermore, diagrams in determining stable, faceted PNTs and fullerene structures were presented¹²⁹ and defect-induced blue PNTs with neglected bending energy were demonstrated to have lower formation energy than round PNTs by density functional theory¹³¹. Although these theoretical predictions at 0 K offered a guidance for future laboratory fabrications, evaluation of the stability of PNTs at finite temperature remains unrealized.

Strain-engineering of PNTs was demonstrated possible. For example, strain could affect the carrier mobility and band structures of PNTs^{127, 130, 132}, and the elastic modulus and conductance¹³² could be varied by its diameter. No significant difference of optical

properties was found by varying the diameter of PNTs, though the chirality and polarization direction dependences were presented¹³⁰. Compared with the phosphorus monolayer, PNTs are more favorable to become practical structures in nanodevice applications, such as strain sensors, photodetectors, and transistors due to the great tunability of electrical and optical properties by size and strain¹³². For the aforementioned strain-engineered applications, the mechanical behaviors of PNTs, including Young's modulus, fracture strength and buckling strain, require further investigation.

In this work, MD simulations are carried out to study the thermal-stability and mechanical behaviors of armPNTs and zigPNTs. Intriguingly, PNTs with larger diameter are likely to withstand higher temperature due to the relatively lower intrinsic hoop strain, and the armPNTs can resist higher thermal load than zigPNTs at the same size. Based on the stable armPNT and zigPNT structures, the size-dependence of Young's modulus and fracture strength are observed. To clarify the underlying mechanism, an analytical continuum model is developed to illustrate the size dependence of the Young's modulus. Finally, upon axial compression, the buckling mode transition of armPNTs from column buckling to shell buckling is observed with increasing tube diameter, which may shed some light for strain-tunable characteristics and operation of future PNTs-based electronics.

2.3.2 Model and Method

Large-scale Atomic/Molecular Massively Parallel Simulator (LAMMPS)-based MD simulations¹³³ are performed. The Stillinger-Weber (SW) potential¹³⁴ validated to describe the mechanical properties of phosphorene is used in the simulation. The boundary in the axial direction of PNT is periodical, while a sufficiently large vacuum space (100 Å)

surrounding the nanotube is applied. For the stability analysis, each initial PNT, having the length of 50 supercells, is relaxed to a thermally stable state with a NPT ensemble at given temperature (0 K~400 K), controlled by the Nose-Hoovers thermostat for 250 ps. The pressure and time step are set at 0 bar and 0.5 fs, respectively.

Mechanical simulations: The above equilibrium structures at 0 K are used to study the deformation behaviors. The mechanical properties under axial tension and compression are studied at a constant strain rate of 10^{-4} ps⁻¹ in the NPT ensemble. The strain is defined as the relative change of simulation box along the axial direction ($\epsilon = \Delta L/L_z$). In order to calculate the stress, the interlayer spacing of phosphorene is taken as the thickness of a PNT, commonly assumed to be 5.24 Å¹²². For the sake of simplicity, only zigPNTs and armPNTs (**Figs. 2.3.1(b) and 2.3.1(c)**) are studied, and other mixed chiralities will be explored in future.

Thermal simulations: In the non-equilibrium Müller–Plathe approach [38], a-PNT is divided into $2N$ ($N = 10$) layers in the axial direction. The kinetic energies of the hottest atom in layer 1 and the coldest atom in the middle layer $N+1$ are exchanged continually for 5 ns to produce a symmetric temperature gradient, thereby forming the equal thermal flux J at both sides separated by the two layers in **Fig. 2.3.1(d)**. By satisfying Fourier’s law of heat conduction, the thermal conductivity is thus calculated as $\kappa = -J \left(\frac{\partial T}{\partial x} \right)^{-1}$.

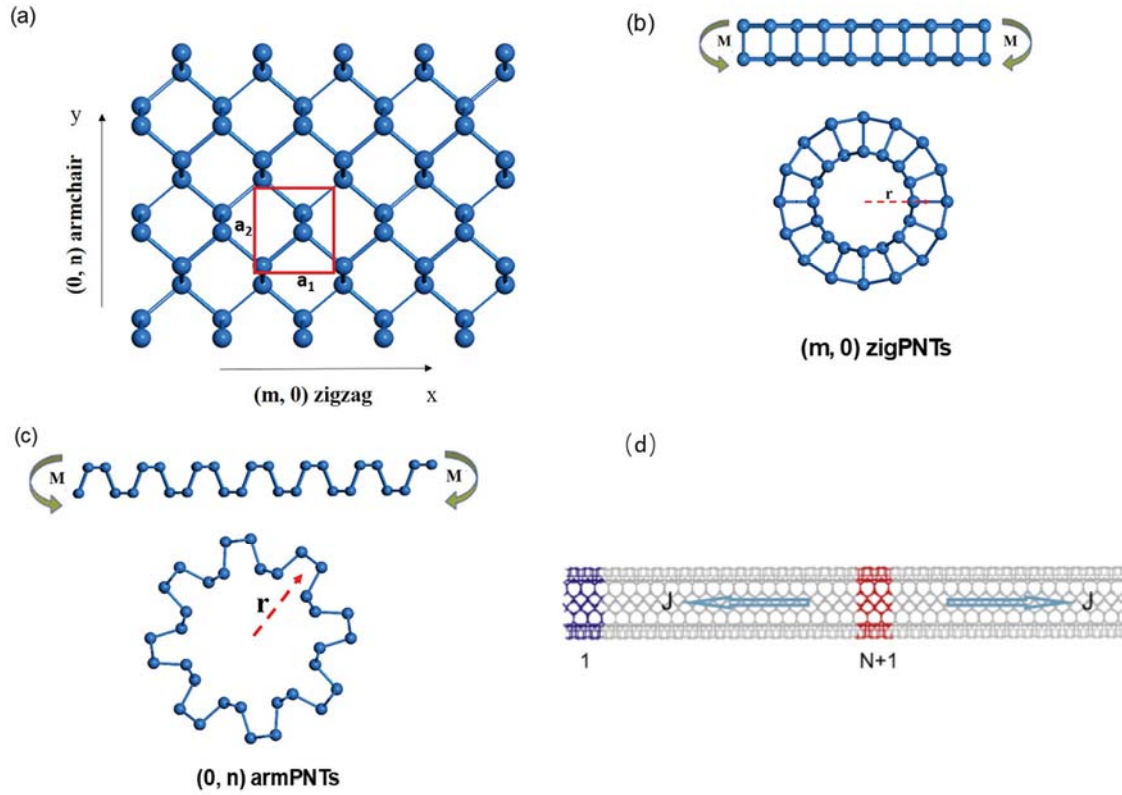


Figure 2.3.1 (a) Top view: crystal structure of 2D phosphorene ($a_1 = 3.3 \text{ \AA}$ and $a_2 = 4.5 \text{ \AA}$); (b) The zigPNT is bended from phosphorene sheet along the wrapping vector $(m, 0)$ ($r = ma_1/2\pi$); (c) the armPNT is bended from MBP along the wrapping vector ($r = a_2/2\pi$); (d) An arm-PNT is divided into $2N$ layers, with the cold layer 1 and hot layer $N+1$.

2.3.3 Thermal stability of PNTs

The strain energy E_s , originating from bending a phosphorene sheet into a PNT is defined as $E_s = (E_{PNT} - E_{BP})/N$, where N is the total numbers of atoms in the simulated PNT, and $E_{PNT} - E_{BP}$ is the potential energy difference in an equilibrium nanotube with respect to the 2D phosphorene sheet (as the reference system) at a given temperature.

Physically, a higher strain energy for nanotube means a larger intrinsic strain in the hoop direction. The results in **Figs. 2.3.2(a) and 2.3.2(b)** provide maps for determining the stable region by varying temperature and size. All single-walled PNTs are inclined to have higher thermal stability as the diameter increases. Taking the (0, 10) armPNT and (0, 20) armPNT as examples, the former is able to resist $T = 175$ K which is lower than that of the later one, $T = 410$ K. **Figs. 2.3.2(c) and 2.3.2(d)** explain the cause of this phenomenon. It is evident that a higher strain energy is stored in a PNT with smaller diameter under higher thermal load after energy minimization. The curvature-dependent strain energy agree well with those in bended phosphorene sheets studied by the MD simulation¹³⁵ and first principle calculations^{128, 130}. As shown in **Fig. 2.3.2(d)**, the temperature-sensitive bending energy in PNTs are found, which is similar with that of phosphorene monolayer¹³⁵. Thus, the higher intrinsic hoop strain in a bended PNT structure is responsible for collapsing at lower thermal load. In addition, the strain energies in the (0, 6) armPNT (0.085 eV/atom) and (17, 0) zigPNT (0.093 eV/atom) are close to the value at fracture (~ 0.1 eV/atom) for a 2D phosphorene sheet under uniaxial tension along both armchair and zigzag directions, indicating the verge of integrity. Hereby, the (0, 6) armPNT and (17, 0) zigPNT are suggested to be the smallest stable PNTs without fracture or phase transition¹²⁸, which echoes with the collapsed smaller structures found in our MD simulation. Compared with other 1D nanostructures, PNTs exhibit weaker thermal stability. For example, CNTs can remain stable at temperature up to 2000 K¹³⁶.

In terms of the effect of chirality, at a particular radius, armPNTs are found to have the ability to withstand much higher thermal loads than zigPNTs, by comparing **Fig. 2.3.2(a)** with Fig. 2(b). This is exemplified by the maximum temperature, $T = 410$ K, upon

which the (0, 20) armPNT could resist, as opposed to that of the (20, 0) zigPNT which may only resist $T = 10$ K. By comparing the strain energies of the two types of PNTs, the values for armPNTs are much lower than that for zigPNTs at all temperatures and sizes shown in **Figs. 2.3.2(c) and 2.3.2(d)**. The structural stability upon different thermal loads provides a preliminary guideline for future synthesis in laboratory and operation of PNTs in applications. Note that some other phases are not considered in the present manuscript, such as the faceted PNTs with joints^{126, 131} and the ones with bending-induced phase transitions¹²⁸. The investigation of their thermal stabilities will be subjected to future research.

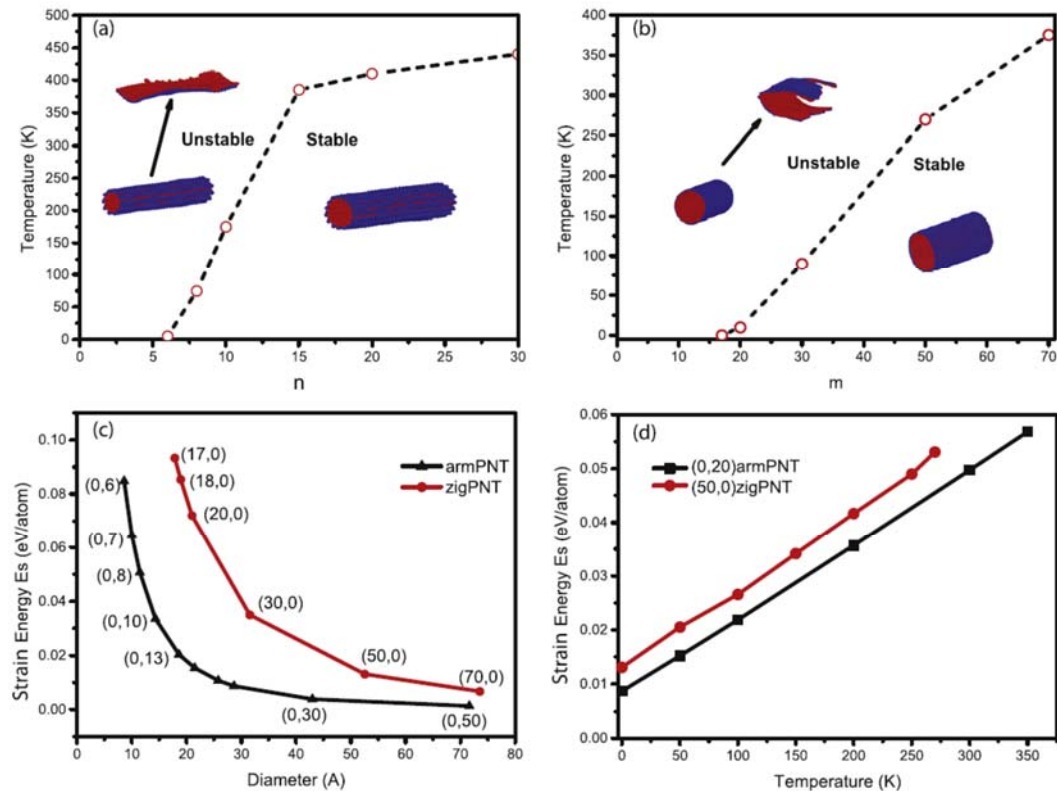


Figure 2.3.2 The phase diagrams for thermal-stability of (a) armPNTs and (b) zigzagPNTs with varying temperature and wrapping vector of nanotube; (c) The strain energy stored in wrapped PNTs as function of the diameter of armPNTs (black triangular) and zigPNTs (red

circles) at $T = 0$ K; (d) The strain energies of (50, 0) zigPNT (red) and (0, 20) armPNT (black) change with temperature.

2.3.4 Size-dependent tensile properties

Since Young's modulus of phosphorene changes slowly with temperature¹³⁵, initially stable PNT structures at 0 K are stretched to further explore the underlying mechanical behaviors of PNTs. **Figs. 2.3.3(a) and 2.3.3(b)** show the nominal stress-axial tensile strain curves of (0, n) armPNTs and (m , 0) zigPNTs, respectively. ArmPNTs (~94 GPa) are stiffer than zigPNTs (~20 GPa), while zigPNTs have larger fracture strain, which originates from the structural anisotropy of phosphorene^{122, 135}. Similar brittle fracture behaviors of carbon nanotubes (CNTs) at low temperature were also observed in PNTs¹³⁷. However, PNTs are much softer than other 1D materials, for example, CNTs (~1.0 TPa)¹³⁸, SiCNT (~0.6 TPa)^{139, 140} and BNNTs (~0.7 TPa)¹⁰⁷ having the higher Young modulus.

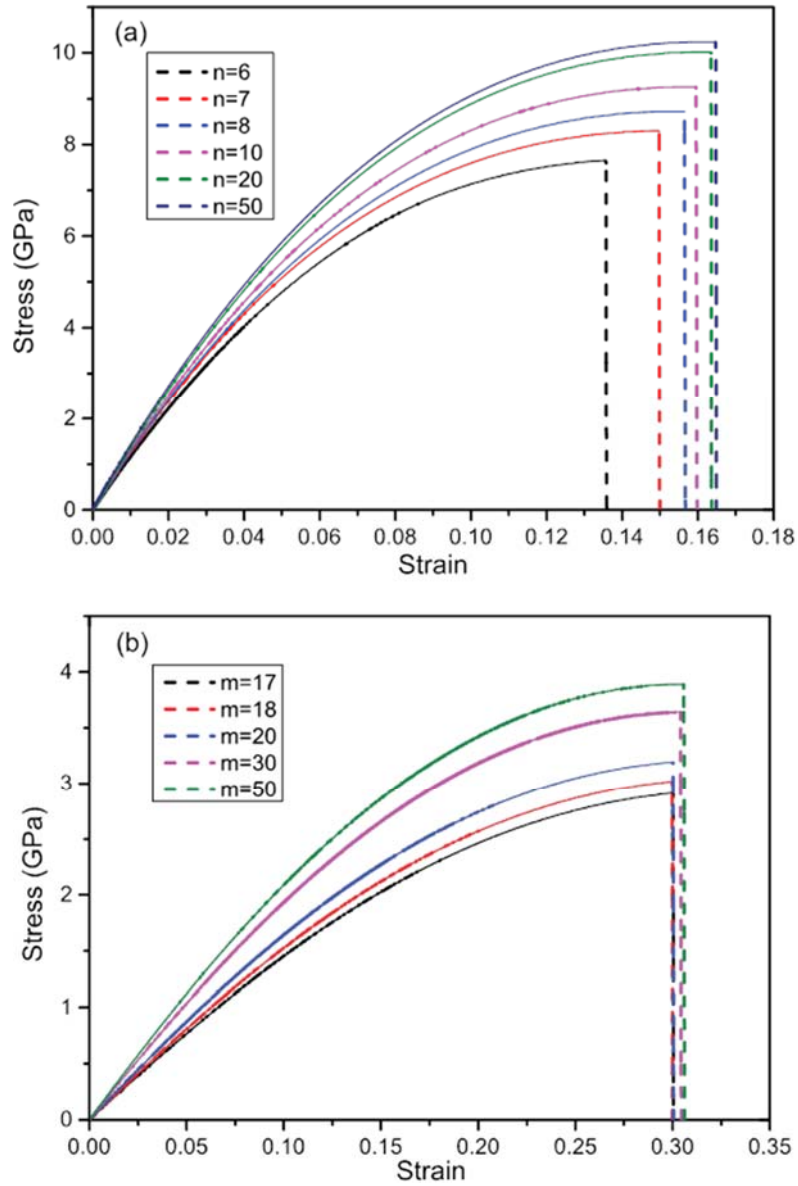


Figure 2.3.3 The axial tensile stress-strain curves for (a) armPNTs and (b) zigPNTs with various wrapping indexes at $T = 0$ K

It is evident that the wrapping index or diameter has a significant influence on the stress-strain curve, showing strong size effect on both the stiffness and strength of the PNTs. The Young's moduli of PNTs in **Figs. 2.3.4(a) and 2.3.4(b)** can be deduced by fitting the stress-

strain curves in the small strain region ($\leq 1.0\%$). As the tube diameter increases, the Young's modulus increases from 84 GPa to 102 GPa for armPNTs and from 15.6 GPa and 24 GPa for zigPNTs. Meanwhile, the effects of diameter on the tensile strength of PNTs are shown in **Figs. 2.3.4(c) and 2.3.4(d)**. The present values of the fracture strength for both armPNTs and zigPNTs increase with increasing nanotube diameter, approaching the limit values of 10.3 GPa and 4.0 GPa for a pristine phosphorene sheet ¹³⁴.

It is interesting to find the existence of bending-induced intrinsic stress along the axial direction in equilibrium PNTs, even before external loads are applied (shown in **Fig. 2.3.4(e)**). The residual compressive stress in the inner sublayer of PNTs is relaxed when the applied strain increases up to ε_0 , which is defined as the initial axial strain. The unique atomic structure (two-sublayers phosphorous atoms shown in **Fig 2.3.4(e)**) differs from monolayer atoms in CNTs ¹⁴¹, and is likely responsible for the intrinsic axial strain. According to **Fig 2.3.4(f)**, the absolute values of intrinsic axial strains for both armPNTs and zigPNTs exponentially decrease as radius increases, approaching zero. Consequently, for the stretched PNT with smaller diameter, the lower fracture strength (**Figs 2.3.4(c) and 2.3.4(d)**) is caused by the larger intrinsic strain in the axial direction.

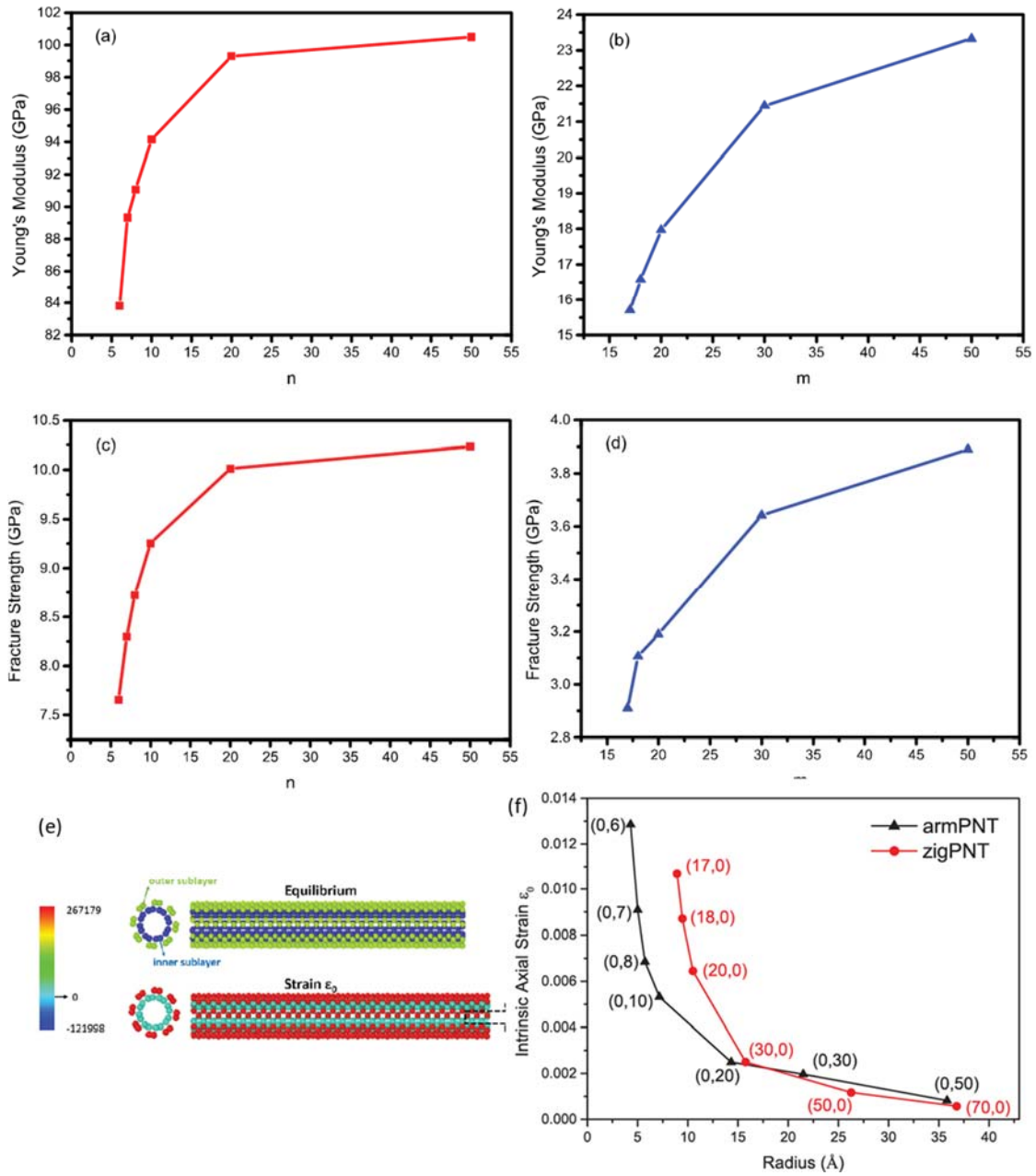


Figure 2.3.4 Size-dependent mechanical properties at $T = 0$ K. Young's modulus of (a) armPNTs and (b) zigPNTs, fracture strength of (c) armPNTs and (d) zigPNTs. (e) The atomic stress (unit: eV/atomic volume) of PNT structures. (f) The intrinsic axial strain in each sublayer of equilibrium armPNTs (black line) and zigPNTs (red line) at $T = 0$ K.

In order to explain the size-dependence of Young's modulus, a simple continuum model is proposed by considering both the intrinsic axial strain and the nonlinear effect of potential. As a first order approach, several simplified assumptions are adopted. First, despite the two sublayers (shown in **Fig. 2.3.4(e)**) in a PNT with bond interaction in between, the continuum model considers only a monolayer tube with a uniform intrinsic axial strain; Second, the effect of curvature on the atomic potential is neglected, although geometry nonlinearity was regarded as being responsible for the size-dependence of stiffness of CNT with diameters less than 0.5 nm¹⁴², the PNTs in the present study are sufficiently large such that the curvature effect may be small. The nonlinear effect of potential is illustrated by the stress-strain curves of a 2D phosphorene sheet under tension at 0 K, presented in **Figs. 2.3.5(a) and 2.3.5(b)**. This nonlinearity suggests that the Young's modulus of phosphorene is also strain-dependent, and the corresponding $E(\varepsilon)$ is plotted in **Fig. 2.3.5(c)** based on the fitting of a simple quadratic function. The result closely matches that calculated by Jiang *et al.*¹²¹.

To take into account the effect of the intrinsic axial strain (ε_0), the Young's modulus of a continuum tube with intrinsic strain can be derived as

$$E^* = \frac{E(\varepsilon_0) + E(-\varepsilon_0)}{2} - \frac{(E(-\varepsilon_0) - E(\varepsilon_0))\varepsilon_0}{2\varepsilon_{app}} \quad (2.3.1)$$

where ε_{app} is the applied strain to deduce Young's modulus, which is sufficiently small region so that the Young's modulus of each sublayer can be regarded as a constant during deduction. For example, ε_{app} is taken as 0.01 in the MD simulation above. Both the magnitude of ε_0 and the nonlinear variation of stiffness with respect to the strain, contribute to the size effect: as the diameter of PNTs increases, **Fig. 2.3.4(b)** shows the

decreased intrinsic axial strain ε_0 . While the first term in Eq. (2.3.1) remains constant due to the assumed linearity of the Young's modulus-strain relation (see **Fig. 2.3.5(c)**), the second decreases based on the **Fig. 2.3.5(c)**, which consequently leads to the increased Young's modulus E^* . The trends given by this model are in qualitative agreement with the size-dependence of Young's modulus derived by our MD simulations (see **Figs. 2.3.4(a) and 2.3.4(b)**) and the previous results by first principle calculations¹³².

Additionally, it is seen that the size-induced stiffening for armPNTs is more sensitive than that for zigPNTs. Basically, the nonlinear effect in zigzag direction is more significant than that in armchair direction as shown in **Fig. 2.3.5(c)**. Specifically, as the strain increases from -0.01 to +0.01, the strain-induced reduction of Young's modulus in zigzag direction (30%) is larger than that in armchair direction (10%). This primary mechanism for size-dependence of Young's modulus is different from that for CNTs, where no intrinsic axial strain exists^{142, 143}.

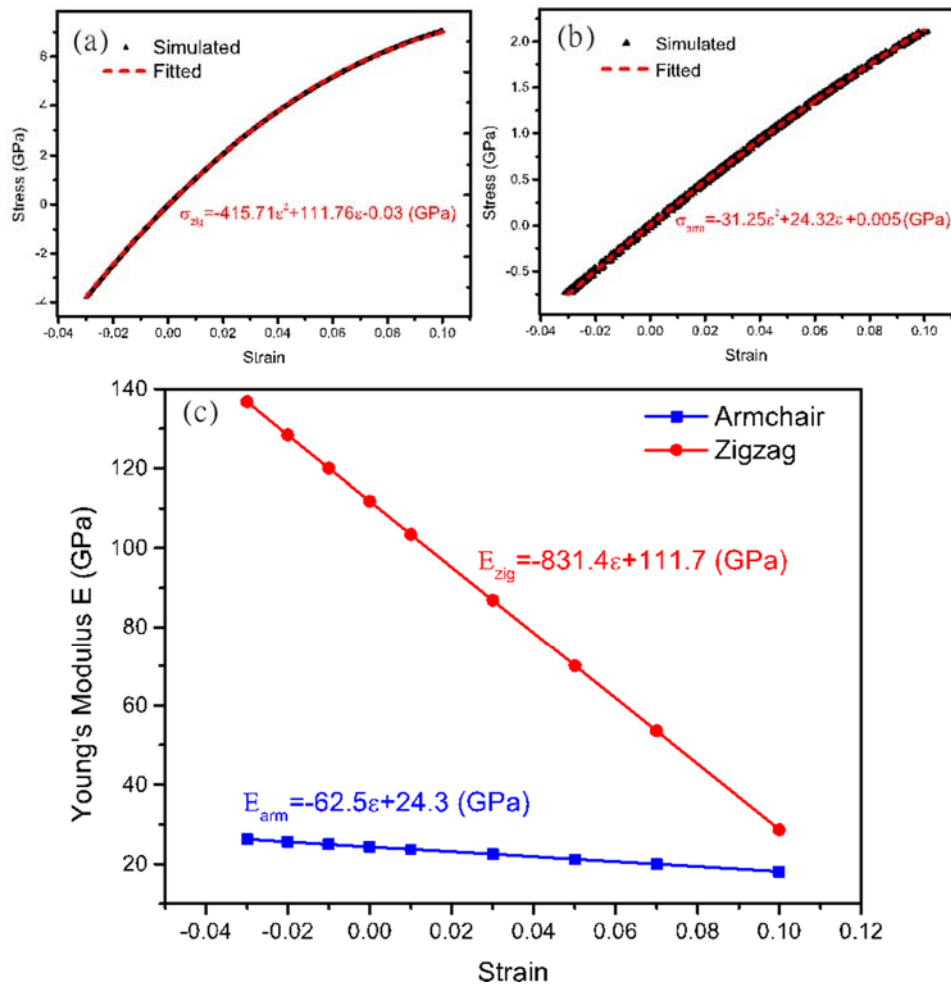


Figure 2.3.5 The nonlinear stress-strain curves of a 2D phosphorene sheet simulated by MD at $T = 0$ K along the (a) zigzag direction and (b) armchair direction; The Young's moduli of the phosphorene sheet along zigzag direction (red line) and armchair direction (blue line) are fitted and plotted as a function of the applied strain, in (c).

2.3.5 Size-dependent thermal conductivity

The size-dependent thermal conductivity is explored for the optimized a-PNTs. In **Fig. 2.3.6(b)**, it shows the thermal conductivity κ with various n , associated with the diameter of the nanotube by $D = na_2/\pi$, at temperature $T = 300$ K. The length of the

nanotube is chosen to be 100 nm, while a periodic boundary condition is applied along the axial direction for each a-PNT. **Fig. 2.3.6(b)** clearly demonstrates that as n increases, κ sharply increases and then comes to a gentle rise after $n = 20$. As the characteristic size scales down to the order of nanometers, the phonon confinement leads to reduced phonon group velocities and phonon mean-free path (MFP), thereby weakening the thermal transport. In previous studies, this size effect was also observed in silicon nanowires and carbon nanotubes [39–41]. Besides, the thermal conductivity of the nanotube strongly depends on the length. To investigate this effect, **Fig. 2.3.6(c)** illustrates the relationship of thermal conductivity and length for the (0, 20) a-PNT. As shown in **Fig. 2.3.6(c)**, κ gradually increases with increasing length. Therefore, the size effect of thermal transport is related to not only the diameter, but the length. As studied here, the length of the simulation system L is not significantly longer than the phonon MFP, resulting in phonon scattering occurring at the interfaces between the heat source and sink. In other words, κ is largely limited by the size, known as the Casimir limit. The thermal conductivity of infinite PNT can be calculated by using linear extrapolation, which takes the following form [42].

$$\frac{1}{\kappa} = C\left(\frac{1}{l_{\infty}} + \frac{1}{L}\right)$$

where l_{∞} is the phonon MFP of infinite (0, 20) a-PNT, and C is a constant. Given that the representative MFP along the zigzag direction is 66 nm for the phosphorene sheet [11], the lengths of 150–300 nm are employed for the linear fitting between $1/\kappa$ and $1/L$. The fitted relationship reads $1/\kappa = 3.1/L + 0.02233$, and hence it yields the estimated thermal conductivity of 44.8 WmK^{-1} in the limit $1/L = 0$ and the phonon MFP of infinite (0, 20) a-PNT $l_{\infty} = 35\text{nm}$. In a previous study, Hong et al used the same SW potential and reported the thermal conductivity of 110.7 WmK^{-1} along the zigzag direction for

phosphorene sheet [14]. Hence, the thermal conductivity of PNT is greatly reduced compared to that of 2D phosphorene, largely originating from the restricted paths for phonon transport in PNTs, as the phonon MFP shrinks down to 35 nm of a-PNT against 66 nm of 2D phosphorene. In spite of the difference, the thermal conductivity of a-PNTs will converge to the value of phosphorene as the diameter and length increase.

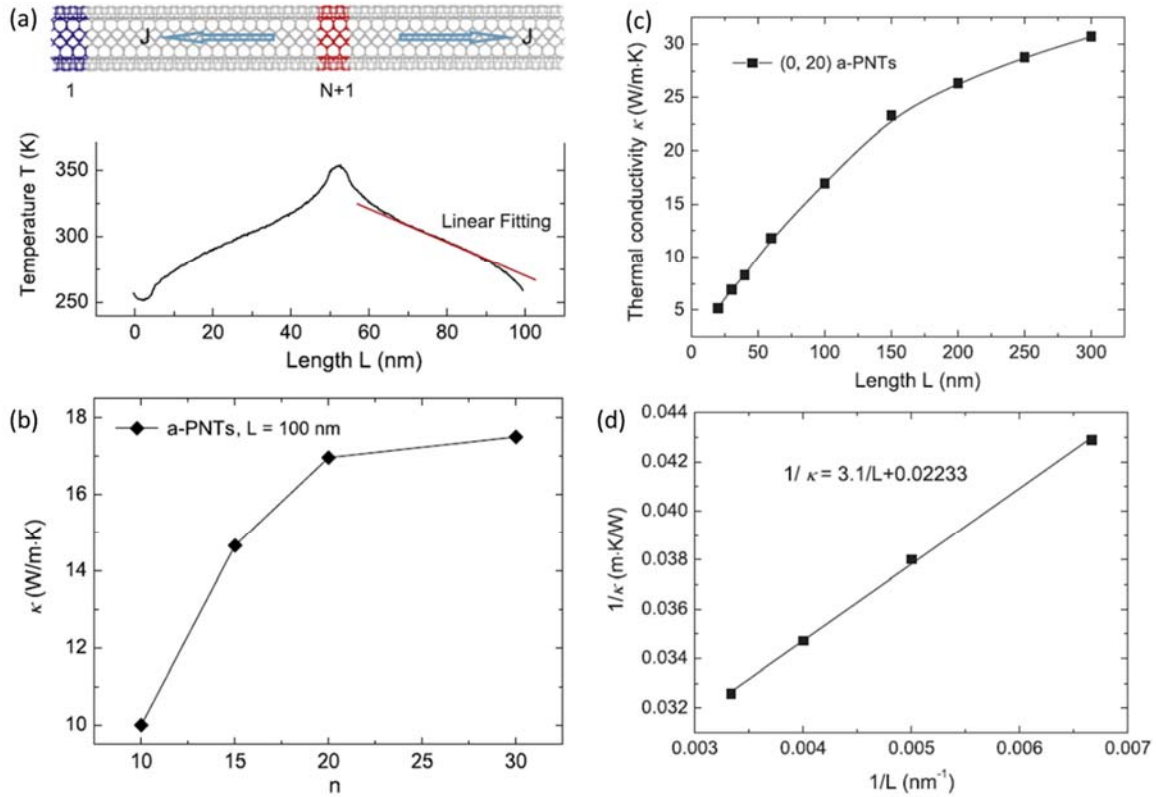


Figure 2.3.6 (a) An arm-PNT is divided into $2N$ layers, with the cold layer 1 and hot layer $N + 1$; (b) The diameter-dependent thermal conductivity of arm-PNT; (c) The thermal conductivity κ of arm-PNT with varying axial length under temperature $T = 300$ K; (d) Linear fitting of the relationship between the inverse of κ and the inverse of L .

2.3.6 Conclusions

We carried out MD simulations on single-wall PNTs to study the structural stability and mechanical behaviors of PNTs. The results indicated that PNTs with a larger diameter are able to resist higher temperature. However, zigPNTs have lower resistance to the thermal loads due to high intrinsic hoop strain in the wrapped structures. Also, the remarkable size-effect of mechanical properties was revealed, and both Young's modulus and fracture strength of PNTs decrease as the diameter decreases. In addition, a continuum model was developed to uncover the role of the intrinsic axial strain on the size-dependence. Compared to 2D phosphorene, the thermal conductivity of a-PNT evidently decreases due to phonon confinement, exhibiting remarkable size effects, which relies on not only the diameter but on the length.

2.4 Closed-edged Bilayer Phosphorene Nanoribbons

In this section, we further apply the point forces to press the tube-like morphology rolled as discussed in Section 2.2, the bilayer structure with closed edges is formed with tunable electrical properties of band gap, enriching the applications in nanoribbon-based devices.¹⁴⁴

2.4.1 Introduction

As a novel two-dimensional material, black phosphorene has recently become the focus of extensive research efforts. It may be fabricated via micromechanical cleavage¹¹³, Ar⁺ plasma thinning process¹¹⁴ and liquid exfoliation method¹¹⁵. Phosphorene exhibits comparably high carrier mobility ($\sim 1000 \text{ cm}^2\text{V}^{-1}\text{s}^{-1}$) as well as significant band gap (0.3–2 eV)^{116–98}. Additionally, its puckered structure enables its significant anisotropy of band dispersion, thermal conductivity¹¹⁷⁻¹¹⁹, mechanical properties¹²⁰⁻¹²². Besides black phosphorene, several other phosphorene allotropes were also proposed. Among the 2D allotropes, the most common monolayers are $\alpha - \text{P}$, $\beta - \text{P}$, $\gamma - \text{P}$ and $\delta - \text{P}$, which enrich the variety of phosphorous family¹⁴⁵.

Despite these advances, the tremendous needs for functional nanoelectronics require controllable engineering of phosphorene nanostructures. Considerable efforts have been paid to low-dimensional phosphorene isomeric forms, among which the most common are phosphorene nanotubes (PNTs) and nanoribbons (PNRs). Previous studies showed that the mechanical, thermal and electrical properties for both PNTs and PNRs were not only size-dependent due to quantum confinement, but also tuned through external strain and electrical field^{16, 97, 146, 147}. In addition, structurally robust PNRs were considered as a potential candidate for thermoelectric applications because of the enhanced Seebeck

coefficient¹⁴⁸. Accordingly, it is crucial to find a practical way to fabricate PNRs with desired size, which is a precondition for broad applications of PNR-based devices, for example, thermo-electronics^{147, 149}.

Although PNRs-based nanodevices can be prepared via a top-down microfabrication from phosphorene flakes, including electron beam lithography and reactive ion etching^{149, 150}, the synthesis of narrow nanoribbons with well-defined edges remains a great challenge. The spontaneous collapse of carbon nanotubes (CNTs) suggested an effective strategy for the fabrication of closed-edged bilayer graphene nanoribbons (CBCNRs)¹⁵¹⁻¹⁵³. The advantage of this potential method is that the width and thickness of nanoribbons can be tuned by unzipping available nanotubes. With radially deforming CNTs, the energetic stability and fascinating electronic properties of nanoribbons were extensively investigated^{154, 155}. As an analogy of collapsed CNTs, can spontaneous formation of phosphorene nanoribbons with tailored size happen for the PNTs? What is the change of physical and chemical properties from PNTs to corresponding nanoribbon structures?

In this study, we investigate the dynamic characteristic of radially deforming PNTs and the energetic stability of the derived closed-edged bilayer phosphorene nanoribbons (CBPNRs). We focus on the armchair PNTs which have lower strain energy than zigzag PNTs⁹⁷. The potential energy of CBPNRs is shown to be much less than the corresponding PNTs. In addition, our *ab initio* calculations demonstrate the change of band structures from PNTs to CBPNRs and the size-dependent bandgap of obtained CBPNRs. This work provides a potential technique to fabricate phosphorene nanoribbons with well-defined edges and enrich the applications in nanoribbon-based devices^{149, 156, 157}.

2.4.2 Model and Method

The LAMMPS-based Molecular Dynamics (MD) simulations¹³³ are performed to investigate the dynamic configuration of PNTs undergoing radially deformation. We adopt the reactive force field validated to describe the chemical and mechanical properties of various phosphorous allotropes¹⁵⁸. Two types of nanotubes including armchair PNTs and zigzag PNTs have been predicted, and the $(0, n)$ armchair PNT can be constructed by rolling up n times of units cells in armchair direction of phosphorene⁹⁷. The boundary in the axial direction of PNTs is periodical, while a sufficiently large vacuum space (100 Å) surrounding the nanotubes is added. All the MD simulations consist of two steps: loading process and collapsing process. First, two virtual point forces, van der Waals (vdW) interaction with PNTs, are placed at the top and bottom of the round PNT (**Fig 2.4.1(a)**) and then move toward each other. Second, the point forces are removed once the vertical shortest distance between the facing phosphorous atoms is 5 Å, forming a collapsed PNTs. The simulations with time step of 0.5 fs are performed in NPT ensemble at temperature 0 K in order to emphasize the configurational evolution without thermal fluctuation. The simulation for each case is run long enough to achieve an equilibrium state.

The geometrical optimization and electronic structure calculations are carried out within the density-functional theory using generalized gradient approximation (GGA) with the Perdew-Burke-Ernzerhof (PBE) exchange-correlation functional¹⁵⁹, as implemented in the Quantum Espresso Package¹⁶⁰. The plane-wave cutoff energy for wave function is set to 400eV. The van der Waals correction are described by DFT-D3 method of Grimme, which has been validated reliable for multilayer phosphorene¹⁶¹. The electron-ion interactions are described by ultrasoft pseudopotentials. When geometrically relaxing the

structures of PNTs and CBPNRs obtained from MD simulations, $1 \times 10 \times 1$ Monkhorst-Park k -meshes are used. The atoms are relaxed until the forces are converged to $5 \times 10^{-3} eV/\text{\AA}$ and the energy convergence criteria of $1 \times 10^{-5} eV$. The periodic boundary condition is applied to the axial direction of the simulated structures separated by the vacuum layer of 25\AA to eliminate the coupling effect of neighboring slabs. For electronic properties, we adopt a k -point density equivalent to $1 \times 20 \times 1$ Monkhorst-Pack mesh.

2.4.3 Deformation and collapsing of PNTs

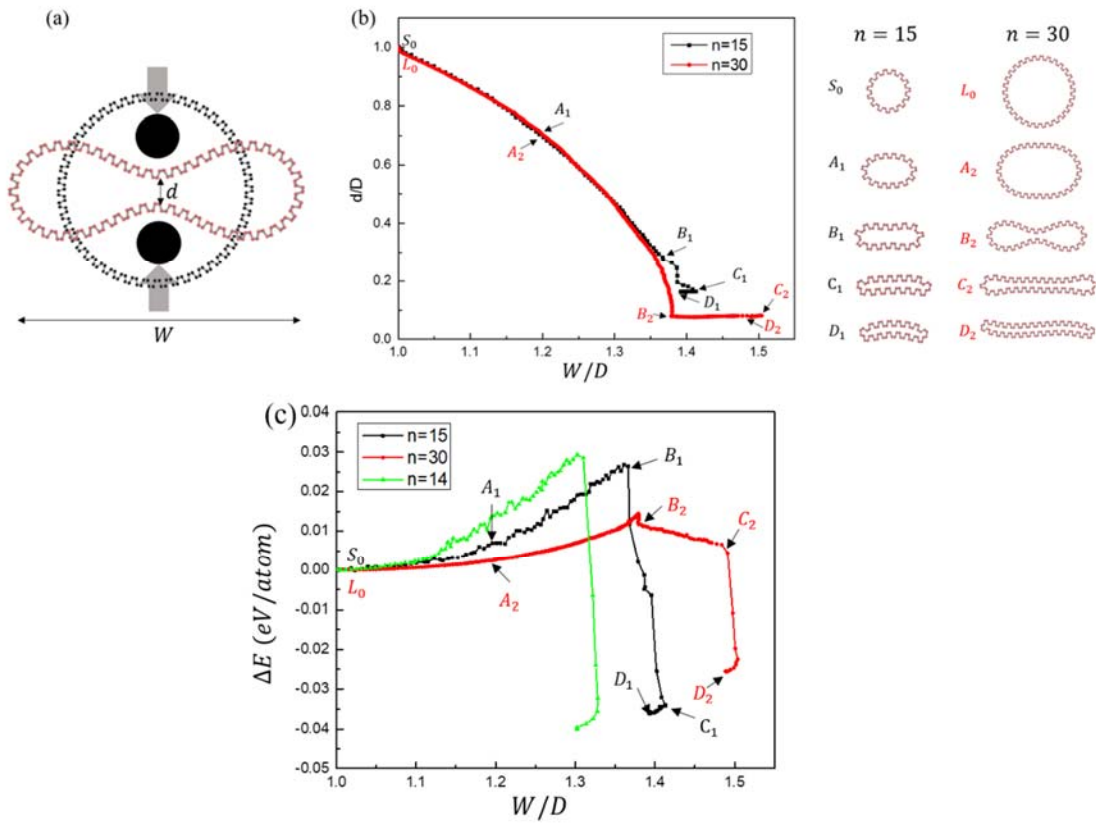


Figure 2.4.1 (a) The schematic of deforming armchair PNT; (b) The deformation pathways of (0,15) and (0,30) armchair PNTs (left) projected to the $d - W$ plane; (c) The strain energy ΔE along deformation pathway as a function of W .

We simulate the radial deformation of armchair PNTs subjected to the compression by point forces as illustrated in **Fig 2.4.1(a)**. During loading and collapsing steps, the distance between atoms on the opposing faces undergoes shrinking (d) or expansion (W). The strain energy is defined, $\Delta E = (E_d - E_0)/N$, where N is the total numbers of atoms and $E_d - E_0$ is the potential energy difference between the deformed and original tubes. We plot the variation of values (d, W) for (0,15) and (0,30) armPNTs in **Fig 2.4.1(b)**, which maps their transformation pathways. Initially, the circle cross-sections (S_0, L_0) of tubes deform into oval shapes (A_1, A_2) and then peanut-like shapes (B_1, B_2), which is similar to the radial deformation in CNTs¹⁵¹. These oval and peanut-like shapes are unstable configurations because of positive strain energies illustrated in Figure 1c, which shows the evolution of energy change as a function of W .

After removing the point forces, the subsequent simulation continues and the collapsing pathway of PNTs is revealed by the snapshots ($B \rightarrow C \rightarrow D$) shown in **Fig 2.4.1(b)**. From B_1 to C_1 configurations of the (0, 15) PNT, the shortest distance d continues reducing with increasing width W but not smoothly since the phase transformation of black-to-blue phosphorene occurs at the edged atoms. The phase change comprises of a high bending energy due to large curvature at the two edges, verified by the sudden drop of strain energy shown in **Fig 2.4.1(c)** when the C_1 configuration forms. Then, the roughly planar configuration (C_1) relaxes and shrink back into an overall curved structure with smaller width, that is, arc-like CBPNRs (D_1). The curvature is attributed to the odd number of n , and hence, the number mismatch of unit cells between the two sublayers. However, for the larger tube, (0, 30) PNT, we observe the configurational

pathway ($B_2 \rightarrow C_2$) with the constant value of d shown in **Fig 2.4.1(b)** and an increase of contact area leads to the steady declination of strain energy in **Fig 2.4.1(c)**. The continuously spreading of self-collapse is driven by the release of stored vdW energy in the nanotube, which was reported to dominate the collapse of CNTs¹⁵¹. Furthermore, the black-to-blue phosphorene transformation occurs in the two edges of C_2 configuration and the sequent relaxation drives the formation of the sigmoidal CBPNRs (D_2) with locally curved edges. **Fig 2.4.1(c)** shows that this bilayer nanoribbon has much lower strain energy compared with the original (0,30) PNT. The above results underpin a potential method to fabricate the energetically stable CBPNRs based on PNTs.

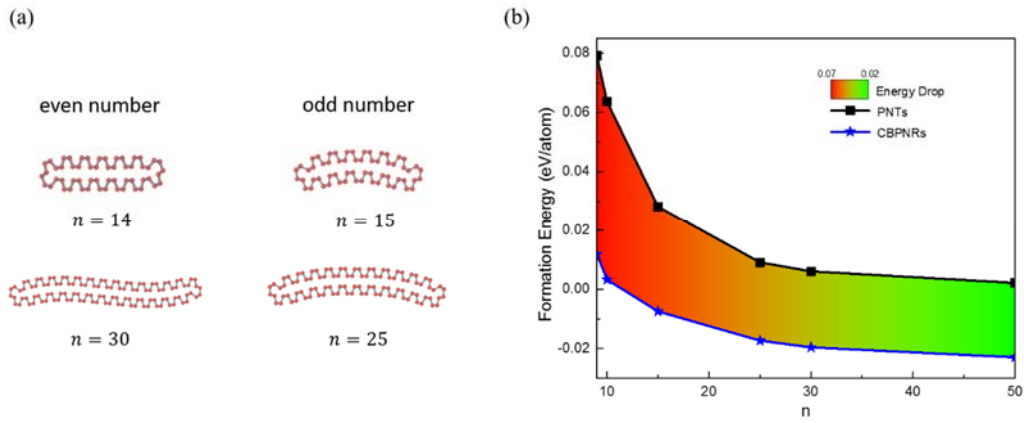


Figure 2.4.2 (a) The CBPNR configurations derived from the PNTs with odd or even value of n .; (b) The formation energy of PNTs and CBPNRs relative to that of monolayer phosphorene is dependent on the size n .

Through our systematical studies shown in **Fig 2.4.2(a)**, all PNTs with odd number of unit cells (for example, $n = 15, 25$) are found to collapse into an arc-like structure with

overall curvature, while sigmoidal CBPNRs with locally curved edges are originated from the PNTs with even number (for example, $n = 14,30$). Since extremely small nanotubes were verified to be structurally unstable⁹⁷, we only consider the cases with $n \geq 9$. Additionally, the formation energies per atom for both CBPNRs and armchair PNTs relative to that of monolayer phosphorene are plotted as a function of n in **Fig 2.4.2(b)**. It's evident that these energies decline with the increase of tubes' diameter. Of importance is the energy loss for forming CBPNRs from corresponding PNTs illustrated in **Fig 2.4.2(b)**. The energy loss per atom is higher for the bilayer ribbons with smaller size. It is noted that the released vdW energy between the two opposing walls is approximately proportional to the ribbon size. However, the results in **Fig 2.4.1(c)** confirm that the energy change for local black-to-blue phosphorene transition dominates the energy drop from PNTs to CBPNRs, which is independent of the initial tube size. Hence, the energy loss per atom from PNTs with larger diameter is relatively small. Since the thermal fluctuation energy is much smaller than that from local phase transition as well as vdW interaction, the thermal effect is not considered in this study although thermal perturbation may affect the onset of collapse of PNTs and will be subjected to future work.

2.2.4 Electronic Properties of Closed-edged Bilayer Nanoribbons

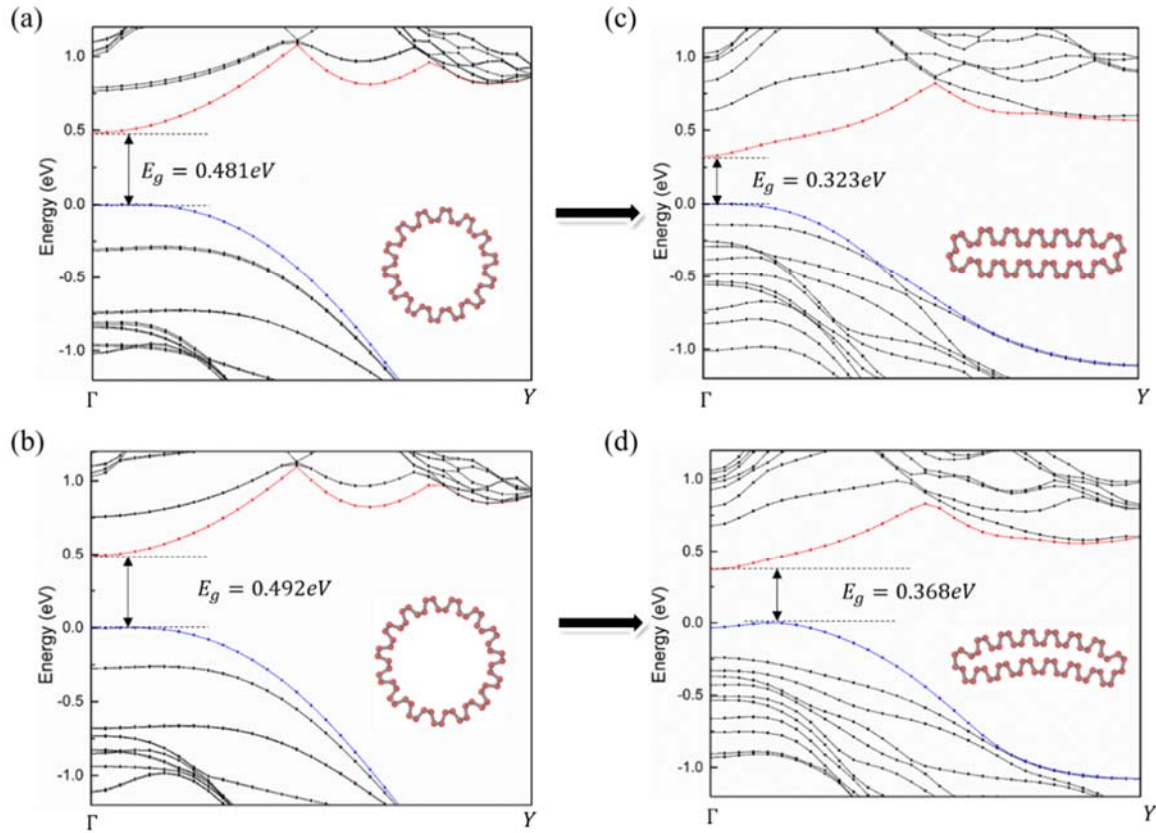


Figure 2.4.3 The band structures of the (0,14) (a) pristine nanotube and (b) corresponding sigmoidal nanoribbon; The band structures of the (0,15) (c) pristine nanotube and (d) corresponding arc-like nanoribbon.

Of great significance is to investigate the electronic properties of the collapsed structures predicted by MD simulations as mentioned above, since it is crucial for future CBPNRs-based nanodevices. **Fig 2.4.3** shows the electronic band structures along the irreducible Brillouin zone for bilayer nanoribbons and their comparisons of nanotubes. The original armPNTs of (0,14) and (0,15) demonstrate semiconducting behaviors with direct band gaps of 0.481eV and 0.492eV shown in **Figure 2.4.3(a)** and **2.4.3(b)**, respectively. These band gaps are in good agreement with previous studies^{127, 132}, although the values of

band gap are underestimated by the PBE functional. After the collapse of (0,14) PNT, the position of valence band minimum (VBM) keeps almost unchanged, while its conduction band minimum (CBM) shifts downward at the high-symmetry point Γ , resulting in a reduced band gap of 0.323 eV shown in Figure 3c. Interestingly, it's found in **Fig 2.4.3(d)** that the arc-like CBPNR fabricated from the (0,15) PNT exhibits an indirect band gap of 0.368 eV, where the valence maximum band significantly shifts away from Γ point. Noticeably, the arc-like CBPNR presents a dramatic difference with the sigmoidal one, and the origin of this direct-to-indirect transition is possibly attributed to the high strain in the arc-like collapsed structure. Taking (0,15) CBPNRs as an example, the intrinsic strain of roughly 7% is estimated in the curved bilayer nanoribbon. Furthermore, **Fig 2.4.3(c)** illustrates lower strain energy in the collapsed tube of $n = 14$ than that of $n = 15$ by $6 \times 10^{-3} \text{ eV/atom}$, although the difference of strain energy between these two original tubes is neglected ($7 \times 10^{-4} \text{ eV/atom}$). Thus, this strain energy was found to be responsible for the direct-to-indirect gap transition of phosphorene¹⁶². This unique property for arc-like CBPNRs is qualitatively different from both the recent study of direct-to-indirect gap transition at smaller PNTs¹⁶³ and the transition originated from axial strain in PNTs¹²⁷. Therefore, both of direct and indirect band gaps allow flexibly tuning electronic properties of CBPNRs.

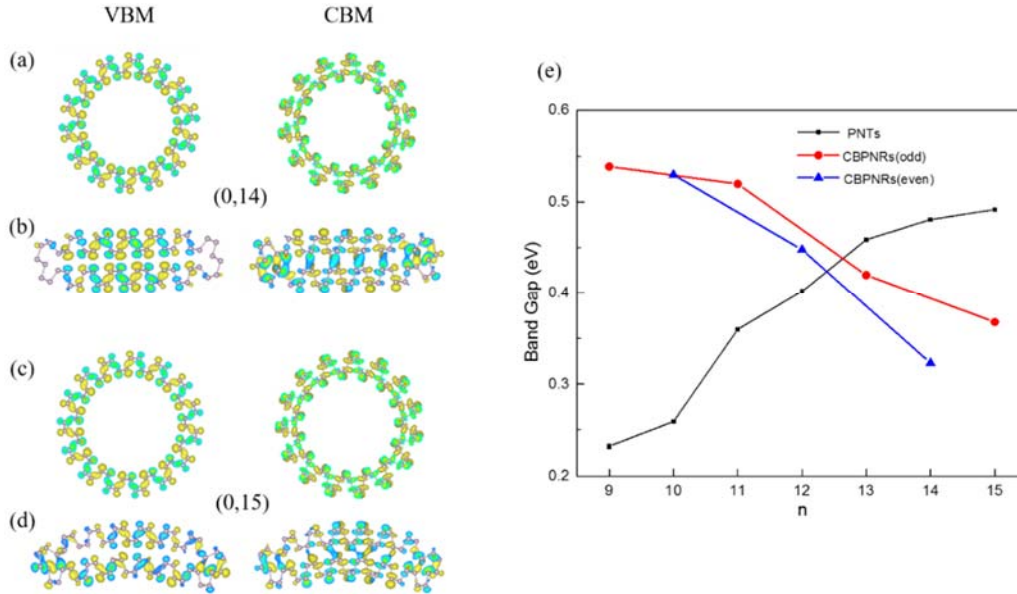


Figure 2.4.4 The spatial charge density associated with the VBM and CBM for the (a, c) PNTs and (c, d) CBPNRs for the size (0,14) and (0,15). The isosurface is set to $0.008 e/b_0^3$, and b_0 is the lattice parameter along nanotube axis. (e) The band gaps of armchair PNTs and CBPNRs are plotted as a function of tube size n .

Interestingly, we observe the dramatic change of band gap once squeezing round PNTs into CBPNRs in **Fig 2.4.1**. To understand this difference, we plot the isosurfaces of the charge density associated with CBM and VBM for (0,14) and (0,15) structures in **Fig 2.4.4 (a)-(d)**. **Fig 2.4.4 (a) and (c)** show that the localized states of phosphorus atoms contribute to the charge density at VBM, while the delocalized states play a key role in the CBM¹⁶⁴. Compared with the (0,14) PNTs, the charge density of VBM in the collapsed structure is nonuniform and sparse in the edge region with the dominating phase of blue phosphorene. It's apparent that the charge density of CBM overlaps between the two planar walls implying the formation of new bonds after the (0,14) PNT collapsing. Unlike the

(0,14) CBPNR, the charge density of (0,15) CBPNR at VBM due to the overall curvature becomes asymmetric with large concentration in the lower sublayer with compressive strain. This symmetry breaking is speculated to play an important role in the shift of VBM away from the Γ point and hence, the direct-indirect band gap transition shown in **Fig 2.4.3 (d)**. Additionally, the density overlaps and bonding forms in the (0,15) CBPNR. The above results show that the mixed phase of black-blue phosphorene and bond formation significantly result in the change of band gap from the round tubes to the closed-edged bilayer nanoribbons.

Last, we show the band gaps of round tubes and fabricated CBPNRs by varying the size n in **Fig 2.4.4 (e)**. As expected, the band gap of round tube increases with diameter, converging to the infinite limit of monolayer phosphorene¹³². However, for the two types of fabricated CBPNRs, the predicted band gaps decrease sharply with increasing ribbon width (or increasing value of n). The monotonically declining behavior is similar to the usual $1/w^2$ relation for monolayer phosphorene nanoribbon due to quantum confinement¹⁴⁷. However, the discrepancy is likely to be attributed to the restrictive edge configuration and vdW interaction between stacked layers of CBPNRs. Additionally, for all cases studied, both the VBM and CBM are located at the Γ point of sigmoidal CBPNRs, while the arc-like nanoribbons exhibit indirect band gap. Hence, the size-dependence of band structures makes CBPNRs promising components for applications in nanoscale field-effect transistors.

2.4.5 Conclusion

We proposed that the collapse of armchair PNT (through radial deformation) is an effective approach to fabricate stable nanostructure: closed-edged bilayer phosphorene nanoribbons, which enrich the family of nanodevices' components. The number of n in PNTs can determine two different structures: arc-like and sigmoidal bilayer nanoribbons. We also found the distinction of band structures upon the structural transformation, and the size-dependent band gap with nanoribbon width. The underlying mechanism was revealed to lie in the combined effect of black-to-blue phosphorene transition and bond formation between two facing walls in the CBPNRs. More importantly, the direct-to-indirect transition of band gap was observed in the arc-like CBPNRs but not in the sigmoidal ones. Even though the direct-to-indirect transition of band gap was reported in PNTs ¹⁶³, the extremely small tube corresponding to the transition point was revealed to be energetically unstable ⁹⁷.

Chapter 3 Engineered morphologies on microscale material structures

Beyond nanoscale material structures, we further investigate the morphologies in microscale systems, where continuum equations of thermodynamics can dominate the morphological dynamic but not using atomic/electron interactions. In this section, the thin film in core/shell microsphere evolves from flat surface to crack-like grooves, ripples and island-like pattern, driven by surface instability considering surface energy¹⁶⁻¹⁸.

3.1 Self-Assembly of Islands on Spherical Substrates by Surface Instability

3.1.1 Introduction

Surface instability of thin films not only plays a critical role in the evolution of surface morphologies observed in natural and biological systems,¹⁶⁵⁻¹⁶⁷ but also underpins a promising micro/nanofabrication technique for mechanical self-assembly of surface patterns.¹⁶⁸⁻¹⁷⁰ Many previous studies of surface instability were based on spontaneous wrinkles in stiff film/compliant substrate systems. These have demonstrated the feasibility and tunability of two-dimensional (2D) patterns of thin film on planar substrates, including stripes,¹⁷¹⁻¹⁷³ herringbones and zigzag labyrinths by varying the anisotropy of membrane force.¹⁷⁴⁻¹⁷⁷ Studies on curved and closed substrates were inspired by the observation of the triangular/Fibonacci patterns of spherules on the Ag core/SiO₂ shell microstructures upon cooling,¹⁷⁸⁻¹⁸⁰ followed were intensive theoretical models and experiments which were carried out to investigate the spontaneous organization of 3D wrinkling morphologies such as buckyball-like, labyrinth-like and ridged patterns in spheroidal systems^{165, 175, 181, 182} with controllable geometrical/material parameters.

Nevertheless, an intriguing mystery remains unresolved. In the pioneering study of instability of curved surface of Ag core/SiO₂ shell microstructures, the mechanism of wrinkling/buckling failed to explain the protruding features of spherules.^{178, 180} The buckling theory can only deduce dent-like morphologies, but not the more interesting protruding ones. Since the pioneering work has been widely cited, its unreasonable explanation misled a large amount of scholars working in this field. Due to the big impact from the misinterpretation, a sound clarification of the mechanism behind spherules patterns on spherical substrate is urgent. In fact, in those Ag core/SiO₂ shell microsystems the ratio of surface energy to strain energy is comparable with the typical roughness wavelength,¹⁷⁵ and at the high annealing temperature of 1270 K the surface diffusion of SiO₂ becomes noticeable.^{178, 183} However, the classic buckling analysis¹⁷⁵ can incorporate neither surface energy nor mass diffusion. Here we propose a mechanism that the formation of such protruding morphologies may be controlled by the competition between strain energy and surface energy as well as surface-diffusion. The elucidation of the mechanism of diffusion-controlled surface instability may not only help to explain the spontaneous islands on spherical core/shell microstructures, but also enrich the pathways of mechanical self-assembly.

The morphological instability based on diffusion in strained thin film was elucidated by Asaro and Tiller, Grinfeld and Srolovitz (referred as ATG instability).¹⁸⁴⁻¹⁸⁶ The growth of thin films on lattice-mismatched substrates, such as InGaAs/GaAs and Si_{1-x}Ge_x/Si,^{187, 188} usually follows the ATG instability mode. This can lead to the evolution of various surface morphologies, such as the crack-like grooves, ripples and islands. Unlike those on planar substrates, anti-correlated islands^{183, 189} and periodic shells^{168, 190} where

were observed to evolve on cylindrical nanowire surfaces, this implies the controllability of morphologies by size and curvature.

Inspired by these experimental results, extensive studies have theoretically explored the stability and kinetics of the surface morphology. The critical parameters and initial modes of instability in various planar film/substrate^{191, 192} or cylindrical^{183, 193, 194} systems were deduced through the linear perturbation analysis. The competition between two stress-relaxation mechanisms during the epitaxial growth of thin film: misfit dislocation and undulation of free surface, was also investigated.^{192, 195} To explore the nonlinear surface evolution, significant research efforts have been devoted to various numerical methods. Based on the Galerkin finite element methods, Yang *et al.* predicted the formation of ordered quantum structures in strained epitaxial film^{196, 197} and core/shell nanowire.¹⁹⁸ Free from singularities, the phase field model by Ginzburg-Landau approach is a promising numerical technique. The simultaneous growth and coarsening of quantum islands was obtained in two and three dimensional (3D) phase field simulations.^{199, 200} Furthermore, the method was used to quantitatively explore the controllability of self-assembled patterns on planar and curved substrates by tuning geometrical size, elastic and misfit-strain anisotropies.^{168, 200-202}

Despite these advances, the study of ATG instability of closed and curved thin films/substrate system is rare. Among the limited literatures, the microstructural stability and evolution of one particle in contact with its melt subjected to mass rearrangement and a growing spherical precipitate-matrix interface has been analytically and numerically explored.²⁰³⁻²⁰⁵ Although Colin deduced the growth rate of fluctuation in the case of two stressed spherical shell,²⁰⁶ the elastic heterogeneity was not considered. The mechanism of

stressed-driven instability *via* surface diffusion in spherical core/shell systems remains unclear. Indeed, surface instability modes of closed core/shell systems (such as spherical) could enrich the family of surface diffusion-driven assembly of spontaneous patterns on curved microstructures and complement those induced by buckling. In this study, the linear perturbation analysis considering elastic heterogeneity is analytically performed and linked to the surface instability at the very initial stage. In addition, using 3D phase field modeling, we numerically explore the nonlinear evolution of surface instability on the spherical core/shell microstructures in the presence of misfit-strain. The geometrical/material properties and misfit-strain affecting the kinetics of morphological evolution are discussed, which qualitatively echoes with those predicted by linear analysis. Finally, we experimentally explore the controlled self-assemblies on spherical Ag core/SiO₂ shell microstructures to verify the pattern features of islands.

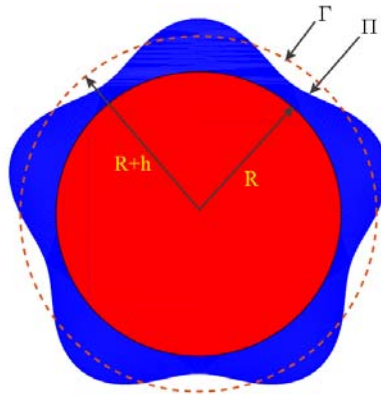


Figure 3.1.1. The schematic of a spherical core/shell structure: the radius of core is denoted by R and the shell have thickness h .

3.1.2 Phase Field Modeling and Experimental Methods

Numerical Model: A model of spherical core/shell composite (**Fig 3.1.1**) is established using spherical coordinates to investigate the surface instability of a thin film enclosing a closed and curved substrate under stress. The core and shell with isotropic elasticity have different shear moduli μ_c and μ_s ($\beta = \mu_c/\mu_s$), while the Poisson's ratio ν is taken to be the same for simplicity. An isotropic intrinsic strain $\boldsymbol{\varepsilon}^* = H(r - R)diag(\varepsilon^*, \varepsilon^*, \varepsilon^*)$ is introduced in the core, and the interface between core and shell are assumed to be coherent without involving misfit dislocations. Basically, the intrinsic strain can mimic the misfit of thermal expansion or the lattice mismatch in epitaxial crystalline growth during the annealing process.²⁰⁶

Experimental details: The detailed experimental setup and parameters can be found in the previous work.^{178, 180} After evaporating the mixture of AgO₂/SiO₂ powders in a Al₂O₃ crucible chamber, which was filled with a gas mixture of 90%Ar+10% H₂ to a pressure of $3 \times 10^4 \text{ Pa} \sim 4 \times 10^4 \text{ Pa}$. The size of formed Ag core/SiO₂ shells in the vapor can be controlled by the base pressure, and the ratio of AgO₂/SiO₂ powders determines the thickness of SiO₂ layer. Ag core/SiO₂ shell microstructures were collected on a sapphire substrate placed 1 cm over the powders mixture surface. At the beginning, the power mixture was heated to $\sim 1535 \text{ K}$ and the substrate was kept at $\sim 1270 \text{ K}$. Liquid droplets were formed on the way flying to the substrate, and then evolving to a Ag core/SiO₂ shell structure due to poor miscibility between Ag and SiO₂. The Ag core/SiO₂ shell microstructures with a radius of 1-10 μm were observed on the substrate. For a controlled study of surface roughness, three groups of SiO₂ shell/Ag core microstructures were annealed at the same temperature but for different durations. Then, we cooled down the

system at a fast rate of ~ 350 K/min such that the evolved morphologies at the high annealing temperature could be kept. The morphologies of the core/shell structures were imaged through *Ex Situ* observation using a scanning electron microscope (SEM; FEI, SERION). The elemental compositions of core and shell were verified from the energy-dispersive X-ray spectrometer.

3.1.3 Linear Stability Analysis

To study the combined effect of substrate radius R , modulus ratio β and eigenstrain ϵ^* on the kinetics of morphological evolution, we extend Colin's work²⁰⁶ for our case of spherical core/shell microstructure, where β does not equal to one (refer to the Supporting Information). The growth rate (see Equation (S3)) can be reduced to that in Colin's work²⁰⁶ with the special case of $\beta = 1$. The critical radius, below which the fluctuation may not develop, is determined from the expression, $(1 + h/R)^5 = 21(1 - \nu)\alpha R / (2(7 + 5\nu)R^*)$. It is apparent that the critical radius is sensitive to the modulus ratio and eigenstrain, matching with those in previous works.^{203, 205-207} The typical parameters: $\epsilon^* = 0.02$, $\gamma = 1.5 \text{ Jm}^{-2}$, $\mu_s = 30 \text{ GPa}$, $\nu = 0.3$ ¹⁷⁵, are taken and they correspond to the Ag core/SiO₂ shell system in the parallel experiment below and their variations with temperature are neglected.^{199, 200}

Based on Equation (S3) relating the growth rate to fluctuation amplitude, the positive growth rate leads to development of a fluctuated morphology, whereas a stable surface results from the negative value. We plot the dimensionless growth rate ω as a function of degree l for increasing normalized sizes R/h in **Fig 3.1.2(a)**. It is observed that with increasing value of R/h , not only does the number of mode degree l for positive

growth rate increase, but also the value of growth rate. Thus, the amplitude of perturbed surface grows faster in the system with larger R/h value. Furthermore, the most possible instability mode l_f is defined to correspond to the fastest growth rate among all perturbation modes, and it refers to the typical wavenumber of rough surface after instability. As shown in **Fig 3.1.2(a)**, the value of l_f decreases as the normalized size R/h is reduced, implying a denser morphology in a larger structure just at the initial stage of surface undulating. The similar trends were also revealed in Colin's work with $\beta = 1$.

In addition, the effects of eigenstrain and modulus ratio on the growth rate are shown in **Fig 3.1.2(b)** and **2(c)**, respectively. It can be noticed that the surface roughness of a misfit-strained system develops slower than the one with larger misfit strain and the growth rate of fluctuated morphology decreases as the modulus ratio of core to shell decreases. Retracting and comparing the values of l_f in **Fig 3.1.2(b)** and **2(c)**, we can expect a denser protruding pattern in the structure with either larger modulus ratio or intrinsic strain. Therefore, the linear stability analysis preliminarily underlines the controllability of self-assembled morphologies on spherical substrate.

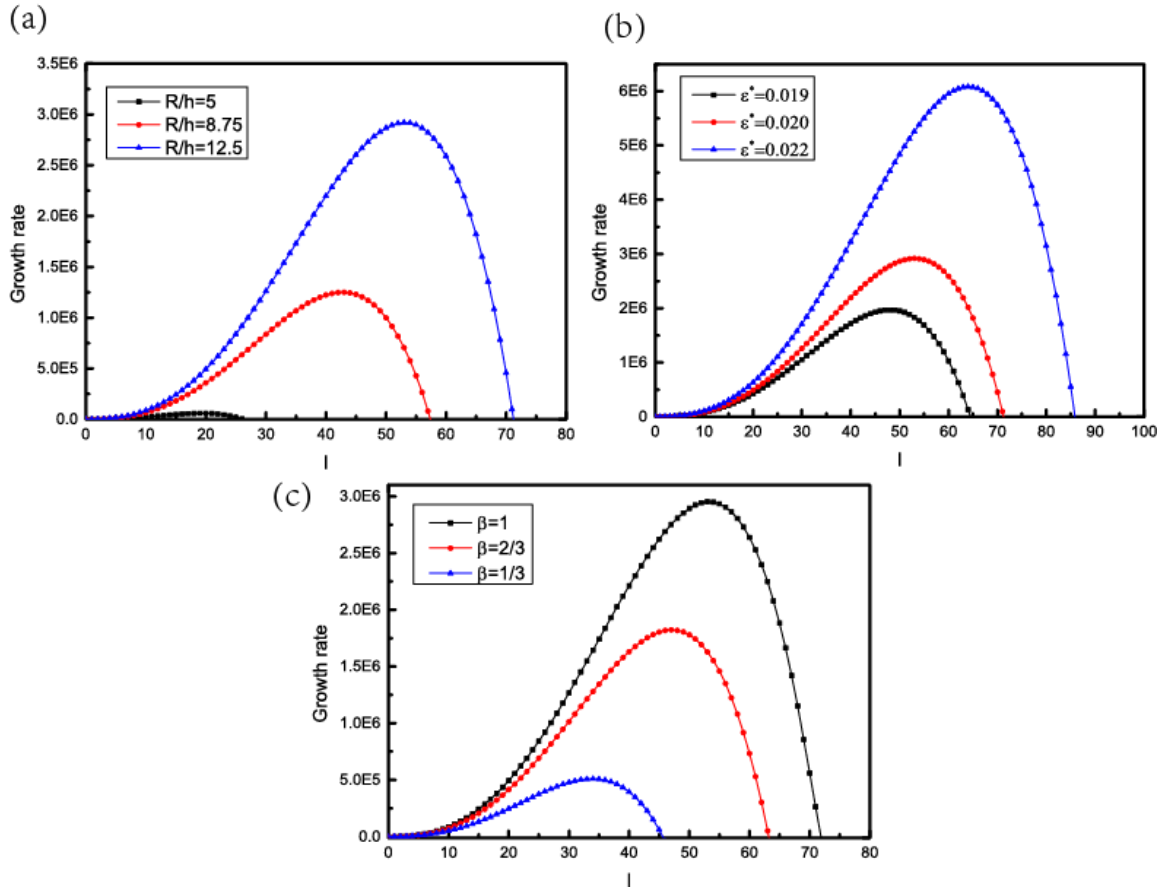


Figure 3.1.2 The dimensionless growth rate plots as a function of various fluctuation mode degree l characterizing the evolved morphology at various values of (a) normalized size R/h , (b) intrinsic strain ϵ^* and (c) modulus ratio β

3.1.4 Nonlinear Dynamics Simulation

Since the abovementioned analysis only predicts the surface evolution at the very initial stage, we adopt a 3D phase field approach¹⁹⁹⁻²⁰¹ to study the nonlinear surface instability (see the Methods section for details). The development of the surface undulation in a representative spherical core/shell structure with misfit-strain is shown in the inset of **Fig 3.1.3(a)**. As the simulation time proceeds, the morphological pattern evolves from

initial fluctuation (described as Equation (S10)) to flat surface ($t = 2\tau$), several grooves ($t = 50\tau$), ripples ($t = 75\tau$) and islands ($t = 150\tau$). Even though the coarsening of islands continues after $t = 150\tau$, the topology of pattern after $t = 300\tau$ changes little and thus suggesting the system is pretty close to the equilibrium state due to the extremely slow growth rate thereafter. It is noted that within the context of the mesh roughness and initial random fluctuations, the close-to-equilibrium pattern of islands should be regarded as quasi-periodic.

The strain energy of the system is plotted as a function of dimensionless time in **Fig 3.1.3(a)**. It clearly shows that the development of surface roughness is associated with elastic energy relaxation, followed by a plateau where the islands coarsen. Specifically, the first stage ($t = 0 \sim 2\tau$) of stress relaxation corresponds to the smoothing of initially random undulation. Subsequently, as shown in **Fig 3.1.3(a)**, the relaxation of strain energy has two fast stages: the formation of grooves until exposure of the substrate ($A \rightarrow B \rightarrow C$), and the breaking of ripples into a set of islands ($C \rightarrow D$). The reduction of strain energy implies that the formation of islands is thermodynamically driven. Finally, there is a slower process ($D \rightarrow E$) corresponding to islands refinement due to the achievement of stress relaxation. Moreover, the small variation of strain energy ($D \rightarrow E$) verifies the kinetically unfavorable process of further coarsening and refinement of islands, since both the slow growth rate and numerical imperfections make it difficult for the evolution of an ideally periodic pattern with commensurate islands within a limited simulation time. The quasi-equilibrium pattern of islands on spherical substrate is very likely to be the result of stress relaxation due to surface instability, not due to deformation as mechanical buckling.^{169, 177}

To quantitatively explore the kinetics of morphological evolution, the coverage parameter ξ characterizing the extent of surface evolution is defined as the percentage of mass left inside the otherwise smooth, non-evolving surface (dash circle in **Fig 3.1.1**), e.g. $\xi = 1$ at the beginning of surface instability. The extent of evolution ξ as a function of time t is plotted in **Fig 3.1.3(b)** for increasing values of substrate curvature. It is seen that the growth rate, denoted by the slope of the curves, decreases exponentially with simulation time. This can be compared with the morphological evolution in **Fig 3.1.3(a)** which illustrates the fast evolution occurring at the initial times and close-to-equilibrium after $t = 400\tau$. Furthermore, the faster evolution is evidently associated with larger substrate radius, showing the curvature-dependent kinetics of undulation growth and a unique feature to the closed and curved substrate. The results in **Fig 3.1.2(a)** bear a resemblance to the trends here, although they are just valid at the very initial stage of surface instability. Therefore, the self-assembly of small spherules on spherical substrate is feasible through tuning evolution time and substrate curvature, implying an alternative route to future fabrication of ordered structures on spherical substrates.

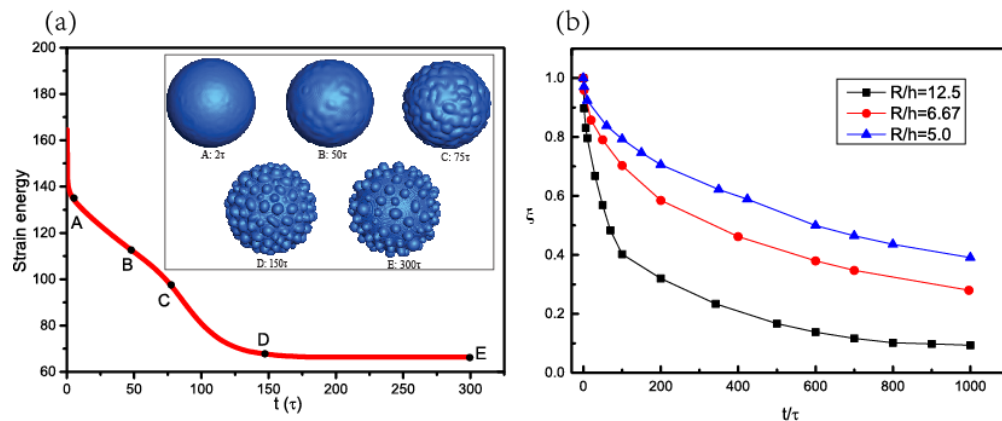


Figure 3.1.3 (a) The evolution of strain energy of the spherical core/shell particle ($R = 50l, h = 4l, \beta = 1/3$) as a function of dimensionless time. (b) The coverage parameter ξ as a function of simulation time for three cases: $R/h = 12.5; R/h = 6.67; R/h = 5.0$.

Furthermore, the effects of normalized size R/h , eigenstrain ε^* and modulus ratio β , were explored. Unless otherwise noted, the results below are for the shell having thickness $h = 4l$ and shear modulus $\mu_s = 30$ GPa. Besides the coverage parameter ξ , the dimensionless average height (normalized by l) of the island peaks relative to the initial radius of shell, $R + h$, is another quantitative parameter to describe the extent of undulation. Due to the mass conservation in a given system, the increase of average height roughly corresponds to the declination in the number of islands. A morphological map at $t = 100\tau$ is constructed with respect to the substrate radius and intrinsic strain in **Fig 3.1.4(a)**, which shows the transition from stable surface to the pattern of separated islands. For a given value of R/h , the surface undulation grows faster with the increase of ε^* , and when ε^* is fixed, the grooves transit to islands as the substrate curvature is reduced. In addition, the distribution of islands on the substrate are denser than that on the substrate with smaller radius. Moreover, the average heights not only illustrate the undisturbed morphology when both R/h and ε^* are small, implying the existence of a critical curvature corresponding to stable surface, but also validate the amplitude of undulation growing faster in larger particles as revealed by the linear analysis.

In the second morphological map in **Fig 3.1.4(b)**, the spontaneous patterns at $t = 80\tau$ are selected to further study the competition of geometrical parameter R/h and modulus ratio β between core and shell. From the cases with a certain value of R/h , the

transition from grooves to islands occurs earlier in the systems with harder substrate. Based on the diagram, it is evident that the denser distribution of islands is in favor when β and R/h become larger. Meanwhile, the effect of larger modulus ratio resulting in faster morphological evolution is consolidated by the average height of islands shown in **Fig 3.1.4(b)**. Comparing with $t = 80\tau$ and $t = 100\tau$ in **Fig 3.1.4(a)** and **4(b)** respectively, the morphologies at $t = 200\tau$ show the decreasing number of islands, with an increase in the dimensionless average height. The maps in Figure 4 provide a promising and controllable way for self-assembling ordered structures on spherical substrates by controlling the evolution time, geometrical/material properties and misfit-strain.

In the 3D simulation abovementioned, the difference of the diffusivity in the surface, interface and bulk is neglected in the phase field model for simplicity, and the surface diffusion could be much faster than the others, whose role will be explored in future. The intrinsic strain and elastic properties adopted in the current study may be regarded as effective averaged parameters. Through uncovering some of essential factors affecting the dynamics of diffusional surface evolution, the model could be refined to incorporate more complicated geometries, temperature-dependent and anisotropic elasticity and eigenstrain parameters which possibly offers ways for designing various surface topologies on the closed/curves substrate. Parallel experimental realizations are explored below to enrich our purposes.

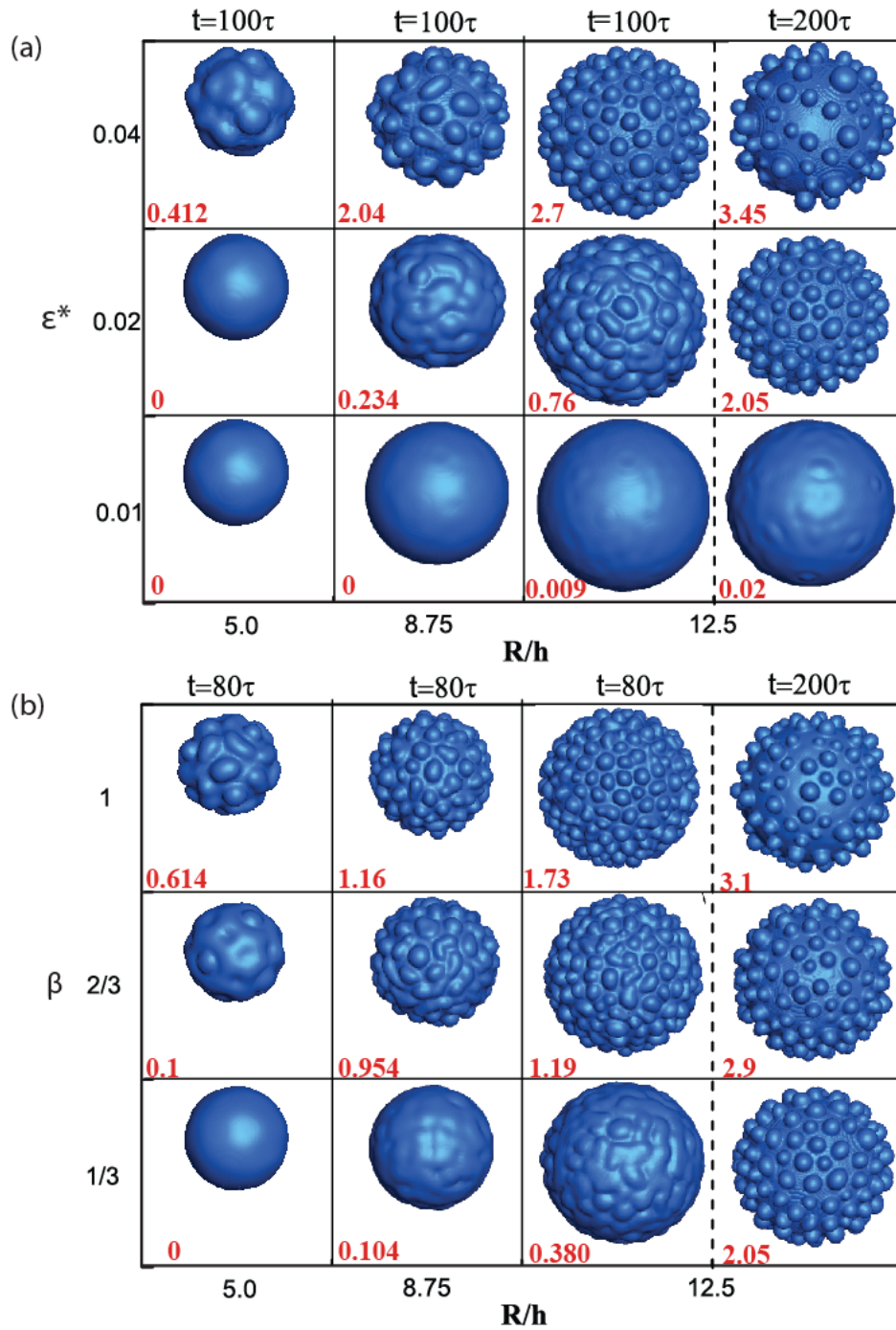


Figure 3.1.4. Diagrams for surface morphology at given time (a) $t = 80 \tau$ and (b) $t = 100 \tau$. The morphologies of the structure ($R/h = 12.5$) at $t = 200 \tau$ are shown on right sides of (a) and (b).

3.1.5 Experimental Verification

As discussed above, uniform islands are able to be self-assembled on the closed and curved (*e.g.* spherical substrate) through the mechanism of diffusional surface instability, the kinetic of which is highly dependent on substrate curvature, mismatch strain and modulus ratio between the substrate and shell. In this section, the morphologies with protruding features are experimentally studied with emphasis on the spherical Ag core/SiO₂ shell microstructures, which may promise manipulation of 3D patterns on closed and curved substrates.

Ag core/SiO₂ shell samples were synthesized by thermal evaporation of SiO and Ag₂O mixture into sapphire substrates, which was heated to 1270 K. Before cooling, we kept the system at 1535 K for different durations in order to investigate the effect of annealing time. The profiles of Ag core/SiO₂ shell microstructures, annealed for 1 min, 5 min and 10 min, are respectively shown in **Fig 3.1.5(a)**, **5(b)** and **5(c)**. The chemical compositions of Ag, Si and O at the red dash region in **Fig 3.1.5(c)** were characterized by the energy-dispersive X-ray spectrometer (**Fig 3.1.S1**). These three samples have approximately the same diameter of 5 μm , and with more time allowed the morphological transition from smooth surface to uniform islands and finally to relatively sparse and bigger islands. Although the misfit-strain in the film can drive surface undulating, the mass diffusion of SiO₂ in **Fig 3.1.5(a)** is insignificant and its surface keep remains smooth due to the short annealing time. However, given longer annealing time in Figure 5(b), the uniform island-like spherules are likely the result of adequate diffusion. When the core/shell microstructure is further annealed, surface diffusion is responsible for islands coarsening, which is exemplified by **Fig 3.1.5(c)**. The experimental transition from Figure

5(a) to (c) is consistent with the numerically simulated morphologies illustrated in the inset of **Fig 3.1.3(a)** (A→D→E), although it's very difficult to experimentally capture the fast transition from state A to C in **Fig 3.1.3(a)**. This transition is similar to the experimental observations in the diffusion-based growth of Si core/Ge shell nanowire, during which extended time for annealing makes smaller islands disappear while larger islands continue to coarsen resulting in the morphology with low island density.¹⁸³ Additionally, it's evident that the average distance between islands in **Fig 3.1.5(b)** (roughly 0.5 μm) is smaller than that in **Fig 3.1.5(c)** (roughly 1.0 μm), which further confirms the coarsening of islands as the annealing time increases. Therefore, the formation of protruding features in **Fig 3.1.5(b)** and **5(c)** are likely to be diffusion-controlled.

Defects may induce non-uniformity in the core/shell structure. The profile (**Fig 3.1.S2**) shows non-uniform islands near the interface between the microstructure and sapphire substrate, while nearly uniform islands can be seen in the region far from the interface. The local non-uniformity may be induced by geometrical constraints. We also find that a large cooling rate (500 K/min) could lead to broken structures, shown in **Fig 3.1.6(d)**, which is possibly due to large thermal mismatch stress fast occurs in the SiO₂ shell.

In addition, the size of formed Ag core/SiO₂ shells in the vapor can be controlled by the base pressure, and the ratio of AgO₂/SiO₂ powders determines the thickness of SiO₂ layer.²⁰⁸ Thus, we kept the mass ratio of Ag₂O/SiO powders as 5:1, and the Ag core/SiO₂ shell microstructures with a radius of 1-10 μm were obtained by varying the base pressure within the range of $3 \times 10^4 \text{ Pa} \sim 4 \times 10^4 \text{ Pa}$. Then we annealed the systems for 5 min before cooling it. The thickness of SiO₂ layer can be measured as 150 nm from some broken

structures similar to that in **Fig 3.1.6(d)**, and the thickness is approximately constant among the microstructures with various sizes due to the unchanged composition of the $\text{Ag}_2\text{O}/\text{SiO}$ precursor. As shown in **Fig 3.1.6**, spontaneous SiO_2 spherules are observed on spherical Ag substrates (where $\beta \approx 1/3$, $\epsilon^* \approx 0.02$), with approximate radii $2.5 \mu\text{m}$ for (a), $4.0 \mu\text{m}$ for (b) and $7.5 \mu\text{m}$ for (c). The observation of denser array of islands on larger microstructure are in qualitative agreement with both numerical results in Figure 4 and analytical predictions in **Fig 3.1.2(a)**. Interestingly, the smooth surface of exposed Ag core, shown in **Fig 3.1.5(d)**, verifies no deformation in the substrate. The evidence excludes the mechanism of mechanical buckling, which would result in the dent-like and ridged patterns for the same microstructures.^{165, 175} These agreements effectively strengthen the diffusion-controlled mechanism behind the formation of islands on spherical substrates.

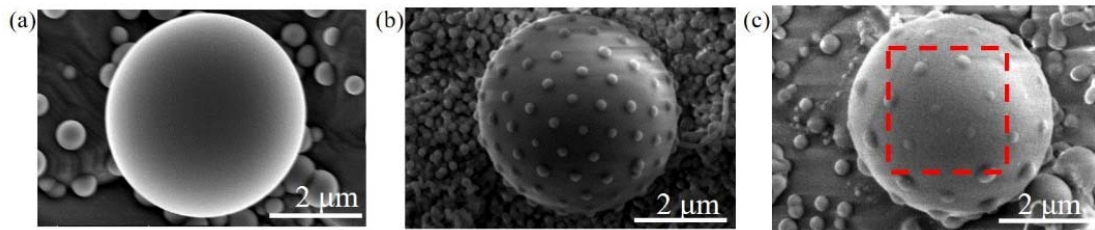


Figure 3.1.5 Three representative surface patterns of the Ag core/ SiO_2 shell microstructures with approximate radius of $2.5 \mu\text{m}$: (a) smooth surface; (b) uniform islands; (c) relatively sparse and bigger islands.

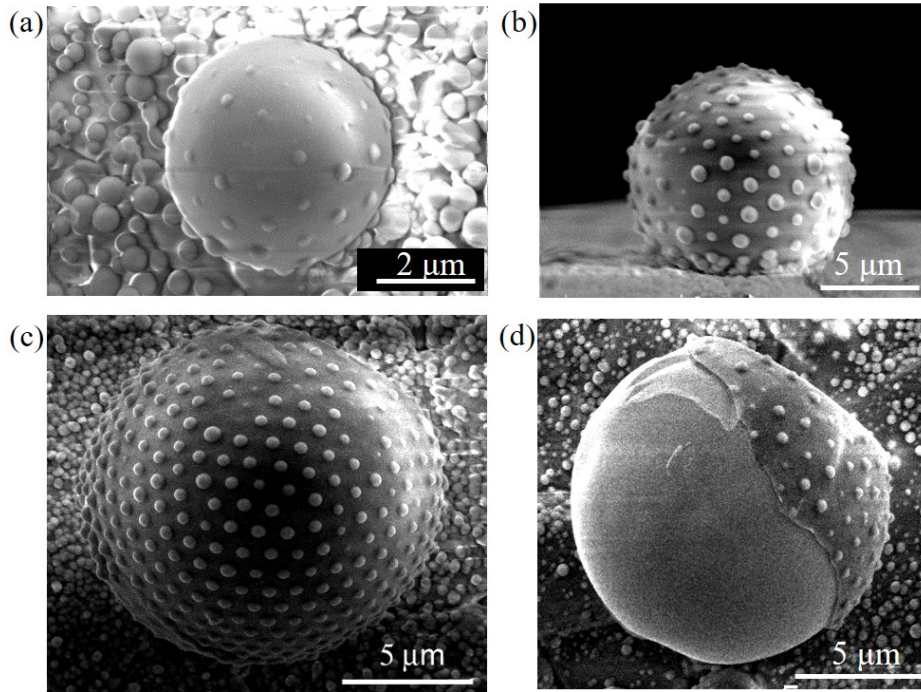


Figure 3.1.6 SEM micrographs of the Ag core/SiO₂ shell microstructures annealed for 10 min, with approximate radii (a) 2.5 μm, (b) 4.0 μm and (c) 7.5 μm. A broken sample with smooth Ag core partially covered by SiO₂ shell is shown in (d) under a cooling rate of 500 K/min.

3.1.6 Conclusion

In summary, the nonlinear phase field simulations and linear stability analysis were performed to explore the spontaneous patterns induced by diffusional surface instability on spherical core/shell systems. At a given evolution time, the transition of morphologies, from flat surface, to grooves and ripples and eventually the assembly of islands with roughly uniform size, could be controlled since the growth rate of undulation is highly dependent on the substrate curvature, modulus ratio and intrinsic strain. With the increased eigenstrain, radius and stiffness of substrate, the self-organization occurs faster. In the

parallel experiments, the surface patterns of SiO₂ islands were also successfully formed on Ag substrate. Thus, the surface instability *via* diffusion may dominate the self-assembly of islands on spherical particles observed in pioneering study,¹⁷⁸ whose mechanism remain obscure until the present study.

3.1.7 Appendix

1) Linear Stability Analysis.

The shell surface is perturbed as the expression²⁰⁶

$$r(\theta, \phi, t) = (R + h)(1 + eY_l^m(\theta, \phi)) \quad (\text{S1})$$

in which t , e are the time and dimensionless perturbation amplitude, respectively; $Y_l^m(\theta, \phi)$ denotes the complete spherical harmonic function with degree l and order m . We analytically deduce the development of perturbation amplitude:

$$e(t) = e(0)\exp\left(\frac{\omega t}{\omega_0}\right) \quad (\text{S2})$$

with the dimensionless growth rate,

$$\omega = -l(l+1)(l+2)(l-1 - \frac{\alpha(1-\nu)R^6}{2(l^2+(1+2\nu)l+1+\nu)(R+h)^5 R^*}) \quad (\text{S3})$$

and ω_0 is the constant dependent on diffusivity and material properties. In addition, $R^* =$

$\frac{(1-\nu)^2\gamma}{4\mu_s(1+\nu)^2\varepsilon^*2}$ is the characteristic length and the coefficient α marks the effect of modulus

ratio β on the growth rate:

$$\alpha = \frac{9\beta^2(1-\nu)^2(R+h)^6}{(2R^3(1-\beta)(1-2\nu)+((1+\nu)\beta+2-4\nu)(R+h)^3)^2} \quad (\text{S4})$$

2) 3D Phase Field Modeling

Two long-range field variables, $\phi_1(\mathbf{r}, t)$ and $\phi_2(\mathbf{r}, t)$, are introduced to characterize the configuration of the spherical core/shell system, *e.g.* $\phi_1 = 1 - \phi_2 = 1$ in the shell, $\phi_2 = 1 - \phi_1 = 1$ in the core and $\phi_1 = \phi_2 = 0$ in the vacuum. The free surface is denoted by a smooth change of ϕ_1 from 0 to 1. The coordinate-dependent modulus $C_{ijkl}(\mathbf{r}, t)$ can be described as $C_{ijkl}(\mathbf{r}, t) = \phi_1 C_{ijkl}^0 + \phi_2 (\beta C_{ijkl}^0)$, where $C_{ijkl}^0 = \frac{2\mu\nu}{1-2\nu} \delta_{ij} \delta_{kl} + \mu(\delta_{ik} \delta_{jl} + \delta_{il} \delta_{jk})$. The morphological evolution of the external free surface $\phi_1(\mathbf{r}, t)$ is governed by the Cahn-Hilliard equation

$$\frac{\partial \phi_1}{\partial t} = \nabla [M(\phi_1) \nabla \frac{\delta E^{total}}{\delta \phi_1}] \quad (S5)$$

where the surface mobility, relating diffusivity D and absolute temperature T by $M(\phi_1) = \frac{D(\phi_1)}{\Lambda k_B T}$, is assumed to be zero in the core and constant in the shell and vacuum; Λ and k_B are respectively the atom numbers per volume and the Boltzmann's constant.

The total free energy is a function of $\phi_1(\mathbf{r}, t)$, $\phi_2(\mathbf{r}, t)$,

$$E^{total} = \int_V \{f(\phi_1) + \lambda_0 [\nabla \phi_1(\mathbf{r})]^2 + f_{el}(\phi_1, \phi_2)\} d^3r \quad (S6)$$

where the bulk chemical free energy $f(\phi_1)$ is a double-well function $a\phi^2(1 - \phi)^2$ with the Landau coefficient a ; $\lambda_0 [\nabla \phi_1(\mathbf{r})]^2$ is the gradient energy characterizing surface energy with the gradient coefficient λ_0 ; the third term is the strain energy density

$$f_{el} = \frac{1}{2} C_{ijkl}(\mathbf{r}, t) (\varepsilon_{ij} - \varepsilon_{ij}^*(\mathbf{r})) (\varepsilon_{kl} - \varepsilon_{kl}^*(\mathbf{r})) \quad (S7)$$

in which $\varepsilon_{ij}^*(\mathbf{r})$ is the intrinsic strain. ε_{ij} can be calculated through the phase field microelasticity (PFM) model.²⁰⁹ Without losing generality, the elastic and strain anisotropy could be taken into account in the present model.^{200, 202} By establishing an equivalent homogeneous system with constant stiffness tensor C_{ijkl}^0 and an effective eigenstrain

$\varepsilon_{kl}^0(\mathbf{r})$ in the way, $C_{ijkl}^0(\varepsilon_{kl} - \varepsilon_{kl}^0(\mathbf{r})) = C_{ijkl}(\mathbf{r}, t)(\varepsilon_{kl} - \varepsilon_{kl}^*(\mathbf{r}))$, the elastic strain and stress field of the original system are evaluated. The distribution of $\varepsilon_{ij}^0(\mathbf{r}, t)$ can be obtained by solving the PFM kinetic equation:

$$\frac{\partial \varepsilon_{ij}^0(\mathbf{r}, t)}{\partial t} = -K_{ijkl} \frac{\delta E^{equiv}}{\delta \varepsilon_{ij}^0(\mathbf{r}, t)} \quad (\text{S8})$$

in which $K_{ijkl} = K\delta_{ik}\delta_{jl}$ is an artificially kinetic coefficient, and the strain energy of this equivalent system can be calculated as below:

$$\begin{aligned} E^{equiv} = & \frac{1}{2} \int_V C_{ijkl}^0 \varepsilon_{ij}^0 \varepsilon_{kl}^0 d^3r + \frac{1}{2} \int_V C_{ijkl}^0 \bar{\varepsilon}_{ij} \bar{\varepsilon}_{kl} d^3r - \bar{\varepsilon}_{ij} \int_V C_{ijkl}^0 \varepsilon_{kl}^0 d^3r - \\ & \frac{1}{2} \int_{\xi \neq 0} \frac{d^3\xi}{(2\pi)^3} \xi_i \tilde{\sigma}_{ij}^0(\xi) \tilde{G}_{jk}(\xi) \tilde{\sigma}_{kl}^0(\xi)^* \xi_l + \frac{1}{2} \int_V (C_{ijmn}^0 \Delta S_{mnpq} C_{ijmn}^0 - C_{ijkl}^0) (\varepsilon_{ij}^0 - \varepsilon_{ij}^*) (\varepsilon_{kl}^0 - \\ & \varepsilon_{kl}^*) d^3r \quad (\text{S9}) \end{aligned}$$

where $\bar{\varepsilon}_{ij} = \frac{1}{V} \int_V \varepsilon_{ij}(\mathbf{r}) d^3r$, and $\int_{\xi \neq 0}$ represents the integral in the Fourier space excludes the point $\xi = 0$; $\tilde{G}_{jk}(\xi)$, $\tilde{\sigma}_{ij}^0(\xi)$ and ξ_i are respectively the components of Green's function tensor, effective stress and basic vector in Fourier space.

Equation (4) is reduced by physical length l and time $\tau = \lambda_0/Da$, and then numerically solved in the computational domain $150l \times 150l \times 150l$. At the early stage of surface instability, $l_0 = \gamma/\mu_s \varepsilon^{*2}$ characterizes the wavelength of surface roughness. In order to reduce the computational cost, l is set as $l_0/2$ ($l = 62.5 \text{ nm}$) while keeping the kinetics mainly unaltered.^{200, 210} The initial fluctuation of the morphology is described as the superposition of m static plane waves with amplitude δ_m , wave numbers k_m^θ , k_m^ϕ and random phase shift angles θ_m , ϕ_m ,

$$r(\theta, \phi) = R + h + \sum_{m=1}^{32} \delta_m \sin(k_m^\theta \theta + \theta_m) \cos(k_m^\phi \phi + \phi_m) \quad (\text{S10})$$

where R and h are the core radius and shell thickness, respectively; $\delta_m = 0.04$, $k_m^\theta = k_m^\phi = m$ are given. The external free surface of the core/shell microstructure is extracted from the isosurface of $\phi_1(\mathbf{r}, t) = 0.5$.

3) Supplementary Figures

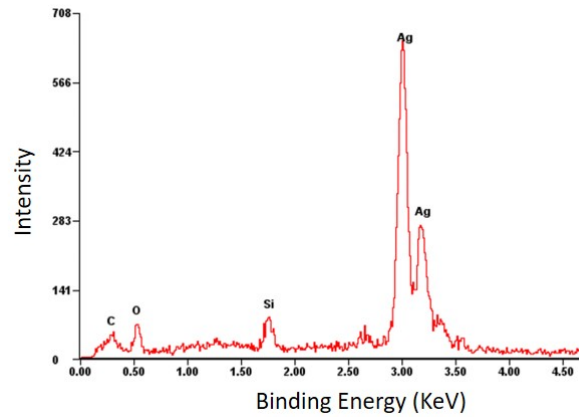


Figure 3.1.S1. EDS spectra obtained at the red dash region (in Figure 5(c)) by X-ray spectrometer.

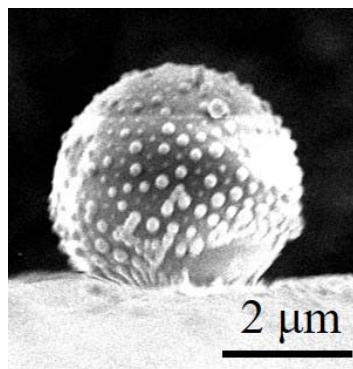


Figure 3.1.S2. The Ag core/SiO₂ shell microstructures (approximate radius of 2.5 μm) shows a non-uniform pattern of islands and the annealing time is 5 min.

Chapter 4 Engineered morphologies on macroscale material structures

In the section, we turn up to macroscale systems where long-distance elastic interaction dominates morphology of material structures, which usually serve as substrates for transferring nanomaterials and is important for manipulating nanoscale morphologies. Mechanical buckling as a fundamental mechanism for structural transformation on surface can be initiated by either external loading or intrinsic strain-mismatch. In this chapter, pre-patterned defects of cavities and in-plane compression are introduced to both soft materials and the bilayer structure, and varieties of surface morphologies are self-assembled^{20, 21}.

4.1 Tunable Surface Morphology via Patterned Cavities in Soft Materials

4.1.1 Introduction

Surface features play a significant role in the behaviors of natural and biological systems^{169, 177, 211}. For example, folds in the brain help enhance intellectual capacity and furrows grow on plant surfaces during aging process. In engineering systems, various methods have been developed to engineer such surface topologies, including periodic wrinkles, random bumps and local creases. It has also been shown that the reversibility of these features allows not only extensive applications in optics²¹² and flexible electronics²¹³, but also in tuning the properties of surface adhesion²¹⁴ and hydrophobicity²¹⁵, etc. Recent studies have focused on the stressed layered systems and the sinusoidal pattern of wrinkles²¹¹. More fascinating wrinkling patterns including stripes, herringbones, zigzag labyrinths^{171, 216}, and buckyball-like features are obtained by tuning anisotropic stress in

bilayers^{165, 181, 182}. Beyond wrinkles, a variety of surface localizations, including folding^{217, 218}, ridging and delaminated buckling, were also observed^{177, 219-221}.

Defects (for example, voids, rigid elements) have traditionally been regarded as imperfections that affect the formation of surface wrinkles or localizations^{222, 223}. Conversely, researchers have recently utilized the pre-patterned holes and rigid particles to produce new intriguing surface features in bilayers^{224, 225}. In addition, the composite of soft material with embedded particles was studied to allow the controllability of surface topographies²²⁶. While this study benefits many applications, the features are local and not overall triggered. Despite extensive works on engineering the surface of composite systems, limited studies focus on homogeneous materials.

Here, we focus on the cavity-embedded soft materials (CESMs) with pre-patterned cavities below the surface. The design of cavity patterns opens a new avenue to exploit periodic surface features in homogeneous materials under external in-plane compression. Through finite element calculations, the surface morphology is found to be controllable by the shape and spacing of inter-cavities when the soft materials are subjected to external stimuli. Our parallel experiments based on 3D-printed prototypes consolidate the simulation results. Thus, this method enables the reversibility and continuity of surface changes and is applicable for structures/materials across multiple length scales.

4.1.2 Model and Method

Numerical Model: Both the 2D and 3D nonlinear numerical simulations were performed through commercial software ABAQUS to investigate the changes of surface features. The CESMs was modeled as a nearly incompressible material using neo-Hookean

constitution, which has initial shear modulus $G = 0.50$ MPa corresponding to the commercial rubber (TangoPlus) used in the experiments. Periodic boundary conditions were applied to the lateral sides. Neither vertical displacement nor shear traction was allowed on the bottom surface.

Experimental Methods: The physical prototypes were fabricated by an Objet500 Connex 3D Printer. The prototypes were made of photo-sensitive polymeric materials, TangoPlus. We conducted the uniaxial compression tests with a Zwick/Roell Z2.5 mechanical tester. To ensure plane strain conditions in the compressive test, the samples were sandwiched between two optically clear acrylic plates and another plate was placed below the samples. The friction between the plates and the sample was reduced by using mineral oil. 20% global compressive strain was applied to each sample with a strain rate of 0.0005 s^{-1} . A high resolution camera was placed in front of the sample and took a picture every minute.

4.1.3 Results in 2D Modeling

We start from the 2D representative segment of CESMs shown in **Fig. 4.1.1(a)**. Underneath the top surfaces, there is one row of circular cavities with diameter a_1 , inter-cavity spacing b_1 and depth c . We construct the dimensionless parameters: relative inter-cavity spacing $\alpha = \frac{b_1 - a_1}{a_1}$, relative distance from the surface $\beta = \frac{c}{a_1}$. When subjected to increasing uniaxial global compression ε_g^u , two representative CESMs with different inter-cavity distances show different morphological evolutions, with the phase diagram illustrated in **Fig. 4.1.1(b)**. When the relative inter-cavity distance is small, for example, $\alpha = 0.1$, the initially flat surface transits from local bumps to periodic waves with the

wavelength of doubling cavity spacing, followed by one cavity collapsing. Upon the global strain reaching 6.8%, the array of cavities suddenly transforms into a periodic pattern of alternating, mutually orthogonal ones. This buckling mechanism should be responsible for the periodic surface feature and the cavity collapsing release under further compression. However, because of the interaction between adjacent cavities in the CESMs with larger inter-cavity distance ($\alpha = 0.45$) is small, only local ridges right above cavities are formed. Further compression (up to 45%) induces the close of cavity and the high amplitude-to-wavelength ratio ridges, which allows the application in super-hydrophobic coatings. The amplitude is half of the distance between the peak and the valley in the surface buckling texture, and the wavelength is the closest distance between peaks. Furthermore, the transition value of relative inter-cavity spacing, $\alpha = 0.25$, can differentiate the two deformation mechanisms.

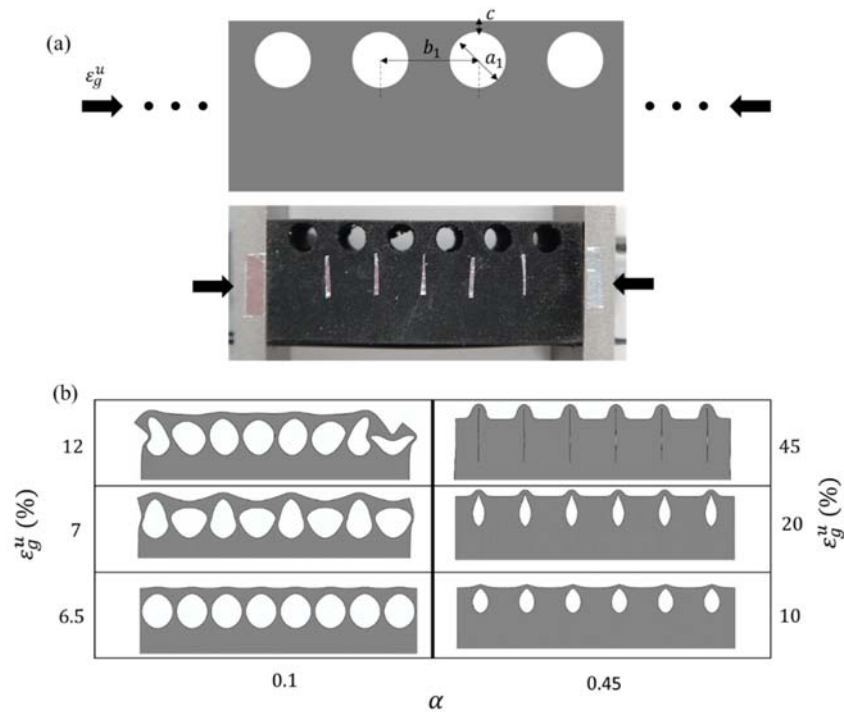


Figure 4.1.1 (a) The top figure: a representative segment of a CESM under a global compressive strain and with labeled geometrical dimensions; the bottom figure: the experimental setup of uniaxial compressing the 3D printed material. (b) The phase diagram of simulated surface textures with respect to the uniaxial compressive strain.

To validate the simulation results, we fabricated the cavity-embedded substrate samples using 3D printing and compressed them by only 25% global strain to avoid global buckling of samples, illustrated in the bottom of **Fig 4.1.2(a)**. The images of surface patterns for both $\alpha = 0.1$ and $\alpha = 0.45$ were captured by a camera. As shown in **Fig 4.1.2(a)**, the morphological evolutions for these two samples undergoing increasing compression are qualitatively consistent with those simulation results in **Fig 4.1.1(b)**. Quantitatively, the critical global strain for inter-cavity instability in the experiment is 6.0% for $\alpha = 0.1$, which matches well with the simulated value of 6.8% above. The small deviation may be attributed to the non-periodic boundary conditions at the compressor heads and the dynamic effect induced by the relatively high loading rate. Furthermore, we plot the experimental and simulated results of the amplitude-to-wavelength ratio for $\alpha = 0.45$ as the global strain increasing in **Fig 4.1.2(b)**, indicating quantitative agreement between the experiment and simulation. Therefore, the controllability of surface morphologies through varying global strain and geometrical parameters offers a new strategy to reversibly and repeatedly switch surface topography by involving embedded cavities within a soft material.

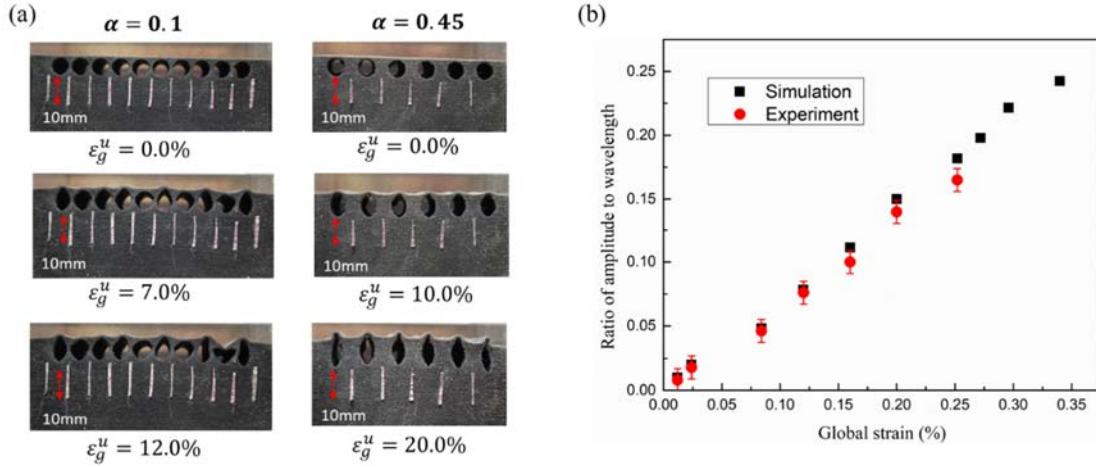


Figure 4.1.2 (a) Experimental surface evolutions of 3D-printed CESM prototypes with different values of α , while β is set to be 0.2. (b) The comparison of amplitude-wavelength ratio between the simulation and experiment for $\alpha = 0.45$

4.1.4 Results in 3D Modeling

To investigate more fascinating surface-patterns in soft materials, 3D cavities with different shapes are introduced underneath material surfaces. The exemplary 3D segment of CESM shown in **Fig 4.1.3** includes cuboidal cavities. Note that other geometries for cavity can also be embedded, for example, spherical cavities. We construct the dimensionless parameters: relative inter-cavity spacing $\alpha_i = \frac{b_i - a_i}{a_i}$ ($i = 1, 2$), relative distance from the surface $\beta = \frac{c}{a_2}$, and aspect ratio $\gamma = \frac{a_1}{a_2}$, to study the effect of cavity geometry on surface features. Based on the finite element simulation, the morphological evolutions of 3D CESMs undergoing either uniaxial ϵ_g^u or biaxial compressive strain ϵ_g^b are studied.

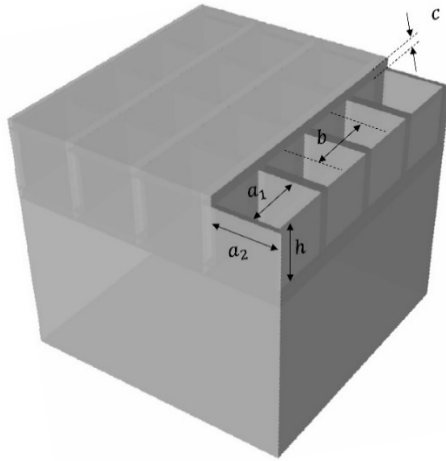


Figure 4.1.3. Schematics of representative CESMs with patterned cuboidal cavities.

Fig 4.1.4(a) shows the diagram of cross sections of CESMs with cuboidal cavity patterns with respect to the uniaxial compressive strain and the geometrical parameter γ . In the case of $\gamma = 1$, the surface keeps flat until the critical compressive strain reaches 5.5%, and then, the checkerboard pattern is triggered by the mechanical buckling, forming the alternate concave and convex feature shown in **Fig 4.1.4(b)**. The compressive strain in the plates is released by out-of-plane bending deformation, further compression still maintains this topology but increases the amplitude. As shown in the side views of deformed CESMs in **Fig 4.1.4(a)**, the instability-induced transformation of original cavity geometry should be responsible for the checkerboard pattern with the wavelength of $2a_1$. However, for the cavities with aspect ratio $\gamma = 2$, the high-order checkerboard pattern with the wavelength of a_1 occurs firstly at the critical strain of 7.2% shown in **Fig 4.1.4(a)**. At 14%, two checkerboard surface textures with different wavelengths are demonstrated in **Fig 4.1.4(c)**.

To address the effect of aspect ratio on surface pattern, we adopt a simple stability analysis. A plate with lateral periodicity (the thickness of t , length of a_1 and width of a_2), right above cavities, is adopted for analysis and subjected to uniaxial compression in the a_1 direction. The critical membrane force in the length direction for buckling is calculated as $N_{xcr} = \frac{\pi^2 D}{a_1^2} \left(m + \frac{1}{m} \frac{a_1^2}{a_2^2} \right)^2$, where D is the bending stiffness of plate and m refers to the number of half-wavelength of the buckling plate²²⁷. The relation of N_{xcr} with a_1/a_2 is plotted in **Fig 4.1.4(c)** for different values of m . It's illustrated that the critical force for $m = 1$ is smaller than that for $m = 2$ in the case of $\frac{a_1}{a_2} = 1$, which explains the preference of the checkerboard pattern with wavelength of $2a_1$ as applying uniaxial compression in our simulation. However, the buckling mode of $m = 2$, corresponding the wavelength of a_1 , is illustrated to occur preferably when the aspect ratio is 2. It is consistent with our simulation result shown in **Fig 4.1.4(a)**. Although vertical walls in between cavities are not considered in this model, the qualitative agreement with the simulation results emphasize the significance of cavity aspect ratio on buckling patterns.

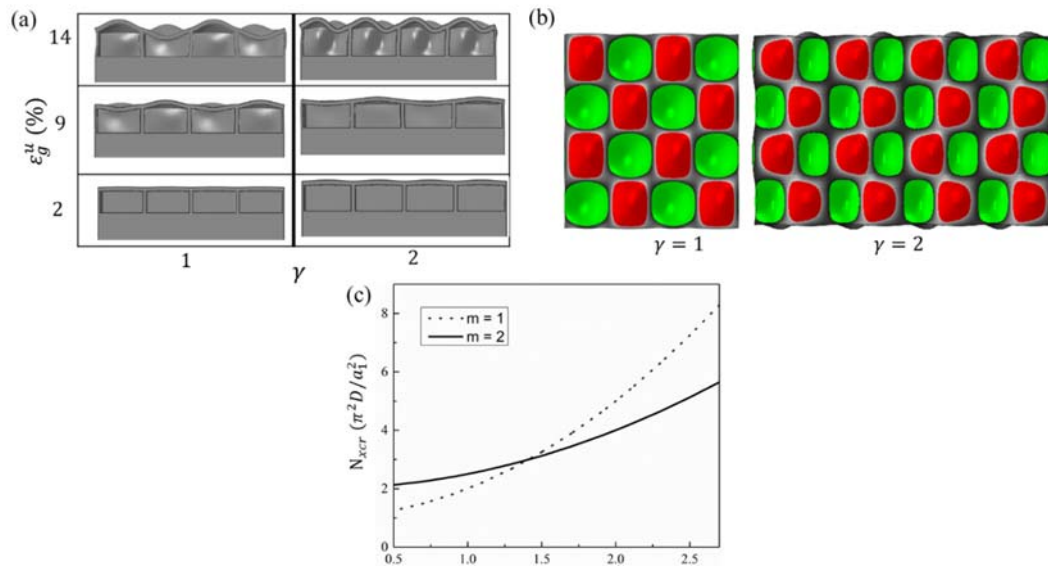


Figure 4.1.4 (a) The phase diagram of simulated surface textures and (b) the surface morphologies of cuboidal cavity embedded CESMs for $\gamma = 1$ and $\gamma = 2$ at the uniaxial global compression of 14%. (c) Theoretically critical membrane forces of plates for different buckling modes m as a function of the aspect ratio γ .

Besides the aspect ratio, other parameters of cavity can be used to switch the surface topologies, including loading strategies and cavity shapes, *etc.* **Fig 4.1.5** shows the surface patterns of CESMs at 12% biaxial compressive strain for values of $\alpha = 0.15, 0.85, 2.5$, and all cavities are kept cuboidal. With increasing relative inter-cavity spacing, the surface topology varies from checkerboard pattern to alternating mutually orthogonal peanuts, followed by local features: quadrangular bumps. The mechanism changes from buckling-induced inter-cavity instability to local deformation due to weaker interaction between cavities at the case of larger α value.

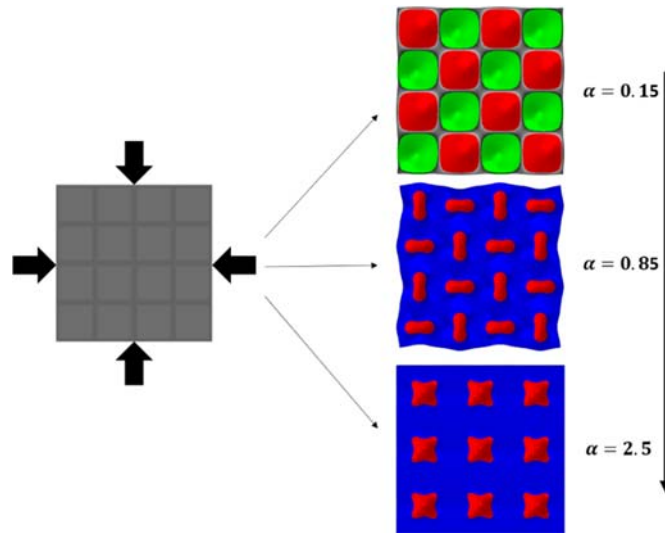


Figure 4.1.5 The surface morphologies of cuboidal cavity embedded CESMs with α undergoing the same biaxial global compression of 12%.

We further study the effect of cavity shape and row number on the topological evolution of CESMs under different loading conditions: uniaxial and biaxial compression. The inter-cavity spacing, relative distance from surface and aspect ratio are set to be constant for all cases. **Fig 4.1.6(a)** presents the results of surface topology for spherical cavity with square lattice and biaxial global compression, and shows the square array of convex bumps transforms into alternating mutually orthogonal peanuts when the global compressive strain increases from 13% to 16%. However, the surface patterns with larger bumps followed by alternating mutually orthogonal ellipses are observed when we initially introduce hemispherical cavities, which are demonstrated in **Fig 4.1.6(b)**. This difference is mainly due to the center of hemispherical cavity is closer to the top surface compared to the spherical cavity scenario when the value of β is the same. Furthermore, row number can be used to change the surface topography. We arrange a single row of cavities in the line with loading direction. The surface morphology in **Fig 4.1.6(c)** is similar to those in **Fig 4.1.6(a)** for the square array of spherical cavities, but the hemispherical cavities induce a non-symmetric surface pattern at the global strain of 24% in **Fig 4.1.6(d)**, which is much different from the square array of hemispherical cavities under biaxial compression. This transition from symmetric into non-symmetric surface is caused by the instability of underneath cavities. It's found that the instability occurs upon reaching a critical compressive strain. Although our results demonstrate that a single row of cavities is able to trigger the symmetric to non-symmetric surface morphology transition, there are other potentially important parameters for tuning the surface morphology, including heterogeneous shapes, mixture of cavity and hard particles and cavity patterns, which will be subjected to further study.

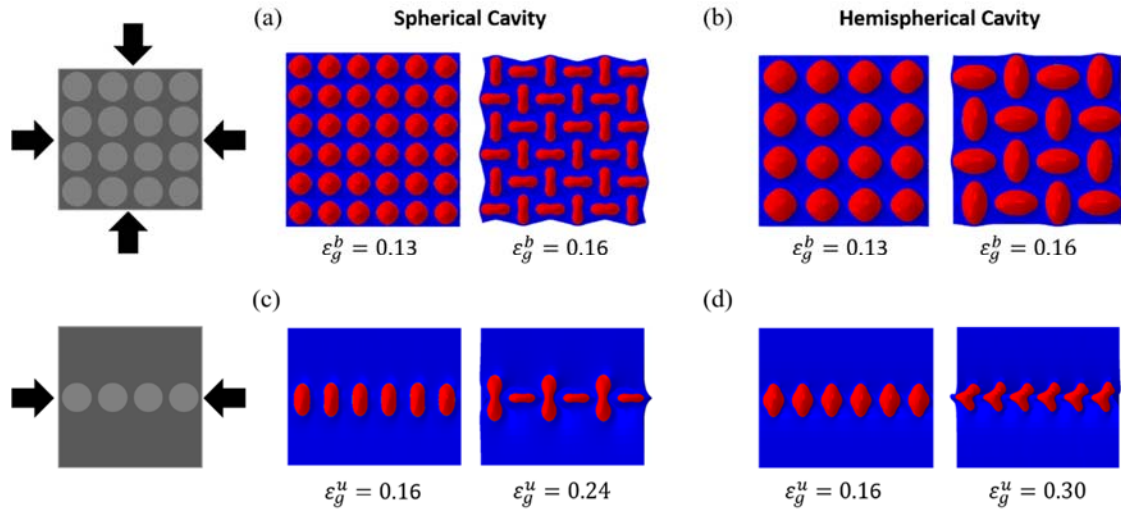


Figure 4.1.6 The surface morphologies of CESMs with square patterns of (a) spherical and (b) hemispherical cavities undergoing different biaxial global compression. The surface morphologies of CESMs with one column of (c) spherical and (d) hemispherical cavities undergoing different uniaxial global compression.

4.1.5 Conclusion

In this study, a series of 2D and 3D surface topographies were created in soft materials with embedded cavity array. Both simulation and experimental efforts confirmed that by varying the geometries of cavities (sizes, shapes, arrays) and loading methods (uniaxial and biaxial compression), we can dynamically tune the surface evolutions. The variety of overall and local morphologies was revealed to be based on the inter-cavity instability and local deformation of top plates, respectively.

4.2 Unconventional Localization Prior to Wrinkles and Controllable Surface Patterns of Film/Substrate Bilayers through Patterned Cavities

4.2.1 Introduction

A rich range of surface morphologies, from overall wrinkles to local bumps or channels/folds, can be often observed in natural and biological systems.^{169, 177, 211} The controllability of such features allows not only potential applications in optics²¹² and flexible electronics²¹³, but also tuning surface properties including adhesion²¹⁴ and hydrophobicity,²¹⁵ among others. For example, overall spreading sinusoidal wrinkles form in a stiff film/soft substrate bilayer subjected to uniaxial compression.²¹¹ Anisotropy of membrane force can result in more intriguing overall wrinkling features including stripes, herringbones, and zigzag labyrinths on planar substrates,^{171, 216} and buckyball-like and labyrinth features on spheroidal substrates.^{165, 181, 182}

While these overall wrinkles have been widely studied, dynamically and locally tunable surface features are also intriguing. Upon further compression, the sinusoidal pattern may transit to periodic-doubling patterns, ultimately followed by localized folds in the bilayer.²²⁰ It has been also found that pre-compression applied to the substrate can facilitate the formation of folds, while a different advanced mode of instability, termed localized mountain ridge, occurs after wrinkling if the substrate is subjected to pre-stretching.^{228, 229} In addition, the transitions from wrinkles to sharp folds and large aspect ratio of ridges have been experimentally observed.^{217, 230} However, the highly non-linear elasticity of substrate determining the difference of advanced localizations limits the choice of substrate materials, and pre-compression/stretch experimentally also complicates the fabrication. Moreover, both ridge and fold modes may co-exist at relatively high

compressive strain.^{217, 231} While enhanced compression can induce transition between different patterns, the control of surface undulations is sometimes difficult and the pattern variation is limited. It is therefore desirable to better control the surface morphological transition through new methods (such as varying substrate features) that are complementary to compressive loading. Note that in particle-enhanced soft materials (without film attachment), locally controllable deformations were achieved,²²⁶ however the study of tunable and reversible local surface features by controlling the defects in substrate is rare.

In fact, defects are experimentally inevitable and likely to affect the formation of wrinkles or localizations.^{222, 223} Available literature studies focused on elastically heterogeneity of thin film including patterned holes^{224, 232} and rigid elements^{221, 233} where the wrinkling pattern is disordered in the distance scaling with characteristic wavelength. However, the influence of cavities inside the substrate on controlling the surface patterns of bilayer has not received much attention. Here, we demonstrate that bilayer with pre-patterned cavities below the interface of film/substrate can attain highly ordered buckles and the pattern transition may be different than those in pristine substrates. Both finite element simulations and parallel experiments are conducted to investigate how the spatial and geometrical variations of cavities impact the evolution of surface patterns when the bilayer undergoes uniaxial compression. The presence of cavities served as strain relief can induce an unconventional transition from localized ridges to folds prior to wrinkles. We further study the dependence of initial bifurcation strain and advanced patterns on the cavity geometries. The findings of this paper may provide guidelines for using substrate

cavities to enrich surface geometries and their transitions under various levels of compression.

4.2.2 Modeling and Experimental Method

Numerical method: The representative segment of defected bilayer in plane-strain model is shown in **Fig 4.2.1**, consisting of a thin film adhered to a substrate with patterned through cylindrical cavities. Periodic boundary condition in the x direction is applied to the vertical sides of the model. Neither vertical displacement nor shear traction is allowed on the bottom surface. Here, nonlinear numerical simulations are performed through commercial software ABAQUS and four-node plane strain quadrilateral elements are used. In all cases, the mesh density is verified by mesh convergence studies. Without losing generality, the film and substrate with linear isotropic elasticity have different Young's modulus, $E_f/E_s = 300$, while the Poisson's ratio is taken to be the same for simplicity. The modulus ratio is consistent with that in the parallel experiment and similar approach can be applied to other material systems. Although we focus on 2D morphological designs, our design concept can be easily extended to 3D systems. In these calculations, a linear perturbation analysis is first conducted to identify the onset of first bifurcation including the morphological mode. We adopt the pseudo-dynamic method to study the advanced instability transitions within the frame of quasi-static deformation and kinetic effects are negligible. The compressive strain applied on the film is ε_a , which can be controlled through the mismatched deformation and constraint of the substrate.

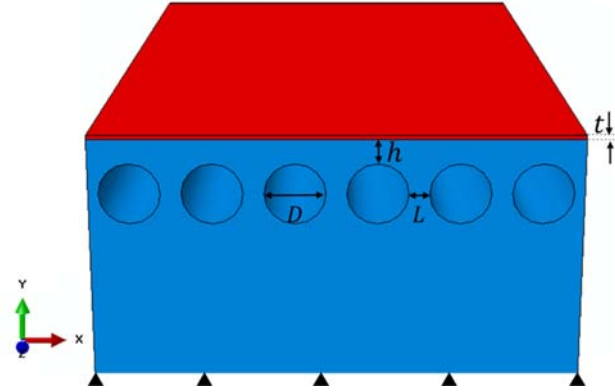


Figure 4.2.1. A representative segment of thin film (red) adhered to defected substrate (blue) with pre-patterned holes.

Experimental Method: The physical prototypes were fabricated by an Objet500 Connex 3D Printer. The thin film and substrate was made of photo-sensitive polymeric materials, TangoPlus and VeroBlack, respectively. We conducted the uniaxial compression tests with a Zwick/Roell Z2.5 mechanical tester. To ensure plane strain conditions in the compressive test, the samples were sandwiched between two optically clear acrylic plates and another plate was placed below the samples. The friction between the plates and the sample was reduced by using mineral oil. 20% global compressive strain was applied to each sample with a strain rate of 0.001 s^{-1} . A camera with high resolution was placed in front of the sample and took a picture every minute.

4.2.3 Results and Discussion

For a cavity-free substrate, the critical compressive strain ε_{wc} and wrinkling wavelength λ_{wc} are calculated by²¹¹

$$\varepsilon_{wc} = \frac{1}{4} \left(3\overline{E_s}/\overline{E_f} \right)^{2/3} = 1.16\% \quad (1)$$

$$\lambda_{wc} = 2\pi t(\overline{E_f}/\overline{E_s})^{1/3} = 29.0t \quad (2)$$

with the Young's modulus ratio $\overline{E_f}/\overline{E_s} = 300$. In the defected bilayer shown in **Fig 4.2.1**, L is the inter-cavity distance and the circular cavities has diameter D and depth h . We define the initial bifurcation with the critical strain ε_c , when the flat surface transits to an uneven morphology, but not limited to wrinkles. To avoid the boundary effect, we set the thickness of substrate as $10\lambda_{wc}$.

To study the effect of cavities on the evolution of surface patterns, the system with $D/\lambda_{wc} = 1$, $h/\lambda_{wc} = 0.1$ and $L/\lambda_{wc} = 5$, is taken as a representative example. As shown in **Fig 4.2.2(a)**, the surface pattern transits from flat surface to local bumps, mountain ridges, folds and the co-existing phase of folds and wrinkles with increasing compressive strain. At the initial bifurcation with the critical strain 0.62%, the flat surface locally undulates upward at the location right above cavities. After that, the film starts to pull material outward from the substrate, resulting in the formation of ridges. However, it is hard to achieve mountain ridges without the conditions of non-linear elasticity for substrate and pre-stretching in cavity-free bilayers.²²⁹ Additionally, wrinkles form at a critical value that is lower than that predicted by Equation (1), that is, the defected bilayer is easier to relax the film compression by localizations rather than overall spreading wrinkles. At the compressive strain of 6.0%, the mountain ridges snap downward and evolve into the folding pattern since ridges can no longer energetically favorable. Finally, another strain-relief mode, surface wrinkles, emerges in the flat region between two adjacent holes, leading to the co-existing phase of both folds and wrinkles; these surface wrinkles have the characteristic wavelength determined by Equation (2). Interestingly, the surface wrinkles

appear far later than the localizations of ridges and folds, this is opposite to the traditional wrinkle to ridge/fold transition in cavity-free bilayers.²²⁰

To validate the simulation result of the unconventional transition of surface morphology, we fabricated the stiff film/compliant substrate bilayer prototype with only one cylindrical cavity inside. The wrinkling wavelength was measured to be $\lambda_{wc} = 6.6 \text{ mm}$ by a pristine bilayer system. Since the length of sample, 33 mm , is far large than λ_{wc} and cavity diameter of $\lambda_{wc} = 6.6 \text{ mm}$, the experimental test is able to mimic no interaction between cavities in the simulation. From **Fig 4.2.2(b)**, there is good qualitative agreement in the morphological evolution between simulation and experimental results.

Although imperfections such as small cavities are unavoidable in most systems,^{222,}²²³ the pre-patterned cavities in the substrate may be useful in some sense. First, the presence of cavities can easily trigger the localizations at relatively small compression strain of 0.62%. The ridges/folds are easier to form in systems with cavities than in cavity-free systems (which typically require pre-compression/stretching). Moreover, the strain for wrinkles occurring in systems with cavities, approximate 18%, is much larger than that in cavity-free system (1.16%), which underpins a potential method by pre-patterning cavities to suppress widespread wrinkles.

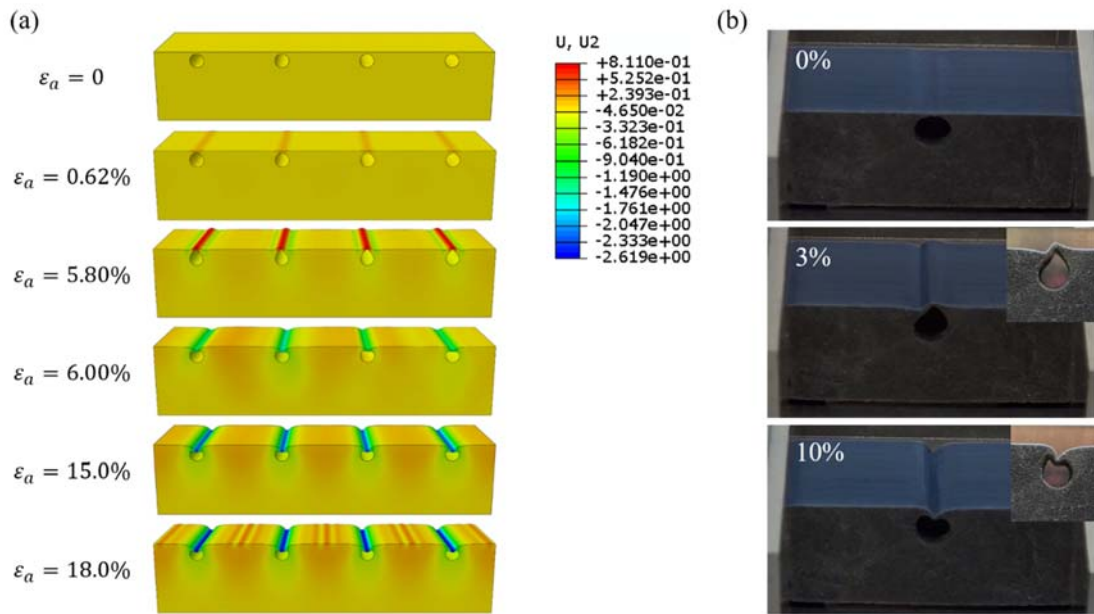


Figure 4.2.2. Simulation (a) and experiment (b) images of the defected bilayer structure at various compressive strains, where $D/\lambda_{wc} = 1$, $h/\lambda_{wc} = 0.1$ and $L/\lambda_{wc} = 5$.

In order to study how the spatial arrangement of cavities affects morphological evolution, we calculate the critical strain for the initial mode of instability as a function of the normalized spacing, illustrated in **Fig 4.2.3**. For this system, ε_{wc} is computed to be 1.21% for cavity-free one, which is close to that predicted by Equation (1). Shown by the serial cases of $D/\lambda_{wc} = 1$ and $h/\lambda_{wc} = 0.1$ (black curve), the critical strain increases as the spacing L becomes larger, approaching a plateau. The reason for increasing critical strain lies in less interaction between two adjacent defects as the spacing increases, thus the mechanism of initial bifurcation varies with the spacing L : the pattern of waves occurs if the spacing is small, while large spacing only allows local upward undulation. For the

case of small spacing, circle cavities transform into a mutually orthogonal and alternating pattern with the wavelength of doubling spacing.

The position and size of cavities can also affect the initial buckling mode. Take the examples with fixed diameter $D/\lambda_{wc} = 1$, it's observed that the critical strain becomes larger when cavities locate deeper relative to the film/substrate interface. When the depth is beyond half of characteristic wavelength λ_{wc} , the critical strain approaches the value for wrinkling in cavity-free system since the effect of cavities on surface pattern is negligible. Additionally, larger cavities result in smaller critical strain. If the cavity size is very small, then the cavities have no pronounced influence on wrinkling pattern. In short, the initial instability morphology for defected bilayer shows little difference with the cavity-free bilayer if the cavity size is much smaller than λ_{wc} or the cavities locate far from the film/substrate interface.

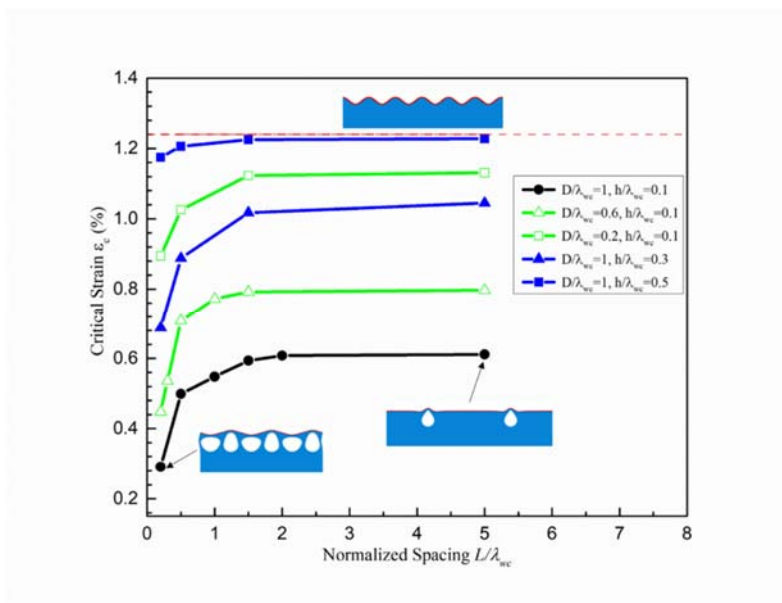


Figure 4.2.3. The strain for first bifurcation as a function of spacing L in the bilayer with cavities having different diameters and depths.

After initial mode of instability, further compression is applied to the bilayer system. The diagram of advanced surface pattern is plotted with regard to applied strain ε_a and normalized spacing L/λ_{wc} in **Fig 4.2.4(a)**. When two adjacent cavities are relatively close, the amplitude of waves builds up with increasing applied strain after the initial bifurcation. The continuously applied compression induces locally ridged pattern followed by the folding and wrinkling configuration for the case of large spacing, for example, $L = 5\lambda_{wc}$. The morphological difference due to the hole spacing is experimentally validated by the images at the global strain of 0.1 shown in **Fig 4.2.4(b)**. The non-uniformity of pattern in **Fig 4.2.4(b)** is possibly caused by the loose boundary conditions and the limited number of fabricated cavities in experimental setup. In addition, if the spacing is $L = \lambda_{wc}$, we observe the saw-like pattern, which possibly results from the interaction between the local buckling morphology and the overall wave. With further compression, the saw-like pattern evolves into the pattern with partial folds. Thus, the inter-cavity spacing plays an important role in surface pattern formation.

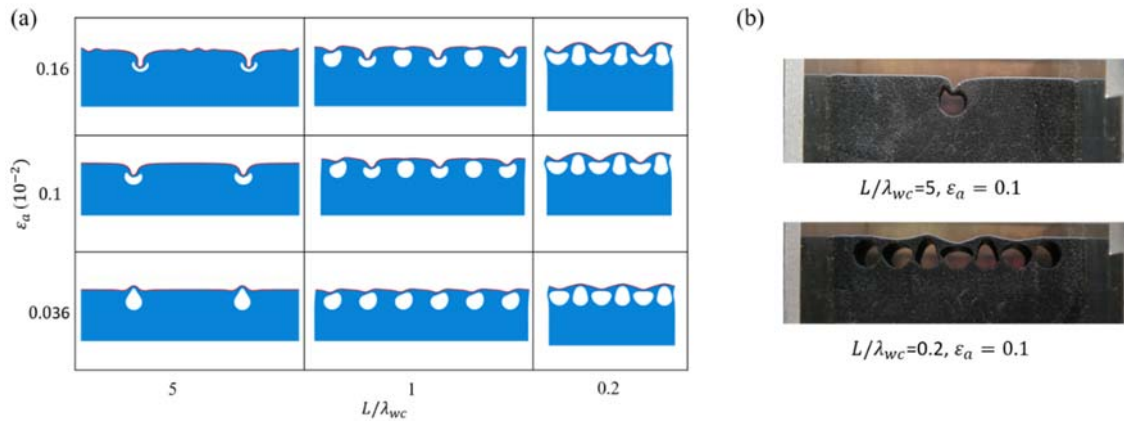


Figure 4.2.4. The diagram of buckling morphologies for the defected structures ($D/\lambda_{wc} = 1$ and $h/\lambda_{wc} = 0.1$) against applied strain and normalized spacing.

Fig 4.2.5 shows the diagram of surface patterns against normalized diameter D/h and normalized spacing L/λ_{wc} . All the morphologies are captured at the strain of 2.0%, slightly larger than ε_{wc} . When the diameter is relatively small, we observed that wrinkling patterns were slightly perturbed by the defects inside substrate. Note that perfect wrinkling morphologies are expected in cavity-free systems ($D/h \rightarrow 0$). However, in the cases of $D/h = 2$ and $L/\lambda_{wc} = 0.2$, the wavelength of waved pattern is spacing-tripling and it's a new instability configuration due to defects interaction. Based on these diagrams, the defected bilayer system can bifurcate into diverse modes: localized ridges, localized folds, saw-like and waved patterns, depending on the size, position and spacing of defects.

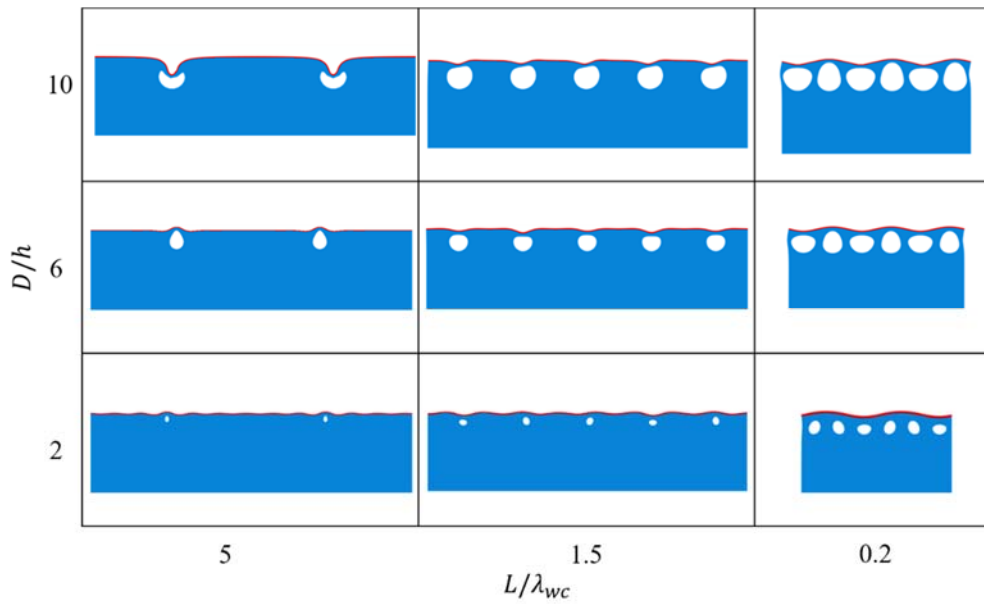


Figure 4.2.5. The diagram of surface morphologies for the defected structures ($h/\lambda_{wc} = 0.1$), where the applied strain is fixed at $\varepsilon_a = 0.02$, against normalized diameter D/h and normalized spacing L/λ_{wc}

Although the current study is based on 2D models, similar approach can be easily extended to 3D systems, where the more varieties of cavity (or controlled defect)

geometries, anisotropy of loading and instability mechanisms may further enrich the family of surface pattern transition in the bilayer. Besides mismatched expansion, one may also impose various ways of inducing compressive strain in the film, including mechanical compression, active material responding to environmental stimulus, *e.g.*, pH, electrical field and humidity, etc., in practice. The material constitutive behavior can also be nonlinear, *e.g.* the incompressible neo-Hookean materials, which may further fine tune the morphological features and will be subjected to the future work.

4.2.4 Conclusion

In this study, we numerically and experimentally validated that the conventional transition, of wrinkles to localizations (folds or ridges) in film/substrate bilayers subjected to increasing uniaxial compression, can be reversed through the pre-patterned cavities in the substrate. Compared with cavity-free bilayers, the localizable surface topologies were achieved at relatively small strain even within a linear-elastic substrate. The presence of holes not only simplified the conditions for creating localized folding-like morphologies, but also served as a strain-relief mechanism to suppress the formation of overall spreading wrinkles. Additionally, the surface patterns of defected bilayers were highly dependent on the spatial and geometric configurations of cavities beneath the surface.

Chapter 5 Functional devices enabled by morphology manipulation

Based on the studies of multiscale materials, chemical/physical properties could be optimized through varying strain-engineered morphologies. Beyond material-level, the strategy of morphology manipulation is adopted to search for functional devices to figure out practical challenges in the field of energy. In this chapter, we firstly proposed a novel energy conversion system: chemical-loop reduction of CO₂ with atomically modified perovskite, and then demonstrate the flexible battery with macroscale design of electrode structures²³⁴⁻²³⁶.

5.1 Reduction of Air-containing CO₂: Chemical Looping Based on

Perovskite Nanocomposites by Cu doping

5.1.1 Introduction

Carbon utilization is one of the economical solutions to mitigate anthropogenic carbon dioxide (CO₂) emission apart from carbon sequestration. Substantial efforts have been invested in the reduction of CO₂ to carbon monoxide (CO), as gaseous fuels²³⁷⁻²⁴¹ or the intermediate for higher-value chemicals²⁴²⁻²⁴⁶, which are desirable for closing the carbon loop and hopefully producing new venues for chemical industries. Photocatalytic splitting of CO₂ into CO can make use of solar energy, but challenged by the unsatisfactory efficiency of less than 0.2%^{240, 247-249}. Although electrocatalytic reduction and thermal reforming are more scalable technologies for the cycling of CO₂^{238, 240, 250}, their activity and selectivity for CO₂ reduction are challenged by the high O₂ sensitivity. The oxygen-tolerance was less than 2 %v/v for the electrocatalytic condition of fast electrons

collections^{251, 252}, while the portion of 3 %v/v O₂ can lead inevitable oxidation of the catalysts at above 1000 K²⁵³⁻²⁵⁵. Consequently, most carbon utilization progresses either targeted converting high-purity CO₂ or exhibited low CO₂ conversion in the presence of O₂.

According to a report recently released by the Royal Academy of Engineering²⁵⁶, among various carbon capture techniques²⁵⁷⁻²⁵⁹, the distributed direct-air-capture (DAC) of CO₂ is perhaps the only feasible engineering solution for greenhouse gas removal. Recent advances in humidity-swing direct air capture (HSDAC) have significantly reduced the complexity and cost of CO₂ capture, since it only requires substrate drying or wetting for chemically absorbing or releasing CO₂²⁶⁰⁻²⁶². When separation or vacuum process is not needed, air-containing CO₂ (with typical 50 v% CO₂) can be easily attained through HSDAC at extremely low cost, and the captured CO₂ is free of contaminant (unlike post combustion capture (PCC))^{258, 259, 261, 263}. The distributed DAC may inspire series of new industrial utilizations and applications. Indeed, separation/vacuum process can also be very costly for PCC, like any capturing process for obtaining high-purity CO₂^{258, 261, 264, 265}. Therefore, it is of paramount importance to develop both oxygen-tolerant and high-selectivity process for CO₂ reduction, otherwise, expensive upstream CO₂ purification would limit the efficiency of downstream utilization. This is a vital step for closing the synthetic carbon cycle.

Chemical looping has been widely used for CO₂ conversion²⁶⁶⁻²⁶⁹. The co-utilization of CO₂ with CH₄ as a reducer feedstock has been optimized to produce high-purity syngas, along with various oxidants, such as air, O₂ and H₂O^{250, 270-272}. As a re-oxidant in the methane-assisted CO₂ splitting, CO₂ has also been effectively converted to CO^{268, 272, 273}.

However, conventional chemical looping schemes have rarely studied the efficiency of CO₂ conversion with the presence of air or oxygen gas as co-oxidants. Intrinsically, the re-oxidation of reduced oxygen carriers is sensitive to the composition of extra reductant or oxidant (*e.g.*, CH₄, O₂) in CO₂ feedstock, and thus likely declining the qualities and/or yields of produced CO in the condition of impure feedstock stream of CO₂²⁶⁸. For example, the Sr₃La₂O₇ perovskite oxide was found to be theoretically unfavorable for high CO₂ conversion at high oxygen pressure due to the strong competition from the highly oxidative capacity of O₂²⁶⁸. Thus, these limitations make the conventional schemes difficult and costly integrating with the upstream HSDAC technique, and it motivates the current study to efficiently integrate CO₂ capture and utilization.

Combining the HSDAC and chemical looping techniques, we propose a novel carbon-looping scheme (**Fig 5.1.1**) to convert air-containing CO₂, which produces pure CO and syngas through successive cyclic redox process for further production of valued-added chemicals. This scalable scheme can economically and efficiently take advantage of the low-cost captured air-containing CO₂ with only additive of reducing agent (*e.g.*, CH₄), and the high temperature required for reaction can be potentially sustained though concentrated solar thermal energy²⁶⁸.

Herein, by using the strategy of substituting A sites in perovskites, Cu-doped LaFeO₃ as oxygen carrier in cyclic redox was developed to efficiently split air-containing CO₂ into CO in the cyclic redox scheme with CH₄ undergoing partial oxidation. With air-rich CO₂ stream (1:5 O₂/CO₂ ratio, mimicking 1:1 CO₂/air mixture) in the CO₂ splitter, this perovskite demonstrated remarkable performance: 87% CO₂-to-CO conversion and the CO yield of 2.28 mol/kg per step, compare to only 27.5% and 0.41 mol/kg respectively, for

conventional pristine LaFeO_3 . Furthermore, the partial substitution of La with Cu ions also promoted the efficacy of methane oxidation: the syngas yield (11 mol/kg) increased by 113% and CH_4 conversion doubled to 72%, while 95% syngas selectivity was still achieved. This air-stable scheme offers an effective pathway to directly converting atmospheric CO_2 into methanol and acetic acid as valuable productions, reducing energy consumption by 67.3% and mitigating net CO_2 emission by 94.5%, thus offering an economic engineered approach to close the carbon loop.

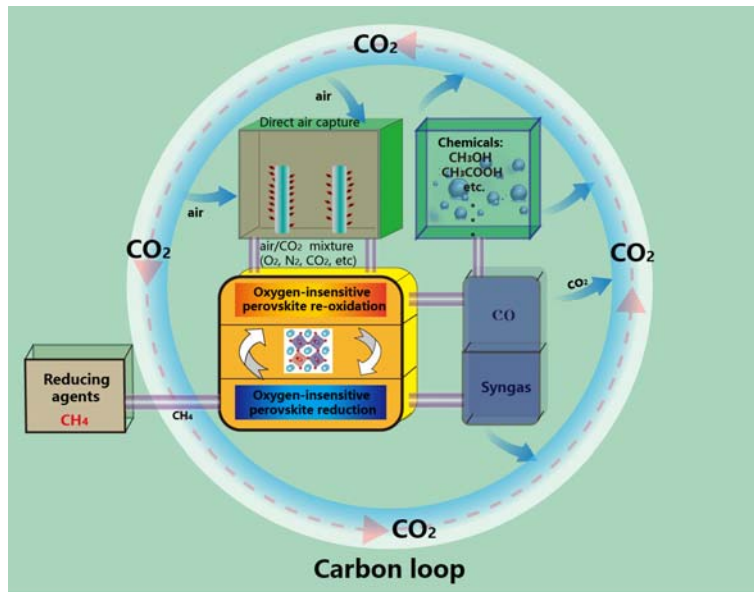


Figure 5.1.1. Schematic of cyclic redox scheme and its contribution to close the carbon looping. Three key processes are included: upstream direct-air-capture for producing air-containing CO_2 , perovskites-based chemical looping reactor for syngas and CO production, downstream utilization of CO /syngas and subsequent CO_2 emission.

5.1.2 Model and Method

Synthesis of perovskite nanocomposites: Three-dimensional ordered macroporous LaFeO_3 , $\text{La}_x\text{FeCu}_{1-x}\text{O}_{3-\delta}$ and $\text{LaFe}_x\text{Cu}_{1-x}\text{O}_{3-\delta}$ were prepared by methyl methacrylate (PMMA)-templating method. According to the chemical formula of designed oxygen carriers, required amounts of $\text{La}(\text{NO}_3)_3 \cdot 6\text{H}_2\text{O}$, $\text{Fe}(\text{NO}_3)_3 \cdot 9\text{H}_2\text{O}$, and/or $\text{Cu}(\text{NO}_3)_2 \cdot 3\text{H}_2\text{O}$ (the total concentration of the cations in the solution is kept at 0.25 mol/L) were dissolved in deionized water and stirred for 3 h. Then, citric acid (the molar ratio of citric acid to metal ions is 1:1) and PMMA template were added into the above solution, subsequently followed by stirring for 4 h, drying at 100 °C for 24 h and calcinated at 600 °C for 2 h.

Characterizations: The X-ray diffraction (XRD) patterns were acquired on a Rigaku diffractometer using $\text{Cu K}\alpha$ radiation ($\lambda = 0.15406$ nm, $U=40$ kV, $I=200$ mA). The *in situ* XPS experiment was conducted on a PHI 5000 Versaprobe II instrument according to the following processes: the sample was first pretreated in H_2 atmosphere heated from room temperature to 800 °C and then cooled to room temperature in Ar atmosphere. After that the catalyst was treated in CO_2 or (CO_2+O_2) stream heated from room temperature to 800 °C. The fresh, reduced and re-oxidized samples are tested by the XPS instrument, respectively. The element distribution was analyzed by transmission electron microscopy (TEM, JEOL JEM-2100) equipped with energy dispersive X-ray spectroscopy (EDS) instrument. The morphology of the sample was observed by scanning electron microscopy (SEM) on a NOVA NANOSEM 450 instrument. Temperature programmed reduction of hydrogen (H_2 -TPR) experiments were performed on a TPR Win instrument (produced by Quantachrome Instruments Co.) under a flow of 10% H_2/Ar mixture (25 mL/min) over

50 mg catalyst. CH₄-TPR experiments were performed on a microreactor (CATLAB, produced by Hiden Analytical Co.) with a flow of 5% CH₄/Ar mixture gas (50 mL/min) over 50 mg oxygen carriers, and the temperature was increased from room temperature to 900 °C. After the CH₄-TPR experiments, the CO₂-TPO experiments were carried out. The samples were exposed to 5% CO₂/Ar (50 mL/min) from room temperature to 900 °C. The outlet gases were measured by an online mass spectrometer (QGA, produced by Hiden Analytical Co., England).

The *In situ* Diffuse reflectance infrared Fourier transform spectroscopy (DRIFTS) analysis was performed on an FTIR spectrometer (vertex 70, Bruker, Germany) equipped with a liquid N₂ cooled Mercury-Cadmium-Telluride (MCT) detector. A Pike Technologies HC-900 DRIFTS cell with nominal cell volume of 6 cm³ was used. Scans were collected from 4000 to 1000 cm⁻¹ at a resolution of 4cm⁻¹. The reduced oxygen carriers were placed in a DRIFTS cell equipped with CaF₂ windows and was pretreated in flowing Ar (25mL/min) at 600 °C for 1 h. Then, the pretreated sample was exposed to CO₂ (10%)/O₂ (2%)/Ar(88%) for 30 min and the IR spectra were recorded.

Isothermal reaction and cyclic redox experiment: For the qualitative analysis on the performance of different oxygen carriers, the samples (0.1 g) were pretreated in a microreactor (CATLAB) in Ar at 300 °C for 10 min, and then reacted with methane mixed gas 5% CH₄/Ar (30 mL/min) at 850 °C for 10 min in the POx step. After that, the oxygen carriers were purged with pure Ar (99.99%, 50 mL/min) for 10 min. Then, the mixed gas CO₂ (10%) +O₂ (2%) balanced with Ar (30 mL/min) were introduced into the reactor and CO₂ splitting lasted for 10 min. The gas was detected using the online mass spectrometer (QGA). For calculating methane conversion, CO₂ conversion and yields of syngas and CO,

oxygen carriers (1.8 g) were placed in a fixed bed reactor (quartz tube with a diameter of 16 mm) and pretreated in Ar at 300 °C for 30 min. Methane stream (5% CH₄/Ar) with a flowrate of 200 mL/min was fed for 31 min at 850 °C. After that, the oxygen carriers were purged with pure N₂ (99.99%, 150 mL/min) for 30 min, and then the mixed gas CO₂ (10%) + O₂ (2%) balanced with Ar (200 mL/min) were introduced into the reactor for 20 min. The PO_x-CO₂ splitting cycle was repeated 50 times. The outlet gas composition was measured by a gas chromatograph (7890A GC System, produced by Agilent Co.)

***Ab-initio* calculation:** The calculations were performed with the spin-polarized density functional theory (DFT) method using the *ab initio* code QUANTUM-ESPRESSO²⁷⁴. The Perdew-Burke-Ernzerhof (PBE) exchange-correlation functional of the generalized gradient approximation (GGA) was used. Ultrasoft pseudopotentials were used to describe electron-ion interactions, a plane-wave cutoff energy of 50 Ry was used. Given the strongly correlated nature of LaFeO₃, a *U* Hubbard-like correction is introduced into the DFT energy functional (DFT+*U*) to account for the on-site Coulomb interactions in d orbitals²⁷⁵. For Cu atoms, the *U* parameter is set to 6.52 eV, as in previous studies of copper containing systems²⁷⁶. For Fe atoms, the *U* parameter is set to 4.5 eV²⁷⁷, providing a good description of the magnetic moment of Fe³⁺ ions and the band gap in LaFeO₃. A 4×4×1 Monkhorst-Pack *k*-point grids (centered at the Γ point) was used for Brillouin zone sampling. A 4-layer slab with the bottom layer fixed was used to model the LaFeO₃(110) surface and the thickness of vacuum is set at 20 Å. The conjugate gradient method (CG) was used to optimize the atomic positions until the change in total energy was less than 5 ×10⁻⁶ eV/atom, maximum Hellmann–Feynman force within 0.01 eV Å⁻¹, and the maximum displacement of atoms was less than 5 ×10⁻⁵ Å.

5.1.3 Performance of Cu-doped LaFeO₃

Owing to its unique electronic properties, LaFeO₃ perovskites were found to exhibit promising activity and selectivity in catalytic reductions in the presence of O₂^{278, 279}. Since the performance of perovskite may be improved by substituting A or B sites with other ions^{280, 281}, we prepared two types of oxygen carriers with various Cu doping ratios: La_{1-x}Cu_xFeO_{3-δ} and LaCu_xFe_{1-x}O_{3-δ} ($x = 0.05, 0.1, 0.15, 0.2$). Firstly, the redox performances of these Cu-doped perovskites were evaluated through isothermal reactions of methane partial oxidation (POx) and O₂-containing CO₂ splitting. Over pure LaFeO₃, the methane conversion was only 34.7% with the syngas yield of 5.15 mol/kg and the H₂/CO ratio of 2.3 in the POx step, comparable with previous studies over iron-based perovskites²⁷². However, the substitutions of La or Fe site with Cu atom improved the methane conversion and syngas productivity. Interestingly, La_{0.95}Cu_{0.05}FeO_{3-δ} exhibited exceptional performances among such doped perovskites. Compared to pure LaFeO₃, the syngas productivity of La_{0.95}Cu_{0.05}FeO_{3-δ} nearly doubled (11.0 mol/kg) with much higher CH₄ conversion (71.4%), and the H₂/CO ratio being closer to 2 (**Fig 5.1.2(a)-2(c)**). By comparing the redox performances among representative oxygen carriers (**Table 5.1.S1**), La_{0.95}Cu_{0.05}FeO_{3-δ} was identified among the best oxide for methane partial oxidation. Through the methane temperature-programmed reduction (CH₄-TPR) (**Fig 5.1.S1**), the peaks of CO and H₂ generation for La_{0.95}Cu_{0.05}FeO_{3-δ} corresponded to the lowest temperature (775 °C) among all the doped perovskites and the smallest amount of undesired CO₂ was produced. In the carbon dioxide temperature programmed oxidation (CO₂-TPO) and oxygen temperature programmed desorption (O₂-TPD) (see **Fig 5.1.S2**), La_{0.95}Cu_{0.05}FeO_{3-δ} significantly outperformed to pure LaFeO₃ in the intensity of CO

generation (more than three times higher) and O₂ desorption. It is evident that 5 at% Cu substitution to La sites could assist the kinetics of reductivity and re-oxidation of the LaFeO₃ perovskite, desirable for methane selective oxidation and CO₂ splitting simultaneously.

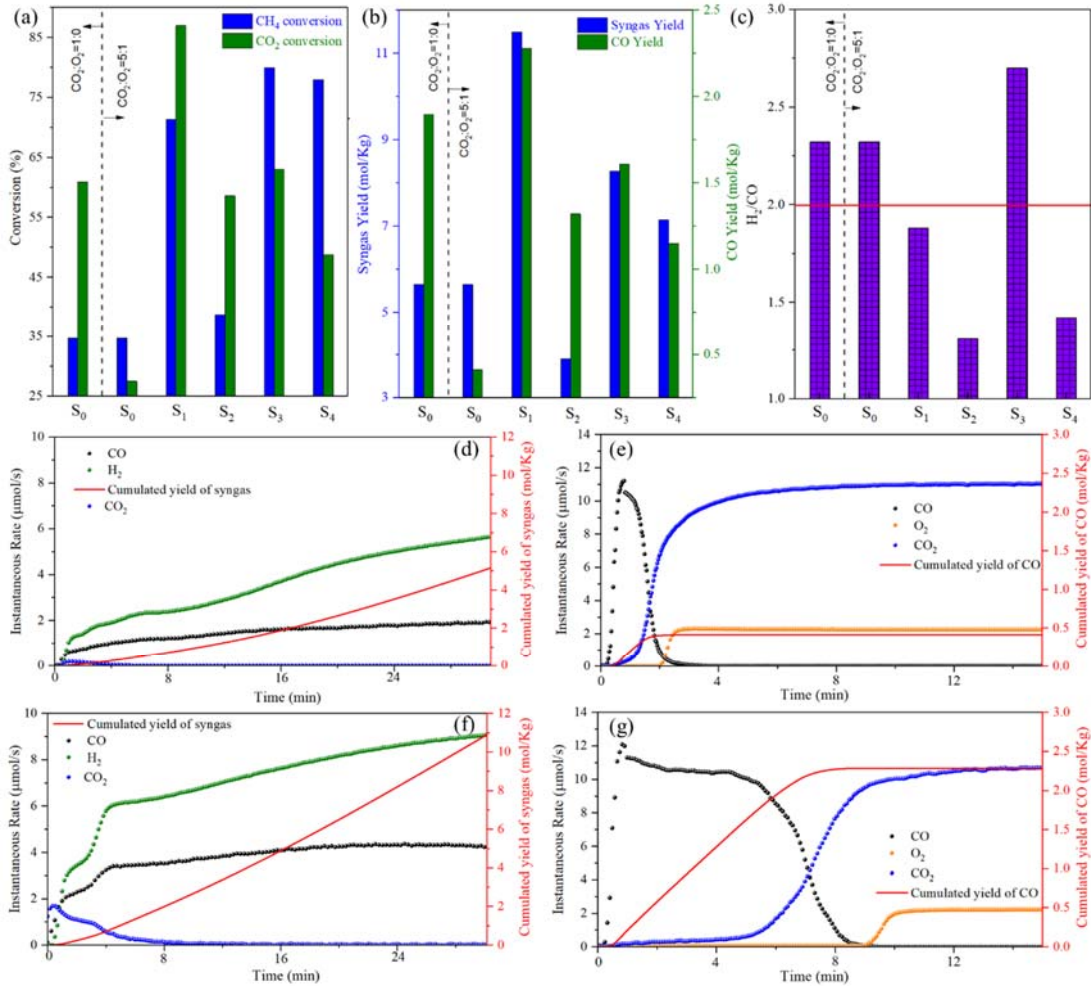


Figure 5.4.2 Redox performances of Cu-doped LaFeO₃. (a) Conversions of methane and CO₂, (b) yields of syngas and CO, (c) H₂/CO molar ratios in the steps of methane PO_x and/or CO₂ splitting using LaFeO₃ perovskites with different Cu contents: LaFeO₃ (S₀), La_{0.95}Cu_{0.05}FeO_{3-δ} (S₁), La_{0.8}Cu_{0.2}FeO_{3-δ} (S₂), LaCu_{0.05}Fe_{0.95}O_{3-δ} (S₃), LaCu_{0.2}Fe_{0.8}O_{3-δ} (S₄). The left and right sides of dash line indicate that the feedstock stream of CO₂ splitting step

contains pure CO₂ (CO₂:O₂=1:0) and O₂-containing CO₂ (CO₂:O₂=5:1), respectively. Comparison of instantaneous performances between (d, e) pure LaFeO₃ and (f, g) La_{0.95}Cu_{0.05}FeO_{3-δ}: the elution profiles (CO, H₂, CO₂) and cumulative syngas yield in (d, f) the step methane PO_x step; the elution profiles (CO, O₂, CO₂) and cumulative CO yield in (e, g) the step of O₂-containing CO₂ (CO₂:O₂=5:1) splitting.

Next, splitting of O₂-containing CO₂ (CO₂:O₂=5:1) was investigated. The substitution of 5% La with Cu also significantly enhanced both CO₂ conversion (87%) and CO yield (2.28 mol/kg) (**Fig 5.1.2(a)-2(b)**), while pure LaFeO₃ exhibited unsatisfactory performances (27.5% CO₂ conversion and 0.414 mol/kg CO yield). In terms of CO₂ conversion and CO yield, La_{0.95}Cu_{0.05}FeO_{3-δ} highly outperformed the other doped perovskites and pure LaFeO₃ even for splitting O₂-free CO₂. To the best of our knowledge, the proposed Cu-doped perovskite, La_{0.95}Cu_{0.05}FeO_{3-δ}, was for the first time shown to effectively split air-containing CO₂. Note that the Cu-doped perovskites underwent complete reduction/oxidation herein, unlike the fact that the strategy of partially replenishing the active lattice oxygen was reported to achieve high CO₂ conversion²⁶⁸. Interestingly, the presence of O₂ as the feedstock of CO₂-splitter can enhance CO₂ conversion when compared with that fed with pure CO₂ for the La_{0.95}Cu_{0.05}FeO_{3-δ} sample, since the reaction between the reduced Cu and Fe species in oxygen carrier and O₂ gas releases heat to assist CO₂ conversion (**Figure 5.1.S3**).

To emphasize the redox activity of La_{0.95}Cu_{0.05}FeO_{3-δ}, **Fig 5.4.2(d)-2(g)** display the profiles of gaseous elution for complete reduction/oxidation over the La_{0.95}Cu_{0.05}FeO_{3-δ} sample. While both CO and H₂ accumulated with reaction time and

small amount of CO₂ was initially eluted during the POx step, La_{0.95}Cu_{0.05}FeO_{3-δ} demonstrated a syngas productivity rate of 6.13 mmol kg⁻¹s⁻¹, which was much larger than that over pure LaFeO₃ (3.2 mmol kg⁻¹s⁻¹). After feeding the O₂-containing CO₂ stream over pure LaFeO₃, the duration for near-complete CO₂ conversion (>95%) was only 54 s, corresponding to a CO yield rate of 5.6 mmol kg⁻¹s⁻¹. By contrast, the new oxygen carrier La_{0.95}Cu_{0.05}FeO_{3-δ} exhibited a significantly longer duration (300 s) for such CO₂ conversion (>95%), which was almost constant before fully replenishing the active lattice oxygen. The average rate of CO yield over La_{0.95}Cu_{0.05}FeO_{3-δ} (4.75 mmol kg⁻¹s⁻¹) was one order of magnitude higher than that over pure LaFeO₃ (0.86 mmol kg⁻¹s⁻¹) and was even higher than that for pure LaFeO₃ under pure CO₂ (O₂-free) feeding stream (**Fig 5.1.S3**). Therefore, with the presence of O₂ in the feeding stream of CO₂, the dopant of Cu to the A site of LaFeO₃ perovskite can significantly improve the CO₂ conversion while keeping higher redox activity to partially oxidize methane.

5.1.4 Structural evolution during redox cycles

To shed light on the mechanism for improved performances after 5 at% Cu substitution, the structural evolution of La_{0.95}Cu_{0.05}FeO_{3-δ} sample was further investigated. The morphologies of as prepared and reduced La_{0.95}Cu_{0.05}FeO_{3-δ} samples were investigated by SEM and TEM technologies. The SEM images (**Fig 5.1.S4**) showed a three-dimensional periodic framework with uniform pore size of 100 ± 10 nm, which benefited the redox activity compared with nonporous samples (**Fig 5.1.S5**). Both of HRTEM and Fourier Transform images (**Fig 5.1.3(a)-3(c)**) revealed the sample's crystal surface with a fringe spacing of 0.279 nm corresponding to the (1 1 0) plane. While no clusters of doped Cu or CuO were observed in the STEM images, the elemental mapping

(Fig 5.1.3(d)-3(f)) by energy dispersive X-ray spectroscopy (EDS) suggested that all elements were uniformly dispersed in the as-prepared sample. To further verify the substitution position of Cu, the X-ray diffraction (XRD) patterns and Rietveld refinement of fresh pure LaFeO_3 and $\text{La}_{0.95}\text{Cu}_{0.05}\text{FeO}_{3-\delta}$ (Fig 5.1.S6) validated the pure perovskite phase with no impurities oxides detected for the Cu-doped sample, and 4.8 at.% A sites in perovskite were substituted by Cu atoms (Table 5.1.S2-5.1.S3), unlike B sites substituted in most of studies in Cu-doped LaFeO_3 ^{279, 282, 283}.

Once reacted with reductive gases, the reduced $\text{La}_{0.95}\text{Cu}_{0.05}\text{FeO}_{3-\delta}$ sample was characterized through XRD techniques. Fig 5.1.3(g) shows the XRD patterns of the perovskite undergoing varying reduced time in the CH_4 atmosphere. With continuously feeding CH_4 stream, the pure perovskite structure was maintained until the reduced time went beyond 5 min, after which other oxides composites (La_2O_3 , FeO_x) and metallic Fe^0 particles appeared without complete collapse of the perovskite structure. Similar oxides and metallic phases were reported in the previous studies of reduced perovskites^{268, 272, 284}. The deep reduction of Fe cations into metallic Fe^0 particles of 20-40 nm was also identified through STEM and EDS mapping images (Fig 5.1.S7), while Cu and La elements were uniformly distributed. When the reduced sample was exposed to an O_2 -containing CO_2 environment, the perovskite structure was totally restored and no structural evolution was suggested by the identical XRD patterns for the fresh sample and the re-oxidized sample (Fig 5.1.3(g)), confirmed by the absence of metallic Fe^0 particles in the re-oxidized sample. Interestingly, the metallic Cu^0 signal was detected when the sample was reduced by 14 min (Fig 5.1.3(h)), and disappeared once undergoing the re-oxidation step. However, it is worth

stressing that the effect of Cu substitution on the redox activity and the metallic Cu⁰ on the followed step of O₂-containing CO₂ splitting remained unclear.

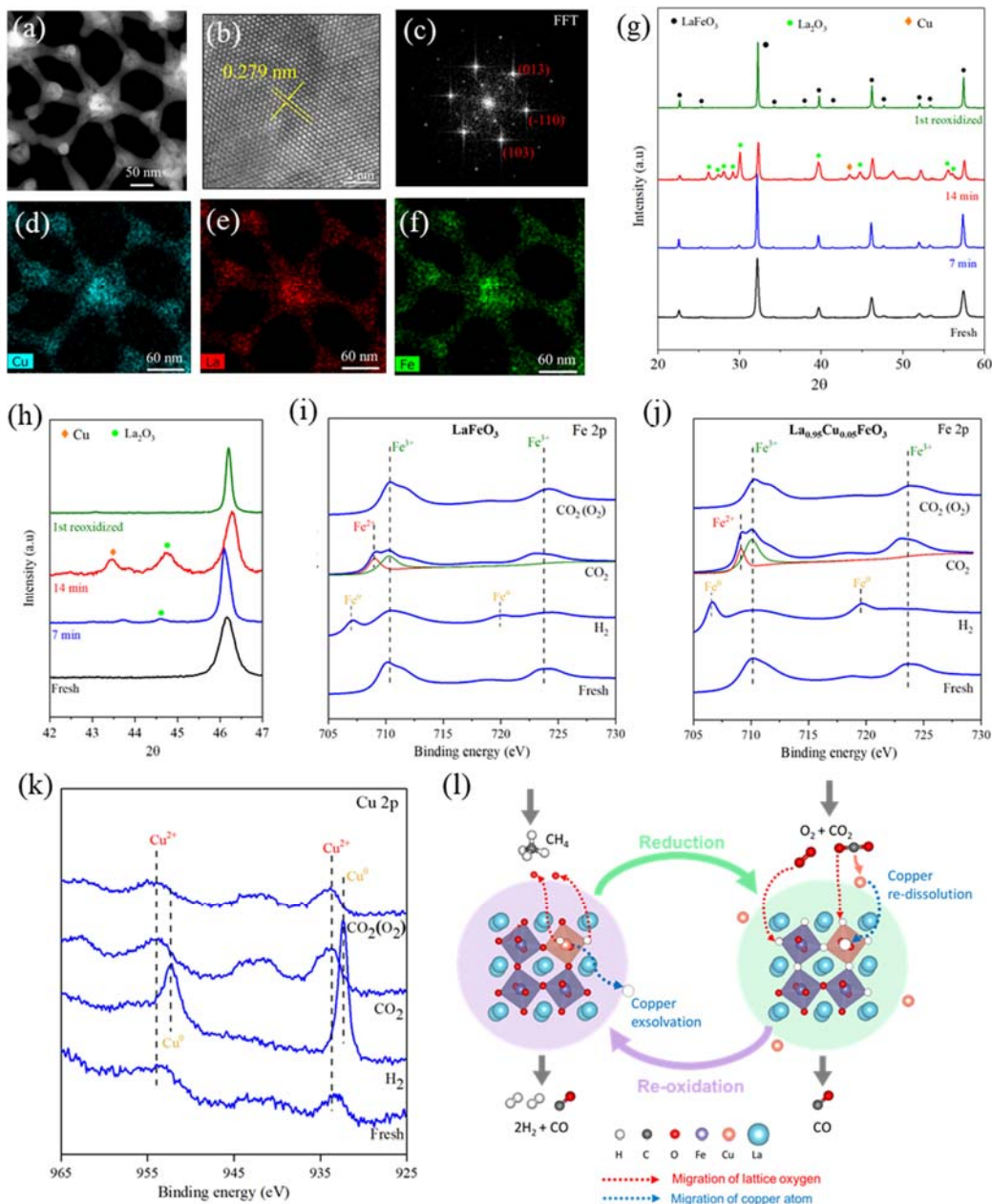


Figure 5.1.3 Structural and compositional characterizations for fresh and spent $\text{La}_{0.95}\text{Cu}_{0.05}\text{FeO}_{3-\delta}$. (a) STEM image, (b) HRTEM image, (c) the corresponding Fast Fourier Transform image, (d-f) EDS maps for as-prepared $\text{La}_{0.95}\text{Cu}_{0.05}\text{FeO}_{3-\delta}$ sample. (g)

XRD patterns for as-prepared sample, the spent samples reduced by methane for 7 min and 14 min, and the sample 1st re-oxidized in the step of by O₂-containing CO₂ splitting. (h) The XRD patterns with magnified regions to illustrate the appearance of metallic Cu. Fe 2p XPS patterns for (i) LaFeO₃ and (j) La_{0.95}Cu_{0.05}FeO₃ samples reduced/oxidized by different gases: as-prepared (label: Fresh), reduced by H₂ (label: H₂), re-oxidized by CO₂ (label: CO₂) and re-oxidized by O₂-containing CO₂ (label: CO₂ (O₂)). (k) Cu 2p XPS patterns for the La_{0.95}Cu_{0.05}FeO₃ sample. (l) Proposed structural evolution during cyclic redox with self-regeneration of metallic Cu, which assists improved efficiency for splitting O₂-containing CO₂.

5.1.5 Mechanistic investigation

In-situ XPS technique was used to characterize the evolution of elemental oxidation state during redox cycle. Note that the surface adsorbed oxygen took a great proportion (93%) of surface elements for fresh La_{0.95}Cu_{0.05}FeO_{3- δ} sample, larger than that of pure LaFeO₃ (**Fig 5.1.S8**). This likely accounts for the more active deep oxidation of methane to CO₂ at the initial time of POx step (**Fig 5.1.2(d) and 2(f)**). It is well known that the ratio of surface adsorbed oxygen to lattice oxygen is related to the concentration of oxygen vacancies²⁷². The O 1s XPS patterns (**Fig 5.1.S9**) demonstrated a higher value for such ratio (~0.75) in the fresh samples after 5% substitution of La sites, hence, indicating more oxygen defects in La_{0.95}Cu_{0.05}FeO_{3- δ} samples. After reduction by H₂, the XPS patterns (**Fig 5.1.3(i) and 3(j)**) identified the formation of metallic Fe⁰ on perovskite surfaces for both pure LaFeO₃ and La_{0.95}Cu_{0.05}FeO_{3- δ} , confirming the XRD patterns above. However, less proportion of surface Fe elements for La_{0.95}Cu_{0.05}FeO_{3- δ} (**Fig 5.1.S8**) may be helpful

to reduce the coke formation, because the metallic Fe^0 species is active for methane decomposition.

Shown in **Fig 5.1.3(k)**, the Cu 2 XPS patterns evidently illustrated the formation of metallic Cu^0 on the surface of reduced $\text{La}_{0.95}\text{Cu}_{0.05}\text{FeO}_{3-\delta}$ sample, and note that this Cu^0 signal can never be detected but only faint intensity of Cu^{2+} peaks after re-oxidation by the mixture. Quantitatively, the Cu element occupied a 4 at.% proportion of surface elements in the reduced sample, with respect to the imperceptible amount of Cu element on the perovskite surface upon re-oxidation (**Fig 5.1.S8**). The surface metallic Cu^0 verified the crystal peak in XRD pattern and indicated that the Cu species may migrate in and out of the perovskite lattice during reduction-oxidation cycles. Interestingly, this phenomenon (see the schematic in **Fig 5.1.3(l)**), so called self-regeneration property, have been previously observed in precious metal modified perovskites (*e.g.*, Pb-doped LaFeO_3)²⁸⁵⁻²⁸⁷. Compared to pure LaFeO_3 , the metallic Cu^0 on the surface of reduced sample should play an important role for enhancing the conversion of CO_2 into CO in the presence of O_2 , and even serve as a promoter for CO producing.

There are two possible reasons proposed for the high oxygen-tolerance. Firstly, Cu-substitution improves the oxygen mobility to replenish bulk vacancies, hindering undesired back reaction of produced CO with surface oxygen. In contrast, when the reduced pure LaFeO_3 is exposed to the atmosphere of O_2 -containing CO_2 , the perovskite surface is occupied with produced oxygen from O_2 owing to the relatively slow delivery rate of oxygen into bulk perovskite lattice, thus suppressing CO_2 conversion. The evidences of much higher CO peak in CO_2 -TPO and the oxygen desorption peak in O_2 -TPD over the $\text{La}_{0.95}\text{Cu}_{0.05}\text{FeO}_{3-\delta}$ confirmed its higher oxygen mobility than pure LaFeO_3 sample. On

the other hand, as shown in **Fig 5.1.3(g) and 3(h)**, the distinct Fe 2p peaks at ~ 710 eV highlighted the larger value of $\text{Fe}^{3+}/\text{Fe}^{2+}$ ratio in the oxidized $\text{La}_{0.95}\text{Cu}_{0.05}\text{FeO}_{3-\delta}$ sample. Thus, Cu substitution could improve the formation of oxygen vacancy, accelerating the mobility of lattice oxygen, which is consistent with the much higher rate of syngas productivity and other catalytic reductions by Cu doped Fe-based perovskites^{279, 282}.

Secondly, indicated by the XRD and XPS evidences of Cu exsolution, the metallic Cu^0 on the reduced sample may serve as a catalyst to promote CO_2 adsorption and splitting, with little influence on the kinetics of O_2 splitting after Cu is doped into LaFeO_3 perovskite. *In situ* Diffuse Reflectance Infrared Fourier Transform Spectroscopy (DRIFTS) was performed on the two reduced samples in pure CO_2 and air containing CO_2 , as shown **Fig 5.1.S10**. Much higher IR intensity for carbonate species (in the region of $1000\text{-}1800\text{ cm}^{-1}$) was detected over the reduced $\text{La}_{0.95}\text{Cu}_{0.05}\text{FeO}_{3-\delta}$ than the pure LaFeO_3 , and the amount of formed carbonate species was enhanced over the reduced $\text{La}_{0.95}\text{Cu}_{0.05}\text{FeO}_{3-\delta}$ samples when changing pure CO_2 to air containing CO_2 as feed gas. This indicated that the Cu species in the reduced LaFeO_3 system could strongly improve the adsorption ability of CO_2 especially in the presence of O_2 .

The mechanism for the enhanced performances was further explored through *ab initio* simulations, and we calculated the binding free energy and reaction barrier for CO_2 and O_2 splitting reaction on the (110) surface of reduced LaFeO_3 (with oxygen vacancies) in the presence/absence of Cu adatoms. As shown in **Fig 5.1.4**, the additional binding Cu^0 site exhibited significant increase by 191.2% in CO_2 binding energy ($E_{ad} = -0.99\text{ eV}$) as well as reduction by 52.5% in the barrier ($E_{ba} = 0.28\text{ eV}$) for C-O bond breaking in CO_2 splitting, compared with those ($E_{ad} = -0.34\text{ eV}$ and $E_{ba} = 0.59\text{ eV}$) on the only binding

site of Fe in pure LaFeO_3 . The most stable adsorption sites of CO_2 and O_2 on the reduced LaFeO_3 (110) surface with or without Cu adatom were shown in **Fig 5.1.S11**, respectively. These changes implied that the reaction of CO_2 splitting was accelerated in the presence of metallic Cu atom.

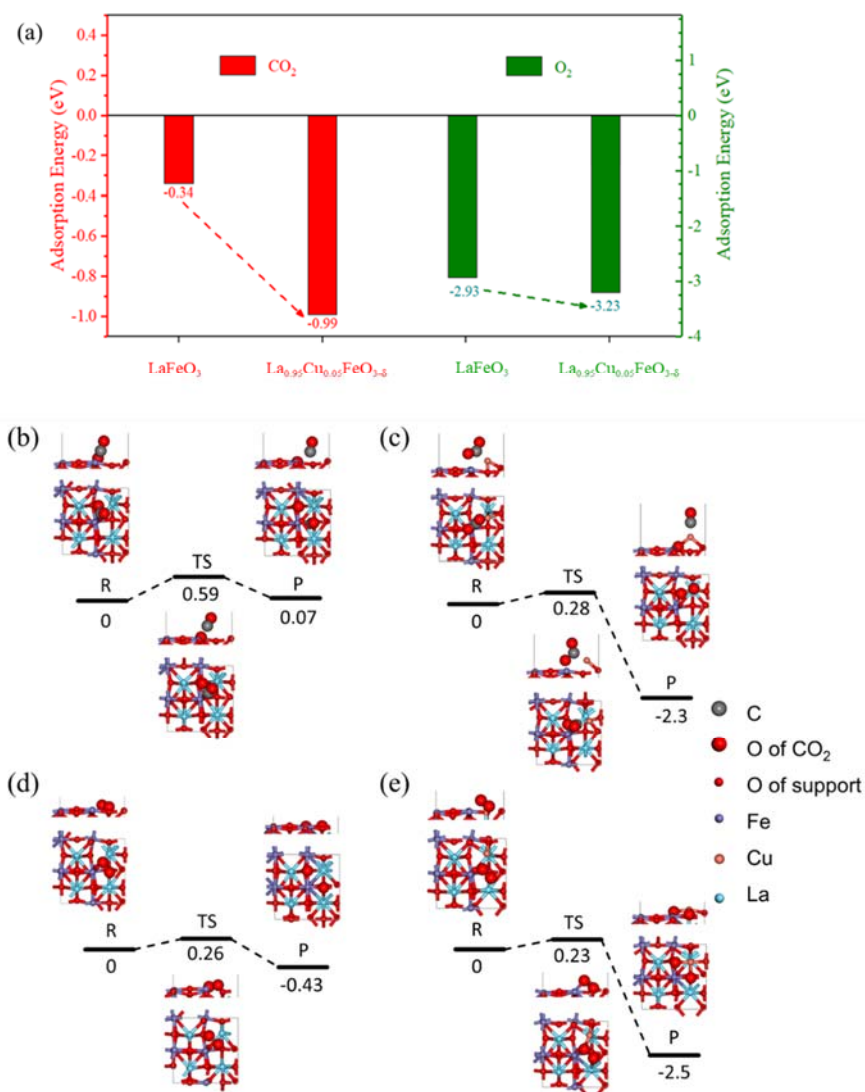


Figure 5.1.4 DFT simulation results. (a) Comparison of adsorption energies for CO_2 and O_2 on the (110) surfaces of reduced LaFeO_3 with and without Cu adatom; Reaction pathways of CO_2 splitting into oxygen atom and monoxide molecule on (b) the reduced LaFeO_3 (110) surface and (c) the reduced LaFeO_3 (110) surface with Cu adatom; Reaction

pathways of O₂ dissociation on (d) the reduced LaFeO₃ (110) surface (e) the reduced LaFeO₃ (110) surface with Cu adatom. The side and top views of atomic structures showing adsorption sites for each state are given. The unit in reaction pathway is eV.

On the other hand, the adsorption of O₂, as the oxidative competitor with CO₂, became weaker and the binding energy increased only by 10.2% (−2.93 eV to −3.23 eV) when the Cu atoms presented on the perovskite surface. The barrier of O₂ splitting was slightly lowered by 11.0% (0.26 eV to 0.23 eV) due to the unstraightforward pathway for the simultaneous diffusion of two generated oxygen atoms. Overall, the catalytical function of Cu atoms could enhance the competitiveness of CO₂ splitting to the O₂ splitting on the reduced LaFeO₃. Subsequently, higher CO₂ conversion and CO productivity are expected with the further assistance of subsequent fast diffusion of the produced oxygen to replenish vacancies as we discussed above. Therefore, both the substitution of Cu and exsolution of metallic Cu are verified to be responsible for mitigating the oxidative competition between CO₂ and O₂, and improving performances of CO₂ splitting even in the presence of O₂.

5.1.6 Redox stability

To demonstrate the redox durability of the La_{0.95}Cu_{0.05}FeO_{3-δ} sample, we continuously repeated the complete oxidation/reduction for 50 cycles, as shown in **Fig 5.1.5**. For the POx step, the syngas (H₂/CO≅1.87) yield maintained at 10.9 mol/kg with stable methane conversion of 71.0%. In the step of splitting O₂-containing CO₂, the high CO₂ conversion (86.5%) and CO productivity (2.2 kg/mol) were retained without apparent decay after 50 cycles (**Fig 5.1.S12 and S13**). We further confirmed the structural stability by XRD analysis (**Fig 5.1.S14**), demonstrating the identical XRD patterns for the as-prepared sample and the re-oxidized sample after 50 cycles, with only small portion of iron

oxides left. The excellent structural reversibility thus contributes to the long-term redox reactions and the stability of such performances.

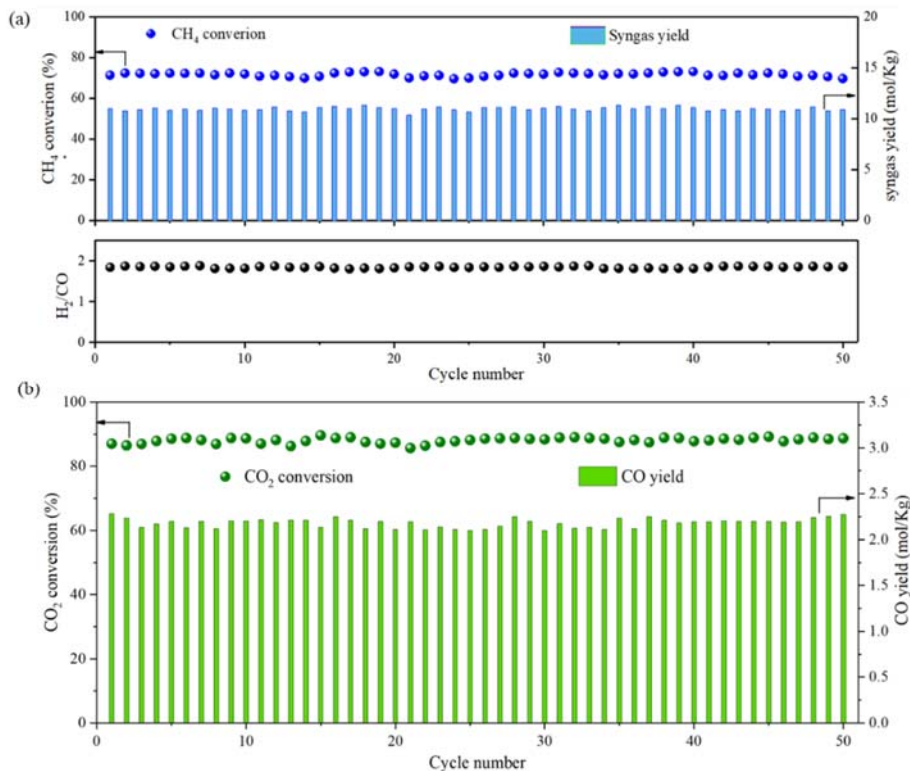


Figure 5.1.5. Redox stability of $\text{La}_{0.95}\text{Cu}_{0.05}\text{FeO}_3$ over 50 cycles. (a) Methane conversion, syngas yield and H_2/CO molar ratio in the step of methane POx. (b) CO_2 conversion and CO yield in the step of O_2 -containing CO_2 ($\text{CO}_2:\text{O}_2=5:1$) splitting.

5.1.7 Conclusion

We proposed a novel copper-containing perovskite as an effective oxygen carrier to efficiently split air-containing CO_2 into gaseous fuel CO in the cyclic redox scheme. A high CO yield (2.28 mol/kg) was achieved for converting the mixture of CO_2/O_2 (molar ratio 5:1). The CO productivity was even comparable to those for reported redox materials

(SrFeO₃-CaO, CeO₂/Fe₂O₃, LaSrFeAlO₃, etc) at 980°C and the cases for reducing pure O₂ (**Table S1**). Meanwhile, exceptionally high syngas productivity (11.0 mol/kg) makes the Cu-containing perovskite highly attractive, and this yield was two times higher than other cyclic redox schemes. At relatively lower 850°C, such activities were stably maintained during the 50 cycles. The exsolution and self-regeneration of metallic Cu on the perovskite surface was experimentally and theoretically elucidated to be responsible for highly efficient CO₂ splitting even in the presence of O₂.

The present study is perhaps the first to efficiently splitting air-containing CO₂ into CO. The proposed La_{0.95}Cu_{0.05}FeO_{3-δ}-based redox scheme can take advantage of the extreme low-cost CO₂/air mixture obtained from upstream HSDAC setups, and it may also work well directly with flue gas (*e.g.* PCC) in some other scenarios. To highlight the cost-efficiency and environmental compatibility of directly utilizing the impure CO₂, we investigated synthesis of methanol (CH₃OH)²⁸⁸ and acetic acid (CH₃COOH)²⁸⁹ using the upstream yield of syngas and CO from three main models (**Fig 5.1.S15**): 1) state-of-art route of coal gasification (CG model) followed by excess purification/separation processes²⁹⁰; 2) 100% CO₂ stream from HSDAC is fed into the La_{0.95}Cu_{0.05}FeO_{3-δ} chemical looping scheme (CL model) ; 3) 50% air-containing CO₂ stream from HSDAC employed as the carbon feedstock for the same CL scheme. For CL model with 50% CO₂/air mixture, both methanol and acetic acid are valuable products since the ratio of syngas/CO is not one, while acetic acid is the only product for both CG model and CL model with 100% CO₂.

Using ASPEN PlusTM, we calculated the overall energy and net carbon emission using those three models (**Fig 5.1.6**). The CL model using 50% CO₂ mixture required 11.0

GJ thermal energy to produce one metric ton of products (methanol and acetic acid), while 33.7 GJ and 17.0 GJ was needed for CG model and CL model using pure CO₂, respectively. Process simulations indicate that the net CO₂ emission by using 50% CO₂ mixture can be mitigated by 94.5% and 42.8%, when compared with the state-of-art route and CL model using 100% CO₂ respectively. Apart from costly purification setups, the energy demand of vacuum/concentration operations for achieving 100% CO₂ by HSDAC or PCC is significantly higher than that for 50% CO₂ capture by HSDAC^{261, 265}. Therefore, considering the whole synthetic carbon cycle (**Fig 5.1.1**), the integration of upstream HSDAC and as-designed downstream CL reactor could even save more energy and yield less emission, making it one of the most economic, efficient, scalable and promising negative emission pathways.

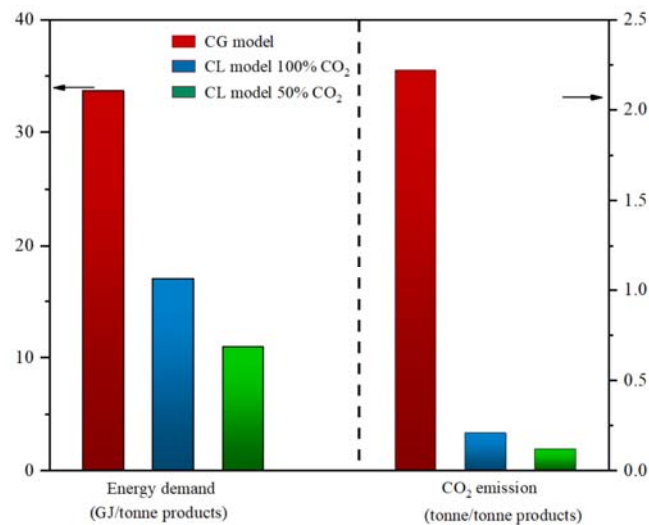


Figure 5.1.6. ASPEN simulation results. Comparison of (a) energy demand and (b) CO₂ emission for generating one metric ton of methanol and acetic acid as valuable products among three main models: the state-of-art coal gasification model, the chemical looping model using 50% CO₂ mixture and using 100% CO₂.

5.1.8 Appendix

1) Definitions of yield, conversion and yield

Methane conversion and syngas yield for the methane partial oxidation (POx) step and CO₂ conversion and CO yield for the CO₂ splitting step were evaluated as follow.

- In the POx step:

$$CH_4 \text{ conversion} = \frac{(CH_4 \text{ moles})_{in} - (CH_4 \text{ moles})_{out}}{(CH_4 \text{ moles})_{in}} * 100\%$$

$$\text{Syngas yield} = \frac{CO \text{ moles} + H_2 \text{ moles}}{\text{Catalyst mass}}$$

- In the CO₂-splitting step:

$$CO_2 \text{ conversion} = \frac{(CO_2 \text{ moles})_{in} - (CO_2 \text{ moles})_{out}}{(CO_2 \text{ moles})_{in}} * 100\%$$

$$CO \text{ yield} = \frac{\text{produced CO moles}}{\text{Catalyst mass}}$$

2) *Ab initio* calculations

The orthorhombic perovskite structure of LaFeO₃ crystal (*Pnma* (62)) was modelled in our *ab initio* calculations. By cleaving the bulk LaFeO₃, FeO-terminated and LaO-terminated LaFeO₃ (110) surfaces was formed. Because of the multivalent character of the Fe atom, oxygen reduction occurs more easily on the FeO termination than the LaO termination. Thus, we focused on the adsorption of CO₂ and O₂ on the FeO-terminated

surface. The model of the reduced LaFeO₃ (110) surface was created by removing two adjacent oxygen atoms at the FeO-terminated (110) surface layer of the LaFeO₃ crystal. The most energetically favorable adsorption site of Cu adatom on the reduced LaFeO₃ (110) surface is shown in Figure S11(b). That is, Cu adatom is located between the two oxygen vacancies. The most stable adsorption sites of CO₂ and O₂ on the reduced LaFeO₃ (110) surface with or without Cu adatom are shown in Figure S11(a) and S11(b), respectively.

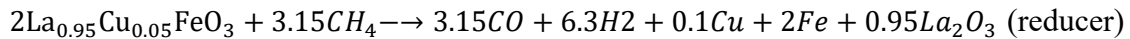
3) ASPEN Plus simulations

3.1) Modeling:

The three main routes for synthesizing acetic acid and methanol are summarized in Figure S14. For each route, three sections of syngas production, methanol synthesis and acetic acid reactor are included. We adopt a commercial process [1] with Cu/Zn/Al₂O₃ catalyst to synthesizing methanol from mixture of syngas and CO₂, and an RStoic model in ASPEN Plus is used. The synthesis of acetic acid using methanol and CO is conducted using the CativaTM process [2], and a two-reactor scheme via an iridium-containing complex and hydrogen iodide are adopted here to modeling the process. The partial pressure of CO as feedstock in acetic synthesis is 22 bar. More details of modeling can refer to our previous work [3].

- CG model: The traditional coal gasifier (CG) process, model by an adiabatic RGibbs reactor operating at 30 bar, is used to obtain syngas. The water gas shift (WGS) reaction and subsequent CO₂ separation are adopted to keep the composition of CO: CO₂: H₂=24:6:70, desirable for the synthesis of methanol. An additional gasification of coal followed by the CO₂ and H₂ separation provides the CO required for acetic acid reaction. The final product is acetic acid.

- CL model: The chemical looping (CL) scheme is used to generate syngas, and the redox catalyst is $\text{La}_{0.95}\text{Cu}_{0.05}\text{FeO}_3$. Oxygen carriers of La_2O_3 , Fe_2O_3 , CuO are used in ASPEN Plus to approximate the real catalyst. For consistency with experimental data, La_2O_3 is assumed to be inert during the reduction/oxidation steps. Fe_2O_3 and CuO get reduced to Fe and Cu , respectively. For the CL using 100% CO_2 , the two-step reactions are:



Both the reducer and oxidizer are operated at 850°C and ambient pressure, with 71.4% methane conversion and 87% CO_2 conversion in the separated reactors. Note that in the CO_2 splitter for treating 50% CO_2 /air mixture, the CO_2 conversion is 89% and the reduced oxygen carriers are assumed to be oxidized by the O_2 firstly. RStoic reactor models are adopted, and no other byproducts is assumedly to be produced. The produced syngas and CO are fed into the reactors of methanol and subsequent acetic acid synthesis. The final products for the route using 100% CO_2 are acetic acid, while both acetic acid and methanol are the valuable products for the route treating 50% CO_2 /air mixture. The net reaction for those two CL based routes are:



3.2) Process analysis

- Energy demand: Based on the Aspen Plus model, total energy requirement (thermal basis) for the processes is obtained. The electrical-to-thermal conversion is assumed

with 40% efficiency, and all the energy demands are normalized per tonne of the products (acetic acid or acetic acid/methanol)

- CO₂ emission: The CO₂ footprint considers the contributions from upstream CH₄/coal processing, facility to meet energy demand, and CO₂ used in the feedstock of CL model is credited in the overall process. CO₂ emissions due to methane and coal upstream processing is assumed to be 9.1 g CO₂/MJ and 10 g CO₂/MJ [3], respectively. The thermal requirements are met by burning the corresponding amount of methane with 100% combustion efficiency.

4) Supplementary Tables and Figures

Table 5.1.S1 Comparison of redox performances over different oxygen carriers.

Material	Process	Reduction		Oxidation		Refs.
		Tr (°C)	Syngas yield (mol kg ⁻¹)	To (°C)	CO yield (mol kg ⁻¹)	
LaFeO ₃	MPO-CDS (with O ₂)	850	5.15	850	0.414	This work
La _{0.95} Cu _{0.05} FeO _{3-δ}	MPO-CDS (with O ₂)	850	11.0	850	2.28	This work
Sr ₃ Fe ₂ O _{7-δ} -Ca _{0.5} Mn _{0.5} O	MPO-CDS	900	4.42	900	1.74	[3]
3% Ce Mn ₃ O ₄	MPO-CDS	900	4.34	900	1.3	[4]
Ni/CeO ₂ -Fe ₂ O ₃	MC-CDS	700	--	700	1.6	[5]
Ni _{0.3} WO _x /Al ₂ O ₃	MPO	800	2.1	--	--	[6]
La _{0.8} Sr _{0.2} FeO _{3-δ}	MPO	900	15.7	--	--	[7]
Ce _{0.75} Zr _{0.25} O ₂	CDS	--	--	1000	0.093	[8]
La _{0.5} Ca _{0.5} MnO ₃	CDS	--	--	1100	0.525	[9]
LaFe _{0.5} Co _{0.5} O ₃ /SiO ₂	CDS	--	--	1100	0.28	[10]

- T_R: reduction temperature; T_O: oxidation temperature; MPO: methane partial oxidation; MC: methane combustion; CDS: carbon dioxide splitting.

Table 5.1.S1 summarizes the performances of $\text{La}_{0.95}\text{Cu}_{0.05}\text{FeO}_{3-\delta}$ and other reported oxygen carriers for syngas generation from methane partial oxidation and/or CO production from CO_2 splitting. Among the materials, $\text{La}_{0.95}\text{Cu}_{0.05}\text{FeO}_{3-\delta}$ in this work shows a lower reduction and oxidation reaction temperature and exhibits higher yields of syngas and CO.

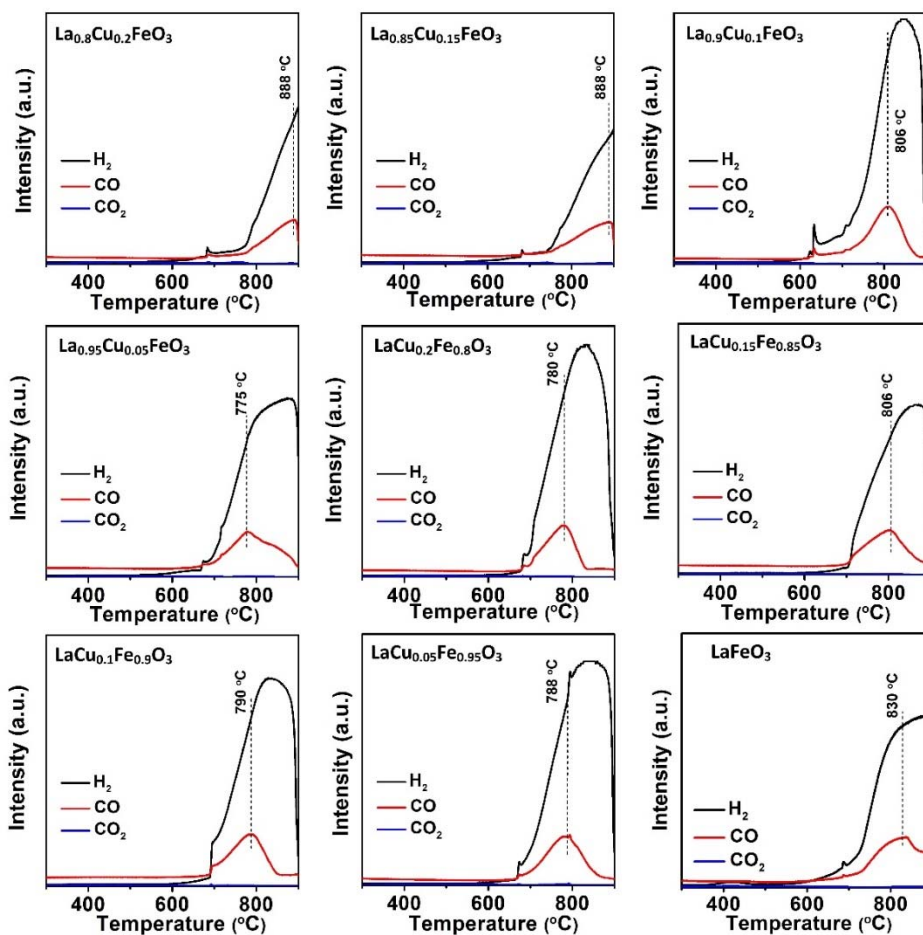


Figure 5.1.S1. Methane temperature-programmed reduction (CH_4 -TPR) for the samples ($\text{La}_{1-x}\text{Cu}_x\text{FeO}_{3-\delta}$ and $\text{LaCu}_x\text{Fe}_{1-x}\text{O}_{3-\delta}$ ($x = 0.05, 0.1, 0.15, 0.2$)). It can be seen that CO and H_2 are the major products, and little amount of CO_2 are detected. The CO over $\text{La}_{0.95}\text{Cu}_{0.05}\text{FeO}_{3-\delta}$ reached to the highest intensity for CO formation at 775 °C which is the lowest temperature among all the samples. After that, the amount of CO began to decrease, while the H_2 production continued to increase due to the occurrence of methane decomposition.

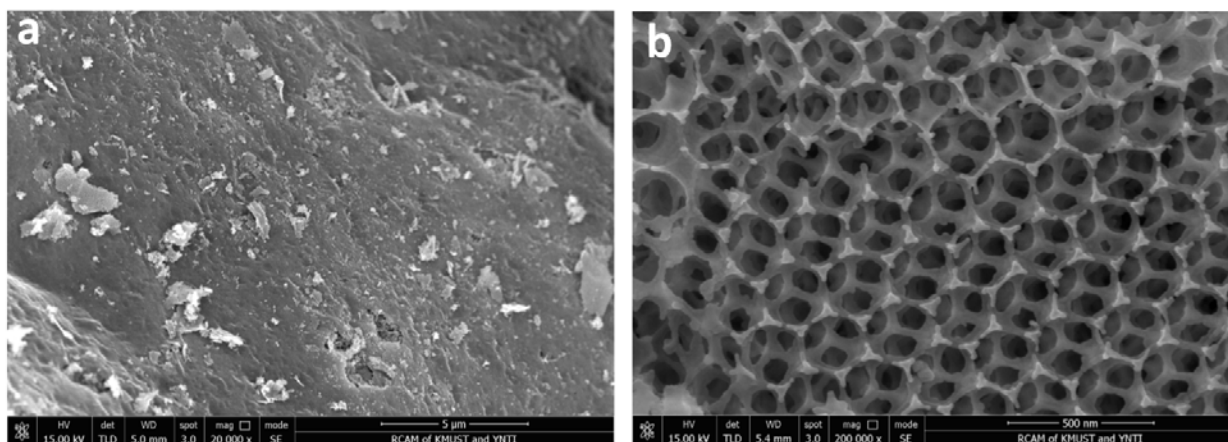


Figure 5.1.S4. SEM images of the (a) conventional and (b) macroporous $\text{La}_{0.95}\text{Cu}_{0.05}\text{FeO}_{3-\delta}$ samples.

The macroporous $\text{La}_{0.95}\text{Cu}_{0.05}\text{FeO}_3$ exhibited a well-defined three-dimensional periodic framework with the pore diameter of 100 ± 10 nm.

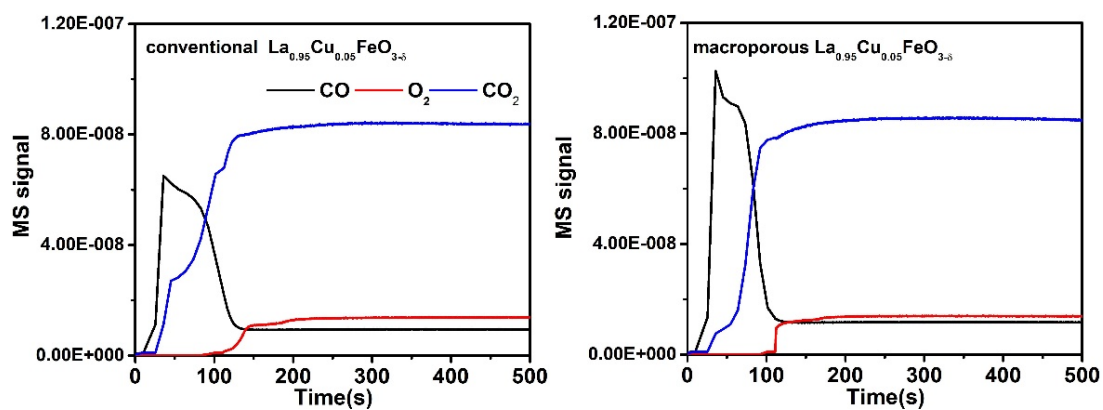


Figure 5.1.S5. The oxidation of reduced conventional and macroporous $\text{La}_{0.95}\text{Cu}_{0.05}\text{FeO}_{3-\delta}$ samples by the O_2 -containing CO_2 .

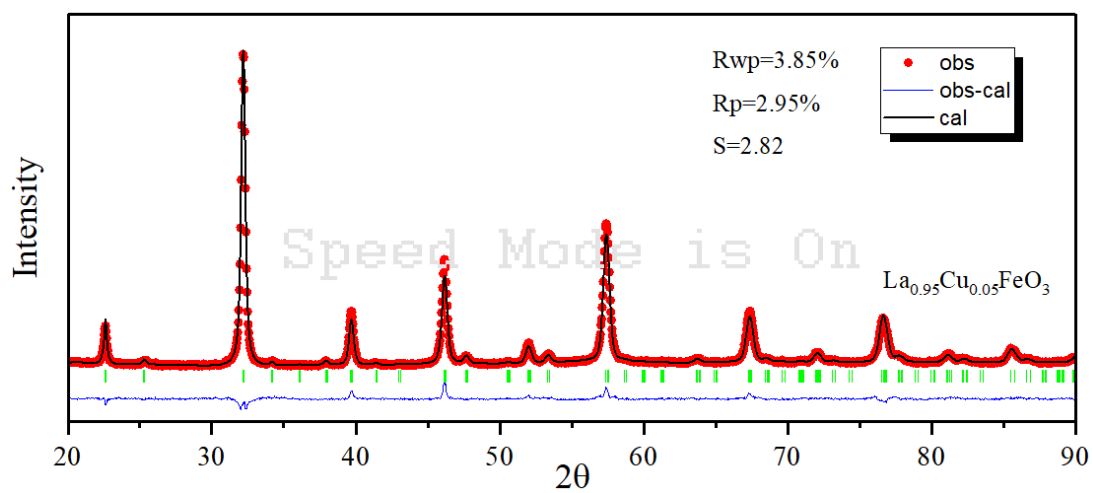
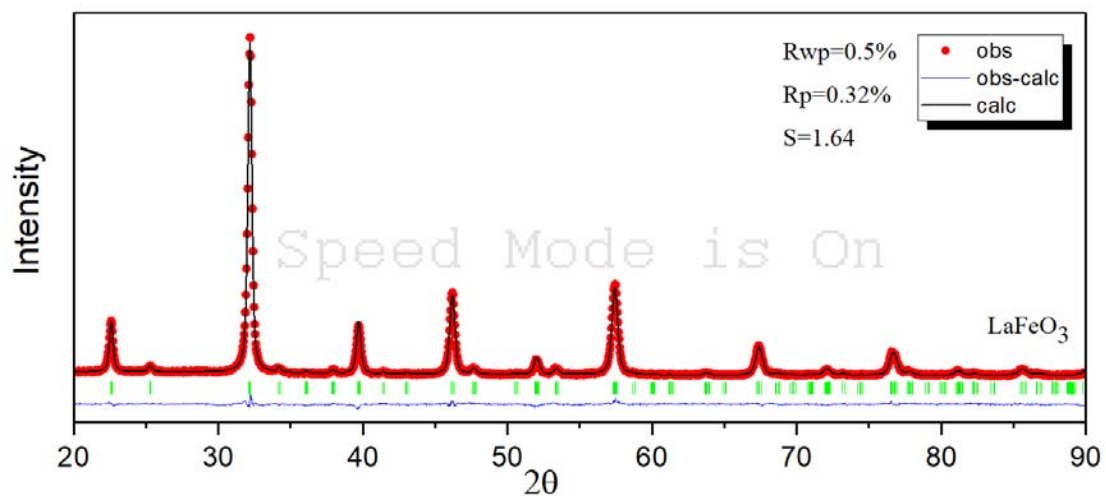


Figure 5.1.S6. XRD and Rietveld results for fresh LaFeO₃ and La_{0.95}Cu_{0.05}FeO_{3-δ}.

Table 5.1.S2. Average crystal parameters of LaFeO₃.

Cell of LaFeO ₃				
a (Å)	b (Å)	c (Å)		
5.565174	5.551856	7.843398		
Atomic occupancy in cell				
elements	fraction	x	y	z
O ⁻²	1	0.750485	0.303234	0.02201
Fe ⁺³	1	0	0.5	0
O ⁻²	1	0.088753	0.492357	0.25
La ⁺³	1	1.000264	0.024019	0.25

Table 5.1.S3. Average crystal parameters of La_{0.95}Cu_{0.05}FeO_{3-δ}.

Cell of La _{0.95} Cu _{0.05} FeO _{3-δ}				
a (Å)	b (Å)	c (Å)		
5.559667	5.559667	7.849131		
Atomic occupancy in cell				
elements	fraction	x	y	z
O ⁻²	1	0.738	0.296	0.0552
Fe ⁺³	1	0	0.5	0
O ⁻²	1	0.47418	0.49034	0.25
La ⁺³	0.8998	0.996	0.024	0.25
Cu	0.0478	1	0.02	0.25

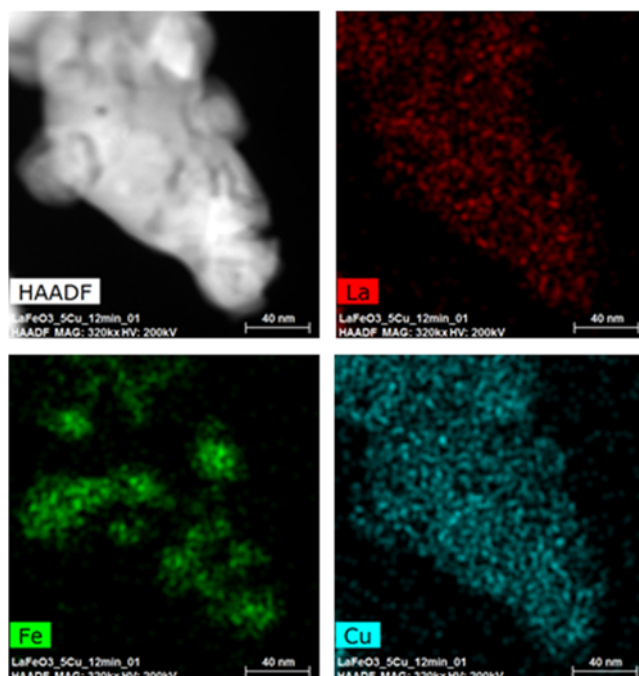


Figure 5.1.S7. STEM and EDS mapping images of deeply reduced $\text{La}_{0.95}\text{Cu}_{0.05}\text{FeO}_{3-\delta}$ sample.

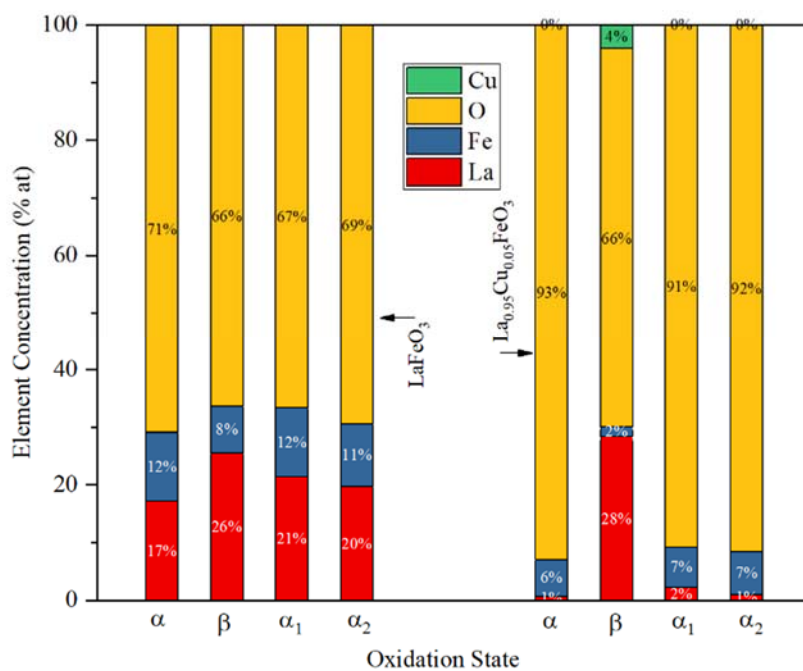


Figure 5.1.S8. Surface elemental composition (XPS data) of LaFeO_3 and $\text{La}_{0.95}\text{Cu}_{0.05}\text{FeO}_{3-\delta}$ samples under different oxidation states: as-prepared (label: α), reduced by H_2 (label: β), re-oxidized by CO_2 (label: α_1) and re-oxidized by O_2 -containing CO_2 (label: α_2).

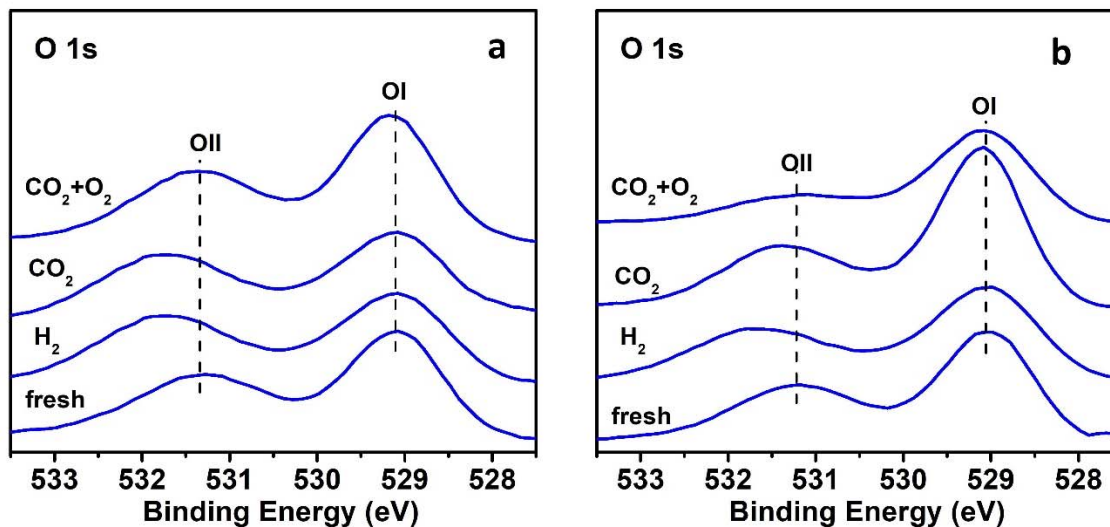


Figure 5.1.S9. O 1s XPS patterns for fresh, reduced, re-oxidized (by pure CO₂ or O₂-containing CO₂) (a) LaFeO₃ and (b) La_{0.95}Cu_{0.05}FeO_{3-δ} samples: as-prepared (label: fresh), reduced by H₂ (label: H₂), re-oxidized by CO₂ (label: CO₂) and re-oxidized by O₂-containing CO₂ (label: CO₂(O₂)). Two oxygen peaks were observed at 531.4 eV (labelled as OII) and 529.1 eV (labelled as OI), which can be ascribed to surface adsorbed oxygen (O_{ads}) and lattice oxygen (O_{latt}), respectively. It should note that the O_{ads}/O_{latt} (OII/OI) molar ratios over La_{0.95}Cu_{0.05}FeO₃ is much higher than that over LaFeO₃, indicating that the introduction of Cu into the LaFeO₃ lattice could enhance the formation of oxygen defects.

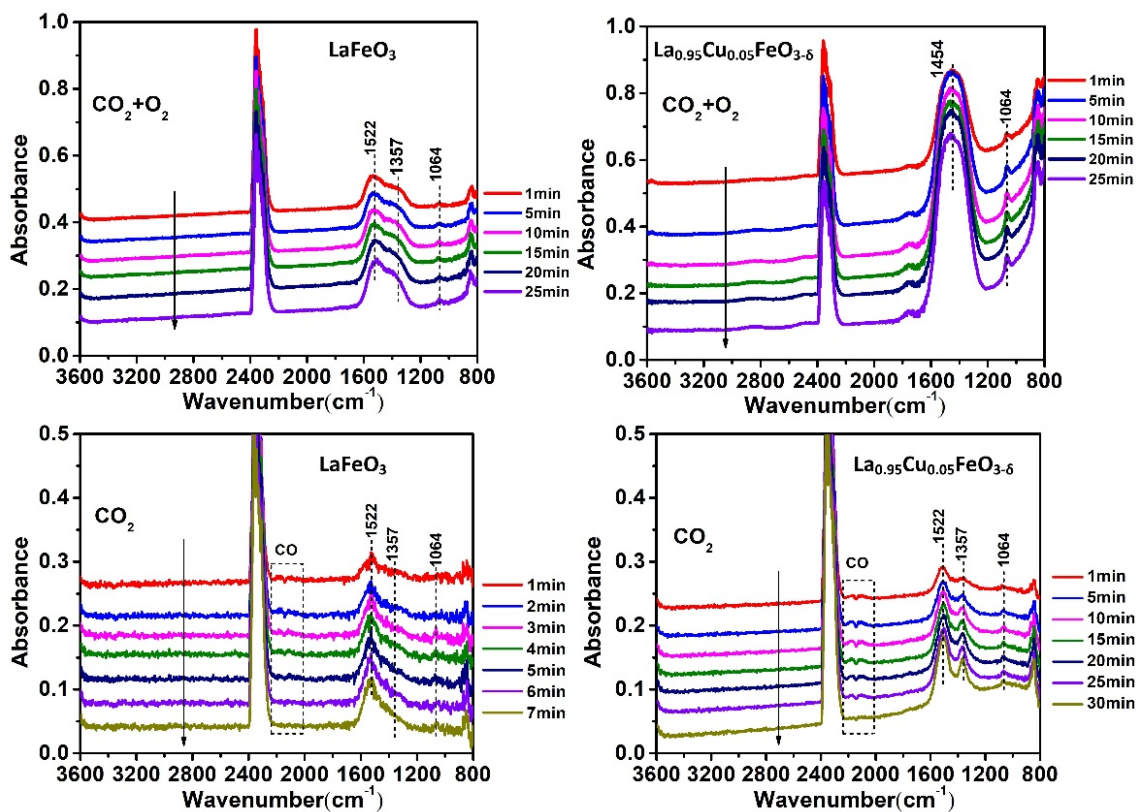


Figure 5.1.S10. *In situ* DRIFTS spectra collected during re-oxidation by CO₂ and O₂-containing CO₂ over the reduced LaFeO₃ and La_{0.95}Cu_{0.05}FeO_{3-δ}. In the environment of CO₂/O₂ mixture gas, more carbonate species (in the region of 1000-1800 cm⁻¹) [11] due to the adsorption of CO₂ were detected over the reduced La_{0.95}Cu_{0.05}FeO_{3-δ} than LaFeO₃. The intensity of carbonate species increases with time over both the two samples. In the CO₂ gas, CO peaks (located at 2000-2200 cm⁻¹) can be detected. The CO peaks disappeared after 7 min over the reduced LaFeO₃, while they are detectable for 30 min over the reduced La_{0.95}Cu_{0.05}FeO_{3-δ}. It is very interesting that bidentate carbonate (at ~1522 and 1357 cm⁻¹) was detected on the reduced LaFeO₃ in O₂-containing CO₂, while it is monodentate carbonate (at ~1454 cm⁻¹) on the reduced La_{0.95}Cu_{0.05}FeO_{3-δ} which is usually generated by the adsorbed CO [11,12]. These phenomena indicate that more CO is produced on the reduced La_{0.95}Cu_{0.05}FeO_{3-δ} owing to the splitting of CO₂.

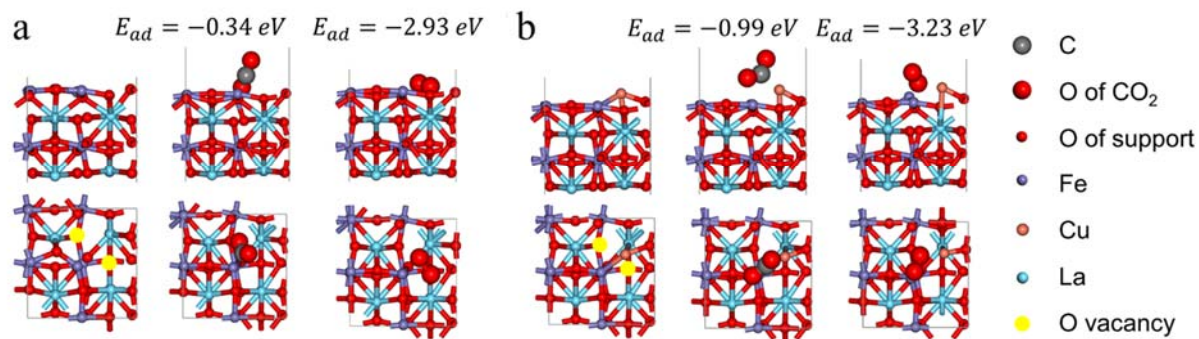


Figure 51.S11. (a) Side views and top views of the reduced LaFeO₃(110) surface (left) and its CO₂ (middle) and O₂ (right) adsorption configurations. (b) Side views and top views of the Cu atom supported by reduced LaFeO₃(110) surface (left) and its CO₂ (middle) and O₂ (right) adsorption configurations.

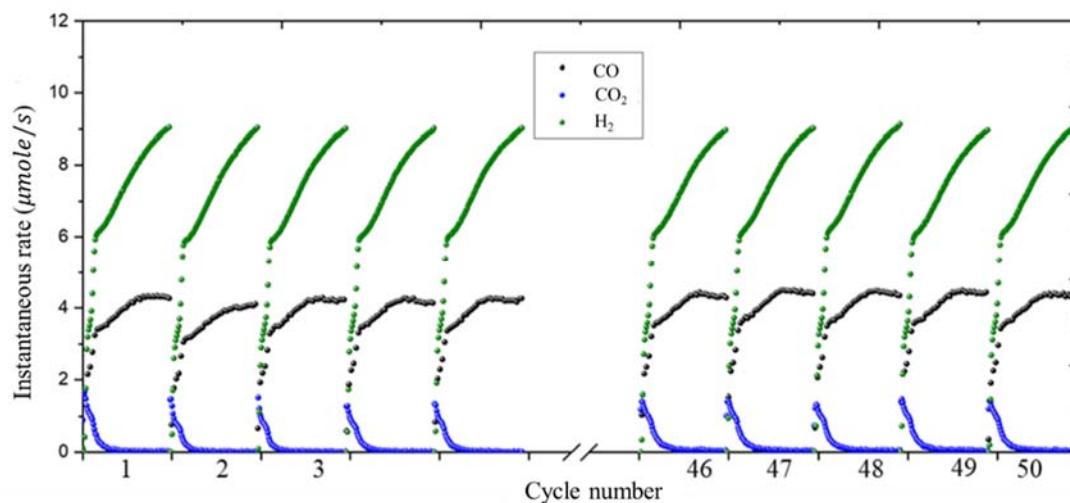


Figure 5.1.S12. The cyclic elution profiles for La_{0.95}Cu_{0.05}FeO_{3- δ} in the POx step over 50 cycles.

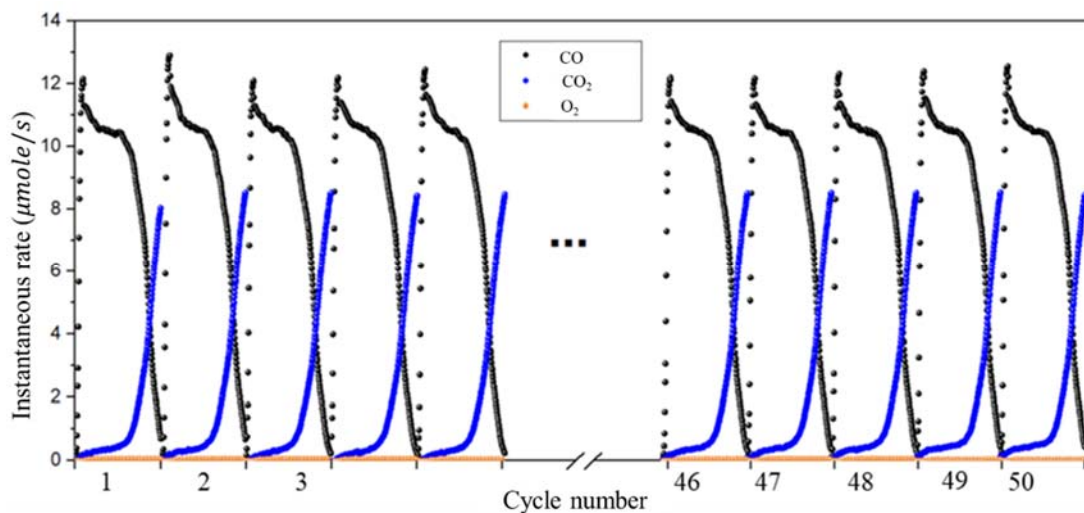


Figure 5.1.S13. The cyclic elution profiles for $\text{La}_{0.95}\text{Cu}_{0.05}\text{FeO}_{3-\delta}$ in the step of O_2 -containing CO_2 (CO_2 : $\text{O}_2 = 5:1$) splitting over 50 cycles.

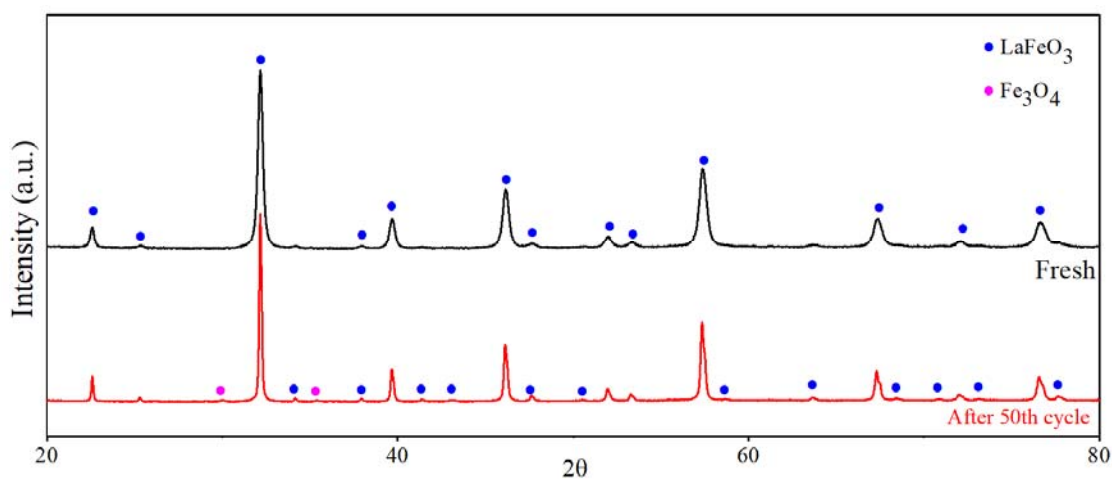


Figure 5.1.S14. The XRD patterns for the as-prepared and the re-oxidized $\text{La}_{0.95}\text{Cu}_{0.05}\text{FeO}_{3-\delta}$ sample after 50 cycles.

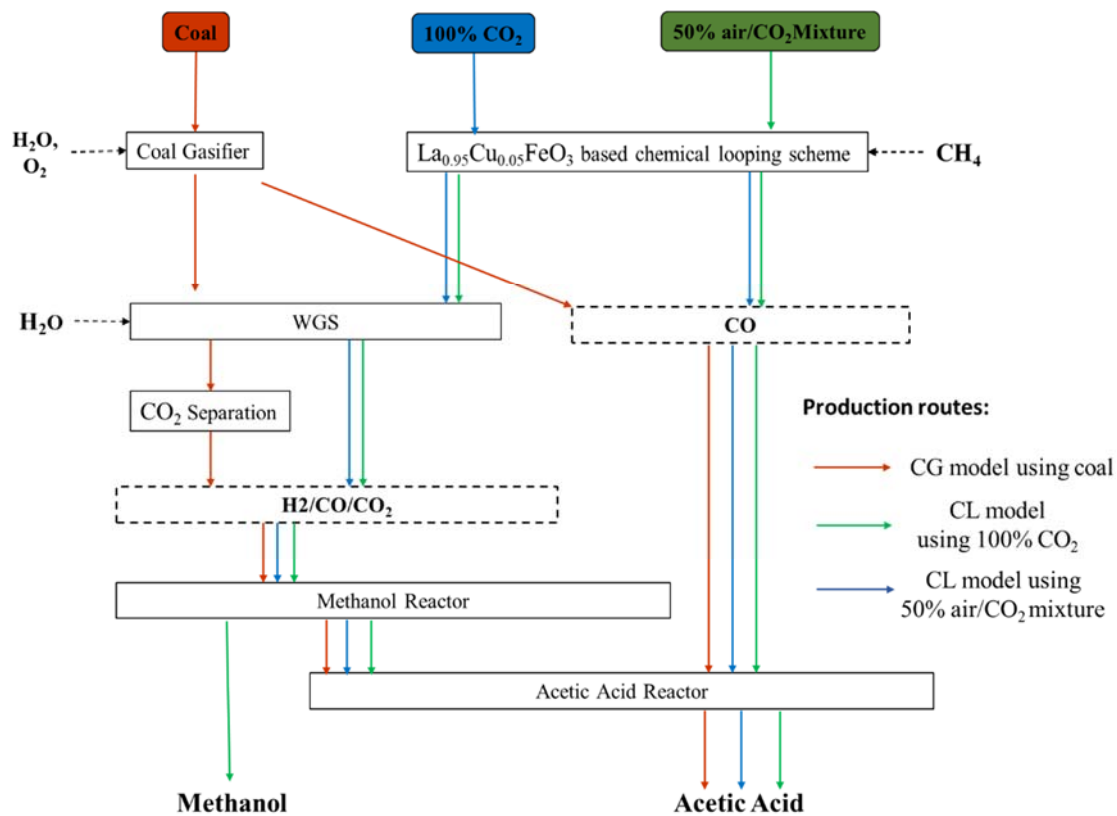


Figure 5.1.S15. Diagram of routes for synthesizing methanol and acetic acid using CG and CL models.

5.2 High-Energy-Density Foldable Battery Enabled by Zigzag-like Design

5.2.1 Introduction

Wearable electronics have attracted increasing attention in the applications of health care²⁹¹⁻²⁹⁴ and sensing devices.²⁹⁵⁻²⁹⁸ Despite the upcoming success of commercialization of flexible displays and epidermal electronics,²⁹³ the lack of deformable power sources represents a serious bottleneck for the deployment of wearable electronics. Since the energy-storage systems (i.e. batteries) must be conformal to complex deformations of flexible electronics, their capabilities of flexibility have been a focal point of research. In recent years, considerable efforts have been made to improve the deformability of lithium ion batteries (LIBs),^{291, 294, 299, 300} the current mainstream of power source. Various efforts have been devoted to enhance the flexibility of electrodes of LIBs, such as making them slim³⁰¹, incorporate carbon-based³⁰² and polymer-based conductive materials, etc.³⁰³ Additionally, new electrode architectures such as sponge,³⁰⁴ textile^{305, 306} and wire-like shapes^{307, 308} have been fabricated, showing both improved electrochemical performance and mechanical robustness.

Besides the advance of battery components, new schemes of system-level integration of LIBs with deformability were proposed, which are perhaps more compatible with standard manufacturing process and cost-effective. By decoupling the energy storage and deformable parts, highly deformable LIBs have been fabricated.^{235, 299, 309} Stretchable and bendable LIBs were assembled through a segment design of electrode disks connected by a self-similar soft serpentine structure,³¹⁰ aided by origami patterned electrodes.³¹¹ Nevertheless, due to the excessive use of the deformable segment, the mass loading of active materials was low and the cost for assembly was high. Although our previous spine-

like design achieved simultaneously both flexibility and high energy density with 86.1% of a standard pouch cell, however, the system was unable to accommodate escalating deformation, such as folding, while maintaining high energy density, since the design must sacrifice active materials and give room to more deformable parts in order to undergo larger deformation.²³⁵ During fabrication, the complex cutting of comb-like pattern not only causes incomplete utilization of electrode sheets, but also increases the cost. A drastically new system design is urgently needed, which may simultaneously incorporate high energy density and tolerance to extreme deformation (such as foldability), hence calling the need for more efficient coupling between energy storage and deformable parts, as well as simplifying the fabrication process and being more cost-effective for scale-up industrial production of flexible LIBs.

Herein, inspired by origami folding, we design a facile approach to fabricate novel flexible Li-ion batteries with superior foldability and high energy density. As shown in **Fig 5.2.1**, the conventional graphite anode/separator/ lithium cobalt oxide (LCO) cathode stack maintains its integrity and being simply folded into strip-like origami segments, connected by division segments (3 mm in length, green in **Fig 5.2.1**) which serve as future folding joints. To protect these “weak points” that may undergo excessive deformation and fatigue in practice, protective thin tape is adopted to cover metal foils in these division joints (and on both sides). The tape is only applied to joint area, which only occupies less than 4% of the area, so its sacrifice little energy density (e.g. <0.5%). Note that within a stack, the spacing between division joints may be varied, which affects energy density and foldability and is discussed later. The main energy storage is borne by the alternatively self-folded and self-wrapped origami strips, which are much thicker and rigid compare to the division

joints. Such an assembly strategy not only allows superior foldability (thanks to the flexible and tough division joints) and attains high energy density (since the gap between two thick segments may approach zero when folded), but also the fabrication process is simple and easy to scale up, since the integrity of the entire stack is well maintained.

The cell thus fabricated with energy density of 275 Wh L^{-1} can reach 96.4% of the conventional stacking cell using the same parameters. The zigzag-like structural design could accommodate up to 180° folding between the two rigid origami units, although a small gap between the thick stacking segments is needed in practice (to accommodate packaging and provide extra tolerance to large deformation, and such a gap is typically $\sim 1.0\text{mm}$). The cell also performs well under cyclic charging and fatigue cycles: after over 100 cycles of charge/discharge at 0.5 C, 96% battery capacity is remained even under alternative bending deformations. After 45,000 cycles of continuously dynamic folding loads, the discharge capacity of 124.2 mAh g^{-1} is survived at 1 C ($1 \text{ C} = 145 \text{ mAh g}^{-1}$). Furthermore, no smoke or fire is observed when the cell is shorted by a stainless steel nail. Therefore, this novel zigzag-like battery structure and its facile fabrication may attract great promise for practical applications in flexible battery with superior foldability.

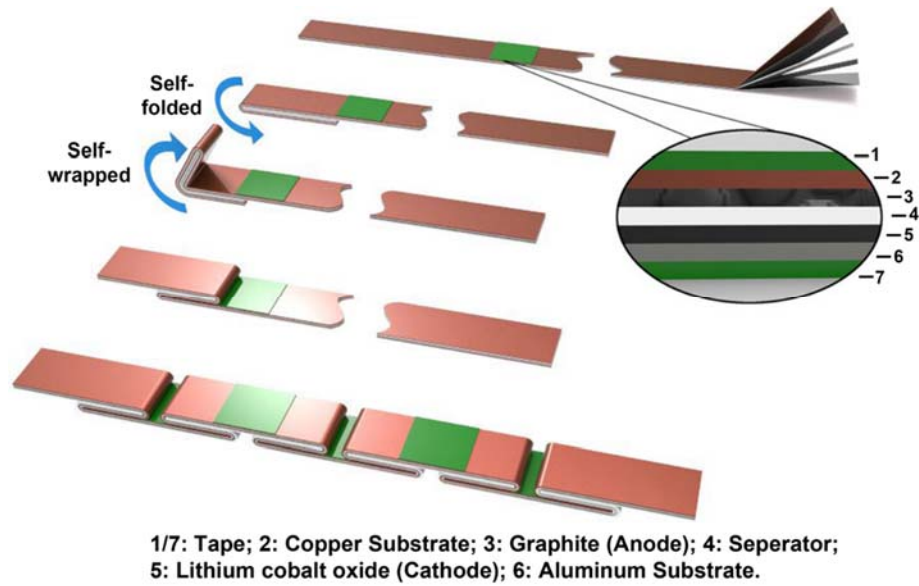


Figure 5.2.1 Fabrication process of the zigzag-like foldable battery.

5.2.2 Model and Method

Mechanical Simulation: We simulated the deformation of zigzag-like battery using 2D nonlinear finite element method, implemented in the commercial software ABAQUS⁶⁷. In all cases, four-node quadrilateral stress/displacement elements with reduced integration were used. The energy storage units were considered as rigid parts and the sheet of folding joints is the stack of tape/anode/tape/double separators/tape/aluminum foil/tape. For simplicity, linear isotropic elasticity was adopted for the battery structure with effective modulus and Poisson ratio based on experimental parameters. The length and thickness of joints layer are 6 mm and 132 μm , respectively. For each layer in terms of thickness, tape is 32 μm . Cu foil: 18 μm ; Al foil: 24 μm , and separator is 25 μm . The pressure of 1 atm is applied to both sides of deformable layers to simulate the vacuum conditions inside the aluminized pouch bag. The originally flat origami-inspired structure was subjected to angle displacement load for realizing folding configuration.

Battery Fabrication: Commercial LiCoO₂ and graphite electrodes (Custom Electronics Inc.) were used as cathode and anode respectively. Then the electrodes and separators (Celgard 2500) were cut into required size. Protective tap was used to enhance the ability of large folding. After that, the aluminized polyethylene (Sigma-Aldrich) package was used to pack the battery and then transferred into the argon-filled glovebox (O₂ < 0.1 ppm, H₂O < 0.1 ppm) to drop ethylene carbonate/diethyl carbonate (1:1 vol/vol) (Gotion Corp.) electrolyte. After resting for 6 h, the aluminized polyethylene package was vacuum sealed using a high temperature sealer. The total length and width of the cell were 61.1 mm and 1.5 mm, respectively and each unit was 7 mm long.

Electrochemical Tests: The foldable LCO/Graphite batteries were firstly charged to 4.2 V and held at 4.2 V until the current density decreased to 0.05 C to ensure the batteries could be fully charged. The cut off voltage of discharge was 3.0 V. The batteries were tested using the battery analyzers of Landt Instruments (Model: CT 2001) and Biologic Potentiostat (Model: VMP3).

5.2.3 Structure-Mechanical Property Relation

Optimization of structural design in such zigzag-like battery is required to realize excellent flexibility while maintaining electrochemical performances in practice. With the present asymmetric zigzag-like structure, the best folding deformation should follow that in Scheme A in **Fig 5.2.2(a)**, where the two adjacent joints are bent in opposite directions. The uni-directional bending (Scheme B) is also acceptable although the overall folding angle is limited at one joint. Scheme C, however, should be avoided in practice since it may cause deleterious stretch in the joints and contact stress between two thick stacking segments.

To show the mechanical foldability and durability of the cell, finite-element calculations are carried out to evaluate the deformation at folding joints. The result in **Fig 5.2.2(b)** shows that the zigzag-like structure with zero gap can be folded by 180° (by following Scheme A) and become self-compacted, and the smallest bending diameter d_0 at folding joints is $0.3 L$. Here, L is the length of the thick stack (1 cm for the fabricated battery), and h is its thickness. **Fig 5.2.2(c)** shows the strain contours of multilayer stack at joints with and without protective tapes under 180° folding deformation. Since large shear deformation is borne by the soft components (tapes and separators), the maximum strain in metal foil (e.g. aluminum) is only 0.5% with the presence of protective tape, much smaller than that (5.5%) for the naked joint. Therefore, the adhesive tape covering both sides of the folding joints is capable for enhancing the mechanical durability of flexible battery upon continuous folding.

In case some battery joints are bent in an undesired direction, e.g. unidirectional bending in Scheme B, a necessary gap length (δ_0) of the joint is needed to tolerate excessive deformation and contact between stacking units (whose thickness is h), but unavoidable of sacrificing its energy density. The balance between acceptable bending radius (beyond which excessive stretch can damage joints) and relative energy density is sought after in **Fig 5.2.2(c)**. When $\delta_0/h = 0.5$, the minimum dimensionless bending radius for Scheme B is $R_{min}/L = 1.7$ with uniform bending imposed at each joint, and a high relative energy density of 91% can be retained, compared with the battery without the foldable part but having the same parameters. However, for the operation in Scheme C, owing to excessive segment contact or joint stretching, the acceptable folding angles at joints are only 34° and 15° for exemplified parameters $\delta_0/h = 0.5$ and $\delta_0/h = 0.25$, respectively. Therefore, the

requirements for function-oriented operations of such zigzag-like battery are highly dependent on the geometric design and deployment strategy. Systematic designs, including tape thickness, property, origami pattern etc., are subjected to future study.

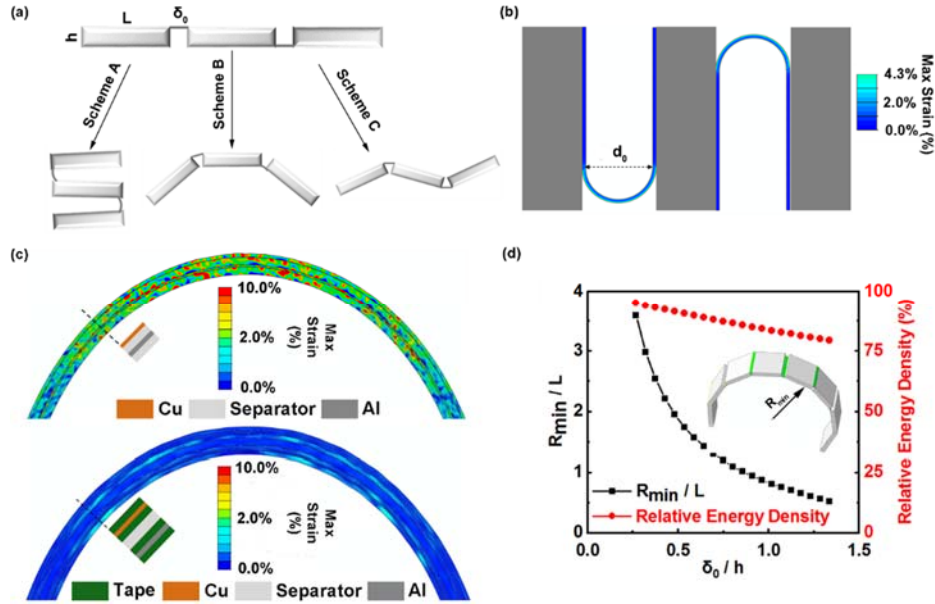


Figure 5.2.2 Structural design for the zigzag foldable battery.

5.2.4 Electrochemical Performance of Foldable Batteries

In order to demonstrate the electrometrical performance of the foldable battery, a full cell (LiCoO₂ (LCO)/Graphite) was tested at 0.5 C, while under various mechanical deformation configurations (**Fig 5.2.S1**) for 100 cycles. As shown in **Fig 5.2.3(a)**, the battery was first run in the flat configuration (region I, **Fig 5.2.S1(a)**) for 15 cycles. Its capacity slightly decayed from 148.6 to 147.2 mAh/g (0.06% per cycle). Then, the battery was manually bent as Scheme B with a diameter of ~2 cm ($D = 2$ cm, **Fig 5.2.S1(b)**) for 1,000 times, then it was cycled in the bent configuration ($D = 6$ cm, **Fig 5.2.S1(c)**) in region II. The discharge capacity first increased to 148.5 mAh g⁻¹ after flexing, and remained at 146.5 mAh g⁻¹ after 10 cycles. After a flat relaxation in region III, the battery was then

tested in the flexed configuration (region IV, **Fig 5.2.S1(d)**), associated with bending 1,000 times (Scheme B, $R_{min}/L = 1$) in advance. The capacity loss in region IV was only 0.06% per cycle, which was the same as that in the flat state (region I). This implied the repetitive mechanical deformations have almost no impact on the as-designed foldable battery. After being folded (90°) 1,000 times following Scheme A (**Fig 5.2.S1(e)**), the battery was subjected to folded (90°) configuration (region VI), and the total capacity loss was only 1.7 mAh g^{-1} , corresponding to 0.077% loss per cycle. Subsequently, the cell undergone 180° manually folding for 1,000 times (Scheme A), followed by cycling at the static 180° folded configuration for 20 cycles (region VIII, **Fig 5.2.S1(f)**). The total capacity loss was small (1.4 mAh g^{-1}). It is clear that the electrochemical performance was almost unchanged under such harsh folding. Finally, the battery was released into flat configuration (region IX) and steadily ran the last 5 cycles. Even having undergone alternative harsh deformations, a high capacity retention of 96% with an average Coulombic efficiency better than 99.9% after 100 cycles was achieved. The outstanding cycling performance indicates that such a foldable battery with novel zigzag structure is highly resistant to deformations, as the zigzag structure decouples thick energy storage component and thin folding joints, so that most part of electrodes are not subjected to mechanical stress. In addition, an interesting phenomenon observed is that the capacity always increases slightly after bending. This can be attributed to better electrolyte wetting caused by mechanical deformation and better contact among electrode particles and current collectors in the bent state.

To intuitively present the capacity change, **Fig 5.2.3(b)** shows the voltage profiles in different cycles, demonstrating little fading in the specific capacity and overpotential. In

addition, Electrochemical Impedance Spectroscopy (EIS) was applied to further understand the robustness of the foldable battery. The charge transfer resistance changed slightly from 3.27Ω to 3.36Ω (**Fig 5.2.S2**), which implies that the foldable battery is robust enough to bear mechanical deformations.

Practical applications on wearable electronic devices necessitate stable output power under large charging/discharging current. To evaluate the electrochemical performance at high current density, a full cell was fixed into a harshly folded (180°) configuration and continuously cycled at 0.5 C, 1 C, 2 C, 3 C and then back to 0.5 C with 5 cycles for each C-rate (**Fig 5.2.3(c)**). It is demonstrated that the capacity decreased steadily, corresponding to a reduction of 17% totally from 0.5 C to 3 C. Finally, the current density was switched back to 0.5 C after the galvanostatic charge/discharge at 3 C. The total capacity changed from 147.3 mAh g^{-1} to 137.9 mAh g^{-1} (capacity retention was 93.6%) after such 25 cycles. The electrochemical stability and recoverability are insensitive to high current density, which illustrates that the proposed foldable battery is attractive in powering commercial applications. In fact, the capacity stability at high C-rate is due to the zigzag-like design that enables tight contact between different layers, which can prevent electrode materials from peeling off from their substrates. Furthermore, the above deformed and cycled cell was disassembled to examine the morphology of both graphite and LCO layers at folding joints (**Fig 5.2.S3**) where they underwent largest deformation. Although crease with width $< 50 \mu\text{m}$ is observed, no delamination is detected at both cathode and anode. The crease also does not propagate after another 2,000 folding cycles (**Fig 5.2.S4**). As $50 \mu\text{m}$ is much smaller than the distance between two folding joints ($\sim 7 \text{ cm}$). This indicates

very little impact on cell performance, which is also supported by the steady cycling data in Figure 3a. More discussion can be found in the supporting information.

To further illustrate its applications in wearable devices, the durability of the foldable battery under repetitive folding for over thousands of cycles is crucial. Here, we tested the electrochemical performance of our battery while simultaneously conducted a dynamic loading experiment, where one end of the battery was fixed and the other end was bent back and forth by one actuator, which folded the battery repetitively by 130°. As shown in **Fig 5.2.4(a)**, the full cell was charged/discharged flatly for the first 5 cycles at 1 C, and it was then cycled under the dynamic loading for the next 15 cycles. During the experiment, the frequency of transition between the flat and folded (130°) state was 0.5 Hz, which represents 45,000 folding- unfolding times during 15 charging/discharging cycles at 1 C. The voltage change on discharge was less than 5 mV. During these 15 cycles, the capacity subtly changed from 139 to 124.2 mAh g⁻¹ with 0.7% loss per cycle, and the average Coulombic efficiency was above 99.6%. Specifically, the capacity was reduced by 0.38% from the cycle 16 to cycle 20. Illustrated by the voltage profiles in Figure 4b, no apparent change in voltage profile was observed. For comparison, a conventional stacking cell that had the same parameters was fabricated, and its electrochemical performance was also tested. Under a dynamic and small folding angle (30°) deformation with even lower frequency (0.05 Hz), the discharging voltage fluctuated significantly ranging from 4.2 V to 3.4 V. Comparing to the conventional stacking cell, our flexible battery design only suffered little strain in its electrodes during folding and the active materials and metal foil remained stable contact, enabling its high electromechanical stability.

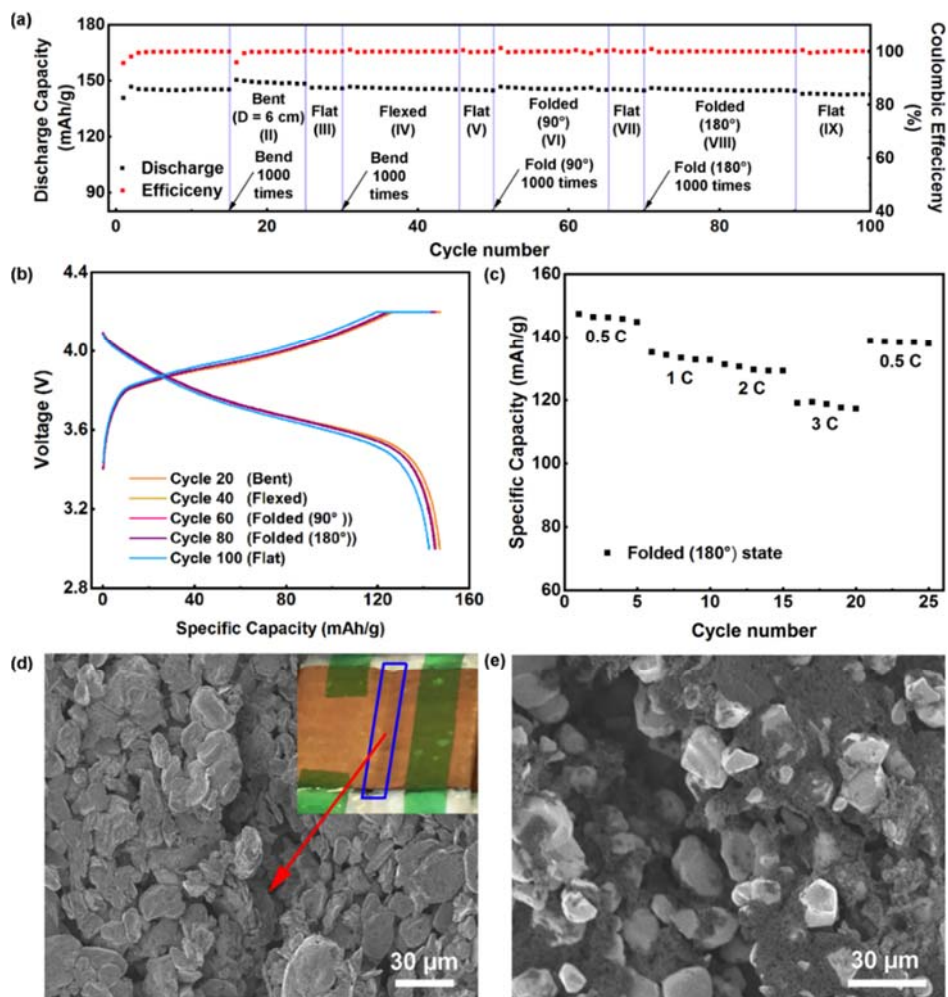


Figure 5.2.3. The electrochemical performance of the foldable battery undergoing different types of deformations. a) Cycling performance in various deforming configurations during 0.5 C charge/discharge for 100 cycles. b) Galvanostatic charge-discharge profiles at different configurations: the 20th, 40th, 60th, 80th, and 100th cycles. c) Rate performance of the foldable battery at high current density ranging from 0.5 C to 3 C and then back to 0.5 C at folded (180°) configuration. d) and e) Scanning Electron Microscopy (SEM) images of d) graphite and e) LCO layers at the folding joint.

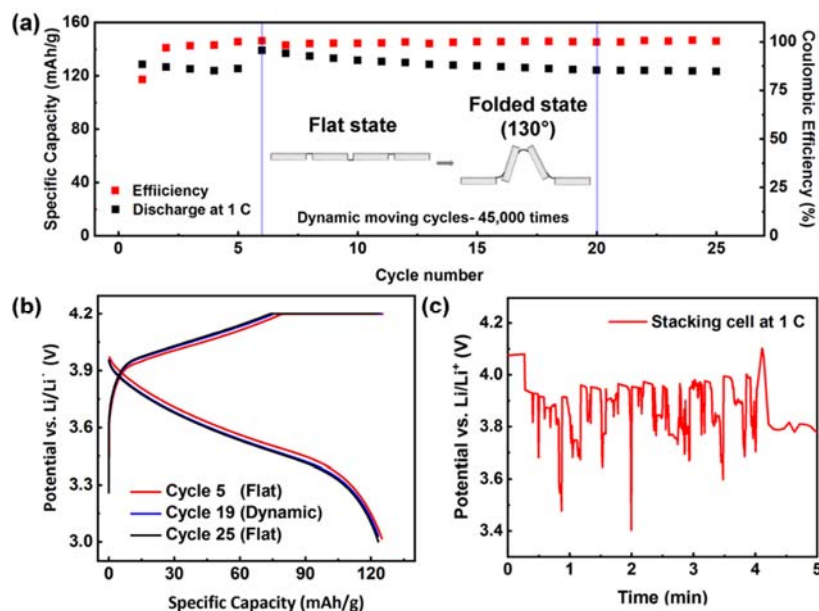


Figure 5.2.4 Dynamic loading test of the foldable battery at 1 C. a) Cycling performance of a zigzag-like foldable battery in different states under dynamic and repetitive fold loading test. The inset shows the schematic of the flat and folding configurations. b) Galvanostatic charge-discharge voltage profiles for 5th, 19th, and 25th cycle. c) The discharge profile of a normal stacking cell at 1 C, subjected to lower folding frequency.

5.2.5 Application Demonstration

To demonstrate its practical application, a fully charged zigzag-like foldable battery was used to power a series of light-emitting diode lights (LEDs). First, the cell was fully charged at 0.5 C with theoretical energy density up to 275 Wh L^{-1} , and then continuously folded by 90° and 180° (Scheme A) during discharge period. After once folding, the cell was flattened back. **Fig 5.2.5(a)** shows that the voltage fluctuation during the discharge period is less than 1 mV, which implies small resistance change of less than 0.5% ($0.04\Omega/8\Omega$). Subsequently, the LEDs showing a “CU” pattern were powered by the

foldable battery in flat, bent, and folded (130°) configurations, shown in Figure 5b, 5c, and 5d, respectively. Regardless of deformations in the battery, the brightness of these LEDs remained unchanged. Furthermore, the same functionality was maintained when continuously harsh folding applied, which implies that our design is applicable to commercial use. Apart from stable electromechanical performance, safety is crucial to be addressed for applications. In our experiment, the foldable battery was fully charged at 0.5 C and then it was punctuated by a nail (Fig 5.2.S5). The voltage dropped to zero once nail penetration without any smoke or fire observed. The thermal stability is possibly due to our zigzag-like battery design in which stores energy in distributed units.

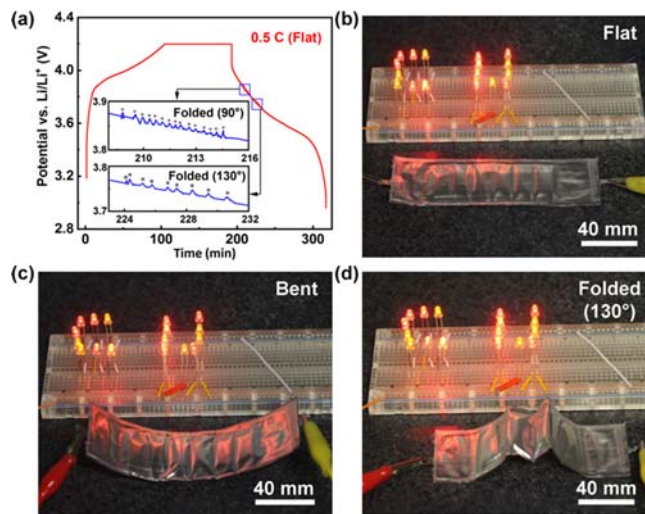


Figure 5.2.5 a) Voltage profile for the foldable battery under continuously and manually 90° and 180° folding during discharge. b-d) Practical applications of foldable battery to power a series of LEDs in flat, bent and folded configurations.

5.2.6 Conclusion

In conclusion, we proposed a facile strategy to fabricate zigzag-like Li-ion battery with superior foldability, high energy density and excellent electrochemical performance and mechanical endurance. The zigzag-like battery can be well fitted to many operation scenarios. The as-constructed battery has an energy density of 275 Wh L⁻¹, which is 96.4% compared with a conventional cell. In addition, even after different mechanical deformations at 0.5 C for 100 cycles, the foldable battery can still remain 96% with an average Coulombic efficiency higher than 99.9%. More importantly, this cell could

ú 切 ú 切 ú 切 ú 切 ú 切 ú 切 ú 切
ú 切 ú 切 ú 切 ú 切 ú 切 ú 切

5.2.7 Appendix

1) Calculation of relative energy density and minimum bending radius for as-designed structure.

As shown in Figure 2a, the height of the foldable battery is defined by h ; the whole length of one energy storage part is L ; the initial gap δ_0 can be stretched up to δ , which is constrained by the failure strain of alumina foil.^[312] In our design, h is 1.71 mm, and L is 10 mm. Before and after fabrication, δ_0 is 3.0 mm and 1.0 mm, respectively.

$$\delta = (3\% + 1)\delta_0$$

$$\text{Relative energy density: } \frac{100L}{(L+\delta)}$$

$$\text{The minimum bending radius } R = L \sqrt{\frac{h^2}{L^2} - \frac{1}{4}}$$

2) The theoretical energy density is calculated in the following way:

Mass loading of Lithium Cobalt Oxide (LCO) cathode material is $12.8\text{mg}/\text{cm}^2$ (single coated). According to our fabrication process, there are total six energy storage parts.

- Total area of LCO: $1.5\text{ cm} \times (6 \times 7\text{ cm} + 5 \times 0.3\text{ cm} + 2 \times 1.5\text{ cm}) = 69.75\text{ cm}^2$;
- Capacity of the foldable battery: $145\text{ mAh g}^{-1} \times 12.8\text{ mg cm}^{-2} \times 69.75\text{ cm}^2 \times 10^{-3} = 129.5\text{ mAh}$.
- For each layer, the thickness is: LCO: $42\text{ }\mu\text{m}$; Aluminum foil: $15\text{ }\mu\text{m}$; Graphite: $40\text{ }\mu\text{m}$; Copper foil: $10\text{ }\mu\text{m}$; Separator: $15\text{ }\mu\text{m}$; Aluminum pouch (single layer): $10.9\text{ }\mu\text{m}$.
- The extra package edge is also taken into consideration. We assume that the width of the edge is 1 mm , and the thickness of it is 0.218 mm .
- After fabrication, the total length of the battery without extra edge is $6\text{ cm} + 5 \times 0.1\text{ cm} + 1.5\text{ cm} \times 2 = 9.5\text{ cm}$
- Volume = $1.5\text{ cm} \times 0.171\text{ cm} \times (6\text{ cm} + 5 \times 0.1\text{ cm}) + 1.5\text{ cm} \times 1.5\text{ cm} \times (42\text{ }\mu\text{m} + 15\text{ }\mu\text{m} + 40\text{ }\mu\text{m} + 10\text{ }\mu\text{m} + 15\text{ }\mu\text{m} \times 2 + 10.9\text{ }\mu\text{m} \times 2) \times 10^{-4} \times 2 + 2 \times (0.1\text{ cm} \times 0.0218\text{ cm} \times 9.5\text{ cm}) + 2 \times (0.1\text{ cm} \times 1.5\text{ cm} \times 0.0218\text{ cm}) = 1.79\text{ cm}^3$
- Energy density: $129.5\text{ mAh} \times 3.8\text{ V} / 1.79\text{ cm}^3 = 275\text{ Wh L}^{-1}$.

3) Supplementary Figures and Tables

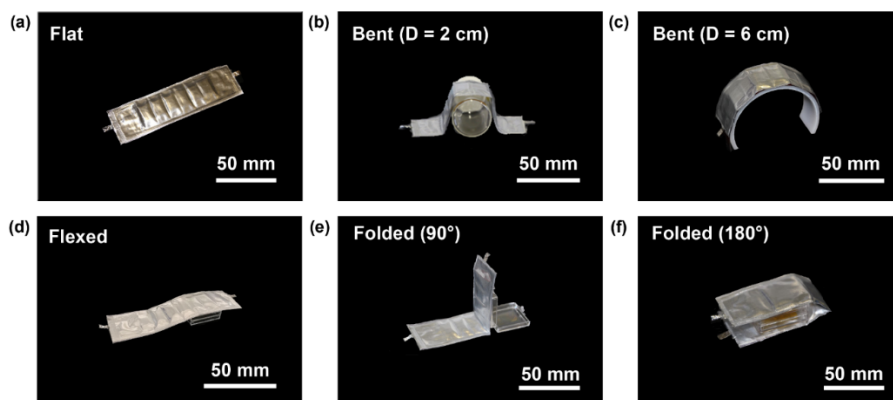


Figure 5.2.S1 Different states of the foldable battery during long cycle performance in **Figure 3a**. a) Flat state. b) Bent state with a bending diameter of 2 cm in which the foldable battery was bent 1,000 times. c) Bent state with a bending diameter of 6 cm under which the foldable battery was tested from cycle 16th to 25th. d) Flexed state. e) Folded state with a folding angle of 90° in which the battery was folded 1,000 times, and then tested under such state in region VI. f) Folded state with a folding angle of 180° in which the battery was folded 1,000 times, and then tested under such state from cycle 70th to 90th.

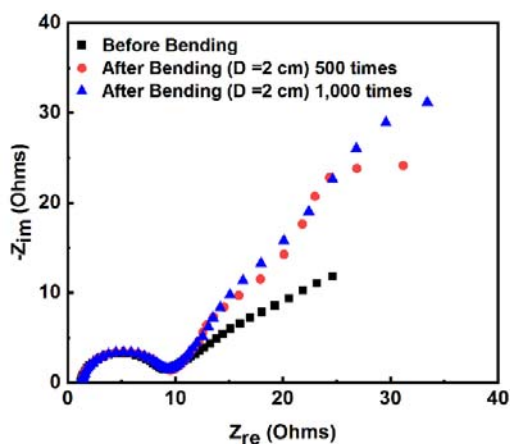


Figure 5.2.S2. Electrochemical Impedance Spectroscopy (EIS) of the foldable battery in the flat state before and after bending 500 and 1,000 times, respectively. The frequency of EIS test is from 1MHz to 0.1 Hz. The data shows that even after bending 1,000 times with a diameter of 2 cm, the charge transfer resistance changed little, which indicates that our battery is mechanically robust.

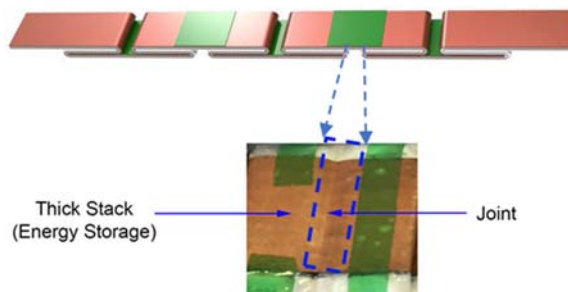


Figure 4.3.S3. The magnified optical image to illustrate the folding joint.

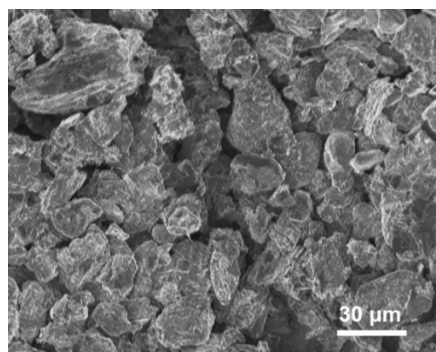


Figure 5.2.S4. The SEM image of anode at the joint with 2,000 more folding cycles than that in **Figure 5.2.3d**. To avoid crease, it is also possible not to coat active materials at the joint regions, as industrial coater can easily perform intermittent coating. Since the joint region has a width of 1 mm and the period between two joint regions is 7 cm, no coating at the joint region only leads to 1.4% reduction of energy density, which is negligible.

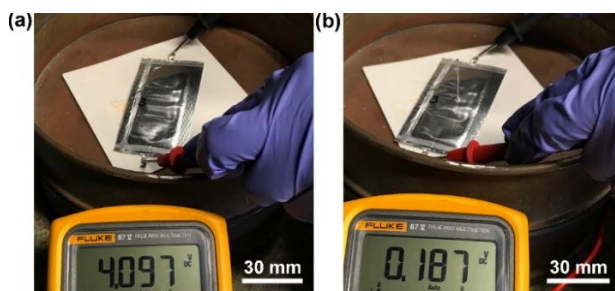


Figure 5.2.S5. The flammable test of the foldable battery. After fully charge at 0.5 C, the voltage image of the foldable battery a) before punctuation and b) after punctuation. The result shows that battery was still in stable condition after punctuation without catching smoke or fire.

Table 5.2.S1. The comparison of electrochemical and mechanical performances among reported studies.

Flexible Battery Type	Current collector	Electrode Materials	Specific Capacity (mAh g⁻¹)	Energy Density (Wh /L⁻¹)	Capacity decay per cycle	Coulombic efficiency (average)	Mechanical performances	Ref.
Foldable	CNT film	LiMn ₂ O ₄ /Li	110	19.1	0.18%	99.0%	No static/fatigue loading test	
Foldable	Au-coated steel	LiCoO ₂ / Li ₄ Ti ₅ O ₁₂	128	4.6	1.5%	99.0%	Only static bending by 2 cm in radius	
Foldable	Ti-coated kapton film	LiVPO ₄ F/ LiVPO ₄ F	60	95	0.003%	>99.0%	Only static folding	
Foldable	CNT paper	LiCoO ₂ / Li ₄ Ti ₅ O ₁₂	128	7.59	0.77%	93.0%	No dynamic folding test	
Foldable	Commercial Cu and Al	LiCoO ₂ / Graphite	145	275	0.04%	>99.9%	45,000 cycles of dynamic folding	Our Design

Chapter 6 Summary

The morphologies of low-dimensional materials (phosphorene, graphene, etc.) and bulk materials/structures were demonstrated to be controllably engineered so that their physical and chemical properties could be desirably modified. We predicted the relationships between morphologies and properties through multiscale simulations, and corresponding experiments further verified them. By using designed morphologies in materials/structures, we figured out several challenges of applications in the field of carbon dioxide reduction, water collection and flexible Li-ion batteries. The main discoveries are summarized as below:

- We proposed a novel perforation process on graphene through modulated strain on pre-deposited SiO₂ NPs beneath the monolayer, and the perforation process was tunable by varying the oxidative time, size and pattern of the NPs. r-MD simulations was employed to verify the potential of periodical nanoporation and the broad applicability of such strain-guided method to a variety of 2D materials and arbitrary choice of nano-protrusions as strain initiators. Both simulation and modeling efforts revealed the mechanism where the C-C bonds are stretched and the reactivity of carbon atoms is highly enhanced in the strain concentrated dome, triggering larger perforation probability. This facile and scalable strain-guided method provides a practical route to efficiently nanopatterning 2D materials. We demonstrated the concept and feasibility of this strain-guided perforation method, further studies will explore ways of pre-patterning orderly nanostructures on substrate to achieve orderly nanopores. Starting from the zero-dimensional strain-initiator herein, future studies on one-dimensional nanowires and other two-dimensional nanostructures may inspire patterning 2D

materials into a rich variety of nanostructures, which underpins the broad applications in electronics, environmental and biological fields^{34, 50, 52}.

- A novel method to control the movement of a nanodroplet on a substrate using strain gradient was proposed, and verified using both MD simulations and theoretical analysis. The driving force, originating from the imbalance of Van der Waals force between the substrate surface and droplet, is in the opposite direction of the applied strain gradient, and its magnitude is proportional to the magnitude of the strain gradient and the square of droplet radius. By properly adjusting the strain gradient and its direction, as well as loading sequence, one may precisely control the acceleration and deceleration the droplet, and even its trajectory. The study may inspire broad applications of directional droplet transport including fog collection⁴¹ and thermal management of devices⁹.
- MD simulations on single-wall PNTs were performed to study the structural stability and mechanical behaviors of PNTs. The results indicated that PNTs with a larger diameter are able to resist higher temperature. However, zigPNTs have lower resistance to the thermal loads due to high intrinsic hoop strain in the the wrapped structures. Also, the remarkable size-effect of mechanical properties was revealed, and both Young's modulus and fracture strength of PNTs decrease as the diameter decreases. Compared to 2D phosphorene, the thermal conductivity of a-PNT evidently decreases due to phonon confinement, exhibiting remarkable size effects, which relies on not only the diameter but on the length. More quantitative modeling effort will be carried out in future. Since PNTs' excellent properties in electrics and thermoelectrics enable them as promising components, the present study on the basic mechanical behaviors of

PNTs may offer a guidance for the fabrication and strain engineering of PNTs-based on nanodevices.

- We proposed that the collapse of armchair PNT (through radial deformation) is an effective approach to fabricate stable nanostructure: closed-edged bilayer phosphorene nanoribbons, which enrich the family of nanodevices' components. The number of n in PNTs can determine two different structures: arc-like and sigmoidal bilayer nanoribbons. We also found the distinction of band structures upon the structural transformation, and the size-dependent band gap with nanoribbon width. The underlying mechanism was revealed to lie in the combined effect of black-to-blue phosphorene transition and bond formation between two facing walls in the CBPNRs. More importantly, the direct-to-indirect transition of band gap was observed in the arc-like CBPNRs but not in the sigmoidal ones. The study here appeared to be a theoretical attempt to predict the sigmoidal and arc-like bilayer nanoribbons, allowing wider applications in electronic nanodevices due to their tunability. It's also important to note that another kind of tube, zigzag PNTs, will be subjected to future study.
- A series of 2D and 3D surface topographies were created in soft materials with embedded cavity array. Both simulation and experimental efforts confirmed that by varying the geometries of cavities (sizes, shapes, arrays) and loading methods (uniaxial and biaxial compression), we can dynamically tune the surface evolutions. The variety of overall and local morphologies was revealed to be based on the inter-cavity instability and local deformation of top plates, respectively. The flexibility provided by CESMs underpins a novel design of tunable surface patterns that can be applied to multiscale applications. The tunable surface topography allows optimization of

chemical and physical properties in real applications which need dynamically controllable surfaces.

- We numerically and experimentally validated that the conventional transition, of wrinkles to localizations (folds or ridges) in film/substrate bilayers subjected to increasing uniaxial compression, can be reversed through the pre-patterned cavities in the substrate. Compared with cavity-free bilayers, the localizable surface topologies were achieved at relatively small strain even within a linear-elastic substrate. Additionally, the surface patterns of defected bilayers were highly dependent on the spatial and geometric configurations of cavities beneath the surface. This controllability offers a novel design of tunable surface patterns, including localized ridges and folds, waves with different wavelengths, saw-like features and co-existing phase of wrinkles and folds. The controlling surface patterns with defected bilayers across a wide range of scales has potential to optimize performance of diverse applications such as surface adhesion, hydrophobicity and friction.^{214, 313}
- The nonlinear phase field simulations and linear stability analysis were performed to explore the spontaneous patterns induced by diffusional surface instability on spherical core/shell systems. At a given evolution time, the transition of morphologies, from flat surface, to grooves and ripples and eventually the assembly of islands with roughly uniform size, could be controlled since the growth rate of undulation is highly dependent on the substrate curvature, modulus ratio and intrinsic strain. With the increased eigenstrain, radius and stiffness of substrate, the self-organization occurs faster. In the parallel experiments, the surface patterns of SiO₂ islands were also successfully formed on Ag substrate. Thus, the surface instability *via* diffusion may

dominate the self-assembly of islands on spherical particles observed in pioneering study,¹⁷⁸ whose mechanism remain obscure until the present study. On a curvature-dependent and closed substrate, the stress generated in the film, upon mismatched strain between the film and substrate, is possibly anisotropic and nonuniform. Also, the surface instability may be constrained in local regions where the boundary effect can further interact with the substrate curvature effect. These enable more varieties of morphological patterns *via* surface diffusion, which underpins self-assembly fabrication of true 3D microstructures and devices. Thus, the study of self-assembling morphological patterns *via* surface diffusion on closed and curved substrate significantly expand applications in electronics, biomedical engineering and optical technologies.^{207, 314, 315}

- We proposed a novel copper-containing perovskite as an effective oxygen carrier to efficiently split air-containing CO₂ into gaseous fuel CO in the cyclic redox scheme. A high CO yield (2.28 mol/kg) was achieved for converting the mixture of CO₂/O₂ (molar ratio 5:1). The CO productivity was even comparable to those for reported redox materials (SrFeO₃-CaO, CeO₂/Fe₂O₃, LaSrFeAlO₃, etc) at 980°C and the cases for reducing pure O₂. Meanwhile, exceptionally high syngas productivity (11.0 mol/kg) makes the Cu-containing perovskite highly attractive, and this yield was two times higher than other cyclic redox schemes. At relatively lower 850°C, such activities were stably maintained during the 50 cycles. The exsolution and self-regeneration of metallic Cu on the perovskite surface was experimentally and theoretically elucidated to be responsible for highly efficient CO₂ splitting even in the presence of O₂.

- Finally, we proposed a facile strategy to fabricate zigzag-like Li-ion battery with superior foldability, high energy density and excellent electrochemical performance and mechanical endurance. The zigzag-like battery can be well fitted to many operation scenarios. The as-constructed battery has an energy density of 275 Wh L^{-1} , which is 96.4% compared with a conventional cell. In addition, even after different mechanical deformations at 0.5 C for 100 cycles, the foldable battery can still remain 96% with an average Coulombic efficiency higher than 99.9%. More importantly, this cell could withstand extreme dynamic folding operation (130° for 45,000 times) while maintain stable capacity at 1 C, demonstrating promising potential practical applications.

Chapter 7 Perspectives

Through fundamental understandings of morphological formation and morphology-property in multiscale material structures, we demonstrated two device-level prototypes via using strain-engineering morphologies in the fields of energy storage and conversion. In the future, we further focus on the field of energy and environment. Starting the energy storage device of structural batteries using designed micromorphology in battery components, we further investigate morphable structures to transfer/convert energies. In the field of environment, the studies of other possible methods for reducing air-containing CO₂ into valuable chemicals, including electrocatalytic and photocatalytic reductions, will be subjected to our future works. Besides energy cycle, the water cycle is another critical point to maintain human lives. Thus, we will also investigate the fundamentals and practical devices for water collection base morphologies. While practical applications of engineered morphologies in the field of energy and environment are important, the fundamental understanding of morphology-property in materials and structures is significant for further optimizing functional devices. The main perspective focuses will be:

7.1 Energy cycle

7.1.1 Structural Batteries

Solid-state lithium batteries have been intensively pursued as promising solutions to safety issues in Li-ion batteries with organic liquid electrolyte, such as leakage, flammability, and unstable solid-electrolyte interface (SEI) formation. Solid electrolyte is critical to the successful development of solid state lithium batteries. However, traditional polymer electrolyte has low conductivity; ceramic electrolyte has high ionic conductivity

but it is very fragile. Structural energy storage of li-ion battery is attractive for aerial applications since such device can function as both the structural component in aerial system and the power source, which significantly saves weight and volume, and enhance operation time. Structural energy storage is challenging since it requires excellent mechanical robustness and stress-bearing capability. While carbon fiber-based electrodes have been demonstrated for this concept, the polymer separator/electrolyte layer remains more challenging, since both high ionic conductivity and high mechanical strength need to be achieved simultaneously³¹⁶⁻³¹⁸.

- We are rationally designing desirable microstructures for ceramic/polymer composite electrolyte to realize both high ionic conductivity and mechanical robustness. The composite electrolyte will also be integrated with various anodes and cathodes to demonstrate full cells. As shown in **Fig 7.1.1**, we are introducing inorganic nanowires, for example, palygorskite as an additional ceramic filler to form solid electrolyte, and cross-linking of nanowires are responsible enhancement in the mechanical strength of polymer membrane as electrolyte, like PVDF and PEO.

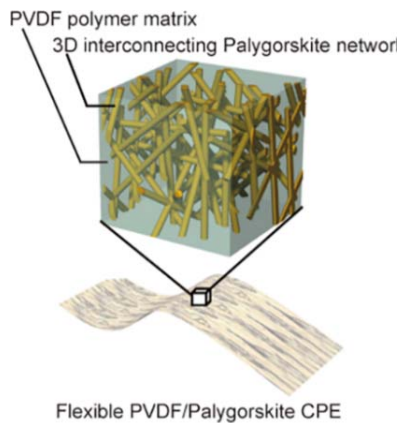


Figure 7.1.1 Schematic of PVDF/palygorskite nanowires composite as solid electrolyte.

- Nacre structure is a staggered composite with microscopic, high-aspect-ratio ceramic plates (bricks), and polymer as mortar providing cohesion and energy dissipation, and it is an attractive structure to enable high strength and high energy absorption simultaneously. Hence, to function as a solid electrolyte with excellent mechanical properties, the ceramic phase should have high modulus, and high aspect ratio. The interface should have high shear strength and strain. The volume portion of ceramic should be optimized to reach a balance between strength and toughness. To create a nacre-like solid electrolyte, the ceramic phase will be replaced by solid electrolytes discussed above, and the polymer phase will be replaced by polymer electrolytes, so that ions can still move through the electrolyte. The thickness of each ceramic layer is 1-10 μm , and the lateral size is 5-50 μm , and the aspect ratio is 5-10. The thickness of the polymer layer is $\sim 10\%$ of the ceramic one.
- An ideal structural energy storage should have high stiffness, strength and toughness simultaneously, and extreme safety under external impact, such as shocking, bending and nailing. The microstructure of carbon fiber contains the fibrils of graphitic crystallites, which can not only provide the mechanical properties through aligning with the fiber axis, but also realize lithiation and delithiation between the turbostratic folded and interlinked carbon layers. Herein, we plan to use carbon fabric as the conductive matrix for both positive electrode of sulfur and negative electrode of lithium metal, in order to achieve the multifunctional goals of the structural li-ion batteries.

7.1.2 Morphable Structures

Buckling morphologies, as a conventional failure of structural beams/plates, can be used to convey the driving forces for robotics via the mechanism of travelling locomotion. While most of studies focused on straight beams/strips and planar constraints, fundamentally understanding the instability of a closed beam subjected to curved substrates and the dynamics of buckled blister are of great importance for applications in soft robotics. Thus,

- We are studying the instability and morphologies of an elastic ring subjected to an annular rigid constraint with smaller radius than that of the ring. The single-blister and higher-order morphologies as shown in **Fig 7.1.2** are main symmetric configurations. Through FEM simulations and theoretical analysis, the stability of each morphology in the view of energy and barriers for morphological transformation will be discussed.

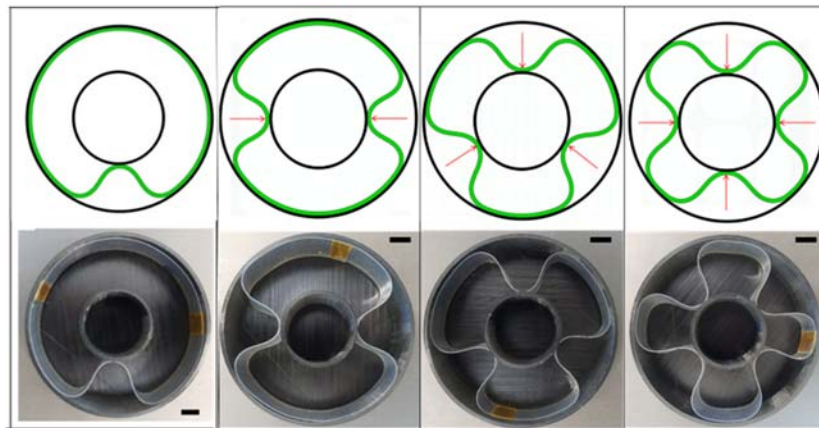


Figure 7.1.2 The morphologies of elastic rings confined in annular solid constraints. Except the single-blister one, external displacements have to be applied as initiators to overcome energy barrier of forming higher-order buckling morphologies.

- Confined in solid or soft constraints, the buckling ring is a system with constant energy wherever blisters rotate so that a small external initiation can stimulate the rotation of

buckling rings. The travelling of blisters is critical for applications of peristaltic pumps, soft locomotion cars and artificial joints. The fundamental dynamic mechanism of blister travelling will be investigated by analytical model and simulations.

- The magnetic-driven, dielectric-driven, thermal-driven and pneumatic-driven actuator elements are being studied and optimized as the bending initiator for blister travelling. We will fabricate the blister-based prototype robotics for loading carry and medical applications, and investigate the effect of energy efficiency.

7.2 Carbon Cycle

To address carbon loop as a whole, carbon utilization should follow and be intimately bonded to carbon capture, which provides the source of CO₂ conversion. A scalable and economical approach of carbon utilization must first ensure that the captured CO₂ is of low cost, large scale, and widely available^{319, 320}. The current challenge of reducing CO₂ directly from air is to develop O₂-insensitive catalysts for CO₂ reduction into valuable chemicals, otherwise the cost for capturing high-purity CO₂ is high. In Section 5.1, one efficient solution of chemical loop with modified perovskite as oxygen carrier has been demonstrated. However, it's still urgent to develop more possibilities of catalytic pathways with higher cost-efficiency and lower carbon footprint, in order to practically close carbon loop. There are two catalytic routes we will focus on:

7.2.1 Electrocatalytic reduction

Extensive research progresses in electrocatalytically converting CO₂ has demonstrated the production of gaseous carbon products of CO, methane and ethylene, as well as C₁ liquids. Heterogeneous electrocatalysts with enhanced reduction reactivity have been developed, including metals of Au, Cu, Ag, Pd, metal oxides, carbon-based materials.

Despite of promising energy conversion process due to mild reaction conditions, low catalytic activity and poor selectivity in aqueous solutions challenge practical and scale-up applications^{241, 242}. Furthermore, the sensitivity of current electrocatalysts to O₂ present in the CO₂ mixture is still unclear. Since the morphology and structure of synthesized catalyst can tune chemical reactivity, optimization of the catalytic performances by tailoring particle morphology and defect density through strain-engineering is possible.

7.2.2 Photocatalytic reduction

As the simulation of natural photosynthesis in plants, artificial photocatalytic reduction of CO₂ into hydrocarbon fuels is promising solution to reduce carbon emission and utilize solar source. Especially, coupled with a matched oxidative half-reaction of water oxidation, the half-reaction of CO₂ can achieve a carbon neutral cycle. However, current photosynthetic processes are challenged by low photoconversion efficiency and selectivity, and most of them targeted to utilize pure CO₂ without oxidative O₂. Based on our progresses in this thesis, strain-engineering is an efficient way to tune properties of band-structure, oxygen vacancy and micro/mesoporous structures.²⁴⁹ Therefore, it's possible to tune macro/meso/micro morphology and nano-structure for photocatalysts in order to improve performances.

7.3 Water Collection

It's much important to understand how water-repellency is influenced by the microscale and nanoscale of surfaces. The irregular surface textures in biological systems, such as creases and veins in lotus, underpins superhydrophobic surfaces, and the variation in morphological texture and chemical composition of synthetic surfaces can lead to spot-to-spot difference of wetting properties, which are potentially useful for droplet mobility.

Extensive efforts have been paid on changing the contact angle and realizing the movement of liquid droplets on surfaces with pre-designed microstructures, however, studies of active control of droplet movement are limited. Actively engineered morphologies via external deformation are planned to control the local contact angle of droplet so that the droplet can be driven desirably. Among many microstructures, micro-pillars are of particular interest since micro-scale morphology, and the roughness factor have been confirmed to play an important role in wettability⁸³. As shown in Fig 6.3.1, a , h , b_1 and b_2 denote the width, height, horizontal space and vertical space of micro-pillars. Pneumatic elastomers with microchannels can be used to locally control the structure of micro-pillars, for example, the geometric parameters of a , h , b_1 and b_2 , just above the elastomer surface, thus, the local contact angle is actively controlled as illustrated in Fig 6.3.2.

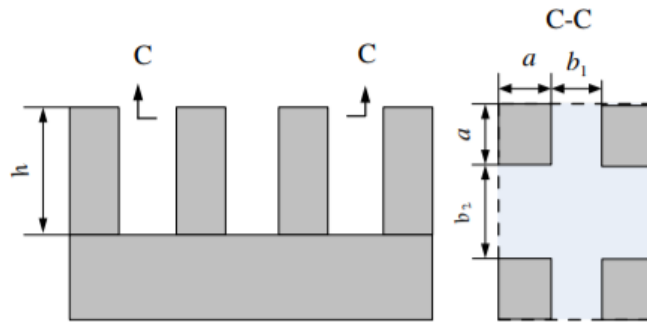


Figure 7.3.1 Schematic of micro-pillars

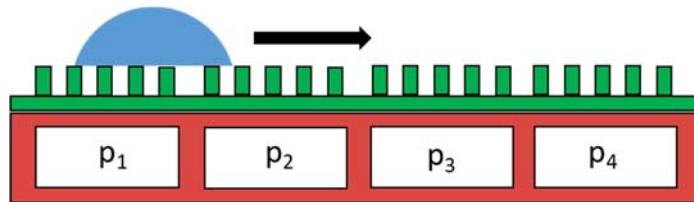


Figure 7.3.2 Schematic of controlling the local geometrics of micro-pillars through pneumatic elastomer with microchannels.

Bibliography

1. Sanyal, M. K.; Datta, A.; Hazra, S., Morphology of nanostructured materials. In *Pure and Applied Chemistry*, 2002; Vol. 74, p 1553.
2. Evans, C. J.; Bryan, J. B. J. C. A., “Structured”, “textured” or “engineered” surfaces. **1999**, *48* (2), 541-556.
3. Coblas, D. G.; Fatu, A.; Maoui, A.; Hajjam, M., Manufacturing textured surfaces: State of art and recent developments. *Proceedings of the Institution of Mechanical Engineers, Part J: Journal of Engineering Tribology* **2014**, *229* (1), 3-29.
4. Chen, Y.; Liao, X.; Shi, X.; Xiao, H.; Liu, Y.; Chen, X., Three-dimensional auxetic properties in group V-VI binary monolayer crystals X₃M₂ (X = S, Se; M = N, P, As). *Phys Chem Chem Phys* **2019**, *21* (11), 5916-5924.
5. Hao, F.; Liao, X.; Li, M.; Xiao, H.; Chen, X., Oxidation-induced negative Poisson's ratio of phosphorene. *J Phys Condens Matter* **2018**, *30* (31), 315302.
6. Hao, F.; Liao, X.; Xiao, H.; Chen, X., Thermal conductivity of armchair black phosphorus nanotubes: a molecular dynamics study. *Nanotechnology* **2016**, *27* (15), 155703.
7. Xiao, H.; Shi, X.; Liao, X.; Zhang, Y.; Chen, X., Prediction of a two-dimensional S₃N₂ solid for optoelectronic applications. *Physical Review Materials* **2018**, *2* (2).
8. Xiao, H.; Shi, X.; Zhang, Y.; Li, M.; Liao, X.; Chen, X., Predicting a two-dimensional P₂S₃ monolayer: A global minimum structure. *Computational Materials Science* **2018**, *155*, 288-292.
9. Deng, S.; Berry, V., Wrinkled, rippled and crumpled graphene: an overview of formation mechanism, electronic properties, and applications. *Materials Today* **2016**, *19* (4), 197-212.
10. Bruzzone, A. A. G.; Costa, H. L.; Lonardo, P. M.; Lucca, D. A., Advances in engineered surfaces for functional performance. *CIRP Annals* **2008**, *57* (2), 750-769.
11. Si, C.; Sun, Z.; Liu, F., Strain engineering of graphene: a review. *Nanoscale* **2016**, *8* (6), 3207-17.
12. Deng, S.; Sumant, A. V.; Berry, V., Strain engineering in two-dimensional nanomaterials beyond graphene. *Nano Today* **2018**, *22*, 14-35.
13. Mukherjee, R.; Sharma, A., Instability, self-organization and pattern formation in thin soft films. *Soft Matter* **2015**, *11* (45), 8717-40.
14. Chen, X.; Yin, J., Buckling patterns of thin films on curved compliant substrates with applications to morphogenesis and three-dimensional micro-fabrication. *Soft Matter* **2010**, *6* (22).
15. Li, J.; Shan, Z.; Ma, E., Elastic strain engineering for unprecedented materials properties. *MRS Bulletin* **2014**, *39* (2), 108-114.
16. Liao, X.; Xiao, J.; Ni, Y.; Li, C.; Chen, X., Self-Assembly of Islands on Spherical Substrates by Surface Instability. *ACS Nano* **2017**, *11* (3), 2611-2617.
17. Liao, X. B.; Ni, Y.; Yang, H.; He, L. H., Role of modulus mismatch in vertically aligned nanocomposite formation during spinodal decomposition in constrained films. *Applied Physics Letters* **2013**, *103* (14).
18. Ni, Y.; He, L. H.; Liao, X. B., Stress anisotropy controlled morphological evolution in core-shell nanowires. *Extreme Mechanics Letters* **2016**, *8*, 160-166.
19. Chen, Y.; Liao, X.; Liu, Y.; Chen, X., Helical buckling of wires embedded in a soft

- matrix under axial compression. *Extreme Mechanics Letters* **2017**, *17*, 71-76.
20. Liao, X.; Nagakura, T.; Chen, Y.; Zhu, L.; Shi, X.; Yonezu, A.; Chen, X.; Xiao, H., Tunable surface morphology via patterned cavities in soft materials. *Physical Review E* **2018**, *98* (6).
 21. Liao, X.; Chen, Y.; Nagakura, T.; Zhu, L.; Li, M.; Shi, X.; Yonezu, A.; Xiao, H.; Chen, X., Unconventional localization prior to wrinkles and controllable surface patterns of film/substrate bilayers through patterned cavities. *Extreme Mechanics Letters* **2018**, *25*, 66-70.
 22. Bertoldi, K., Harnessing Instabilities to Design Tunable Architected Cellular Materials. *Annual Review of Materials Research* **2017**, *47* (1), 51-61.
 23. Car, R.; Parrinello, M., Unified Approach for Molecular Dynamics and Density-Functional Theory. *Physical Review Letters* **1985**, *55* (22), 2471-2474.
 24. Derosa, P.; Cagin, T., *Multiscale Modeling: From Atoms to Devices*. CRC press: 2010.
 25. Phillips, J. C.; Braun, R.; Wang, W.; Gumbart, J.; Tajkhorshid, E.; Villa, E.; Chipot, C.; Skeel, R. D.; Kalé, L.; Schulten, K., Scalable molecular dynamics with NAMD. **2005**, *26* (16), 1781-1802.
 26. Xiao, H.; Shi, X.; Hao, F.; Liao, X.; Zhang, Y.; Chen, X., Development of a Transferable Reactive Force Field of P/H Systems: Application to the Chemical and Mechanical Properties of Phosphorene. *J Phys Chem A* **2017**, *121* (32), 6135-6149.
 27. Senftle, T. P.; Hong, S.; Islam, M. M.; Kylasa, S. B.; Zheng, Y.; Shin, Y. K.; Junkermeier, C.; Engel-Herbert, R.; Janik, M. J.; Aktulga, H. M.; Verstraelen, T.; Grama, A.; van Duin, A. C. T., The ReaxFF reactive force-field: development, applications and future directions. *npj Computational Materials* **2016**, *2* (1).
 28. Provatas, N.; Elder, K., *Phase-field methods in materials science and engineering*. John Wiley & Sons: 2011.
 29. Chen, L.-Q., Phase-Field Models for Microstructure Evolution. *Annual Review of Materials Research* **2002**, *32* (1), 113-140.
 30. Zienkiewicz, O. C.; Taylor, R. L.; Nithiarasu, P.; Zhu, J., *The finite element method*. McGraw-hill London: 1977; Vol. 3.
 31. Geim, A. K., Graphene: Status and Prospects. **2009**, *324* (5934), 1530-1534.
 32. Lee, C.; Wei, X.; Kysar, J. W.; Hone, J., Measurement of the Elastic Properties and Intrinsic Strength of Monolayer Graphene. **2008**, *321* (5887), 385-388.
 33. Li, X.; Cai, W.; An, J.; Kim, S.; Nah, J.; Yang, D.; Piner, R.; Velamakanni, A.; Jung, I.; Tutuc, E.; Banerjee, S. K.; Colombo, L.; Ruoff, R. S., Large-Area Synthesis of High-Quality and Uniform Graphene Films on Copper Foils. **2009**, *324* (5932), 1312-1314.
 34. Lin, Y.; Liao, Y.; Chen, Z.; Connell, J. W., Holey graphene: a unique structural derivative of graphene. *Materials Research Letters* **2017**, *5* (4), 209-234.
 35. Yuan, W.; Chen, J.; Shi, G., Nanoporous graphene materials. *Materials Today* **2014**, *17* (2), 77-85.
 36. Barati Farimani, A.; Dibaeinia, P.; Aluru, N. R., DNA Origami-Graphene Hybrid Nanopore for DNA Detection. *ACS Appl Mater Interfaces* **2017**, *9* (1), 92-100.
 37. Cohen-Tanugi, D.; Grossman, J. C., Water desalination across nanoporous graphene. *Nano Lett* **2012**, *12* (7), 3602-8.
 38. Surwade, S. P.; Smirnov, S. N.; Vlassioug, I. V.; Unocic, R. R.; Veith, G. M.; Dai, S.; Mahurin, S. M., Water desalination using nanoporous single-layer graphene. *Nat*

Nanotechnol **2015**, *10* (5), 459-64.

39. Huang, L.; Zhang, M.; Li, C.; Shi, G., Graphene-Based Membranes for Molecular Separation. *J Phys Chem Lett* **2015**, *6* (14), 2806-15.
40. Agrawal, K. V.; Benck, J. D.; Yuan, Z.; Misra, R. P.; Govind Rajan, A.; Eatmon, Y.; Kale, S.; Chu, X. S.; Li, D. O.; Gong, C.; Warner, J.; Wang, Q. H.; Blankschtein, D.; Strano, M. S., Fabrication, Pressure Testing, and Nanopore Formation of Single-Layer Graphene Membranes. *The Journal of Physical Chemistry C* **2017**, *121* (26), 14312-14321.
41. Boutilier, M. S. H.; Jang, D.; Idrobo, J. C.; Kidambi, P. R.; Hadjiconstantinou, N. G.; Karnik, R., Molecular Sieving Across Centimeter-Scale Single-Layer Nanoporous Graphene Membranes. *ACS Nano* **2017**, *11* (6), 5726-5736.
42. Li, Z.; Liu, Y.; Zhao, Y.; Zhang, X.; Qian, L.; Tian, L.; Bai, J.; Qi, W.; Yao, H.; Gao, B.; Liu, J.; Wu, W.; Qiu, H., Selective Separation of Metal Ions via Monolayer Nanoporous Graphene with Carboxyl Groups. *Anal Chem* **2016**, *88* (20), 10002-10010.
43. O'Hern, S. C.; Boutilier, M. S.; Idrobo, J. C.; Song, Y.; Kong, J.; Laoui, T.; Atieh, M.; Karnik, R., Selective ionic transport through tunable subnanometer pores in single-layer graphene membranes. *Nano Lett* **2014**, *14* (3), 1234-41.
44. Madauss, L.; Schumacher, J.; Ghosh, M.; Ochedowski, O.; Meyer, J.; Lebius, H.; Ban-d'Etat, B.; Toimil-Molares, M. E.; Trautmann, C.; Lammertink, R. G. H.; Ulbricht, M.; Schleberger, M., Fabrication of nanoporous graphene/polymer composite membranes. *Nanoscale* **2017**, *9* (29), 10487-10493.
45. Wang, X.-Y.; Narita, A.; Müllen, K., Precision synthesis versus bulk-scale fabrication of graphenes. *Nature Reviews Chemistry* **2017**, *2* (1).
46. Bai, J.; Zhong, X.; Jiang, S.; Huang, Y.; Duan, X., Graphene nanomesh. *Nat Nanotechnol* **2010**, *5* (3), 190-4.
47. Bai, Z.; Zhang, L.; Li, H.; Liu, L., Nanopore Creation in Graphene by Ion Beam Irradiation: Geometry, Quality, and Efficiency. *ACS Appl Mater Interfaces* **2016**, *8* (37), 24803-9.
48. Russo, C. J.; Golovchenko, J. A., Atom-by-atom nucleation and growth of graphene nanopores. *Proc Natl Acad Sci U S A* **2012**, *109* (16), 5953-7.
49. Moreno, C.; Vilas-Varela, M.; Kretz, B.; Garcia-Lekue, A.; Costache, M. V.; Paradinas, M.; Panighel, M.; Ceballos, G.; Valenzuela, S. O.; Peña, D.; Mugarza, A., Bottom-up synthesis of multifunctional nanoporous graphene. **2018**, *360* (6385), 199-203.
50. Lin, Y.; Han, X.; Campbell, C. J.; Kim, J.-W.; Zhao, B.; Luo, W.; Dai, J.; Hu, L.; Connell, J. W., Holey Graphene Nanomanufacturing: Structure, Composition, and Electrochemical Properties. *Advanced Functional Materials* **2015**, *25* (19), 2920-2927.
51. Jia, P.; Pan, F.; Chen, T., Effect of oxygen plasma etching on graphene's mechanical and electrical properties. *IOP Conference Series: Materials Science and Engineering* **2017**, 182.
52. Kim, S.-S.; Sohn, B.-H., Catalytic tailoring of large-area reduced graphene oxide by tunable arrays of Pt nanostructures synthesized from self-assembling diblock copolymers. *Carbon* **2016**, *107*, 124-131.
53. Kim, S.-S.; Park, M. J.; Kim, J.-H.; Ahn, G.; Ryu, S.; Hong, B. H.; Sohn, B.-H., Strain-Assisted Wafer-Scale Nanoperforation of Single-Layer Graphene by Arrayed Pt Nanoparticles. *Chemistry of Materials* **2015**, *27* (20), 7003-7010.
54. Plimpton, S.; Crozier, P.; Thompson, A. J. S. N. L., LAMMPS-large-scale atomic/molecular massively parallel simulator. **2007**, *18*, 43.

55. Chenoweth, K.; Van Duin, A. C.; Goddard, W. A. J. T. J. o. P. C. A., ReaxFF reactive force field for molecular dynamics simulations of hydrocarbon oxidation. **2008**, *112* (5), 1040-1053.
56. Ong, Z.-Y.; Pop, E. J. P. R. B., Molecular dynamics simulation of thermal boundary conductance between carbon nanotubes and SiO₂. **2010**, *81* (15), 155408.
57. Van Duin, A. C.; Dasgupta, S.; Lorant, F.; Goddard, W. A. J. T. J. o. P. C. A., ReaxFF: a reactive force field for hydrocarbons. **2001**, *105* (41), 9396-9409.
58. Wu, Q.; Wu, Y.; Hao, Y.; Geng, J.; Charlton, M.; Chen, S.; Ren, Y.; Ji, H.; Li, H.; Boukhvalov, D. W.; Piner, R. D.; Bielawski, C. W.; Ruoff, R. S., Selective surface functionalization at regions of high local curvature in graphene. *Chem Commun (Camb)* **2013**, *49* (7), 677-9.
59. Liao, Y.; Tu, K.; Han, X.; Hu, L.; Connell, J. W.; Chen, Z.; Lin, Y., Oxidative Etching of Hexagonal Boron Nitride Toward Nanosheets with Defined Edges and Holes. *Scientific Reports* **2015**, *5*, 14510.
60. Liu, F.; Ming, P.; Li, J. J. P. R. B., Ab initio calculation of ideal strength and phonon instability of graphene under tension. **2007**, *76* (6), 064120.
61. Xi, C.; Guoxin, C., A structural mechanics study of single-walled carbon nanotubes generalized from atomistic simulation. *Nanotechnology* **2006**, *17* (4), 1004.
62. Gill, S. T.; Hinnefeld, J. H.; Zhu, S.; Swanson, W. J.; Li, T.; Mason, N., Mechanical Control of Graphene on Engineered Pyramidal Strain Arrays. *ACS Nano* **2015**, *9* (6), 5799-5806.
63. Zhang, Y.; Heiranian, M.; Janicek, B.; Budrikis, Z.; Zapperi, S.; Huang, P. Y.; Johnson, H. T.; Aluru, N. R.; Lyding, J. W.; Mason, N., Strain Modulation of Graphene by Nanoscale Substrate Curvatures: A Molecular View. *Nano Lett* **2018**, *18* (3), 2098-2104.
64. Hinnefeld, J. H.; Gill, S. T.; Mason, N., Graphene transport mediated by micropatterned substrates. *Applied Physics Letters* **2018**, *112* (17).
65. Foppl, A., Vorlesungen iiber Technische Mechanik, Bd. 3. Leipzig: BG Teubner: 1907.
66. Hencky, H. J. Z. M. P., Uber den Spannungszustand in Kreisrunder Platten mit verschwindender Biegesteifigkeit. **1915**, *163*, 311.
67. ABAQUS, C., Analysis user's manual, Version 6.12. ABAQUS: 2012.
68. Zhang, B.; Liao, X.; Chen, Y.; Xiao, H.; Ni, Y.; Chen, X., Rapid Programmable Nanodroplet Motion on a Strain-Gradient Surface. *Langmuir* **2019**, *35* (7), 2865-2870.
69. Ju, J.; Zheng, Y.; Jiang, L., Bioinspired one-dimensional materials for directional liquid transport. *Accounts of chemical research* **2014**, *47* (8), 2342-2352.
70. Feng, L.; Li, S.; Li, Y.; Li, H.; Zhang, L.; Zhai, J.; Song, Y.; Liu, B.; Jiang, L.; Zhu, D., Super-hydrophobic surfaces: from natural to artificial. *Advanced materials* **2002**, *14* (24), 1857-1860.
71. Gao, X.; Jiang, L., Biophysics: water-repellent legs of water striders. *Nature* **2004**, *432* (7013), 36.
72. Sun, T.; Feng, L.; Gao, X.; Jiang, L., Bioinspired surfaces with special wettability. *Accounts of chemical research* **2005**, *38* (8), 644-652.
73. Sun, M.; Watson, G. S.; Zheng, Y.; Watson, J. A.; Liang, A., Wetting properties on nanostructured surfaces of cicada wings. *Journal of Experimental Biology* **2009**, *212* (19), 3148-3155.
74. Zheng, Y.; Gao, X.; Jiang, L., Directional adhesion of superhydrophobic butterfly

- wings. *Soft Matter* **2007**, *3* (2), 178-182.
75. Zhao, B.; Moore, J. S.; Beebe, D. J., Surface-directed liquid flow inside microchannels. *Science* **2001**, *291* (5506), 1023-1026.
 76. Cui, Y.; Li, D.; Bai, H., Bioinspired smart materials for directional liquid transport. *Industrial & Engineering Chemistry Research* **2017**, *56* (17), 4887-4897.
 77. Xu, B.; Qiao, Y.; Li, Y.; Zhou, Q.; Chen, X., An electroactuation system based on nanofluids. *Applied Physics Letters* **2011**, *98* (22), 221909.
 78. Hosseini, S.; Tafreshi, H. V., On the importance of fibers' cross-sectional shape for air filters operating in the slip flow regime. *Powder technology* **2011**, *212* (3), 425-431.
 79. Hernandez, S. C.; Bennett, C. J.; Junkermeier, C. E.; Tsoi, S. D.; Bezares, F. J.; Stine, R.; Robinson, J. T.; Lock, E. H.; Boris, D. R.; Pate, B. D., Chemical gradients on graphene to drive droplet motion. *Acs Nano* **2013**, *7* (6), 4746-4755.
 80. Wei, N.; Lv, C.; Xu, Z., Wetting of graphene oxide: A molecular dynamics study. *Langmuir* **2014**, *30* (12), 3572-3578.
 81. Sun, C.; Zhao, X.-W.; Han, Y.-H.; Gu, Z.-Z., Control of water droplet motion by alteration of roughness gradient on silicon wafer by laser surface treatment. *Thin Solid Films* **2008**, *516* (12), 4059-4063.
 82. Malvadkar, N. A.; Hancock, M. J.; Sekeroglu, K.; Dressick, W. J.; Demirel, M. C., An engineered anisotropic nanofilm with unidirectional wetting properties. *Nature materials* **2010**, *9* (12), 1023.
 83. Lv, C.; Hao, P., Driving droplet by scale effect on microstructured hydrophobic surfaces. *Langmuir* **2012**, *28* (49), 16958-16965.
 84. Gunji, M.; Washizu, M., Self-propulsion of a water droplet in an electric field. *Journal of Physics D: Applied Physics* **2005**, *38* (14), 2417.
 85. Yuan, Z.; Wang, Y.; Chen, D., Preparation and characterization of thermo-, pH-, and magnetic-field-responsive organic/inorganic hybrid microgels based on poly (ethylene glycol). *Journal of materials science* **2014**, *49* (8), 3287-3296.
 86. Daniel, S.; Chaudhury, M. K.; Chen, J. C., Fast drop movements resulting from the phase change on a gradient surface. *Science* **2001**, *291* (5504), 633-636.
 87. Suzuki, A.; Tanaka, T., Phase transition in polymer gels induced by visible light. *Nature* **1990**, *346* (6282), 345.
 88. Toh, W.; Ng, T. Y.; Hu, J.; Liu, Z., Mechanics of inhomogeneous large deformation of photo-thermal sensitive hydrogels. *International Journal of Solids and Structures* **2014**, *51* (25-26), 4440-4451.
 89. Lv, C.; Chen, C.; Chuang, Y.-C.; Tseng, F.-G.; Yin, Y.; Grey, F.; Zheng, Q., Substrate curvature gradient drives rapid droplet motion. *Physical review letters* **2014**, *113* (2), 026101.
 90. Bissett, M. A.; Tsuji, M.; Ago, H., Strain engineering the properties of graphene and other two-dimensional crystals. *Physical Chemistry Chemical Physics* **2014**, *16* (23), 11124-11138.
 91. Si, C.; Sun, Z.; Liu, F., Strain engineering of graphene: a review. *Nanoscale* **2016**, *8* (6), 3207-3217.
 92. Raeber, G.; Lutolf, M.; Hubbell, J., Part II: Fibroblasts preferentially migrate in the direction of principal strain. *Biomechanics and modeling in mechanobiology* **2008**, *7* (3), 215-225.
 93. Xu, B.; Qiao, Y.; Chen, X., Mitigating impact/blast energy via a novel nanofluidic

energy capture mechanism. *Journal of the Mechanics and Physics of Solids* **2014**, *62*, 194-208.

94. Huang, Y.; Zhu, S.; Li, T., Directional transport of molecular mass on graphene by straining. *Extreme Mechanics Letters* **2014**, *1*, 83-89.

95. Wang, J.; Feng, S. P.; Yang, Y.; Hau, N. Y.; Munro, M.; Ferreira-Yang, E.; Chen, G., "Thermal Charging" Phenomenon in Electrical Double Layer Capacitors. *Nano Lett* **2015**, *15* (9), 5784-90.

96. Falk, K.; Sedlmeier, F.; Joly, L.; Netz, R. R.; Bocquet, L., Molecular origin of fast water transport in carbon nanotube membranes: superlubricity versus curvature dependent friction. *Nano letters* **2010**, *10* (10), 4067-4073.

97. Liao, X.; Hao, F.; Xiao, H.; Chen, X., Effects of intrinsic strain on the structural stability and mechanical properties of phosphorene nanotubes. *Nanotechnology* **2016**, *27* (21), 215701.

98. Geim, A. K.; Novoselov, K. S., The rise of graphene. *Nat Mater* **2007**, *6* (3), 183-191.

99. Jin, C.; Lin, F.; Suenaga, K.; Iijima, S., Fabrication of a freestanding boron nitride single layer and its defect assignments. *Physical review letters* **2009**, *102* (19), 195505.

100. Mirnezhad, M.; Ansari, R.; Rouhi, H., Mechanical properties of multilayer boron nitride with different stacking orders. *Superlattices and Microstructures* **2013**, *53*, 223-231.

101. Radisavljevic, B.; Radenovic, A.; Brivio, J.; Giacometti, V.; Kis, A., Single-layer MoS₂ transistors. *Nature nanotechnology* **2011**, *6* (3), 147-150.

102. Tans, S. J.; Verschueren, A. R.; Dekker, C., Room-temperature transistor based on a single carbon nanotube. *Nature* **1998**, *393* (6680), 49-52.

103. Chopra, N. G.; Luyken, R.; Cherrey, K.; Crespi, V. H.; Cohen, M. L.; Louie, S. G.; Zettl, A., Boron nitride nanotubes. *Science* **1995**, *269* (5226), 966-967.

104. Ansari, R.; Mirnezhad, M.; Rouhi, H., Mechanical properties of chiral silicon carbide nanotubes under hydrogen adsorption: a molecular mechanics approach. *Nano* **2014**, *9* (04), 1450043.

105. Ansari, R.; Rouhi, H.; Mirnezhad, M., Stability analysis of boron nitride nanotubes via a combined continuum-atomistic model. *Scientia Iranica. Transaction F, Nanotechnology* **2013**, *20* (6), 2314.

106. Wang, Q.; Varadan, V., Stability analysis of carbon nanotubes via continuum models. *Smart Materials and Structures* **2005**, *14* (1), 281.

107. Ansari, R.; Ajori, S., Molecular dynamics study of the torsional vibration characteristics of boron-nitride nanotubes. *Physics Letters A* **2014**, *378* (38), 2876-2880.

108. Xiang, Y.; Shen, H.-S., Shear buckling of rippled graphene by molecular dynamics simulation. *Materials Today Communications* **2015**, *3*, 149-155.

109. Kulathunga, D. D. T. K.; Ang, K. K., Modeling and simulation of buckling of embedded carbon nanotubes. *Computational Materials Science* **2014**, *81*, 233-238.

110. Martel, R.; Schmidt, T.; Shea, H.; Hertel, T.; Avouris, P., Single- and multi-wall carbon nanotube field-effect transistors. *Applied Physics Letters* **1998**, *73* (17), 2447-2449.

111. Zhao, M.; Xia, Y.; Li, F.; Zhang, R.; Lee, S.-T., Strain energy and electronic structures of silicon carbide nanotubes: density functional calculations. *Physical Review B* **2005**, *71* (8), 085312.

112. Appalakondaiah, S.; Vaitheeswaran, G.; Lebègue, S.; Christensen, N. E.; Svane, A., Effect of van der Waals interactions on the structural and elastic properties of black

- phosphorus. *Physical Review B* **2012**, *86* (3), 035105.
113. Andres, C.-G.; Leonardo, V.; Elsa, P.; Joshua, O. I.; Narasimha-Acharya, K. L.; Sofya, I. B.; Dirk, J. G.; Michele, B.; Gary, A. S.; Alvarez, J. V.; Henny, W. Z.; Palacios, J. J.; Herre, S. J. v. d. Z., Isolation and characterization of few-layer black phosphorus. *2D Materials* **2014**, *1* (2), 025001.
114. Lu, W.; Nan, H.; Hong, J.; Chen, Y.; Zhu, C.; Liang, Z.; Ma, X.; Ni, Z.; Jin, C.; Zhang, Z., Plasma-assisted fabrication of monolayer phosphorene and its Raman characterization. *Nano Research* **2014**, *7* (6), 853-859.
115. Brent, J. R.; Savjani, N.; Lewis, E. A.; Haigh, S. J.; Lewis, D. J.; O'Brien, P., Production of few-layer phosphorene by liquid exfoliation of black phosphorus. *Chemical Communications* **2014**, *50* (87), 13338-13341.
116. Li, L.; Yu, Y.; Ye, G. J.; Ge, Q.; Ou, X.; Wu, H.; Feng, D.; Chen, X. H.; Zhang, Y., Black phosphorus field-effect transistors. *Nat Nano* **2014**, *9* (5), 372-377.
117. Fei, R.; Yang, L., Strain-engineering the anisotropic electrical conductance of few-layer black phosphorus. *Nano letters* **2014**, *14* (5), 2884-2889.
118. Fei, R.; Faghaninia, A.; Soklaski, R.; Yan, J. A.; Lo, C.; Yang, L., Enhanced thermoelectric efficiency via orthogonal electrical and thermal conductances in phosphorene. *Nano Lett* **2014**, *14* (11), 6393-9.
119. Balendhran, S.; Walia, S.; Nili, H.; Sriram, S.; Bhaskaran, M., Elemental analogues of graphene: silicene, germanene, stanene, and phosphorene. *Small* **2015**, *11* (6), 640-52.
120. Wei, Q.; Peng, X., Superior mechanical flexibility of phosphorene and few-layer black phosphorus. *Applied Physics Letters* **2014**, *104* (25), 251915.
121. Jiang, J.-W.; Park, H. S., Negative poisson's ratio in single-layer black phosphorus. *Nat Commun* **2014**, *5*.
122. Sha, Z.-D.; Pei, Q.-X.; Ding, Z.; Jiang, J.-W.; Zhang, Y.-W., Mechanical properties and fracture behavior of single-layer phosphorene at finite temperatures. *Journal of Physics D: Applied Physics* **2015**, *48* (39), 395303.
123. Li, W.; Yang, Y.; Zhang, G.; Zhang, Y.-W., Ultrafast and Directional Diffusion of Lithium in Phosphorene for High-Performance Lithium-Ion Battery. *Nano letters* **2015**, *15* (3), 1691-1697.
124. Ling, X.; Wang, H.; Huang, S.; Xia, F.; Dresselhaus, M. S., The renaissance of black phosphorus. *Proceedings of the National Academy of Sciences* **2015**, *112* (15), 4523-4530.
125. Seifert, G.; Hernández, E., Theoretical prediction of phosphorus nanotubes. *Chemical Physics Letters* **2000**, *318* (4-5), 355-360.
126. Guan, J.; Zhu, Z.; Tománek, D., High Stability of Faceted Nanotubes and Fullerenes of Multiphase Layered Phosphorus: A Computational Study. *Physical Review Letters* **2014**, *113* (22).
127. Guo, H.; Lu, N.; Dai, J.; Wu, X.; Zeng, X. C., Phosphorene Nanoribbons, Phosphorus Nanotubes, and van der Waals Multilayers. *The Journal of Physical Chemistry C* **2014**, *118* (25), 14051-14059.
128. Pan, D.-X.; Wang, T.-C.; Guo, W.-L., Bending-induced phase transition in monolayer black phosphorus. *Chinese Physics B* **2015**, *24* (8), 086401.
129. Cabria, I.; Mintmire, J. W., Stability and electronic structure of phosphorus nanotubes. *EPL (Europhysics Letters)* **2004**, *65* (1), 82.

130. Hu, T.; Hashmi, A.; Hong, J., Geometry, electronic structures and optical properties of phosphorus nanotubes. *Nanotechnology* **2015**, *26* (41), 415702.
131. Aierken, Y.; Leenaerts, O.; Peeters, F. M., Defect-induced faceted blue phosphorene nanotubes. *Physical Review B* **2015**, *92* (10).
132. Yu, S.; Zhu, H.; Eshun, K.; Arab, A.; Badwan, A.; Li, Q., A computational study of the electronic properties of one-dimensional armchair phosphorene nanotubes. *Journal of Applied Physics* **2015**, *118* (16), 164306.
133. Plimpton, S., Fast Parallel Algorithms for Short-Range Molecular Dynamics. *Journal of Computational Physics* **1995**, *117* (1), 1-19.
134. Jin-Wu, J., Parametrization of Stillinger–Weber potential based on valence force field model: application to single-layer MoS₂ and black phosphorus. *Nanotechnology* **2015**, *26* (31), 315706.
135. Yang, Z.; Zhao, J.; Wei, N., Temperature-dependent mechanical properties of monolayer black phosphorus by molecular dynamics simulations. *Applied Physics Letters* **2015**, *107* (2), 023107.
136. Purcell, S.; Vincent, P.; Journet, C.; Binh, V. T., Hot nanotubes: stable heating of individual multiwall carbon nanotubes to 2000 K induced by the field-emission current. *Physical review letters* **2002**, *88* (10), 105502.
137. Nardelli, M. B.; Yakobson, B. I.; Bernholc, J., Brittle and Ductile Behavior in Carbon Nanotubes. *Physical Review Letters* **1998**, *81* (21), 4656-4659.
138. Liew, K. M.; He, X. Q.; Wong, C. H., On the study of elastic and plastic properties of multi-walled carbon nanotubes under axial tension using molecular dynamics simulation. *Acta Materialia* **2004**, *52* (9), 2521-2527.
139. Moon, W. H.; Ham, J. K.; Hwang, H. J. In *Mechanical properties of SiC nanotubes*, Technical Proceedings of the 2003 Nanotechnology Conference and Trade Show, 2003; pp 158-161.
140. Ansari, R.; Rouhi, S.; Aryayi, M.; Mirnezhad, M., On the buckling behavior of single-walled silicon carbide nanotubes. *Scientia Iranica* **2012**, *19* (6), 1984-1990.
141. Iijima, S.; Ichihashi, T., Single-shell carbon nanotubes of 1-nm diameter. **1993**.
142. Chang, T.; Gao, H., Size-dependent elastic properties of a single-walled carbon nanotube via a molecular mechanics model. *Journal of the Mechanics and Physics of Solids* **2003**, *51* (6), 1059-1074.
143. Wang, L.; Zheng, Q.; Liu, J. Z.; Jiang, Q., Size Dependence of the Thin-Shell Model for Carbon Nanotubes. *Physical Review Letters* **2005**, *95* (10), 105501.
144. Liao, X.; Xiao, H.; Lu, X.; Chen, Y.; Shi, X.; Chen, X., Closed-edged bilayer phosphorene nanoribbons producing from collapsing armchair phosphorene nanotubes. *Nanotechnology* **2018**, *29* (8), 085707.
145. Guan, J.; Zhu, Z.; Tomanek, D., Phase coexistence and metal-insulator transition in few-layer phosphorene: a computational study. *Phys Rev Lett* **2014**, *113* (4), 046804.
146. Hao, F.; Chen, X., Mechanical properties of phosphorene nanoribbons and oxides. *Journal of Applied Physics* **2015**, *118* (23), 234304.
147. Han, X.; Stewart, H. M.; Shevlin, S. A.; Catlow, C. R.; Guo, Z. X., Strain and orientation modulated bandgaps and effective masses of phosphorene nanoribbons. *Nano Lett* **2014**, *14* (8), 4607-14.
148. Zhang, J.; Liu, H. J.; Cheng, L.; Wei, J.; Liang, J. H.; Fan, D. D.; Shi, J.; Tang, X. F.; Zhang, Q. J., Phosphorene nanoribbon as a promising candidate for thermoelectric

- applications. *Sci Rep* **2014**, *4*, 6452.
149. Lee, S.; Yang, F.; Suh, J.; Yang, S.; Lee, Y.; Li, G.; Sung Choe, H.; Suslu, A.; Chen, Y.; Ko, C.; Park, J.; Liu, K.; Li, J.; Hippalgaonkar, K.; Urban, J. J.; Tongay, S.; Wu, J., Anisotropic in-plane thermal conductivity of black phosphorus nanoribbons at temperatures higher than 100 K. *Nat Commun* **2015**, *6*, 8573.
150. Masih Das, P.; Danda, G.; Cupo, A.; Parkin, W. M.; Liang, L.; Kharche, N.; Ling, X.; Huang, S.; Dresselhaus, M. S.; Meunier, V.; Drndic, M., Controlled Sculpture of Black Phosphorus Nanoribbons. *ACS Nano* **2016**, *10* (6), 5687-95.
151. Hasegawa, M.; Nishidate, K.; Yoshimoto, N., Collapsed armchair single-walled carbon nanotubes as an analog of closed-edged bilayer graphene nanoribbons. *Physical Review B* **2015**, *92* (24).
152. Li, Y., Edge-closed graphene nanoribbons fabricated by spontaneous collapse of few-walled carbon nanotubes. *Phys Chem Chem Phys* **2014**, *16* (5), 1921-9.
153. Barzegar, H. R.; Yan, A.; Coh, S.; Gracia-Espino, E.; Dunn, G.; Wagberg, T.; Louie, S. G.; Cohen, M. L.; Zettl, A., Electrostatically Driven Nanoballoon Actuator. *Nano Lett* **2016**, *16* (11), 6787-6791.
154. Lu, J. Q.; Wu, J.; Duan, W.; Liu, F.; Zhu, B. F.; Gu, B. L., Metal-to-semiconductor transition in squashed armchair carbon nanotubes. *Phys Rev Lett* **2003**, *90* (15), 156601.
155. Lammert, P. E.; Zhang, P.; Crespi, V. H., Gapping by squashing: metal-insulator and insulator-metal transitions in collapsed carbon nanotubes. *Phys Rev Lett* **2000**, *84* (11), 2453-6.
156. Wang, X.; Jones, A. M.; Seyler, K. L.; Tran, V.; Jia, Y.; Zhao, H.; Wang, H.; Yang, L.; Xu, X.; Xia, F., Highly anisotropic and robust excitons in monolayer black phosphorus. *Nat Nanotechnol* **2015**, *10* (6), 517-21.
157. Baringhaus, J.; Ruan, M.; Edler, F.; Tejada, A.; Sicot, M.; Taleb-Ibrahimi, A.; Li, A. P.; Jiang, Z.; Conrad, E. H.; Berger, C.; Tegenkamp, C.; de Heer, W. A., Exceptional ballistic transport in epitaxial graphene nanoribbons. *Nature* **2014**, *506* (7488), 349-54.
158. Xiao, H.; Shi, X.; Hao, F.; Liao, X.; Zhang, Y.; Chen, X., Development of a Transferable Reactive Force Field of P/H Systems: Application to the Chemical and Mechanical Properties of Phosphorene. *J Phys Chem A* **2017**.
159. Perdew, J. P.; Burke, K.; Ernzerhof, M., Generalized Gradient Approximation Made Simple. *Physical Review Letters* **1996**, *77* (18), 3865-3868.
160. Giannozzi, P.; Baroni, S.; Bonini, N.; Calandra, M.; Car, R.; Cavazzoni, C.; Ceresoli, D.; Chiarotti, G. L.; Cococcioni, M.; Dabo, I.; Dal Corso, A.; de Gironcoli, S.; Fabris, S.; Fratesi, G.; Gebauer, R.; Gerstmann, U.; Gougoussis, C.; Kokalj, A.; Lazzeri, M.; Martin-Samos, L.; Marzari, N.; Mauri, F.; Mazzarello, R.; Paolini, S.; Pasquarello, A.; Paulatto, L.; Sbraccia, C.; Scandolo, S.; Sclauzero, G.; Seitsonen, A. P.; Smogunov, A.; Umari, P.; Wentzcovitch, R. M., QUANTUM ESPRESSO: a modular and open-source software project for quantum simulations of materials. *J Phys Condens Matter* **2009**, *21* (39), 395502.
161. Morgan Stewart, H.; Shevlin, S. A.; Catlow, C. R.; Guo, Z. X., Compressive straining of bilayer phosphorene leads to extraordinary electron mobility at a new conduction band edge. *Nano Lett* **2015**, *15* (3), 2006-10.
162. Wang, C.; Xia, Q.; Nie, Y.; Guo, G., Strain-induced gap transition and anisotropic Dirac-like cones in monolayer and bilayer phosphorene. *Journal of Applied Physics* **2015**, *117* (12), 124302.

163. Allec, S. I.; Wong, B. M., Inconsistencies in the Electronic Properties of Phosphorene Nanotubes: New Insights from Large-Scale DFT Calculations. *J Phys Chem Lett* **2016**, *7* (21), 4340-4345.
164. Dai, J.; Zeng, X. C., Bilayer Phosphorene: Effect of Stacking Order on Bandgap and Its Potential Applications in Thin-Film Solar Cells. *J Phys Chem Lett* **2014**, *5* (7), 1289-93.
165. Yin, J.; Chen, X.; Sheinman, I., Anisotropic buckling patterns in spheroidal film/substrate systems and their implications in some natural and biological systems. *Journal of the Mechanics and Physics of Solids* **2009**, *57* (9), 1470-1484.
166. Bargel, H.; Neinhuis, C., Tomato (*Lycopersicon esculentum* Mill.) fruit growth and ripening as related to the biomechanical properties of fruit skin and isolated cuticle. *Journal of Experimental Botany* **2005**, *56* (413), 1049-1060.
167. Dervaux, J.; Ben Amar, M., Morphogenesis of Growing Soft Tissues. *Physical Review Letters* **2008**, *101* (6).
168. Day, R. W.; Mankin, M. N.; Lieber, C. M., Plateau-Rayleigh crystal growth of nanowire heterostructures: Strain-modified surface chemistry and morphological control in 1, 2 and 3 dimensions. *Nano letters* **2016**.
169. Chen, X.; Yin, J., Buckling patterns of thin films on curved compliant substrates with applications to morphogenesis and three-dimensional micro-fabrication. *Soft Matter* **2010**, *6* (22), 5667-5680.
170. and, Y. X.; Whitesides, G. M., SOFT LITHOGRAPHY. *Annual Review of Materials Science* **1998**, *28* (1), 153-184.
171. Huang, Z. Y.; Hong, W.; Suo, Z., Nonlinear analyses of wrinkles in a film bonded to a compliant substrate. *Journal of the Mechanics and Physics of Solids* **2005**, *53* (9), 2101-2118.
172. Audoly, B.; Boudaoud, A., Buckling of a stiff film bound to a compliant substrate—Part I. *Journal of the Mechanics and Physics of Solids* **2008**, *56* (7), 2401-2421.
173. Song, J.; Jiang, H.; Liu, Z. J.; Khang, D. Y.; Huang, Y.; Rogers, J. A.; Lu, C.; Koh, C. G., Buckling of a stiff thin film on a compliant substrate in large deformation. *International Journal of Solids and Structures* **2008**, *45* (10), 3107-3121.
174. Jin, H.-C.; Abelson, J. R.; Erhardt, M. K.; Nuzzo, R. G., Soft lithographic fabrication of an image sensor array on a curved substrate. *Journal of Vacuum Science & Technology B* **2004**, *22* (5), 2548-2551.
175. Cao, G.; Chen, X.; Li, C.; Ji, A.; Cao, Z., Self-Assembled Triangular and Labyrinth Buckling Patterns of Thin Films on Spherical Substrates. *Physical Review Letters* **2008**, *100* (3).
176. Moon, M.-W.; Lee, S. H.; Sun, J.-Y.; Oh, K. H.; Vaziri, A.; Hutchinson, J. W., Controlled formation of nanoscale wrinkling patterns on polymers using focused ion beam. *Scripta Materialia* **2007**, *57* (8), 747-750.
177. Li, B.; Cao, Y.-P.; Feng, X.-Q.; Gao, H., Mechanics of morphological instabilities and surface wrinkling in soft materials: a review. *Soft Matter* **2012**, *8* (21), 5728-5745.
178. Li, C.; Zhang, X.; Cao, Z., Triangular and Fibonacci Number Patterns Driven by Stress on Core/Shell Microstructures. *Science* **2005**, *309* (5736), 909-911.
179. Li, C. R.; Dong, W. J.; Gao, L.; Cao, Z. X., Stressed triangular lattices on microsized spherical surfaces and their defect management. *Applied Physics Letters* **2008**, *93* (3), 034108.

180. Li, C.-R.; Ji, A.-L.; Gao, L.; Cao, Z.-X., Stressed Triangular Tessellations and Fibonacci Parastichous Spirals on Ag Core/SiO₂ Shell Microstructures. *Advanced Materials* **2009**, *21* (45), 4652-4657.
181. Li, B.; Jia, F.; Cao, Y.-P.; Feng, X.-Q.; Gao, H., Surface Wrinkling Patterns on a Core-Shell Soft Sphere. *Physical Review Letters* **2011**, *106* (23).
182. Yin, J.; Cao, Z.; Li, C.; Sheinman, I.; Chen, X., Stress-driven buckling patterns in spheroidal core/shell structures. *Proc Natl Acad Sci U S A* **2008**, *105* (49), 19132-5.
183. Kwon, S.; Chen, Z. C. Y.; Kim, J.-H.; Xiang, J., Misfit-Guided Self-Organization of Anticorrelated Ge Quantum Dot Arrays on Si Nanowires. *Nano Letters* **2012**, *12* (9), 4757-4762.
184. Asaro, R. J.; Tiller, W. A., Interface morphology development during stress corrosion cracking: Part I. Via surface diffusion. *Metallurgical Transactions* **3** (7), 1789-1796.
185. Grinfeld, M., Equilibrium Shape and Instabilities of Deformable Elastic Crystals. *Lecture given in Heirot-Watt University, Edinburgh* **1989**.
186. Srolovitz, D. J., On the stability of surfaces of stressed solids. *Acta Metallurgica* **1989**, *37* (2), 621-625.
187. Ozkan, C. S.; Nix, W. D.; Gao, H., Strain relaxation and defect formation in heteroepitaxial Si_{1-x}Ge_x films via surface roughening induced by controlled annealing experiments. *Applied Physics Letters* **1997**, *70* (17), 2247-2249.
188. Eaglesham, D. J.; Cerullo, M., Dislocation-free Stranski-Krastanow growth of Ge on Si(100). *Physical Review Letters* **1990**, *64* (16), 1943-1946.
189. Pan, L.; Lew, K.-K.; Redwing, J. M.; Dickey, E. C., Stranski-Krastanow Growth of Germanium on Silicon Nanowires. *Nano Letters* **2005**, *5* (6), 1081-1085.
190. Day, R. W.; Mankin, M. N.; Gao, R.; No, Y.-S.; Kim, S.-K.; Bell, D. C.; Park, H.-G.; Lieber, C. M., Plateau-Rayleigh crystal growth of periodic shells on one-dimensional substrates. *Nature nanotechnology* **2015**, *10* (4), 345-352.
191. Spencer, B. J.; Voorhees, P. W.; Davis, S. H., Morphological instability in epitaxially strained dislocation-free solid films: Linear stability theory. *Journal of Applied Physics* **1993**, *73* (10), 4955.
192. Gao, H.; Nix, W. D., SURFACE ROUGHENING OF HETEROEPITAXIAL THIN FILMS. *Annual Review of Materials Science* **1999**, *29* (1), 173-209.
193. Wang, H.; Upmanyu, M.; Ciobanu, C. V., Morphology of Epitaxial Core-Shell Nanowires. *Nano Letters* **2008**, *8* (12), 4305-4311.
194. Duan, H. L.; Weissmüller, J.; Wang, Y., Instabilities of core-shell heterostructured cylinders due to diffusions and epitaxy: Spheroidization and blossom of nanowires. *Journal of the Mechanics and Physics of Solids* **2008**, *56* (5), 1831-1851.
195. Tersoff, J.; LeGoues, F. K., Competing relaxation mechanisms in strained layers. *Physical Review Letters* **1994**, *72* (22), 3570-3573.
196. Zhang, Y. W.; Bower, A. F., Numerical simulations of island formation in a coherent strained epitaxial thin film system. *Journal of the Mechanics and Physics of Solids* **1999**, *47* (11), 2273-2297.
197. Long, F.; Gill, S. P. A.; Cocks, A. C. F., Effect of surface-energy anisotropy on the kinetics of quantum dot formation. *Physical Review B* **2001**, *64* (12), 121307.
198. Guo, J. Y.; Zhang, Y. W.; Shenoy, V. B., Morphological evolution and ordered quantum structure formation in heteroepitaxial core-shell nanowires. *ACS Nano* **2010**, *4*

(8), 4455-62.

199. Wang, Y. U.; Jin, Y. M.; Khachaturyan, A. G., Phase field microelasticity modeling of surface instability of heteroepitaxial thin films. *Acta Materialia* **2004**, *52* (1), 81-92.
200. Ni, Y.; He, L. H.; Soh, A. K., Three-dimensional phase field simulation for surface roughening of heteroepitaxial films with elastic anisotropy. *Journal of Crystal Growth* **2005**, *284* (1-2), 281-292.
201. Ni, Y.; He, L. H., Spontaneous formation of vertically anticorrelated epitaxial islands on ultrathin substrates. *Applied Physics Letters* **2010**, *97* (26), 261911.
202. Ni, Y.; He, L. H.; Liao, X. B., Stress anisotropy controlled morphological evolution in core-shell nanowires. *Extreme Mechanics Letters*.
203. Mullins, W. W.; Sekerka, R. F., Morphological Stability of a Particle Growing by Diffusion or Heat Flow. *Journal of Applied Physics* **1963**, *34* (2), 323-329.
204. Li, X.; Lowengrub, J.; Nie, Q.; Cristini, V.; Leo, P., Microstructure evolution in three-dimensional inhomogeneous elastic media. *Metallurgical and Materials Transactions A* **34** (7), 1421-1431.
205. Leo, P. H.; Iwan, J.; Alexander, D.; Sekerka, R. F., Elastic fields about a perturbed spherical inclusion. *Acta Metallurgica* **1985**, *33* (6), 985-989.
206. Colin, J., Morphological instability of two stressed spherical shells. *International Journal of Solids and Structures* **2007**, *44* (10), 3218-3230.
207. Hu, J.; Ouyang, M.; Yang, P.; Lieber, C. M., Controlled growth and electrical properties of heterojunctions of carbon nanotubes and silicon nanowires. *Nature* **1999**, *399* (6731), 48-51.
208. Gao, L.; Ji, A.; Lu, N.; Li, C.; Cao, Z., Fast vapor phase growth of SiO₂ nanowires via surface-flow on Ag core/SiO₂ shell structure. *AIP Advances* **2012**, *2* (1), 012187.
209. Wang, Y. U.; Jin, Y. M.; Khachaturyan, A. G., Phase field microelasticity theory and modeling of elastically and structurally inhomogeneous solid. *Journal of Applied Physics* **2002**, *92* (3), 1351-1360.
210. Shen, C.; Chen, Q.; Wen, Y. H.; Simmons, J. P.; Wang, Y., Increasing length scale of quantitative phase field modeling of growth-dominant or coarsening-dominant process. *Scripta Materialia* **2004**, *50* (7), 1023-1028.
211. Bowden, N.; Brittain, S.; Evans, A. G.; Hutchinson, J. W.; Whitesides, G. M., Spontaneous formation of ordered structures in thin films of metals supported on an elastomeric polymer. *Nature* **1998**, *393* (6681), 146-149.
212. Mathger, L. M.; Denton, E. J.; Marshall, N. J.; Hanlon, R. T., Mechanisms and behavioural functions of structural coloration in cephalopods. *J R Soc Interface* **2009**, *6* Suppl 2, S149-63.
213. Khang, D.-Y.; Jiang, H.; Huang, Y.; Rogers, J. A., A Stretchable Form of Single-Crystal Silicon for High-Performance Electronics on Rubber Substrates. *Science* **2006**, *311* (5758), 208-212.
214. Chan, E. P.; Smith, E. J.; Hayward, R. C.; Crosby, A. J., Surface Wrinkles for Smart Adhesion. *Advanced Materials* **2008**, *20* (4), 711-716.
215. Yang, S.; Khare, K.; Lin, P.-C., Harnessing Surface Wrinkle Patterns in Soft Matter. *Advanced Functional Materials* **2010**, *20* (16), 2550-2564.
216. Chen, X.; Hutchinson, J. W., A family of herringbone patterns in thin films. *Scripta Materialia* **2004**, *50* (6), 797-801.
217. Cao, C.; Chan, H. F.; Zang, J.; Leong, K. W.; Zhao, X., Harnessing localized

- ridges for high-aspect-ratio hierarchical patterns with dynamic tunability and multifunctionality. *Adv Mater* **2014**, *26* (11), 1763-70.
218. Singamaneni, S.; McConney, M. E.; Tsukruk, V. V., Spontaneous self-folding in confined ultrathin polymer gels. *Adv Mater* **2010**, *22* (11), 1263-8.
219. Kim, J. B.; Kim, P.; Pégard, N. C.; Oh, S. J.; Kagan, C. R.; Fleischer, J. W.; Stone, H. A.; Loo, Y.-L., Wrinkles and deep folds as photonic structures in photovoltaics. *Nature Photonics* **2012**, *6* (5), 327-332.
220. Brau, F.; Damman, P.; Diamant, H.; Witten, T. A., Wrinkle to fold transition: influence of the substrate response. *Soft Matter* **2013**, *9* (34), 8177.
221. Gurmessa, B. J.; Croll, A. B., Localization in an idealized heterogeneous elastic sheet. *Soft Matter* **2017**, *13* (9), 1764-1772.
222. Zhao, Y.; Huang, W. M.; Fu, Y. Q., Formation of micro/nano-scale wrinkling patterns atop shape memory polymers. *Journal of Micromechanics and Microengineering* **2011**, *21* (6), 067007.
223. Vandeparre, H.; Gabriele, S.; Brau, F.; Gay, C.; Parker, K. K.; Damman, P., Hierarchical wrinkling patterns. *Soft Matter* **2010**, *6* (22), 5751-5756.
224. Paci, J. T.; Chapman, C. T.; Lee, W. K.; Odom, T. W.; Schatz, G. C., Wrinkles in Polytetrafluoroethylene on Polystyrene: Persistence Lengths and the Effect of Nano-inclusions. *ACS Appl Mater Interfaces* **2017**, *9* (10), 9079-9088.
225. Zheng, Y.; Li, G.-Y.; Cao, Y.; Feng, X.-Q., Wrinkling of a stiff film resting on a fiber-filled soft substrate and its potential application as tunable metamaterials. *Extreme Mechanics Letters* **2017**, *11*, 121-127.
226. Guttag, M.; Boyce, M. C., Locally and Dynamically Controllable Surface Topography Through the Use of Particle-Enhanced Soft Composites. *Advanced Functional Materials* **2015**, *25* (24), 3641-3647.
227. Timoshenko, S. P.; Gere, J. M., Theory of elastic stability. 1961. *McGrawHill-Kogakusha Ltd, Tokyo* **1961**, 109.
228. Cao, Y.; Hutchinson, J. W., Wrinkling Phenomena in Neo-Hookean Film/Substrate Bilayers. *Journal of Applied Mechanics* **2012**, *79* (3), 031019.
229. Jin, L.; Takei, A.; Hutchinson, J. W., Mechanics of wrinkle/ridge transitions in thin film/substrate systems. *Journal of the Mechanics and Physics of Solids* **2015**, *81*, 22-40.
230. Pocivavsek, L.; Dellsy, R.; Kern, A.; Johnson, S.; Lin, B.; Lee, K. Y. C.; Cerda, E., Stress and Fold Localization in Thin Elastic Membranes. *Science* **2008**, *320* (5878), 912-916.
231. Zang, J.; Zhao, X.; Cao, Y.; Hutchinson, J. W., Localized ridge wrinkling of stiff films on compliant substrates. *Journal of the Mechanics and Physics of Solids* **2012**, *60* (7), 1265-1279.
232. Flores-Johnson, E. A.; Rupert, T. J.; Hemker, K. J.; Gianola, D. S.; Gan, Y., Modelling wrinkling interactions produced by patterned defects in metal thin films. *Extreme Mechanics Letters* **2015**, *4*, 175-185.
233. Yan, D.; Huangfu, D.; Zhang, K.; Hu, G., Wrinkling of the membrane with square rigid elements. *EPL (Europhysics Letters)* **2016**, *116* (2), 24005.
234. Shi, C.; Wang, T.; Liao, X.; Qie, B.; Yang, P.; Chen, M.; Wang, X.; Srinivasan, A.; Cheng, Q.; Ye, Q.; Li, A. C.; Chen, X.; Yang, Y., Accordion-like stretchable Li-ion batteries with high energy density. *Energy Storage Materials* **2019**, *17*, 136-142.
235. Qian, G.; Zhu, B.; Liao, X.; Zhai, H.; Srinivasan, A.; Fritz, N. J.; Cheng, Q.;

- Ning, M.; Qie, B.; Li, Y.; Yuan, S.; Zhu, J.; Chen, X.; Yang, Y., Bioinspired, Spine-Like, Flexible, Rechargeable Lithium-Ion Batteries with High Energy Density. *Adv Mater* **2018**, *30* (12), e1704947.
236. Liao, X.; Shi, C.; Wang, T.; Qie, B.; Chen, Y.; Yang, P.; Cheng, Q.; Zhai, H.; Chen, M.; Wang, X.; Chen, X.; Yang, Y., High-Energy-Density Foldable Battery Enabled by Zigzag-Like Design. *Advanced Energy Materials* **2018**.
237. Chen, J. G., Electrochemical CO₂ Reduction via Low-Valent Nickel Single-Atom Catalyst. *Joule* **2018**, *2* (4), 587-589.
238. Jiang, K.; Siahrostami, S.; Zheng, T.; Hu, Y.; Hwang, S.; Stavitski, E.; Peng, Y.; Dynes, J.; Gangisetty, M.; Su, D.; Attenkofer, K.; Wang, H., Isolated Ni single atoms in graphene nanosheets for high-performance CO₂ reduction. *Energy & Environmental Science* **2018**, *11* (4), 893-903.
239. Laitar, D. S.; Müller, P.; Sadighi, J. P. J. J. o. t. A. C. S., Efficient Homogeneous Catalysis in the Reduction of CO₂ to CO. **2005**, *127* (49), 17196-17197.
240. Schreier, M.; Héroguel, F.; Steier, L.; Ahmad, S.; Luterbacher, J. S.; Mayer, M. T.; Luo, J.; Grätzel, M., Solar conversion of CO₂ to CO using Earth-abundant electrocatalysts prepared by atomic layer modification of CuO. *Nature Energy* **2017**, *2* (7).
241. Li, J.; Chen, G.; Zhu, Y.; Liang, Z.; Pei, A.; Wu, C.-L.; Wang, H.; Lee, H. R.; Liu, K.; Chu, S.; Cui, Y., Efficient electrocatalytic CO₂ reduction on a three-phase interface. *Nature Catalysis* **2018**, *1* (8), 592-600.
242. Zhuang, T.-T.; Liang, Z.-Q.; Seifitokaldani, A.; Li, Y.; De Luna, P.; Burdyny, T.; Che, F.; Meng, F.; Min, Y.; Quintero-Bermudez, R.; Dinh, C. T.; Pang, Y.; Zhong, M.; Zhang, B.; Li, J.; Chen, P.-N.; Zheng, X.-L.; Liang, H.; Ge, W.-N.; Ye, B.-J.; Sinton, D.; Yu, S.-H.; Sargent, E. H., Steering post-C-C coupling selectivity enables high efficiency electroreduction of carbon dioxide to multi-carbon alcohols. *Nature Catalysis* **2018**, *1* (6), 421-428.
243. Zhang, Q.; Kang, J.; Wang, Y., Development of Novel Catalysts for Fischer-Tropsch Synthesis: Tuning the Product Selectivity. *ChemCatChem* **2010**, *2* (9), 1030-1058.
244. Kattel, S.; Liu, P.; Chen, J. G., Tuning Selectivity of CO₂ Hydrogenation Reactions at the Metal/Oxide Interface. *J Am Chem Soc* **2017**, *139* (29), 9739-9754.
245. Jiang, K.; Sandberg, R. B.; Akey, A. J.; Liu, X.; Bell, D. C.; Nørskov, J. K.; Chan, K.; Wang, H., Metal ion cycling of Cu foil for selective C-C coupling in electrochemical CO₂ reduction. *Nature Catalysis* **2018**, *1* (2), 111-119.
246. Wei, J.; Ge, Q.; Yao, R.; Wen, Z.; Fang, C.; Guo, L.; Xu, H.; Sun, J., Directly converting CO₂ into a gasoline fuel. *Nat Commun* **2017**, *8*, 15174.
247. Kho, E. T.; Tan, T. H.; Lovell, E.; Wong, R. J.; Scott, J.; Amal, R., A review on photo-thermal catalytic conversion of carbon dioxide. *Green Energy & Environment* **2017**, *2* (3), 204-217.
248. mod, E. C.; Roy, S.; Ernst, J.; Kharchenko, P. V.; Kheradpour, P.; Negre, N.; Eaton, M. L.; Landolin, J. M.; Bristow, C. A.; Ma, L.; Lin, M. F.; Washietl, S.; Arshinoff, B. I.; Ay, F.; Meyer, P. E.; Robine, N.; Washington, N. L.; Di Stefano, L.; Berezikov, E.; Brown, C. D.; Candeias, R.; Carlson, J. W.; Carr, A.; Jungreis, I.; Marbach, D.; Sealfon, R.; Tolstorukov, M. Y.; Will, S.; Alekseyenko, A. A.; Artieri, C.; Booth, B. W.; Brooks, A. N.; Dai, Q.; Davis, C. A.; Duff, M. O.; Feng, X.; Gorchakov, A. A.; Gu, T.; Henikoff, J. G.; Kapranov, P.; Li, R.; MacAlpine, H. K.; Malone, J.; Minoda, A.; Nordman, J.; Okamura, K.; Perry, M.; Powell, S. K.; Riddle, N. C.; Sakai, A.

- Samsonova, A.; Sandler, J. E.; Schwartz, Y. B.; Sher, N.; Spokony, R.; Sturgill, D.; van Baren, M.; Wan, K. H.; Yang, L.; Yu, C.; Feingold, E.; Good, P.; Guyer, M.; Lowdon, R.; Ahmad, K.; Andrews, J.; Berger, B.; Brenner, S. E.; Brent, M. R.; Cherbas, L.; Elgin, S. C.; Gingeras, T. R.; Grossman, R.; Hoskins, R. A.; Kaufman, T. C.; Kent, W.; Kuroda, M. I.; Orr-Weaver, T.; Perrimon, N.; Pirrotta, V.; Posakony, J. W.; Ren, B.; Russell, S.; Cherbas, P.; Graveley, B. R.; Lewis, S.; Micklem, G.; Oliver, B.; Park, P. J.; Celniker, S. E.; Henikoff, S.; Karpen, G. H.; Lai, E. C.; MacAlpine, D. M.; Stein, L. D.; White, K. P.; Kellis, M., Identification of functional elements and regulatory circuits by *Drosophila* modENCODE. *Science* **2010**, *330* (6012), 1787-97.
249. Tu, W.; Zhou, Y.; Zou, Z. J. A. M., Photocatalytic conversion of CO₂ into renewable hydrocarbon fuels: state-of-the-art accomplishment, challenges, and prospects. *2014*, *26* (27), 4607-4626.
250. Buelens, L. C.; Galvita, V. V.; Poelman, H.; Detavernier, C.; Marin, G. B., Super-dry reforming of methane intensifies CO₂ utilization via Le Chatelier's principle. *Science* **2016**, *354* (6311), 449-452.
251. Mondal, B.; Dey, A., Development of air-stable hydrogen evolution catalysts. *Chem Commun (Camb)* **2017**, *53* (55), 7707-7715.
252. Oughli, A. A.; Ruff, A.; Boralugodage, N. P.; Rodriguez-Macia, P.; Plumere, N.; Lubitz, W.; Shaw, W. J.; Schuhmann, W.; Rudiger, O., Dual properties of a hydrogen oxidation Ni-catalyst entrapped within a polymer promote self-defense against oxygen. *Nat Commun* **2018**, *9* (1), 864.
253. Argyle, M.; Bartholomew, C., Heterogeneous Catalyst Deactivation and Regeneration: A Review. *Catalysts* **2015**, *5* (1), 145-269.
254. Beuls, A.; Swalus, C.; Jacquemin, M.; Heyen, G.; Karelavic, A.; Ruiz, P., Methanation of CO₂: Further insight into the mechanism over Rh/γ-Al₂O₃ catalyst. *Applied Catalysis B: Environmental* **2012**, *113-114*, 2-10.
255. Frontera, P.; Macario, A.; Ferraro, M.; Antonucci, P., Supported Catalysts for CO₂ Methanation: A Review. *Catalysts* **2017**, *7* (12).
256. Greenhouse Gas Removal. <http://royalsociety.org/greenhouse-gas-removal> **2018**, (Royal Academy of Engineering).
257. Rochelle, G. T., Amine Scrubbing for CO₂ Capture. **2009**, *325* (5948), 1652-1654.
258. Sanz-Perez, E. S.; Murdock, C. R.; Didas, S. A.; Jones, C. W., Direct Capture of CO₂ from Ambient Air. *Chem Rev* **2016**, *116* (19), 11840-11876.
259. Goeppert, A.; Czaun, M.; Surya Prakash, G. K.; Olah, G. A., Air as the renewable carbon source of the future: an overview of CO₂ capture from the atmosphere. *Energy & Environmental Science* **2012**, *5* (7).
260. Krekel, D.; Samsun, R. C.; Peters, R.; Stolten, D., The separation of CO₂ from ambient air – A techno-economic assessment. *Applied Energy* **2018**, *218*, 361-381.
261. van der Giesen, C.; Meinrenken, C. J.; Kleijn, R.; Sprecher, B.; Lackner, K. S.; Kramer, G. J., A Life Cycle Assessment Case Study of Coal-Fired Electricity Generation with Humidity Swing Direct Air Capture of CO₂ versus MEA-Based Postcombustion Capture. *Environ Sci Technol* **2017**, *51* (2), 1024-1034.
262. Shi, X.; Xiao, H.; Lackner, K. S.; Chen, X. J. A. C., Capture CO₂ from ambient air using nanoconfined ion hydration. *Angewandte Chemie* **2016**, *128* (12), 4094-4097.
263. House, K. Z.; Baclig, A. C.; Ranjan, M.; van Nierop, E. A.; Wilcox, J.; Herzog,

- H. J., Economic and energetic analysis of capturing CO₂ from ambient air. *Proc Natl Acad Sci U S A* **2011**, *108* (51), 20428-33.
264. Rubin, E. S.; Davison, J. E.; Herzog, H. J., The cost of CO₂ capture and storage. *International Journal of Greenhouse Gas Control* **2015**, *40*, 378-400.
265. Brethomé, F. M.; Williams, N. J.; Seipp, C. A.; Kidder, M. K.; Custelcean, R., Direct air capture of CO₂ via aqueous-phase absorption and crystalline-phase release using concentrated solar power. *Nature Energy* **2018**, *3* (7), 553-559.
266. Kang, D.; Lee, M.; Lim, H. S.; Lee, J. W., Chemical looping partial oxidation of methane with CO₂ utilization on the ceria-enhanced mesoporous Fe₂O₃ oxygen carrier. *Fuel* **2018**, *215*, 787-798.
267. Neal, L. M.; Shafiefarhood, A.; Li, F., Dynamic Methane Partial Oxidation Using a Fe₂O₃@La_{0.8}Sr_{0.2}FeO_{3-δ} Core-Shell Redox Catalyst in the Absence of Gaseous Oxygen. *ACS Catalysis* **2014**, *4* (10), 3560-3569.
268. Zhang, J.; Haribal, V.; Li, F., Sr Perovskite nanocomposites as effective CO₂-splitting agents in a cyclic redox scheme. *Sci Adv* **2017**, *3* (8), e1701184.
269. Zeng, L.; Cheng, Z.; Fan, J. A.; Fan, L.-S.; Gong, J., Metal oxide redox chemistry for chemical looping processes. *Nature Reviews Chemistry* **2018**.
270. Kathe, M.; Empfield, A.; Sandvik, P.; Fryer, C.; Zhang, Y.; Blair, E.; Fan, L.-S., Utilization of CO₂ as a partial substitute for methane feedstock in chemical looping methane-steam redox processes for syngas production. *Energy & Environmental Science* **2017**, *10* (6), 1345-1349.
271. Zhao, X.; Zhou, H.; Sikarwar, V. S.; Zhao, M.; Park, A.-H. A.; Fennell, P. S.; Shen, L.; Fan, L.-S., Biomass-based chemical looping technologies: the good, the bad and the future. *Energy & Environmental Science* **2017**, *10* (9), 1885-1910.
272. Huang, C.; Wu, J.; Chen, Y.-T.; Tian, M.; Rykov, A. I.; Hou, B.; Lin, J.; Chang, C.-R.; Pan, X.; Wang, J.; Wang, A.; Wang, X., In situ encapsulation of iron(0) for solar thermochemical syngas production over iron-based perovskite material. *Communications Chemistry* **2018**, *1* (1).
273. Galvita, V. V.; Poelman, H.; Bliznuk, V.; Detavernier, C.; Marin, G. B., CeO₂-Modified Fe₂O₃ for CO₂ Utilization via Chemical Looping. *Industrial & Engineering Chemistry Research* **2013**, *52* (25), 8416-8426.
274. Giannozzi, P.; Baroni, S.; Bonini, N.; Calandra, M.; Car, R.; Cavazzoni, C.; Ceresoli, D.; Chiarotti, G. L.; Cococcioni, M.; Dabo, I. J. J. o. p. C. m., QUANTUM ESPRESSO: a modular and open-source software project for quantum simulations of materials. **2009**, *21* (39), 395502.
275. Anisimov, V. I.; Zaanen, J.; Andersen, O. K. J. P. R. B., Band theory and Mott insulators: Hubbard U instead of Stoner I. **1991**, *44* (3), 943.
276. Heinemann, M.; Eifert, B.; Heiliger, C. J. P. R. B., Band structure and phase stability of the copper oxides Cu₂O, CuO, and Cu₄O₃. **2013**, *87* (11), 115111.
277. Boateng, I. W.; Tia, R.; Adei, E.; Dzade, N. Y.; Catlow, C. R. A.; De Leeuw, N. H. J. P. C. C. P., A DFT+ U investigation of hydrogen adsorption on the LaFeO₃ (010) surface. **2017**, *19* (10), 7399-7409.
278. Zhang, R.; Alamdari, H.; Kaliaguine, S., Water vapor sensitivity of nanosized La(Co, Mn, Fe)_{1-x}(Cu, Pd)_xO₃ perovskites during NO reduction by C₃H₆ in the presence of oxygen. *Applied Catalysis B: Environmental* **2007**, *72* (3-4), 331-341.
279. Yang, W.; Zhang, R.; Chen, B.; Duprez, D.; Royer, S., New Aspects on the

Mechanism of C₃H₆ selective catalytic reduction of NO in the presence of O₂ over LaFe_{1-x}(Cu, Pd)_xO_{3-δ} perovskites. *Environ Sci Technol* **2012**, *46* (20), 11280-8.

280. Labhassetwar, N.; Saravanan, G.; Kumar Megarajan, S.; Manwar, N.; Khobragade, R.; Doggali, P.; Grasset, F., Perovskite-type catalytic materials for environmental applications. *Sci Technol Adv Mater* **2015**, *16* (3), 036002.

281. Guo, S.; Wu, H.; Puleo, F.; Liotta, L., B-Site Metal (Pd, Pt, Ag, Cu, Zn, Ni) Promoted La_{1-x}Sr_xCo_{1-y}FeyO_{3-δ} Perovskite Oxides as Cathodes for IT-SOFCs. *Catalysts* **2015**, *5* (1), 366-391.

282. Li, P.; Zhang, R.; Liu, N.; Royer, S., Efficiency of Cu and Pd substitution in Fe-based perovskites to promote N₂ formation during NH₃ selective catalytic oxidation (NH₃-SCO). *Applied Catalysis B: Environmental* **2017**, *203*, 174-188.

283. Peng, Q.; Shan, B.; Wen, Y.; Chen, R., Enhanced charge transport of LaFeO₃ via transition metal (Mn, Co, Cu) doping for visible light photoelectrochemical water oxidation. *International Journal of Hydrogen Energy* **2015**, *40* (45), 15423-15431.

284. Zheng, Y.; Li, K.; Wang, H.; Tian, D.; Wang, Y.; Zhu, X.; Wei, Y.; Zheng, M.; Luo, Y., Designed oxygen carriers from macroporous LaFeO₃ supported CeO₂ for chemical-looping reforming of methane. *Applied Catalysis B: Environmental* **2017**, *202*, 51-63.

285. Katz, M. B.; Graham, G. W.; Duan, Y.; Liu, H.; Adamo, C.; Schlom, D. G.; Pan, X., Self-regeneration of Pd-LaFeO₃ catalysts: new insight from atomic-resolution electron microscopy. *J Am Chem Soc* **2011**, *133* (45), 18090-3.

286. Onn, T. M.; Monai, M.; Dai, S.; Fonda, E.; Montini, T.; Pan, X.; Graham, G. W.; Fornasiero, P.; Gorte, R. J., Smart Pd Catalyst with Improved Thermal Stability Supported on High-Surface-Area LaFeO₃ Prepared by Atomic Layer Deposition. *J Am Chem Soc* **2018**, *140* (14), 4841-4848.

287. Liu, C. Y.; Bard, A. J., Pressure-induced insulator conductor transition in a photoconducting organic liquid-crystal film. *Nature* **2002**, *418* (6894), 162-4.

288. Luyben, W. L., Design and Control of a Methanol Reactor/Column Process. *Industrial & Engineering Chemistry Research* **2010**, *49* (13), 6150-6163.

289. Jones, J. H. J. P. M. R., The cativa™ process for the manufacture of acetic acid. **2000**, *44* (3), 94-105.

290. Laboratory, U. S. N. E. T., Types of coal-derived chemicals <https://www.netl.doe.gov/coal/gasification> U.S. Department of Energy, **2016**.

291. Gaikwad, A. M.; Khau, B. V.; Davies, G.; Hertzberg, B.; Steingart, D. A.; Arias, A. C., A High Areal Capacity Flexible Lithium-Ion Battery with a Strain-Compliant Design. *Advanced Energy Materials* **2015**, *5* (3).

292. Kim, D. H.; Lu, N.; Ghaffari, R.; Kim, Y. S.; Lee, S. P.; Xu, L.; Wu, J.; Kim, R. H.; Song, J.; Liu, Z.; Viventi, J.; de Graff, B.; Elolampi, B.; Mansour, M.; Slepian, M. J.; Hwang, S.; Moss, J. D.; Won, S. M.; Huang, Y.; Litt, B.; Rogers, J. A., Materials for multifunctional balloon catheters with capabilities in cardiac electrophysiological mapping and ablation therapy. *Nat Mater* **2011**, *10* (4), 316-23.

293. Kim, D.-H.; Lu, N.; Ma, R.; Kim, Y.-S.; Kim, R.-H.; Wang, S.; Wu, J.; Won, S. M.; Tao, H.; Islam, A. J. s., Epidermal electronics. **2011**, *333* (6044), 838-843.

294. Zhou, G.; Li, F.; Cheng, H.-M., Progress in flexible lithium batteries and future prospects. *Energy Environ. Sci.* **2014**, *7* (4), 1307-1338.

295. Khan, Y.; Ostfeld, A. E.; Lochner, C. M.; Pierre, A.; Arias, A. C., Monitoring of

- Vital Signs with Flexible and Wearable Medical Devices. *Adv Mater* **2016**, *28* (22), 4373-95.
296. Kim, J. S.; Ko, D.; Yoo, D. J.; Jung, D. S.; Yavuz, C. T.; Kim, N. I.; Choi, I. S.; Song, J. Y.; Choi, J. W., A half millimeter thick coplanar flexible battery with wireless recharging capability. *Nano Lett* **2015**, *15* (4), 2350-7.
297. Peng, L.; Peng, X.; Liu, B.; Wu, C.; Xie, Y.; Yu, G., Ultrathin two-dimensional MnO₂/graphene hybrid nanostructures for high-performance, flexible planar supercapacitors. *Nano Lett* **2013**, *13* (5), 2151-7.
298. Schedin, F.; Geim, A. K.; Morozov, S. V.; Hill, E. W.; Blake, P.; Katsnelson, M. I.; Novoselov, K. S., Detection of individual gas molecules adsorbed on graphene. *Nat Mater* **2007**, *6* (9), 652-5.
299. Fu, K. K.; Cheng, J.; Li, T.; Hu, L., Flexible Batteries: From Mechanics to Devices. *ACS Energy Letters* **2016**, *1* (5), 1065-1079.
300. Gwon, H.; Hong, J.; Kim, H.; Seo, D.-H.; Jeon, S.; Kang, K., Recent progress on flexible lithium rechargeable batteries. *Energy Environ. Sci.* **2014**, *7* (2), 538-551.
301. Kammoun, M.; Berg, S.; Ardebili, H., Stretchable spiral thin-film battery capable of out-of-plane deformation. *Journal of Power Sources* **2016**, *332*, 406-412.
302. De Volder, M. F.; Tawfick, S. H.; Baughman, R. H.; Hart, A. J. J. s., Carbon nanotubes: present and future commercial applications. **2013**, *339* (6119), 535-539.
303. Nyholm, L.; Nyström, G.; Mhramyan, A.; Strømme, M. J. A. M., Toward flexible polymer and paper-based energy storage devices. **2011**, *23* (33), 3751-3769.
304. Liu, W.; Chen, Z.; Zhou, G.; Sun, Y.; Lee, H. R.; Liu, C.; Yao, H.; Bao, Z.; Cui, Y. J. A. M., 3D porous sponge-inspired electrode for stretchable lithium-ion batteries. **2016**, *28* (18), 3578-3583.
305. Xu, Y.; Zhao, Y.; Ren, J.; Zhang, Y.; Peng, H., An All-Solid-State Fiber-Shaped Aluminum-Air Battery with Flexibility, Stretchability, and High Electrochemical Performance. *Angew Chem Int Ed Engl* **2016**, *55* (28), 7979-82.
306. Zhang, Y.; Zhao, Y.; Ren, J.; Weng, W.; Peng, H., Advances in Wearable Fiber-Shaped Lithium-Ion Batteries. *Adv Mater* **2016**, *28* (22), 4524-31.
307. Kwon, Y. H.; Woo, S. W.; Jung, H. R.; Yu, H. K.; Kim, K.; Oh, B. H.; Ahn, S.; Lee, S. Y.; Song, S. W.; Cho, J.; Shin, H. C.; Kim, J. Y., Cable-type flexible lithium ion battery based on hollow multi-helix electrodes. *Adv Mater* **2012**, *24* (38), 5192-7, 5145.
308. Lin, H.; Weng, W.; Ren, J.; Qiu, L.; Zhang, Z.; Chen, P.; Chen, X.; Deng, J.; Wang, Y.; Peng, H., Twisted aligned carbon nanotube/silicon composite fiber anode for flexible wire-shaped lithium-ion battery. *Adv Mater* **2014**, *26* (8), 1217-22.
309. Sun, H.; Zhang, Y.; Zhang, J.; Sun, X.; Peng, H., Energy harvesting and storage in 1D devices. *Nature Reviews Materials* **2017**, *2* (6).
310. Xu, S.; Zhang, Y.; Cho, J.; Lee, J.; Huang, X.; Jia, L.; Fan, J. A.; Su, Y.; Su, J.; Zhang, H.; Cheng, H.; Lu, B.; Yu, C.; Chuang, C.; Kim, T. I.; Song, T.; Shigeta, K.; Kang, S.; Dagdeviren, C.; Petrov, I.; Braun, P. V.; Huang, Y.; Paik, U.; Rogers, J. A., Stretchable batteries with self-similar serpentine interconnects and integrated wireless recharging systems. *Nat Commun* **2013**, *4*, 1543.
311. Song, Z.; Ma, T.; Tang, R.; Cheng, Q.; Wang, X.; Krishnaraju, D.; Panat, R.; Chan, C. K.; Yu, H.; Jiang, H., Origami lithium-ion batteries. *Nat Commun* **2014**, *5*, 3140.
312. Bonatti, C.; Mohr, D. J. M. S.; A, E., Anisotropic viscoplasticity and fracture of fine grained metallic aluminum foil used in Li-ion batteries. **2016**, *654*, 329-343.

313. Khare, K.; Zhou, J.; Yang, S., Tunable open-channel microfluidics on soft poly(dimethylsiloxane) (PDMS) substrates with sinusoidal grooves. *Langmuir* **2009**, *25* (21), 12794-9.
314. Stangl, J.; Holý, V.; Bauer, G., Structural properties of self-organized semiconductor nanostructures. *Reviews of Modern Physics* **2004**, *76* (3), 725-783.
315. Li, Y.; Qian, F.; Xiang, J.; Lieber, C. M., Nanowire electronic and optoelectronic devices. *Materials Today* **2006**, *9* (10), 18-27.
316. Yao, P.; Zhu, B.; Zhai, H.; Liao, X.; Zhu, Y.; Xu, W.; Cheng, Q.; Jayyosi, C.; Li, Z.; Zhu, J.; Myers, K. M.; Chen, X.; Yang, Y., PVDF/Palygorskite Nanowire Composite Electrolyte for 4 V Rechargeable Lithium Batteries with High Energy Density. *Nano Lett* **2018**, *18* (10), 6113-6120.
317. Wang, X.; Zhai, H.; Qie, B.; Cheng, Q.; Li, A.; Borovilas, J.; Xu, B.; Shi, C.; Jin, T.; Liao, X.; Li, Y.; He, X.; Du, S.; Fu, Y.; Dontigny, M.; Zaghbi, K.; Yang, Y., Rechargeable solid-state lithium metal batteries with vertically aligned ceramic nanoparticle/polymer composite electrolyte. *Nano Energy* **2019**, *60*, 205-212.
318. Xu, B.; Zhai, H.; Liao, X.; Qie, B.; Mandal, J.; Gong, T.; Tan, L.; Yang, X.; Sun, K.; Cheng, Q.; Chen, M.; Miao, Y.; Wei, M.; Zhu, B.; Fu, Y.; Li, A.; Chen, X.; Min, W.; Nan, C.-W.; Lin, Y.-H.; Yang, Y., Porous insulating matrix for lithium metal anode with long cycling stability and high power. *Energy Storage Materials* **2019**, *17*, 31-37.
319. Xiao, H.; Shi, X.; Zhang, Y.; Liao, X.; Hao, F.; Lackner, K. S.; Chen, X., The catalytic effect of H₂O on the hydrolysis of CO₃(²⁻) in hydrated clusters and its implication in the humidity driven CO₂ air capture. *Phys Chem Chem Phys* **2017**, *19* (40), 27435-27441.
320. Shi, X.; Xiao, H.; Liao, X.; Armstrong, M.; Chen, X.; Lackner, K. S., Humidity effect on ion behaviors of moisture-driven CO₂ sorbents. *J Chem Phys* **2018**, *149* (16), 164708.